IN SITU TEM MECHANICAL TESTING OF IRRADIATED OXIDE DISPERSION STRENGTHENED ALLOYS

by

Kayla H. Yano

A Dissertation

Submitted to the Faculty of Purdue University

In Partial Fulfillment of the Requirements for the degree of

Doctor of Philosophy
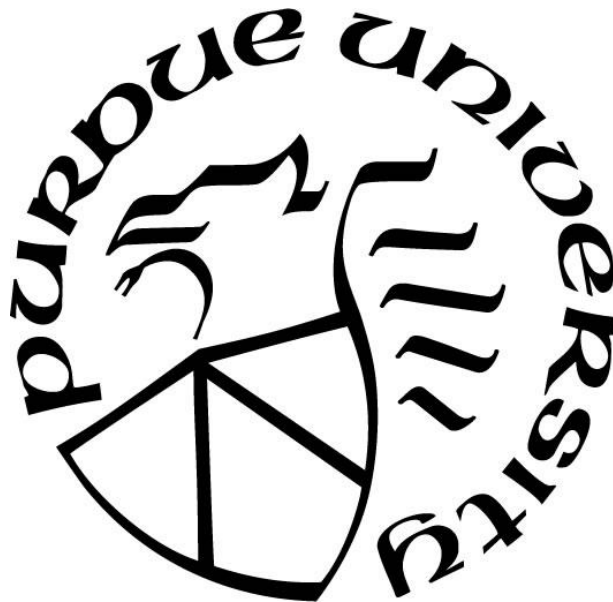
School of Materials Engineering

West Lafayette, Indiana

May 2019

THE PURDUE UNIVERSITY GRADUATE SCHOOL
STATEMENT OF COMMITTEE APPROVAL

Dr. Janelle Wharry, Co-Chair

    School of Nuclear Engineering

Dr. Maria Okuniewski, Co-Chair

    School of Materials Engineering

Dr. David Johnson

    School of Materials Engineering

Dr. Xinghang Zhang

    School of Materials Engineering

Approved by:

    Dr. David Bahr

        Head of the Graduate Program

To my grandparents,

Terou & Jane Yano and Glenn & Katherine Edmison,

you laid the foundation.

I am forever obliged.

ACKNOWLEDGMENTS

Dr. Janelle Wharry, thank you for being my advisor and for making this document and degree possible. Thank you for bringing me on in Boise, and thanks for keeping me on at Purdue. You've been an inspiration to me since day one. I am so grateful that I got to work with you and learn from you. You've made me a better scientist. I only hope someday to be as confident, composed, and impressive as you are while balancing all the projects, students, and service projects that you do.

Without my family this journey would not have been possible. Mom and Dad, thanks for supporting me through all my endeavors. Treya and Aliya, you're amazing sisters and amazing people. Annie, my love, thanks for leaving Idaho for a couple of years to keep me grounded and sane throughout this adventure. Carl and Sue, thanks for being the best parents-in-almost-law. Kaze and Penny, thanks for being (mostly) good fur babies.

I'd be remiss to not thank my friends for putting up with my nonsense these past 4 years: Kat, Brittni, Kendra, little Sara, Garrett, Allison, and the Boo Bears! Thanks for listening to my gripes and rants, being understanding when I've been absent, and always ready to get down when I've been around. Thank you to my group members, Keyou and Priyam for always keeping things in the lab lively and encouraging my Pokémon Go addiction. You're almost there! Best of luck to the new members, y'all are gonna kill it.

TABLE OF CONTENTS

LIST OF TABLES

LIST OF FIGURES

NOMENCLATURE

$2a$	major axis crack length		DBH	Dispersed Barrier Hardening
$2b$	minor axis crack length		DBTT	Ductile-to-Brittle Transition Temperature
a	lattice parameter			
A_m	amplitude		d_g	grain diameter
A	area of crack or cross section		$\overline{d_{ob}}$	weighted average diameter of obstacles
$\boldsymbol{a}$	crack length			
$\boldsymbol{A}$	stress proportionality constant		dpa	Displacements Per Atom
a_0	initial crack length		ds	length increment along Γ path
A_{pl}	area under plastic portion of load-displacement curve		$\mathbf{E}$	potential energy
			E	Young's (elastic) modulus
APT	Atom Probe Tomography		E'	Young's modulus modified for plane stress conditions
$\mathbf{b}$	Burger's vector			
$\boldsymbol{B}$	offset factor		E_0	equilibrium bond energy
B	thickness		EBSD	Electron BackScatter Diffraction
bcc	Body-Centered Cubic		E_d	displacement energy
bct	Body-Centered Tetragonal		EDS	Energy Dispersive x-ray Spectroscopy
c	flow strain			
CAES	Center for Advanced Energy Studies		EELS	Electron Energy Loss Spectroscopy
CCD	Charge-Coupled Device		E_i	projectile energy
C_L	longitudinal wave velocity		E_t	total energy
CT	Compact Tension		F	force between atoms
C_T	transverse wave velocity		F/M	Ferritic/Martensitic
CTOD	Crack Tip Opening Displacement		fcc	Face-Centered Cubic
d	diameter of curved dislocation – characteristic length		FEM	Finite Element Modeling
			FIB	Focus Ion Beam
$\boldsymbol{d}$	displacement		f_{ij}	dimensionless function of θ
dA	incremental crack area		fps	Frames Per Second

$f\left(\frac{a}{w}\right)$	dimensionless geometry factor	$K_{Q,J}$	fracture toughness calculated through J-integral approach
G	Griffith energy release rate	k_t	Inglis stress concentration factor
g_{ij}	dimensionless function of θ for m^{th} term	l	obstacle spacing
GND	Geometrically Necessary Dislocations	L	particle obstacle spacing
hcp	Hexagonal Close-Packed	l_0	initial length
HRR	Hutchinson, Rice, Rosengren method	L_{beam}	length of entire beam
H_v	Vickers hardness	LEFM	Linear Elastic Fracture Mechanics
I_n	integration constant	l_i	instantaneous length
IVAS	Integrated Visualization and Analysis Software	L_{notch}	length between notch and indenter tip
J	energy release rate in J-integral approach	L_{ob}	average obstacle spacing
J_{el}	contribution to J-integral from elastic deformation	L_p	length of pile-up
J_{IC}	critical J value for fracture in Mode I	M	Taylor factor
		N	dislocation number density
J_{pl}	contribution to J-integral from plastic deformation	n'	number of dislocations in pile-up
k	constant in HRR eqn.	n	strain hardening exponent
k	spring constant	$\boldsymbol{n}$	stress exponent
k'	geometry of dislocations constant	n_j	unit vectors normal to Γ path
K	strength coefficient	N_{ob}	sum number density of obstacles
K	stress intensity factor	ODS	Oxide Dispersion Strengthened
K_I	stress intensity factor Mode I	P	applied load
K_{IC}	fracture toughness in Mode I	P_c	cohesive strength
K_{II}	stress intensity factor Mode II	PCC	Percentage of Correct Classification
K_{III}	stress intensity factor Mode III	PED	Precession Electron Diffraction
		PKA	Primary Knock-on Atom
		r	atomic spacing
		$\mathbf{r}$	polar coordinate
		r_0	equilibrium bond spacing
		r_c	dislocation core radius

r_{crack}	radius of crack tip	δ	crack tip opening displacement
r_{part}	particle radius	Δa	crack growth
RIS	Radiation Induced Segregation	Δl	change in length
SEM	Scanning Electron Microscopy	$\Delta\sigma_d$	change in stress at interface
SRIM	Stopping Range of Ions in Matter	$\Delta\sigma_y$	yield stress increment
STEM	Scanning Transmission Electron Microscopy	**ε**	displacement efficiency
		ε	strain
$\bar{T}$	average recoil energy	ε_0	strain at yield strength
T_d	line tension	ε_1	maximum remote normal strain
TEM	Transmission Electron Microscopy	ε_{ij}	strain tensors
T_i	traction vector components	$\tilde{\varepsilon}_{ij}$	dimensionless function of n and θ in HRR eqn.
TIA	Tecnai Imaging Analysis		
U	stored strain energy	ε_t	true strain
u_i	displacement vector components	η	dimensionless constant for J-integral calculation
w	strain energy density		
W	width	θ	polar coordinate
W_f	work done by external loads	λ	angle between slip direction & load direction
w_s	average source spacing		
W_s	work required to create new surfaces	μ	shear modulus
		v	Poisson's ratio
x_0	sample gauge length	Π	potential energy in plate with crack
XFEM	Extended Finite Element Modeling	Π_0	potential energy of uncracked plate
Y	correction factor for stress intensity	ρ	crack curvature
α	dimensionless constant	**ρ**	dislocation density
α	parameter describing obstacle strength	ρ_s	source density
α'	geometrical constant based on dislocation type	σ	stress
		σ'	stress due to frictional forces required to move dislocation
Γ	counter-clockwise path around crack tip	σ_1	maximum principal stress
		σ_A	stress at crack tip
γ_s	surface energy	σ_c	cohesive stress

σ_{crit}	critical stress
σ_f	fracture strength
σ_{flow}	flow stress
σ_{ij}	stress tensor
$\tilde{\sigma}_{ij}$	dimensionless function of n and θ in HRR eqn.
σ_{xx}	stress in x-plane in x-direction
σ_y	yield strength
σ_{yy}	stress in y-plane in y-direction
σ_0	bulk specimen flow stress
τ	shear stress
τ_0	friction forces to move a dislocation without obstacles
τ_a	resolved shear stress applied by a dislocation
τ_{CRSS}	critical resolved shear stress
τ_{Or}	Orowan Stress
φ	angle between slip normal & load direction

ABSTRACT

Author: Yano, Kayla, H. PhD
Institution: Purdue University
Degree Received: May 2019
Title: In Situ TEM Mechanical Testing in Irradiated Oxide Dispersion Strengthened Alloys.
Committee Chairs: Janelle Wharry & Maria Okuniewski

The objective of this dissertation is to demonstrate the use of in situ TEM mechanical testing to find mechanical properties of as received, self-ion, and proton irradiated Fe-9%Cr ODS. The desire to work at small scale in the characterization of irradiated materials to reduce costs and improve throughput, require the development of novel methods to assess mechanical properties in volume-limited irradiation damage layers. Yet at these micrometer or nanometer scales, the mechanical properties can begin to be impacted by size effects. In this work micropillar compression, cantilever bending, lamellae indentation, and clamped beam fracture testing is conducted on ion-irradiated Fe-9%Cr ODS to find yield stress, elastic modulus, flow stress, and fracture toughness. Micropillars in compression allow us to define a minimum sample dimension, which approaches the obstacle spacing of the material, at which size effects are observed. This relationship between sample dimension and obstacle spacing defined through micropillar compression is extended to a new testing geometry, cantilever bending, and material property, flow stress. Lessons learned during the cantilever bending informed the clamped beam design for conducting fracture testing on a ductile engineering alloy at micrometer scales. Finally, lamellae indentation was conducted to link qualitative observations of the microstructure under load with literature strength of obstacle values. By combining an understanding of the microstructure of irradiated Fe-9%Cr ODS and the in situ TEM technique, one can find the bulk-like mechanical properties of ion irradiated Fe-9%Cr ODS.

1. INTRODUCTION

In the study of irradiated materials, there is a desire to work at reduced specimen dimensions. Neutron irradiation is a costly affair; both in large sums of money and in large amounts of time [1]. First, reactor time is precious and if smaller samples can be irradiated, more samples can be included in the reactor at once. Secondly, after the irradiation is complete, working at small dimensions reduces the radioactivity of the sample and therefore reduces the use restrictions on those samples. Again, this saves time and money by allowing the sample to be examined at institutions with a variety of different radiological safety measures.

Ion irradiation is often used as a substitute for neutron irradiation because it reduces monetary costs, the time required to reach relevant dose, and the radioactivity of the materials [1]. While the use of ion irradiation may result in different microstructural damage than neutrons [1], the major constraint is the shallow penetration depth of irradiating ions as compared to neutrons. Fe^{2+} ions penetrate only to about 1 micron in depth, while protons can travel up to tens of microns into the material. A comparison of damage profiles is seen in Figure 1.1, where simulations using the Stopping Range of Ions in Matter (SRIM) program have been run in an Fe-9%Cr alloy [2]. This results in a limited volume of irradiated material to be evaluated. Therefore, in both neutron and ion irradiation testing, there is a need to work at the micro- and nanoscale.

The mechanical properties of structural materials for nuclear reactors are of major concern in the development of new alloys for use both in life-extension efforts of existing light water reactors and in advanced reactor designs [3]. These mechanical properties are driven by the microstructural changes induced by irradiation. In Fe-9%Cr oxide dispersion strengthened (ODS) the differences between neutron irradiation and charged particle irradiation manifest in oxide cluster size; the largest clusters seen in proton irradiation, then self-ion irradiation, and

finally the smallest clusters with the finest dispersion in neutron irradiation [4,5]. However, irradiation (self-ion, proton, and neutron), at similar dose and temperature, induce dislocation loops of a similar size and density in Fe-9%Cr ODS [6,7]. These changes in microstructure can lead to changes in mechanical properties, specifically irradiation hardening [8].

These combined needs of reduced sample size and mechanical testing capabilities can be addressed through transmission electron microscopic (TEM) in situ mechanical testing. TEM techniques use small-scale, electron transparent samples, which can be manufactured out of neutron irradiated samples or from the shallow damaged layers of ion irradiated materials. A depth-sensing TEM in situ mechanical testing holder enables one to collect quantitative load-displacement data, while simultaneously observing the material microstructure, lending insight into qualitative elastic-plastic deformation mechanisms. TEM in situ mechanical testing has often been used in studying mechanical properties and deformation mechanisms in unirradiated materials [9,10]. Some of these studies include compression testing of single and bicrystalline Cu micropillars to better understand twinning behavior [11], dislocation nucleation and escape in Al [12], fracture of stainless steel [13], and hardening of Cu through tensile testing [14]. In contrast, there are few in situ TEM mechanical studies on irradiated materials. This is an area ripe for better understanding of the effects of irradiation on mechanical properties through irradiation induced defects and phenomena.

Yet, one major hurdle in utilizing in situ TEM testing is the impact of size effects on the mechanical properties. At such small micron or nanometer scales, materials can behave differently than bulk samples. Mechanical properties of materials are determined by microstructure [15,16]. For instance, strengthening is dependent on three main mechanisms: solid solution strengthening, dispersion or precipitate strengthening, and grain size refinement

[15]. All three mechanisms work to retard the movement of dislocations, increasing the strength of the material. When reducing the size of a sample, these microstructural elements begin to be superseded by the dimensional constraints of the sample. Essentially, the smaller the dimensions, the less representative of the microstructure the sample becomes [17].

This first results in a reduction of the measured strength as compared to the bulk, but then as the sample dimensions reduce even further, an inflation of the mechanical properties can be seen in theoretical work adapted from Hosemann et al. (blue curve - Figure 1.2) [18]. The threshold between inflated results and bulk measurements has been shown to reach smaller dimensions in irradiated materials (red curve) due to the increased obstacle density from irradiation damage. This theoretically allows for small, nano- to micron-scale samples without size effects. As such, in situ TEM techniques are promising approaches for mechanical testing of irradiated materials. **This dissertation will investigate the effectiveness and applicability of in situ TEM mechanical testing techniques for a model Fe-9%Cr ODS alloy subject to multiple irradiation conditions.**
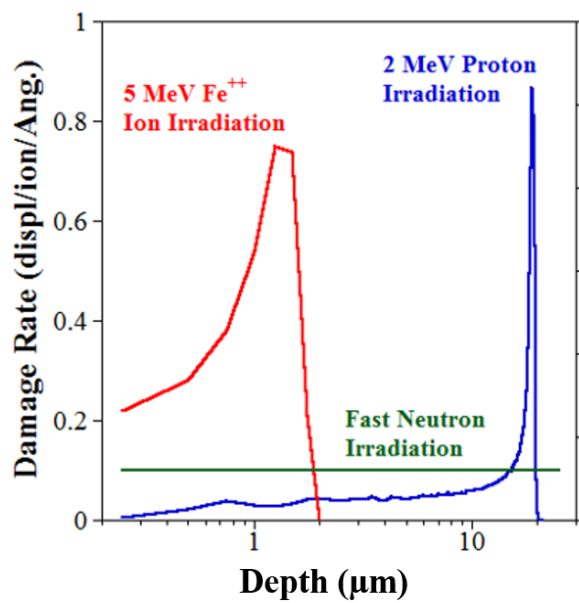
Figure 1.1 - Damage profiles of Fe^{2+} ions, protons, and neutrons as simulated by SRIM on an Fe-9%Cr material
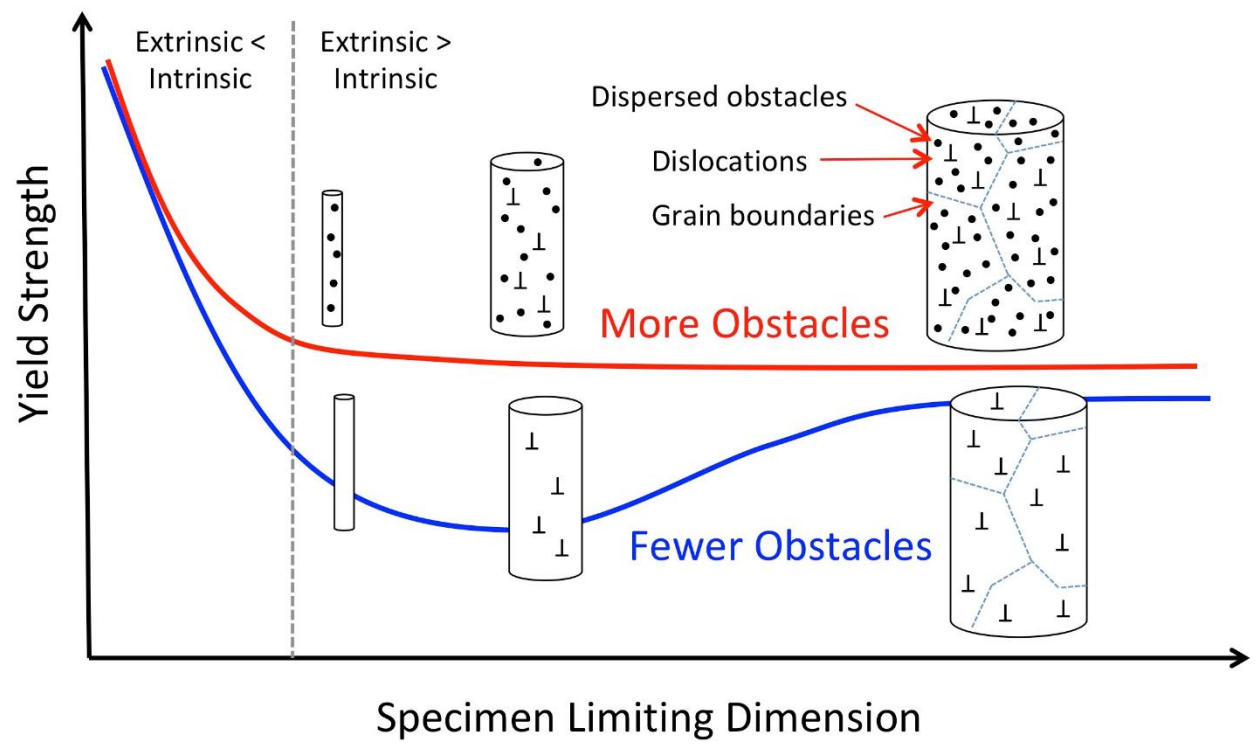
Figure 1.2 – Proposed behavior of polycrystalline materials as specimen dimension reduces in both irradiated and unirradiated materials – reproduced [11]

2. BACKGROUND

A version of this chapter has been published in the following thesis:

1. K.H. Yano, *In Situ TEM Micropillar Compression Testing in Irradiated Oxide Dispersion Strengthened Alloys*. Boise State University, 2017.

2.1   Mechanical Responses in Metals

2.1.1   Bond Stretching and Elastic Deformation

The primary bonding type for metals is metallic bonding, where a "sea of electrons" are shared amongst the atoms [15]. Atoms are organized into crystal structures, with steels most often falling into body-centered cubic (bcc) or face-centered cubic (fcc) structures. In these structures, atoms have an equilibrium spacing, r_0, that minimizes the energy, E_0. This potential energy, $\mathbf{E}$, is shown as a function of atomic spacing, r, in Figure 2.1 [15].

The force, F, between atoms is found by taking the derivative of potential energy with respect to the atomic spacing, r. This curve is shown in Figure 2.2, where strongly bonded atoms have a steep slope at the equilibrium spacing, whereas weakly bonded atoms have a gradual slope at the equilibrium spacing. This slope, or derivative of the force between bonds at the equilibrium spacing is the Elastic or Young's modulus, E: the resistance to stretching (or compression) of the atomic bonds. Elastic deformation is nonpermanent [15].

2.1.2   Defects in Crystalline Materials and Plastic Deformation

Imperfections in crystalline materials are irregularities in the lattice and are generally categorized by geometry. Point defects are on the order of 1 or 2 atoms and consist of vacancies, interstitials, or substitutional atoms. A two-dimensional representation of a crystal lattice is shown with the various point defects defined in Figure 2.3 [15].

Linear defects are called dislocations, and these can be categorized as either edge or screw type, though most dislocations found in materials are of a mixed nature. Figure 2.4 shows dislocations in a three-dimensional crystal. Edge dislocations arise from an incomplete plane, or half-plane, of atoms. The edge of which forms the dislocation line. Screw dislocations occur where the material has been sheared, resulting in planes that have slipped or shifted with respect to the remaining planes [15,16].

Dislocations are described by their Burger's vector, **b**, which defines the magnitude and direction of the lattice distortion. The Burger's vector remains the same though the dislocation changes from screw to mixed to edge in type. Screw dislocations have a Burger's vector parallel to the line direction of the dislocation, whereas edge dislocations have a Burger's vector perpendicular to the line direction [15].

Two-dimensional defects, or interfacial defects, consist of external surfaces, grain boundaries, twin boundaries, phase boundaries, and stacking faults. In polycrystalline materials, grains are regions where the crystal has different orientations. Where these grains come together is an interfacial defect which consists of a dislocation array and can be categorized based on the misorientation. Twin boundaries are a special type of grain boundary where the atoms across the boundary mirror each other. Phase boundaries can occur in materials with multiple phases. Stacking faults can occur when there is a disruption in the arrangement of the close-packed planes [15,16].

Plastic deformation, unlike elastic deformation, is a permanent deformation in the material. Plastic deformation occurs when dislocations move through a material, breaking and reforming atomic bonds as the dislocation progresses [15]. The yield strength, σ_y, is the point at which plastic deformation begins [16]. Figure 2.5 shows the motion of an edge dislocation

through a crystalline material. As a shear load is applied the extra half plane of atoms moves from column A to B, and then to the edge of the crystal. The slip plane is where the atoms are breaking and reforming bonds. This is the preferred plane for dislocations to move along, and they move in the slip direction. Combining the slip plane and slip direction results in a slip system. For bcc iron there are multiple slip plane families {110}, {211}, {321} with a single slip direction <111>. The resulting Burger's vector is b=a/2<111>, where *a* is the lattice parameter [15].

In a single crystal, plastic deformation occurs along the slip planes when the load applied results in a critical resolved shear stress, τ_{CRSS}, on the material. The τ_{CRSS} is related to the material yield strength and the orientation of the crystal with respect to the applied load as shown in Equation 2.1 [15].

$$\sigma_y = \frac{\tau_{CRSS}}{(cos\varphi cos\lambda)_{max}}$$

Equation 2.1

φ and λ are the angles between the slip normal and slip direction, respectively, to the loading axis, as demonstrated in Figure 2.6a. Figure 2.6b shows the idealized macroscopic slip events in a single crystal [15].

Polycrystalline materials have dislocations that move the same way as single crystals, however grain boundaries can hinder dislocation motion [19]. This impacts the strength of the material, a topic for subsequent discussion.

2.1.3   Fracture in Metals

Fracture is the separation of a solid body into two or more parts on the macroscopic scale, meaning at the atomic level, the attractive force bonding atoms has been broken by the application of stresses [16,20]. There are six principle loads that can cause fracture, 1) slow

application of external loads, 2) rapid application of external loads, or impact, 3) cyclic loading, or fatigue, 4) time-dependent deformation, or creep, 5) internal stresses, and 6) environmental effects. The process of fracture caused by these loads can be categorized in the following: 1) damage accumulation, 2) nucleation of one or more cracks or voids, 3) crack growth or coalescence [16]. Essentially, when the energy for crack growth is sufficient to overcome the material resistance, a crack (two free surfaces) is formed and under continued loading the crack propagates until the material is split in two.

Understanding fracture in this way is the energy criterion approach, first proposed by Griffith but developed to the present version by Irwin [20]. These initial efforts examine the behavior of fracture in materials that behave linear elastically, though some corrections for small amounts of plasticity have been considered. Subsequent work to account for nonlinear, plastic, behavior builds upon the linear elastic fracture mechanics (LEFM) models. Therefore, we will first derive the LEFM fundamentals, then discuss the elastic-plastic modifications, and finally examine the microstructural mechanisms driving fracture.

2.1.3.1 Linear Elastic Fracture Mechanics

Theoretically, there is a tensile force required to overcome the cohesive force and the bond energy between two atoms. This was first discussed in §2.1.1 and Figure 2.1. Here we will build on this understanding by defining the bond energy, E_0, as [20]:

$$E_0 = \int_{r_o}^{\infty} P \, dr \hspace{3cm} \text{Equation 2.2}$$

Where, r_0 is still the equilibrium spacing and P is the applied load. This can be seen graphically in Figure 2.7. Approximating the cohesive strength, P_c, as one-half the period of a sine wave where r is the atomic spacing, then the applied force is:

$$P = P_c \sin\left(\frac{\pi x}{r}\right) \hspace{3cm} \text{Equation 2.3}$$

Assuming small displacements and therefore a linear force-displacement relationship, the spring

constant, k, is [20]:

$$k = P_c \frac{\pi}{r} \hspace{3cm} \text{Equation 2.4}$$

Multiplying both sides by the number of bonds per unit area and the sample gage length, x_0, the

spring constant is converted to Young's modulus, E, and the cohesive strength to the cohesive

stress, σ_c [20].

$$\sigma_c = \frac{E\lambda}{\pi x_0} \hspace{3cm} \text{Equation 2.5}$$

The surface energy, γ_s, is one-half the fracture energy per area due to the fact that two surfaces

are created when a material fractures and is estimated as [20]:

$$\gamma_s = \frac{1}{2}\int_0^\lambda \sigma_c \sin\left(\frac{\pi x}{\lambda}\right) dx = \sigma_c \frac{\lambda}{\pi} \hspace{2cm} \text{Equation 2.6}$$

Then substituting equation 2.5 into 2.6, the cohesive stress is given as a function of surface

energy, Young's modulus, and atomic separation by [20]:

$$\sigma_c = \sqrt{\frac{E\gamma_s}{r_0}} \hspace{3cm} \text{Equation 2.7}$$

The theoretical cohesive strength of a material is therefore given by approximately E/π,

yet brittle materials experimentally underperform by 3 to 4 orders of magnitude. Griffith and

others suggested that the flaws in a material must lower the material strength macroscopically by

concentrating the stress locally. This can be seen qualitatively in Figure 2.8a, where stress lines

in the material concentrate at the crack tip. Inglis first demonstrated quantitatively the evidence

of stress concentrations by studying elliptical flaws in flat plates as described in Figure 2.8b [20].

Elliptical flaws have a major axis of length '*2a*' and a minor axis of length '*2b*', while the plate has dimensions $>>2a$ and $>>2b$ so as not to be influenced by the flaw.

The stress at the tip of the major axis is given by [20]:

$$\sigma_A = \sigma\left(1 + \frac{2a}{b}\right)$$
Equation 2.8

Here, the ratio of σ_A/σ is the stress concentration factor, k_t. When $a = b$ the hole is circular, and generally k_t is 3. As $a > b$, the hole sharpens into a crack, with a curvature of $\rho = b^2/a$. so that as $a >> b$ Equation 2.8 becomes [20]:

$$\sigma_A = 2\sigma\sqrt{\frac{a}{\rho}}$$
Equation 2.9

However, there is a problem with this assumption. At an infinitely sharp crack, the curvature approaches zero, such that an infinite stress is predicted. Materials do not behave in this way. Instead, assuming a point where a given material reaches a critical stress and fails, we can say that when $\sigma_A = \sigma_c$ the remote stress estimate for failure is:

$$\sigma_f = \sqrt{\frac{E\gamma_s}{4a}}$$
Equation 2.10 [20]

Yet, even this approximation is insufficient to describe crack propagation. Anderson suggests that one considers a beam under load [20]. Though it may reach the critical stress at the outer fibers, the remainder of the beam has not reached the critical stress and the beam does not fail. A single high stress point does not necessarily result in fracture and failure of a material. To understand this further, Griffith introduced the use of an energy balance in the system, with Irwin refining the approach for ease of use in engineering problems.

Employing the first law of thermodynamics, Griffith postulated that a crack will form (or an existing crack grow) if the total energy decreases or remains constant. Griffith demonstrated the energy balance on an infinitely wide plate, with thickness B, subjected to a constant stress, σ, and with a crack $2a$ long (Figure 2.8c). For this crack to grow, a potential energy must be supplied to overcome the surface energy of the material. Hence, the total energy, E_t, for an increase in the crack area dA can be expressed as the sum of the potential energy, Π, and work to create new surfaces, W_s, over that crack area [20]:

$$\frac{dE_t}{dA} = \frac{d\Pi}{dA} + \frac{dW_s}{dA} = 0 \qquad \text{Equation 2.11}$$

The potential energy is supplied by the internal strain energy and external forces. The potential energy in the plate is defined as a function of the potential energy of the uncracked plate, Π_0, the plate thickness, B, stress applied, σ, crack length, $\boldsymbol{a}$, and Young's modulus, E [20]:

$$\Pi = \Pi_0 - \frac{\pi\sigma^2 \boldsymbol{a}^2 B}{E} \qquad \text{Equation 2.12}$$

The work to create two surfaces is a function of the plate thickness, crack length, and the surface energy of the material [20]:

$$W_s = 4\boldsymbol{a}B\gamma_s \qquad \text{Equation 2.13}$$

Therefore,

$$-\frac{d\Pi}{dA} = \frac{\pi\sigma^2 \boldsymbol{a}}{E} \qquad \text{Equation 2.14}$$

And

$$\frac{dW_s}{dA} = 2\gamma_s \qquad \text{Equation 2.15}$$

Finally, combining Equations 2.14 and 2.15 we can solve for the fracture stress, σ_f:

$$\sigma_f = \sqrt{\frac{E\gamma_s}{\pi \boldsymbol{a}}}$$

Equation 2.16

The Griffith approach can be applied to different crack geometries and while this derivation is for brittle materials, it can also be modified to account for materials with small amounts of plastic flow.

Irwin developed essentially the same model as Griffith but formatted his proposal in an engineering friendly way. He defined an energy release rate, $\boldsymbol{G}$, as the measure of energy available for an increment in crack extension, or the crack driving force [20].

$$\boldsymbol{G} = -\frac{d\Pi}{dA}$$

Equation 2.17

So, for a plate as modeled in Figure 2.8c, $\boldsymbol{G}$, is

$$\boldsymbol{G} = \frac{\pi \sigma^2 \boldsymbol{a}}{E}$$

Equation 2.18

It is now important to discuss the various crack configurations and loading modes that result in closed-form expressions for stresses in the structure, assuming LEFM conditions. When defining a polar coordinate axis with the origin at the crack tip, the following expression defines the stress field in the body [20]:

$$\sigma_{ij} = \left(\frac{\boldsymbol{k}}{\sqrt{\boldsymbol{r}}}\right) f_{ij}(\theta) + \sum_{m=0}^{\infty} A_m \boldsymbol{r}^{\frac{m}{2}} g_{ij}^m(\theta)$$

Equation 2.19

Here, σ_{ij} is the stress tensor, $\boldsymbol{r}$ and θ are the polar coordinates as defined in Figure 2.9a, $\boldsymbol{k}$ is a constant, f_{ij} is a dimensionless function of the θ. In the summation, A_m is the amplitude and g_{ij} is again a dimensionless function of θ for the mth term. While the summation depends on geometry, the first term drives the proportionality of $\frac{1}{\sqrt{r}}$. As r $\rightarrow$0, there is a singularity. This recalls the same failure of Equation 2.9 to describe the stress field at the crack tip. The three crack

configurations where Equation 2.19 is applicable are shown in Figure 2.9b. These can be described as Mode I, opening, Mode II, in-plane shear, and Mode III, out-of-plane shear.

Due to the **k** and f_{ij} factors relying on geometry, it is convenient to replace **k** by the stress intensity factor, K, where $K = \mathbf{k}\sqrt{2\pi}$. Then depending on the mode, K can have subscript K_I, K_{II}, or K_{III}. It is important to note that in Mode I, using cartesian coordinates for the stress tensor, and at $\theta=0$, the stresses in the x and y planes are equal [20]:

$$\sigma_{xx} = \sigma_{yy} = \frac{K_I}{\sqrt{2\pi r}}$$

Equation 2.20

To be useful, K must be linked with the global behavior of the material. Depending on the geometry and loading mode, the expression for K can be adjusted with a correction factor, Y.

$$K_{(I,II,III)} = Y\sigma\sqrt{\pi a}$$

Equation 2.21

Specifically, the K_I factor can be found using an expression of the form:

$$K_I = \frac{P}{B\sqrt{W}} f\left(\frac{a}{w}\right)$$

Equation 2.22

Where P is the load applied, B is the thickness, W is the width, and $f\left(\frac{a}{w}\right)$ is a dimensionless geometry factor.

G, the energy release rate, is a measure of the potential energy from an increment in crack growth. This is a global measure. In contrast, K, the stress intensity factor, is a measure of the stresses, strains, and displacements near the crack tip. This is a local parameter. Combining the two gives a unique relationship for linear elastic materials.

$$G = \frac{K_I^2}{E'}$$

Equation 2.23

Where $E' = E$ for plane stress, and $E' = E/(1 - v^2)$, where v Poisson's ratio, for plane strain conditions. This distinction between plane stress and plane strain will be discussed in later sections.

Attempts to correct for crack tip yielding fall under two methods, the Irwin approach and the strip-yield model. However, both cannot account for extensive yielding. In those cases, the nonlinear material behavior must be considered.

2.1.3.2 Elastic-Plastic Fracture Mechanics

For nonlinear, time-independent behavior in materials, elastic-plastic fracture mechanics applies. This background will cover the J-integral parameter and its use to measure fracture. The J-integral is both an energy parameter and a stress intensity parameter. It characterizes crack tip stresses and strains in a nonlinear elastic material. J is a path-independent integral.

As in LEFM, the J-integral is a measure of the energy release rate. Indeed, the same definition G, in Equation 2.17 can be used here, where J replaces G [20].

$$J = -\frac{d\Pi}{dA}$$
Equation 2.24

Again, Π is the potential energy and A is the area of the crack. The potential energy is given by

$$\Pi = U - W_f$$
Equation 2.25

Where U is the strain energy stored in the body and W_f is the work done by external loads. In fact, J is a more general form of G, where in the case of linear elasticity, $J = G$.

If one were to draw an arbitrary counter-clockwise path (Γ) around a crack tip, as in Figure 2.10, the J-integral is given by

$$J = \int_{\Gamma} \left(w dy - T_i \frac{\partial u_i}{\partial x} ds \right)$$
Equation 2.26

Here, w is the strain energy density, T_i are the traction vector components, while u_i are the

displacement vector components, and ds is a length increment along the path Γ. Strain energy, w

is defined as the integral of the stress tensors, σ_{ij}, with respect to the strain tensors, ε_{ij}.

$$w = \int_0^{\varepsilon_{ij}} \sigma_{ij} d\varepsilon_{ij} \qquad \text{Equation 2.27}$$

The traction, T_i, is essentially the stresses acting at the boundaries of the path and are given by

the stress tensors and the unit vectors normal to the path, n_j.

$$T_i = \sigma_{ij} n_j \qquad \text{Equation 2.28}$$

Independently, Hutchinson, Rice, and Rosengren (HRR) showed that the J-integral can

define the crack tip conditions in a nonlinear elastic material by assuming a power law

relationship between plastic stress and strain. This relationship is known as the Ramberg-Osgood

equation, where σ_y is generally the yield strength, ε_0 is σ_y/E, $\boldsymbol{\alpha}$ is a dimensionless constant, and n

is the strain hardening exponent [20].

$$\frac{\varepsilon}{\varepsilon_0} = \frac{\sigma}{\sigma_y} + \alpha \left(\frac{\sigma}{\sigma_0}\right)^n \qquad \text{Equation 2.29}$$

HRR found that in order for the J-integral to remain path-independent, the stress and strain

needed to be proportional to $1/r_{crack}$ at the crack tip. After applying the necessary boundary

conditions the expressions for stress and strain are as follows:

$$\sigma_{ij} = \sigma_0 \left(\frac{EJ}{\alpha \sigma_0^2 I_n r_{crack}}\right)^{\frac{1}{n+1}} \tilde{\sigma}_{ij}(n, \theta) \qquad \text{Equation 2.30}$$

And

$$\varepsilon_{ij} = \frac{\alpha \sigma_0}{E} \left(\frac{EJ}{\alpha \sigma_0^2 I_n r}\right)^{\frac{n}{n+1}} \tilde{\varepsilon}_{ij}(n, \theta) \qquad \text{Equation 2.31}$$

These parameters depend on the stress state, either plane stress or plane strain. I_n is an integration constant dependent on n. $\tilde{\sigma}_{ij}$ and $\tilde{\varepsilon}_{ij}$ are also dimensionless and functions of n and θ. The J integral defines these equations and therefore uniquely characterizes the crack tip plasticity.

There is a singularity in the HRR model, where at distances less than twice the crack tip opening displacement, δ, the stress field is influenced by crack blunting and not modeled by the HRR equations. At around 6δ from the crack tip, the material begins to behave again in a linearly elastic manner. Here the K-field models the behavior. In between 2δ and 6δ, however, the J-field dominates. This is depicted in Figure 2.11 for both the area around the crack tip in 2.11a and the stress as a function of the distance from the crack in 2.11b.

Finally, when using the J-integral to characterize the crack tip, it is important to understand the resistance curves to the crack growth. Figure 2.12 depicts the J resistance curve as a function of crack growth. Initially the crack will blunt, at a critical J value, J_{IC}, the crack begins to grow.

2.1.3.3   Microstructural Mechanisms of Fracture in Metals

This leads to a discussion of the fracture mechanisms in metals, which fall under three categories: ductile, cleavage, or intergranular fracture and are depicted in Figure 2.13.

In ductile fracture there are three observed stages, 1) at a second-phase particle or inclusion a free surface forms by interface decohesion or particle cracking, 2) the free surface grows around the particle by hydrostatic stress and plastic strain into a void, 3) adjacent growing voids coalesce. The fracture in a metal can be either nucleation-controlled or growth-controlled. Yet when the voids reach a critical size, plastic instability occurs and failure results.

There are two general categories of models describing void nucleation. The first is based on continuum theory, the latter describes dislocation-particle interactions and is necessary for

particles with a diameter <1μm. Argon's continuum model proposed that the interfacial stress on a cylindrical particle is equal to the sum of the hydrostatic and von Mises stresses. Goods' and Brown's model suggests the total maximum interfacial stress is the sum of the maximum principal stress, σ_1, and an increase in the stress, $\Delta\sigma_d$, at the interface of [20]:

$$\Delta\sigma_d = 5.4\alpha\mu\sqrt{\frac{\varepsilon_1 \boldsymbol{b}}{r_{part}}} \qquad\qquad \text{Equation 2.32}$$

Where $\boldsymbol{\alpha}$ is a constant ranging from 0.14-0.33, μ is the shear modulus, ε_1 is the maximum remote normal strain, $\boldsymbol{b}$ is the Burger's vector, and r_{part} is the particle radius. Therefore, void nucleation occurs when the sum of σ_1 and $\Delta\sigma_d$ stresses reach a critical value, σ_{crit}. Yet, these two models neglect any particle cracking contribution, which is likely to occur with nonmetallic inclusions like oxides. These oxides can be damaged during processing, easing the void nucleation process.

Once nucleated, continued application of stress and strain can cause the voids to grow. Figure 2.14 demonstrates the process void nucleation around inclusions, their growth, coalescence, and fracture.

In a pre-existing crack, the behavior is much the same. Figure 2.15 demonstrates the void nucleation and growth at the tip of a crack. When the voids grow, they can coalesce with the initial crack, promoting ductile crack growth.

Cleavage fracture is the rapid propagation of a crack along a specific crystallographic plane. It can be brittle, but it may also be preceded by large-scale plastic flow and ductile crack growth that is then restricted. Generally, cleavage occurs on the lowest packing planes due to the reduced number of bonds that must be broken. bcc metals are particularly affected by cleavage fracture due to the minimal number of slip systems. In contrast, fcc metals have multiple slip systems for plastic flow and ductile behavior to continue.

The restriction of ductile crack growth is driven by a local discontinuity ahead of a macroscopic crack, that elevates the stress greater than the bond strength. Discontinuities consist of sharp microcracks from dislocation interaction, to inclusions, and/or second-phase particles. Figure 2.16 plots the stress ahead of a macroscopic crack, where a small inclusion cracks due to the strain in the matrix. If the stress ahead of the macroscopic crack is enough, $>\sigma_f$, then the microcrack propagates into the matrix, causing cleavage failure. The interaction between the macroscopic crack and the discontinuity plays a role in subsequent discussion of size effects.

The balance between ductile crack growth and cleavage is largely controlled by temperature in bcc metals. The ductile-to-brittle transition temperature (DBTT) is the point at which a metal goes from ductile failure to brittle, rapid failure with an increase in temperature. Figure 2.17 shows a general example of bcc steel behavior around the DBTT.

The final category for fracture in metals is intergranular fracture. Metals generally do not fail by intergranular fracture. Yet a combination of mechanisms can drive this condition. The main mechanisms involved are 1) precipitation of a brittle phase along grain boundaries, 2) environmentally assisted cracking, 3) intergranular corrosion, and 4) grain boundary cavitation and cracking at high temperatures.

2.1.4   Size Effects and Strengthening/Toughening Mechanisms

With a basic understanding of dislocation motion and fracture, we can discuss the various methods used to strengthen a material. We will discuss those that increase the yield strength by retarding dislocation motion these include: 1) solid solution hardening, 2) dispersion or precipitate strengthening, and 3) grain size refinement. Then we will discuss those efforts that can improve fracture resistance, including extrinsic and intrinsic mechanisms.

While discussing these strengthening mechanisms it is important to keep in the mind the role that size effects play. There are two constraints on a material regarding size effects. First, is the set of microstructural constraints, which is defined by the microstructure of the material. The other is the dimensional constraints, which is determined by the specimen size; specimen sizes can generally be classified as either bulk samples (dimensions in the m-mm range) or micro-mechanical (dimensions in the nm-μm range). Size effects occur when these two sets of constraints, microstructural and dimensional, reach the same scales – the fundamentals of mechanical responses begin to change. It is essential to understand the microstructure in context of the dimensions of the tested specimens to utilize micro-mechanical testing validly. The three yield strengthening mechanisms discussed here all affect the microstructural constraints.

Further, there are two sub-categories of microstructural constraints in metals. The first is the characteristic length; one of the most fundamental of types being a Burgers vector of a dislocation. The Burgers vector gives the magnitude and direction of the dislocation. It is a measure of the strength of the lattice distortion caused by the dislocation's presence; it *characterizes* the strength of the lattice distortion [17]. The second sub-category is the size parameter; this could be grain size or obstacle spacing [17]. The interaction of the two, characteristic length and size parameter, has a direct relationship to the microstructural constraint on yield strength. Where applicable, these labels will be used in the following discussion of each strengthening mechanism.

Solid solution hardening consists of introducing impurity atoms into the lattice. This results in lattice strain around the impurity atoms: tension for smaller impurities, compression for larger impurities. A large impurity atom is present in the lattice in Figure 2.18a where the compression effect is shown. As shown in Figure 2.18b, impurity atoms tend to congregate

around dislocations to reduce the lattice strain from the dislocation. This strengthens a material, because any slip would need to move the dislocation away from the impurity atoms, increasing the lattice strain. In this case, the microstructural constraint is defined by the interaction between the edge dislocation (characteristic length) and the spacing of the impurity atoms (size parameter).

Precipitation or dispersion strengthening occurs when small phases or particles, respectively, act as barriers to dislocation motion. A dislocation has a line tension associated with it; as the dislocation attempts to move past a particle, that line tension resists bending around the particle. The line tension, T_d, is given by Equation 2.33, where μ is the shear modulus and **b** the dislocation's Burger's vector [17].

$$T_d = \frac{\mu \mathbf{b}^2}{2}$$

Equation 2.33

The diameter of the curved dislocation, d, under a shear stress, τ, is the characteristic length and is given by:

$$d(\tau) = \frac{\mu b}{\tau}$$

Equation 2.34

The particle type or the spacing between particles is the size parameter in this case.

One of the simplest mechanisms to describe the interaction between the dislocation and the particles in an alloy is described by the Orowan mechanism. The dislocation must fully bypass the obstacles to result in plastic deformation. As can be seen in Figure 2.19, the size parameter is the particle obstacle spacing, L. As the characteristic length, d, approaches the obstacle spacing (2.19b), the dislocation can move past the obstacles.

Adjusting Equation 2.34 using the Orowan stress, τ_{Or}, and the obstacle spacing the result is Equation 2.35 [17].

$$\tau_{Or} = \frac{\mu \boldsymbol{b}}{L}$$
<div align="right">Equation 2.35</div>

With increased dispersion of particles throughout the alloy, a 'dislocation forest' develops, where an average obstacle spacing, L_{ob}, can be calculated through the dislocation density, $\boldsymbol{\rho}$. Dislocation density, $\boldsymbol{\rho}$, is the product of the sum number density of all obstacles, N_{ob}, and the weighted average diameter of the obstacles, $\overline{d_{ob}}$.

$$L_{ob} = \frac{1}{\sqrt{N_{ob}\overline{d_{ob}}.}}$$
<div align="right">Equation 2.36</div>

Combining Equations 2.35 and 2.36 results in the Taylor equation, a classical work-hardening description, where α is a factor describing the penetrability of the obstacles.

$$\tau = \alpha \mu \boldsymbol{b} \sqrt{N_{ob}\overline{d_{ob}}}$$
<div align="right">Equation 2.37</div>

In steels, α can be found through the following relationship [8]:

$$\alpha = \frac{1}{2\pi} \ln \left(\frac{l}{2r_c} \right)$$
<div align="right">Equation 2.38</div>

Where r_c is the dislocation core radius and l is the obstacle spacing. Listed are some general values for α of different obstacle types. In precipitates and voids that cause bowing $\alpha=1$, and for cutting $\alpha=0.3$-0.5. For dislocation loops $\alpha=0.25$-0.5 and for black dots $\alpha<0.2$, but α values can also vary with the size of these obstacles [8].

The final strengthening mechanism is grain size refinement. Grain boundaries act as obstacles (size parameters) for the dislocations (characteristic lengths) to interact with. The more incoherent a grain boundary, the more energy it takes to transmit a dislocation. As such, the number, size, and character of the grains is important to understanding dislocation motion, with more grains, smaller grains, or more high angle grain boundaries strengthening a material.

The increase in energy is due to the pile-up of dislocations along grain boundaries. The resolved shear stress applied by a dislocation is τ_a, and with n' number of dislocations, the stress at the head of the pile-up is $n'\tau_a$. The number of dislocations can be measured using the length of the pile-up, L_p, and that is proportional to the grain diameter, d_g, through [16]:

$$L_p = \frac{\alpha'n'\mu b}{\pi\tau_a}$$
Equation 2.39

α' is a geometrical constant equal to 1 for screw dislocations and $(1-\upsilon)$ for edge dislocations, where υ is Poisson's ratio. If the source of the pileup is located at the center of the grain, then $L_p = d_g/2$, where d_g is the grain diameter. If the stress required to pass through the grain boundary is τ_c, then [16]:

$$\tau_c \leq \frac{\alpha'\pi d_g \tau_a^2}{2\mu b}$$
Equation 2.40

The friction forces required to move a dislocation without obstacles is τ_0 so that we end up with the Hall-Petch relationship:

$$\tau_a \geq \tau_0 + k'd_g^{-\frac{1}{2}}$$
Equation 2.41

Modifying Equation 2.41 for yield strength, results in the following, with σ' and k' being constants of the material due to frictional forces required to move a dislocation and the geometry of the dislocations, respectively [15]:

$$\sigma_y = \sigma' + k'd_g^{-\frac{1}{2}}$$
Equation 2.42

In grain size refinement, the characteristic length is the dislocation pile-up, while the size parameter is the grain size. The interaction between the two can strengthen a material.

Figure 2.20 shows a Hall-Petch plot for iron and low-carbon steel. The accuracy of the Hall-Petch model varies with the alloy system and the grain size range. It is most accurate

between 10-100 µm in grain diameter. Here the yield stress is that stress required to move already existing dislocations. Below 10 µm, the yield stress is limited, reaching the theoretical strength, due to the lack of dislocation source availability. This holds true for small-scale samples as well – fewer dislocations are available, and their population is insufficient to induce plasticity. Thus, the stress required is that needed to create dislocations that will subsequently move through the material during plastic deformation [17].

Each type of obstacle (precipitates, voids, dislocation loops, black dots, or grain boundaries) act as size parameters and, due to their interaction with dislocations, can add to the yield stress increment. Modifying Equation 2.37 results in the yield stress increment, $\Delta\sigma_y$, instead of the shear stress, τ, for any type of obstacle [8].

$$\Delta\sigma_y = \alpha M \mu \boldsymbol{b} \sqrt{Nd} \qquad \text{Equation 2.43}$$

Where N is the dislocation number density, d is the dislocation size (obstacle size parameter), and M is an upper limit for the ratio of uniaxial yield strength to resolved shear strength. M is 3.06 for bcc lattices [8].

Altogether the total yield stress increment due to the dispersed obstacles in the microstructure is generally a linear superposition for obstacles with dissimilar strengths shown below:

$$\Delta\sigma_y = \sum_i \Delta\sigma_{y,i} \qquad \text{Equation 2.44}$$

Or a root-sum-square superposition for obstacles with similar strength.

$$\Delta\sigma_y = \sqrt{\left(\sum_i \Delta\sigma_{y,i}\right)^2} \qquad \text{Equation 2.45}$$

Where the subscript *i* denotes each type of obstacle. Again, Equation 2.45 ultimately describes the relationship between a characteristic length (of the dislocation forest) and the size parameter (of the obstacles inhibiting the dislocation motion). This is the dispersed barrier hardening (DBH) model and will be used to quantify microstructurally predicted changes in the yield strength of the irradiated ODS alloys studied in this dissertation.

While it may sound like strengthening and toughening are causes driving in the same direction, it is often the case that efforts used to strengthen a material reduce the toughness, or resistance to fracture [16,21]. As discussed above, strengthening efforts focus on creating a fine microstructure of grains and inclusions such as precipitates or oxides to hinder dislocation motion. Yet this resistance to dislocation motion often leads to brittle alloys with poor toughness. Hence, a compromise between strengthening and toughening must be made when designing or choosing an alloy for critical applications.

Toughening mechanisms fall into two categories, extrinsic and intrinsic toughening. For metals, and other ductile materials, the main mechanisms for toughening are intrinsic in nature. Brittle materials, such as ceramics, rely on extrinsic mechanisms [21]. Intrinsic mechanisms act ahead of a crack tip, increasing the microstructural resistance by suppressing microcrack and void formation. They include efforts to reduce crack initiation and crack growth. Extrinsic mechanisms act behind the crack tip to reduce the crack driving force. These focus primarily on reducing the crack growth. Figure 2.21 demonstrates mechanisms that fall into these two categories.

In metals, the crack-tip plasticity dominates the toughness. Though usually ductile, metals can fail in a brittle fashion below the DBTT. When brittle fracture is operating, smaller grain sizes and second-phase particles can improve intrinsic toughness by limiting strain

hardening, which in turn limits the stress elevation at the crack tip [15,21]. Conversely, when ductile fracture is in operation, higher strain hardening suppresses strain localization, distributing the damage more widely. With more plastic deformation, the stress intensification at the tip can dissipate through emission of dislocations (ductile fracture) rather than bond breaking (brittle fracture). Though, again, a finer dispersion of second-phase particles can provide resistance to fracture [21].

As with strengthening mechanisms, toughening mechanisms also rely on the microstructure of a material. Again, size effects can dominate the material properties if there is not a representative distribution of the microstructure in small-scale samples.

2.1.5   Mechanical Properties

Now that we have an understanding of elastic deformation, plastic deformation, and fracture in materials we need a discussion of how these behaviors are quantified and measured in engineering terms. For each type of deformation there is a measure of either resistance to that deformation or a point at which that deformation begins. Elastic Modulus is a measure of a material's resistance to bond stretching between atoms. Yield strength is the stress at onset of plastic deformation. Fracture toughness is the material's resistance to crack growth. In this section we will define the engineering equations used to calculate these three material properties.

To understand all three properties, first we must define the stress and strain experienced in a material. Engineering stress, σ, is the force, F, exerted along the initial cross-sectional area, *A*.

$$\sigma = \frac{F}{A}$$

Equation 2.46

Engineering strain, ε, is the change in length $\varDelta l$, over the initial length, l_0, and where l_i is the instantaneous length.

$$\varepsilon = \frac{l_i - l_0}{l_0} = \frac{\varDelta l}{l_0}$$
Equation 2.47

Stress and strain are related through the elastic modulus, E, in the elastic region of deformation through Hooke's Law. This region is linear under both loading and unloading and often applies only to small strains in the materials.

$$\sigma = E\varepsilon$$
Equation 2.48

Yield strength, σ_y, then signifies the onset of plastic deformation and for engineering applications is often measured at a strain offset of 0.002. A stress-strain curve with the 0.002 offset yield strength is indicated in Figure 2.22.

To calculate stress-strain in a more complicated geometry, such as cantilevers. The following equations can be used to relate the cantilever geometry and load (P) displacement (d) data to stress and strain. Here, L_{notch} is the length between the indenter tip and the notch, while L_{beam} is the entire length of the beam.

$$\sigma = \frac{6PL_{notch}}{BW}$$
Equation 2.49

$$\varepsilon = \frac{3L_{notch}B\boldsymbol{d}}{2L_{beam}^3}$$
Equation 2.50

Flow stress, σ_{flow}, is the instantaneous stress required to keep plasticly deforming a material. It is a function of the true strain, ε_t, strength coefficient, $\boldsymbol{K}$, and a strain hardening exponent, n.

$$\sigma_{flow} = \boldsymbol{K}\varepsilon^n$$
Equation 2.51

True strain, ε_t, is the rate of increase in the instantaneous gauge length. It requires active measurement of the change in gauge in length as a stress-strain test is being conducted.

$$\varepsilon_t = \int \frac{dl}{l} = \ln\left(\frac{l}{l_0}\right) = \ln(1 + \varepsilon)$$

<div align="right">Equation 2.52</div>

The strain hardening exponent, n, is dependent on the material.

Quantifying fracture is a more complicated affair. As the field of fracture mechanics has developed over the past 60 years, the agreed upon testing method, plane strain Mode I opening, with a resulting parameter, fracture toughness K_{IC}, has been deemed the appropriate measure for comparison across materials. When conducted in plane strain and with small crack-tip plasticity, K_{IC} is a material property, independent of loading and specimen volume. As stress is to strength, so the generic stress intensity, K, is to the fracture toughness, K_{IC}. While yield strength is the point at which plastic deformation occurs, K_{IC} is the critical stress intensity required for unstable crack propagation [16]. It is important to note that the subscripts, I, II, or III, refer to the opening mode. For a linearly elastic material, K_{IC} can be found in straightforward manner. With elastic-plastic materials a J_{IC} can be found and converted to a K_{IC}-like value for purposes of comparison.

The generic stress intensity is dependent on the remotely applied stress and the characteristic crack length, $\boldsymbol{a}$:

$$K = Y\sigma\sqrt{\pi\boldsymbol{a}} \ or \ K_I = \frac{P}{B\sqrt{W}}f\left(\frac{\boldsymbol{a}}{w}\right)$$

<div align="right">Equation 2.53</div>

For different geometries, the geometry factor, Y, has been derived. These geometries include a plate with a center crack in tension, single edge-notched beam in tension or in bending, double-edge notched beam in tension, and a compact tension geometry. These equations can be found in fracture mechanics texts such as one by Anderson [20] and more general mechanical behavior texts, such as work by Meyers and Chawla [16], or taken directly from the Cracks Handbook by Tada et al [22]. As this dissertation concerns itself with a geometry based on the single edge

notched bending beams, a diagram and the accompanying geometry factor, $f\left(\frac{a}{w}\right)$, are included here.

$$f\left(\frac{a}{w}\right) = \frac{3\left(\frac{S}{W}\right)\sqrt{\frac{a}{W}}}{2\left(1 + 2\left(\frac{a}{W}\right)\right)\left(1 - \left(\frac{a}{W}\right)\right)^{\frac{3}{2}}}\left[1.99 - \frac{a}{W}\left(1 - \frac{a}{W}\right)\{2.15\right.$$

$$\left. - 3.93\left(\frac{a}{W}\right) + 2.7\left(\frac{a}{W}\right)^2\right]$$

Equation 2.54

For elastic-plastic materials, the amount of crack-tip plasticity must be accounted for. This can be done through either measuring the crack tip opening displacement (CTOD) or measuring the crack growth, Δa, and calculating a J-integral value at increments during the testing. This dissertation utilizes the crack growth approach and therefore this method will be discussed in detail here.

The J-integral is comprised of two parts: the elastic contribution, J_{el}, and the plastic contribution, J_{pl} [20].

$$J = J_{el} + J_{pl}$$

Equation 2.55

The elastic portion is calculated from the stress intensity at the notch, K, the elastic modulus, E, and the Poisson ratio of the material, ν.

$$J_{el} = \frac{K^2(1 - \nu^2)}{E}$$

Equation 2.56

If the geometry of the specimen is one of the standard testing arrangements, K can be found using Equation 2.53, if it is not, it must be modified. The use of finite element modeling can assist with this effort. The plastic J is calculated as a function of the plastic area under the load-displacement curve, A_{pl}:

$$J_{pl} = \frac{\eta A_{pl}}{B a_0}$$
<div align="right">Equation 2.57</div>

As well as the specimen thickness, B, the initial crack length, a_0, and η, a dimensionless

constant, where in a single edge notched bend specimen, η = 2.

The J-values are plotted as a function of the crack extension, Δa, as in Figure 2.12. When

the crack extension changes from a crack blunting regime to a crack growth regime, the J value

at this point is the critical J-integral value and is defined as J_{IC}. J_{IC} signifies the onset of unstable

crack propagation. J_{IC} can then be converted to an approximate critical $K_{Q,J}$ value through [23]:

$$K_{Q,J} = \sqrt{\frac{J_{IC} E}{1 - v^2}}$$
<div align="right">Equation 2.58</div>

$K_{Q,J}$ can then be used as a comparison to other materials through their K_{IC} values.

2.2 Irradiation Effects in Metals

Irradiation induces a variety of defects in metals. These defects can impact the mechanical

properties. Hence, it is important to understand 1) how these defects form, 2) the nature of the

defects formed, and finally, 3) their impact on mechanical properties. As such, we will start with

a brief description of the initial radiation damage event.

The energized particle (radiation particle) first interacts with a lattice atom, transferring

kinetic energy and creating the primary knock-on atom (PKA). The PKA is displaced from its

lattice site and moves through the lattice. It can displace other lattice atoms and this chain effect

results in a displacement cascade of point defects. Finally, the PKA will settle into an interstitial

site. A diagram of the damage cascade is demonstrated in Figure 2.24. The damage cascade

consists of multiple interstitial-vacancy pairs, or Frenkel pairs. During the damage event, these

pairs can combine and anneal. The remaining defects that survive are quantified by the displacement efficiency, ε.

Due to differences in the average recoil energy, $\bar{T}$, and displacement efficiency, different irradiating particles will result in different damage cascade morphology. Electrons have a small recoil energy, enough to displace one atom. Protons have slightly higher energy and result in multiple, small, damage regions. Heavy ions leave a single, larger damage region. Finally, neutrons have a high recoil energy and result in large, single damage cascade. This is diagramed in Figure 2.25. Additionally, the recoil energies of each particle are charted in comparison with the projectile energy, E_i, and the displacement energy, E_d.

The remaining defects can cluster or remain isolated. Of the clustered defects, some remain immobile, others mobile with the additional influence of radiation enhanced diffusion. At this point the defects fall into the categories discussed previously: point, line, planar, and volumetric defects. This results in phenomena such as radiation induced segregation (RIS), irradiation induced precipitates, dislocation loops, and voids [8].

Radiation induced segregation occurs from the spatial redistribution of solute and impurity elements due to the elevated temperature irradiation. These solute and impurity atoms can flock to or leave regions such as grain boundaries, surfaces, dislocations, voids, and phase boundaries. This enrichment or depletion can make these boundaries more brittle, resulting in a reduced fracture toughness or strength of the material, due to local microstructural changes.

Irradiation induced precipitates, dislocation loops, and voids act in the same way as the strengthening mechanisms introduced above. Namely, they act as obstacles to dislocation motion. This hardens the material, increasing strength, while reducing ductility, and potentially

reducing toughness. This can affect the fracture toughness and change the DBTT of a metal (Figure 2.26).

The standard of damage quantification to be used in this work is the measure of displacements per atom (dpa). This quantifies the number of times, each atom in the lattice has been displaced during the irradiation. For example, 1 dpa would mean that each lattice atom has been displaced once. At 100 dpa, each lattice atom would have been displaced 100 times. Hence, any material that can retain its properties while undergoing this irradiation, would be desirable in nuclear energy applications.

2.3   Understanding ODS

Nuclear-relevant ODS alloys are often based on an Fe-Cr alloy matrix, which takes a ferrite, martensite, or a duplex ferritic/martensitic (F/M) structure. The two major groupings of Fe-Cr ODS steels are the 9Cr variety which specifically target radiation resistance and the 12-14Cr steels which prioritize corrosion resistance [24]. The material of interest in this work is a model Fe-9%Cr ODS alloy. This section will look at a brief history of the material, then discuss the mechanical properties and irradiation effects specific to the 9Cr and 14Cr classes of Fe-Cr ODS materials, and finally look specifically at the microstructure of the as-received and irradiated conditions of the model Fe-9%Cr ODS used in this study.

Initially, Fe alloys with 9-12 wt% Cr were used in power-generation as boiler and turbine materials. During the 1970's, however, the idea to use this material in nuclear applications, such as fuel cladding and structural materials was introduced. Since then, development of these alloys for nuclear applications is ongoing in the major geographical nuclear energy drivers: Japan, Korea, the European Union, and the United States [25] .

Using strengthening mechanisms, Fe-Cr ODS alloys have been tailored to perform with minimal microstructural change within fast fission and fusion environments. They perform well at high temperature and high dose due to the uniform oxide dispersion, small grain size, and high dislocation density [26].

2.3.1   Fe-Cr ODS

The 9%Cr ODS alloys are generally martensitic, produced through phase transformation, while the 12-14%Cr alloys are ferritic, produced through recrystallization processing [24]. To produce martensite, austenite (γ iron) must be quenched rapidly such that diffusion does not occur. The atoms in the austenite fcc structure quickly shift to body-centered tetragonal (bct) positions. This is a non-equilibrium condition and carbon atoms sit in interstitial locations [15]. Martensite is often tempered below 650°C to relax internal stresses formed during the transition from fcc to bct. Under these conditions, the resulting microstructure is a mix of residual fine ferrite (α) grains and austenite (γ) converted martensite phase [27,28]. Increasing Cr content (>11-12 wt%) reduces the amount of resulting martensite, hence why the 12-14%Cr class of Fe-Cr alloys are considered ferritic [29].

The alloying elements, C, N, Ni, and Mn extend the γ-phase field, while the elements Cr, W, Si, and Ti contract it [25]. The latter elements also form more δ-ferrite. C is the cheapest austenite former, but reduces the toughness of the alloy and results in coarser grain sizes [25]. A balance must be made between the two groups of alloying elements and their accompanying resultant phases.

By adding in elements above their solution limits and uniformly dispersing the Y_2O_3 oxides within the matrix, dislocation motion is retarded, and the material is strengthened. The Y_2O_3 oxides provide high-temperature stability of the alloy because it exhibits little to no

dissolution or growth under increased temperature [24,30,31]. Yet it is important to remember that the mechanical properties in Fe-Cr ODS alloys depend on the distribution and size of these oxides in the matrix [29,32].

As Fe-Cr ODS alloys began to be more widely considered as candidate alloys for nuclear reactor applications, the importance of the oxide distribution within the material on the mechanical performance was recognized. Efforts to understand the processing steps that controlled oxide size, number, and dispersion were undertaken. Ukai et al. first noticed the importance of Ti concentration in ferritic 13Cr ODS steels in creep performance [33]. Then work by Ohtsuka et al. on martensitic 9Cr ODS demonstrated that Ti concentrations >0.2 mass% reduced oxygen contamination and resulted in an ultra-fine dispersion of oxide particles that lead to creep strength improvements [28]. Later, work by Alinger et al. found that increasing consolidation temperature in a 14Cr ODS resulted in larger sized oxides and reduced number densities [34]. Finally, work on 14-Cr ODS by Hoelzer et al. found that increasing number density of oxides resulted in higher yield and ultimate tensile strengths, while ductility was reduced [32]. All of this is to say, that because oxide particles play such an important strengthening role in Fe-Cr ODS alloys, smaller oxide sizes, larger number densities, and more dispersion tend to improve mechanical properties. The next following paragraphs will discuss how these oxide particles contribute to the mechanical properties through α-ferrite content and interaction with dislocations.

Due to the α-ferrite to γ-austenite conversion, α-ferrite has finer oxide particles than the martensite phase [35]. Therefore, the α-ferrite is harder than the martensite and the amount of residual α-ferrite contributes to the yield strength and ductility of Fe-Cr ODS alloys. In a study by Miyata et al. tensile strength is measured as a fraction of residual ferrite from 0 to 47 vol.% in

an Fe-9%Cr ODS [36]. At 0 vol% the tensile strength is 330 MPa while it increases to 450 MPa at 47 vol.%. In contrast, percent elongation drops from 32% at 0 vol.% to 17% elongation at 47 vol.% [36].

Two studies were conducted to understand the impact of temperature on microstructure, deformation mechanisms, and mechanical properties of a 9Cr ODS [37] and a 14Cr ODS [38]. Temperature values ranged from 25°C to 800°C in the former, while temperatures ranged from -196°C to 1000°C in the latter. Both studies found that at low temperatures (< room temperature) the strength was high and ductility low. While at high temperatures (>400°C), strength was low and ductility high.

At temperatures between 25°C - 400°C yield stress remained constant in the 14Cr ODS study. TEM micrographs at these temperatures showed large amounts of dislocation bowing. Authors concluded that the leveling of yield stress at these temperatures was due to the athermal strengthening mechanisms of dislocation-oxide interactions [38]. In contrast, at high temperatures, dislocation lines were straight, suggesting the oxide strengthening here was not due to dislocation interactions.

In the 9Cr ODS study, however, there was a strong oxide-dislocation interaction observed at all temperatures (25°C - 800°C). At moderate temperatures, the same dislocation bowing phenomena was observed as in the 14Cr ODS. However, at higher temperatures the mechanism was different; dislocations were being pinned at the oxide particle/matrix interfaces [37].

Studies on irradiation effects in Fe-Cr alloys are concerned with the precipitate evolution, dislocation loop creation, and radiation induced segregation. Each irradiation induced phenomena can impact the strengthening and therefore the mechanical performance of the Fe-Cr ODS alloys. The next few paragraphs will summarize the literature for each phenomenon.

As oxides play an essential role in strengthening, understanding their evolution under irradiation is essential. Yet studies demonstrate a complex interdependence based on the irradiating particle, dose, and temperature of the irradiation on the precipitate evolution. Neutron irradiation studies on 9Cr and 12Cr ODS at doses of 2.5-15 dpa at 600-773K show little to no changes in oxide size and distribution [39], while doses > 30.5 dpa show some dissolution [40]. Electron irradiations show a large amount of dissolution in 9Cr [41] and 13Cr [40]. Heavy ion irradiation results in a wide variety of oxide particle trends. Using Ni^{2+} Certain found at low temperatures 14Cr ODS underwent solute dissolution, but was stable above 300°C [42].

Dislocation loops can contribute to the hardening in irradiated materials and can also act as sinks for irradiation defects. Loops in bcc Fe-based alloys such as these Fe-Cr ODS alloys consist of two different types: <100>{200} and ½<111>{111} [43]. Loops have diameters ranging from 3 nm to 9 nm in a 12Cr and a 14Cr ODS steel irradiated with He^{2+} at 300°C [44]. In 9Cr ODS, loop diameters of 8-9 nm were found in neutron and proton irradiated samples to 3 dpa at 500°C [7].

RIS can also be found in F/M alloys, though there is limited literature on the ODS specific varieties. Work by Was et al. finds Cr enrichment at grain boundaries for alloys with lower Cr content (~9wt%) and at lower temperatures (400°C) [45]. Alternately, in higher Cr content (~12 wt%) alloys and at higher temperatures (500°C) Cr depletion occurs. Further work, where the inverse Kirkendall model was used, demonstrated the dependence of RIS on temperature in F/M alloys [46]. At low temperature, Cr enriched. At high temperatures, Cr depleted.

Due to the small impact on the oxide particle distribution, mechanical properties of irradiated 9Cr and 12Cr ODS also show little change under neutron irradiation at doses of 15-33

dpa and temperatures of 683K - 1108K [47]. Most of the irradiation damage is accommodated at the pre-existing sink sites around dislocations and oxide interfaces. However, work on a Eurofer (9Cr ODS) alloy at dose of 1.73 dpa at 300°C saw a drop in upper shelf energy of 18% [48]. This could potentially be consistent with the RIS seen at lower temperatures in irradiated F/M alloys, where Cr enrichment drives α' precipitation – a brittle phase [49].

2.3.2   As-received Fe-9%Cr ODS

The model Fe-9%Cr ODS used in this study was previously characterized by Swenson et al. [4,6,7]. As such this information is provided in detail in the background. The matrix element is iron (Fe). It is mechanically alloyed with other elements, chromium (Cr), carbon (C), tungsten (W), titanium (Ti), yttrium oxide (Y_2O_3), iron-yttrium intermetallic compound (Fe_2Y), and iron oxide (Fe_2O_3) powders through ball milling for 48h in an argon gas atmosphere. The resulting powder is sealed in cans and degassed at 673K in a vacuum of 0.1 Pa. This was then hot-extruded at 1423 K and air-cooled [28]. The detailed composition of this model Fe-9%Cr ODS alloy is listed in Table 2.1. This results in a fully martensitic Fe-Cr alloy. The calculated phase diagram for this alloy is shown in Figure 2.27, reproduced from [28].

Using TEM, approximately 100 grains and 36 carbide precipitates were measured. The effective grain diameter is 0.23 μm. Carbide precipitate effective diameter was 0.11 μm with a density of 0.20×10^{20} m^{-3}. The density of dislocation lines was measured to be 19.1×10^{14} m^{-2}. Using atom probe tomography (APT) analysis, 486 oxide nanoclusters were measured in an analysis volume of 856,053 nm^3 resulting in a density of 568×10^{21} m^{-3} [50]. From these measurements, an average obstacle spacing can be calculated using Equation 2.36. Doing the

calculation, the average obstacle spacing for the as received material is $L_{ob} = 17.2$ nm. This data is included in Table 2.2.

A TEM micrograph of the as received material is shown in Figure 2.28. Notice the variety of microstructure adding to the strength and toughness of the alloy: oxide nanoparticles (black small dots), grain boundaries, and dense dislocation regions.

2.3.3 Irradiated Fe-9%Cr ODS

Using the same TEM and APT techniques as used for the as received material, the irradiation induced precipitates, dislocation loops, and voids can be quantified for each irradiated condition of Fe-9%Cr ODS. The irradiation conditions tested in this dissertation include Fe^{2+} ions at 3 dpa and 100 dpa and proton irradiation at 3 dpa. All irradiations were conducted at 500°C.

For the Fe^{2+} at 3 dpa 500°C irradiation, 104 grains were measured with an effective diameter of 0.28 μm. 48 carbides were measured with an effective diameter of 0.08 μm a density of 0.76×10^{20} m^{-3}. Dislocation line density was 22.6×10^{14} m^{-2}. 48 dislocation loops were measured with a density of 2.1×10^{21} m^{-3}. No voids were seen. Oxide nanocluster density was measured to be 171×10^{21} m^{-3}. This resulted in an average obstacle spacing of 33.7 nm [6].

The Fe^{2+} at 100 dpa 500°C irradiation used 105 grains. These had a larger effective diameter of 0.37 μm. Carbide density went down to 0.29×10^{20} m^{-3}. Dislocation line density reduced at 18.4×10^{14} m^{-2}, while dislocation loop density increased to 4.3×10^{21} m^{-3}. Nanocluster density was near as received density at 513×10^{21} m^{-3}. The average obstacle spacing was calculated to be 18.9 nm [6].

The proton irradiation at 3 dpa, 500°C measured 104 grains with an effective diameter of 0.31 μm. 51 carbides were counted with effective diameter 0.07 μm and a density of 0.46×10^{20}

m^{-3}. Dislocation line density was 17.6×10^{14} m^{-2}. 688 dislocation loops were measured with an average diameter of 8.4 nm and a density of 10.2×10^{21} m^{-3}. There were 8 voids measured with an average diameter of 4 nm and a density of 0.34×10^{21} m^{-3}. Finally, 964 oxide nanoclusters were counted with a density of 560×10^{21} m^{-3}. The average obstacle spacing was calculated to be 21.2 nm [7]. The microstructural data for the as received and irradiated conditions are summarized in Table 2.2.

Using the DBH model as described in §2.1.4 the microstructurally predicted change in hardening can be calculated for each of the irradiated Fe-9%Cr ODS as compared to the as received condition. Here the Taylor factor, M, is 3.06 for bcc Fe-Cr alloys [8], the shear modulus, μ, is 82 GPa, and the Burger's vector is 0.248 nm. The values of α used are 0.05 for nanoclusters, 0.44 for loops, and 0.65 for voids. The $\Delta\sigma_{ys}$ for Fe^{2+} irradiated at 3 dpa 500°C is -108 MPa and -10 MPa for Fe^{2+} irradiated at 100 dpa 500°C. Proton irradiation at 3 dpa 500°C predicts a slight hardening of 25 MPa [50]. These values are included in Table 2.2.

2.4   Mechanical Testing

This section will provide background information on conventional testing and the various small-scale testing methods. As well as address the literature concerning size effects in each geometry.

2.4.1   Conventional Mechanical Testing and Nanoindentation

Conventional mechanical testing occurs on length scales of meters to millimeters. Testing methods consist of uniaxial tension and compression to find yield strengths and elastic modulus properties, a variety of hardness tests based on the indenter tip geometry, and Charpy or compact

tension (CT) testing for fracture toughness. Additionally, nanoindentation can be used as an alternative to other small-scale testing methods and will be briefly reviewed.

Uniaxial tension is amongst the most straightforward of tests. Generally, a dog-bone shaped sample is prepared and installed in a tensile tester. The cross-section can be circular or rectangular, but by using a reduced area, plastic deformation can be constrained to the gauge length. These dimensions are identified in Figure 2.29 of a tensile sample. Load is measured with a load cell and the elongation with an extensometer. Compression testing is conducted in a similar manner and the data is analyzed likewise, yet the point of failure can be harder to define in a compression sample due.

After collecting the load and displacement data, the engineering stress and strain can be calculated. The general shape of a tensile specimen tested to failure for a bcc steel is shown in Figure 2.30. Figure 2.30 also demonstrates the impact of irradiation; with increasing dose, the yield strength increases and ductility decreases. The material becomes brittle and unsafe to use. A desirable material for use in reactors is one that can absorb the irradiation induced phenomena without drastically changing its properties.

Bulk mechanical property testing on Fe-Cr alloys have been conducted in the literature in both the as received [28,29,36,37,51–58] and irradiated [48,59,60] conditions. In general, the response of an irradiated Fe-9%Cr alloy is to increase both the yield strength and ultimate tensile strength, while reducing ductility as shown in the figure above.

Tensile testing has been conducted on a variety of different Fe-Cr alloys. Two Fe-14%Cr alloys tested by Fournier resulted in yield strengths of ~1100 MPa [56]. Auger et al. also looked at an Fe-14Cr-0.3Y_2O_3 alloy finding a yield strength of 1250 MPa at room temperature [52]. Dade et al. found a yield strength of 1085 MPa in a room temperature Fe-14Cr ODS [51].

Work by Chauhan studied the temperature dependency of Fe-9%Cr ODS finding a reduction in yield strength with increase in temperature from 929 MPa at room temperature to 160 MPa at 800°C [37]. Toualbi found yield strengths between 1000 and 1200 MPa for an Fe-9%Cr-1%W-0.2%Ti-0.3%Y_2O_3 alloy [57]. Using an Fe-9%Cr with varying Y_2O_3 wt.%, Shi found a range of yield strengths between 1000-1200 MPa at room temperature [55]. Hary tested an Fe-9%Cr ODS steel tube finding a yield strength of 1020 MPa [58]. Ohtsuka, using the same Fe-9%Cr-0.2%Ti as in this study, found a yield strength of ~300 MPa [28].

Tensile tests on irradiated alloys show an increase in yield strength. Lucon tested an Fe-9%Cr-1%W-0.2%V-0.1%Ta alloy and found an increase in yield strength of ~400 MPa after irradiating with neutrons to 1.73 dpa [48]. Henry tested a variety of Fe-Cr alloys all showing an increase in yield strength with irradiation dose [60]. Zinkle collected literature data on Fe-8%Cr and Fe-9%Cr finding a range of elastic moduli of 192-216 GPa between room temperature and 450°C [59]. Toualbi's measurements resulted in a range of between 190-220 GPa [57].

While tension and compression tests are destructive, hardness testing is nondestructive, though just as simple and inexpensive. As such, it is frequently used to measure a material's local resistance to plastic deformation. Hardness testing is inherently a comparison of one material with other known material's hardness and there are multiple scales that can be used; including Rockwell, Vickers, Knoop, and Brinell. Each scale uses its own indentation tip material and shape. Hardness values can be converted to yield strength and elastic modulus for well-studied materials using empirical data [15].

Ohtsuka [28], Miyata [36], and Toualbi [57] all used a Vickers hardness testing method for their respective unirradiated Fe-Cr alloys. Toualbi found Vickers hardness values between

300-400 H_v. Miyata, varying the ferrite wt.%, found a range of 4.2-5 GPa. Ohtuska found a range of Vickers hardness values of 340-370 H_v.

Nanoindentation is conducted on small length scales and is often used due to its simple sample preparation requirements, polishing, and the relative simplicity of conducting the tests. However, it does have a more complicated analysis than other uniaxial small-scale testing. Berkovich and spherical [18,50,61–64] tips are the two indenter tips used. Berkovich tips directly result in hardness values and the unloading curve of an indent can be used to find elastic modulus. Yield stress can be related to the hardness measurements using empirical data, while spherical tips allow for a direct analysis of yield strength as shown in ref. [65].

There are two typical configurations for nanoindentation testing of ion irradiated materials. The first is "top-down" indentation on the irradiated surface, with indent directions parallel to the irradiation direction. This requires an understanding of the deformation volume under the indent to separate the unirradiated substrate contribution from that of the irradiated material. The second method is to indent the cross section of an ion-irradiated sample. Here, a hardness profile can be measured as a function of the ion irradiation damage profile [18]. This allows for a direct comparison between the bulk material properties and the irradiated material. An example of this method is shown in Figure 2.31.

In the study shown in Figure 2.31, Hosemann, et al, tested HT-9, an Fe-12%Cr alloy, irradiated with protons and helium ions at varying dose and temperature [66]. Hardness values increased with irradiation, while the magnitude of increase reduced with increased temperature [66]. Hosemann conducted a similar study on 304 stainless steel (SS) using 2 MeV protons to a dose of 10 dpa, with similar results – increase in hardness with irradiation [18].

Dolph, et al, conducted nanoindentation tests on an Fe-9%Cr alloy using 5 MeV Fe^{2+} ions at 400°C. At a dose of 100 dpa, Dolph found strengthening of ~110-130 MPa [27]. This is half the strengthening mentioned previously in §2.2 for a similar alloy as predicted by microstructural changes. This difference in yield strength change can be accounted for in the higher temperature, 500°C, in the material used in this thesis versus 400 °C used in ref [27]. New work by Heintze et al. on Fe^{2+} irradiated Fe-9%Cr alloys showed an increase in hardness (and subsequently calculated yield strength change of ~200 MPa) at an irradiation temperature of room temperature and 300°C, but no change in hardness at 500°C [67,68]. This is also consistent with the DBH prediction from §2.2.

Conventional fracture testing generally is conducted either through a Charpy impact test or a compact tension (CT) test [20]. Examples of specimens from each type of test is shown in Figure 2.32a-b and 2.32c, respectively. Testing temperature is often varied to understand the DBTT and upper and lower shelf energies. Additionally, after testing, fracture surfaces are micrographed to understand the fracture mechanism(s). Images of the three main categories are provided in Figure 2.33. 2.33a demonstrates brittle, cleavage fracture; smooth surfaces with grooves running in the direction of crack growth. 2.33b demonstrates ductile fracture; dimples where decohesion occurred around inclusions or grain boundaries can be seen. Finally, 2.33c shows intergranular fracture with well-defined grain surfaces left where decohesion occurred.

Fracture studies of Fe-9%Cr alloys in the literature are often focused on the DBTT, though new work reports the $K_{Q,J}$ values of various Fe-Cr nanostructured alloys. Cannon and Gelles conducted Charpy impact testing on Fe-9%Cr-1W and Fe-9%Cr-1%V alloys irradiated with neutrons to 10 dpa at 365°C. They found drops in upper shelf energies between unirradiated and irradiated conditions of Fe-9%Cr-1%W and Fe-9%Cr-1%V alloys of 60 J/cm^2 and 40 J/cm^2,

respectively [69]. Work by Abe et al, found a large influence of specimen size on upper shelf energy in a 9%Cr-2%W-0.1%C steel with full sized specimens reaching 310 J/cm^2. In comparison half-sized specimens and third-sized specimens reached only 180 J/cm^2 and 100 J/cm^2 [70].

An extensive review of Fe-9%Cr and Fe-14%Cr nanostructured alloys was conducted by Byun et al. in ref. [71]. Figure 2.34 is a reproduction from this reference where fracture toughness, $K_{Q,J}$ (MPa m$^{1/2}$) is plotted as a function of yield stress (MPa) for many different alloys [71]. It shows that the inverse relationship between strength and fracture toughness holds true for this material system. It also demonstrates a rather large range for fracture toughness values. Focusing solely on the 9Cr alloys $K_{Q,J}$ values can range from 20 MPa m$^{1/2}$ to 280 MPa m$^{1/2}$ [71].

2.4.2 Micropillar Compression

Micropillar compression is one of the most widely used in situ mechanical testing geometries [72]. The geometry is simple to mill compared to beams or tensile dog bone samples while still allowing for measurements of yield stress and Young's modulus.

Micropillar compression consists of testing either cylindrical [73–77] or rectangular [11,74] micropillars, mostly focus ion beam (FIB) milled from a bulk sample. Figure 2.35 shows both in situ SEM (a) cylindrical and (b) rectangular micropillars [74] as well as in situ TEM (c) cylindrical [78] and (d) rectangular [11] samples from the existing literature. While cylindrical micropillars are more straightforward to mill, they do increase the taper angle and as found in work by Shin, larger taper angles correspond with a wider variation in measured yield stresses [74].

A variety of pure materials have been tested, including Mg [75], Ti [79], Cu [78,80], Fe [81], Cr [82], Au [83], and Mo [83,84]. Single crystals can be compared to either bi-crystalline

or polycrystalline versions of themselves. Again, this relates the microstructure to the dimensions tested. By using simple systems, the basic size-effect mechanisms due to twinning [80] or individual slip events [79] can be qualitatively matched with the quantitative load-displacement curves obtained during the compression. Other studies observe the effect of grain orientation on the resulting yield stress or the impact of loading and strain rate [83,84].

In comparison to pure materials, compression of various alloys introduces more microstructural complexity. Studies have found that alloyed materials are able to reach smaller dimensions before exhibiting size effects due to the increased obstacle density from their alloyed microstructures. Experiments include various ODS alloys [74] including MA6000 [85], PM2000 [86], stainless steels T91 and HT9 [87], a nickel based super alloy [73], and a NiTi alloy [88].

Finally, many studies have been done on irradiated materials [18,74,77,78,86,89]. These are of significance because irradiation changes the microstructural obstacles in a material. This can both increase or decrease obstacle size and number in a material. For example, dislocation loops and precipitates can form. Or if the irradiation is conducted at temperature, the dissolution of precipitates, oxides, and/or grain growth can occur. This change in microstructural obstacles directly impacts the microstructure-sample dimension relationship controlling the size effects.

An example of the impact irradiation can cause is demonstrated by the work of Kiener and Hosemann et al. Where they observe the relationship between microstructural and dimensional constraints in Cu [78]. They compare unirradiated and proton irradiated Cu in the (100) orientation. Lamellae were first FIB milled from bulk Cu then subjected to 1.1 MeV protons at 80˚C. Cylindrical micropillars were FIB milled from both the unirradiated and irradiated lamellae. The irradiated micropillars experienced a dose of 0.8 displacements per atom (dpa). To understand the relationship between the microstructural and dimensional constraints,

the micropillar diameters were varied between 80 nm and 1500 nm and then loaded in situ TEM compression.

Load-displacement data was collected and stress-strain curves were generated. Yield stress values for each micropillar were calculated and plotted against the micropillar diameter (Figure 2.36). The yield stress for the unirradiated Cu behaved logarithmically with the diameter of the sample. As the sample decreased in size, the yield stress increased. In contrast, the irradiated copper, with a higher defect density than the unirradiated material, reaches a size-independent regime above a micropillar diameter of 400 nm. These samples exhibit yield stresses between 220-280 MPa, consistent with the prediction for bulk proton irradiated Cu [78].

There are two main phenomena to understand here. The first is the general increase in yield stress as the sample size reduces. The authors attribute this to the dislocation source size. In smaller samples, dislocation sources are small, and these sources do not interact with the defects, even in the defect denser irradiated Cu. The second behavior is the size-independence of the irradiated material above the 400 nm threshold. Past this threshold, the dislocation sources reach a size large enough to interact with the defects in the irradiated material, hence the 'leveling-off' of the yield stresses above 400 nm [78].

This study of a simple material demonstrates the interaction between sample size (dimensional constraints) and the microstructure (irradiated vs unirradiated). It demonstrates that size-independent sample dimension thresholds can be identified for specific materials and irradiation conditions in micropillar compression. Though this fundamental model is demonstrated here in micropillars, the lessons learned can be applied to other geometries. This relationship between microstructural constraints and sample dimensions provides a foundation that other geometries can build upon.

2.4.3   Lamellae Indentation

One of the simplest TEM in situ mechanical testing experiments to conduct is that of indentation on a thin (i.e. electron-transparent) foil. However, the subsequent analysis and interpretation of the experiment is difficult and presents numerous quantitative and qualitative challenges [90–96]. Quantitatively, the geometry gives rise to a complex stress distribution that is difficult to precisely represent in a finite element-type mesh. But qualitatively, video interpretation is further challenged by several factors, including microstructural complexity, non-optimal imaging conditions, drift and vibrations, and human error.

First, discerning individual slip events or dislocation movements becomes increasingly difficult as the material's compositional and microstructural complexity increases. Materials with simple microstructures, such as pure Al, Cu, Mg, or Zn, allow for relatively easy observation of dislocation motion and obstacle interaction. Individual dislocation nucleation and motion has been clearly observed [12,78,79,90,93,97–102] along with grain boundary coarsening and migration [90–92,101,103–109]. Twin boundary formation can also be observed [75,110–114]. But as material complexity increases, including by way of irradiation, the ability to observe distinct events becomes more difficult and more susceptible to interpretation. There are only limited studies in which individual dislocation motion is seen during in situ TEM straining of microstructurally complex materials [115–117].

Next, because most TEM in situ mechanical testing holders do not allow for double-tilting (both α and β tilt), the experimenter cannot easily guarantee proper crystallographic orientation with respect to the electron beam so as to set up ideal imaging conditions for observation of dislocation motion. In such a case, one can only conduct detailed microstructural characterization of the sample pre- or post-mortem. Even with this pre or post imaging step, it

can be difficult to compare the indentation video to the still microstructure images collected at different tilt angles.

Additionally, once the indenter tip contacts the specimen, mechanical vibrations of the motor driving the tip are transferred to the specimen. This can result in an appearance of "shaking" in the TEM video recorded during the test, which makes it impossible to observe changes from one frame to the next.

Finally, identification of fine features such as dislocation loops or lines in microstructurally complex alloys is subject to interpretation [1]. So even if one is able to see or count features in TEM indentation videos, two different researchers will likely arrive at different results. While some of this subjectivity can be eliminated by using computer-based software to help identify or count microstructural features, these types of software are also less effective for interpreting the images from microstructurally complex materials, such as ion irradiated engineering alloys currently used or under consideration for nuclear reactor structural and cladding components.

2.4.4   Cantilever Bending

The cantilever beam can be utilized to find a variety of mechanical properties including flow stress [118–121], Young's modulus [122], and fracture toughness [23,123–125], though fracture toughness will be discussed in the following section. Again, samples can be FIB milled at both SEM and TEM scales (Figure 2.37) [119,126].

Like the micropillars for compression, many different materials have been tested in this configuration. Systems range from the simple, Cu [118,122,127,128], Ti [121,129], Zr [129], Si [130] and Fe [131], to Au and SiO2 thin films [132], up to the more complex Fe-12%Cr alloy in a study by Armstrong [119].

The work on pure Fe microcantilevers by Halliday [131] compared the flow stress behavior of unirradiated with self-ion irradiation at two different doses. Waisted and uniform cross-section cantilevers (Figure 2.38) were tested in all three conditions. Irradiation hardening was measured in the waisted cantilevers but not the uniform beams. The authors attribute this difference to size effects. The maximum stress is occurring on the underside of the cantilevers and in the uniform cross-sections the volume of material, due to the triangular cross-section, is smaller than that in the rectangular cross-section waisted cantilevers. Hence, the waisted cantilevers experience a size-independence like the large Cu micropillars in the study by Kiener [78], discussed in §2.4.2.

This work by Armstrong demonstrates that the same relationship between microstructure and dimensional constraints exist in irradiated beams. But it also suggests that the added complexity of cantilever geometry must be accounted. Work by Kiener on Cu beams and micropillars compares the size effect in these two geometries. Figure 2.39 shows the results of this study. The horizontally dashed line at 210 MPa is the result from a tensile test on 10 µm grain Cu and can be assumed to be the upper limit of a bulk test on Cu. While both cantilevers and micropillars see an inflated flow stress at smaller dimensions, the cantilevers approach this bulk flow stress at a smaller beam thickness than the micropillars.

While both micropillars and cantilever beams experience the fundamental relationship between microstructure and dimensional constraints, they are impacted differently due to the difference in geometry. Since the impact irradiation has on the microstructure has been discussed, the deep dive into size-effect modeling will be conducted on a study of unirradiated cantilevers.

A power law relationship is used by Kiener to describe the flow stress-sample dimension dependence in the study above [127]. In this section we'll review work by Tarleton on Ti and Zr cantilever beams that looks at this power law relationship closer and the dislocation behavior needed to explain the observations [129].

Tarleton et al. uses a discrete dislocation plasticity model to compare with experimental results. They conduct their experiments on commercially pure Ti and Zr. Using electron backscatter diffraction, they identify and mill their cantilever samples from the same hexagonal close-packed (hcp) orientation they use in the model. This is not the first time a discrete dislocation plasticity study was developed to explain the dislocation pile-up and size-effect seen in the flow stress of bending beams. Cleveringa also looked at this same phenomena, however in that case the study was conducted on a pure bending moment geometry [133]. Tarleton, however, specifically models the cantilever geometry, using a 6:1 length to thickness ratio for the beams. Beam widths, *w*, were varied between 1 and 10 µm. Tests were conducted in situ SEM, loading samples at a constant displacement rate [129].

The model was quasi-static and plain strain, with an assumed elastic isotropy. Dislocation glide was allowed only on the <a> prismatic slip systems with {1010} slip plane normal and <1120> slip directions. Figure 2.40 shows a comparison of the model with experimental beam bending tests. As the beam width increases, the stress reduces, showing less of an inflated size-effect.

There are two main ways to understand the size-effect seen in micro-cantilevers in Figure 2.40. The first is the soft pile-up behavior experienced in bending beams. The second is the geometrically necessary dislocations (GNDs) required to exhibit plastic strain. When bent, cantilever beams experience compression at the bottom surface and tension at the top surface,

with a neutral axis running along the center of the beam. Figure 2.41 shows that dislocations on slip planes with an acute counter-clockwise angle to the neutral axis have a positive burgers vector (+b, blue). These +b dislocations are driven to the neutral axis where there is zero resolved shear stress. Dislocations on slip planes that are at an obtuse angle to the neutral axis have a negative burgers vector (-b, red) and escape to the free surface. The +b dislocations create a soft pile-up. In turn, this soft pile-up creates a stress that acts backwards, increasing the stress needed to reactivate the originating source, hardening the material. This leads to dislocation nucleation on nearby slip planes, creating a plastic strain gradient in the cantilever. The soft pile-up length scales with beam size so that smaller beams display larger hardening and higher flow stresses.

To accommodate the plastic strain gradient, GNDs must also be present and they nucleate from available sources. Hence, if the source density, ρ_s, in the material is the same no matter the size of the sample volume, smaller samples have less sources for GND's to nucleate from. This inflates the stress in the material. In combination these two mechanisms attribute to the size effect seen in the small beams in Figure 2.40.

Ultimately, Tarleton runs a variety of simulations showing the flow stress, σ_f, as a function of the normalized beam size. The normalized beam size is the size of the beam over the average source spacing in the material, w_s. Where $w_s = \frac{1}{\sqrt{\rho_s}}$. The results of these simulations are shown in Figure 2.42. As the normalized sample dimension increased, a limit, or bulk flow stress, of 133 MPa was observed. This flow stress can be compared back with the experimental results shown in Figure 2.40, where indeed, the 10 μm sample reached approximately the same flow stress, suggesting a size-effect threshold of 10 μm for pure Ti.

Tarleton was able to relate the fundamental dislocation behavior (the microstructure) with the dimensional constraints (beam size) using a discrete dislocation model of an in situ SEM cantilever bending experiment on Ti. While the experimental sample was not irradiated, this model adequately captures the relationship between the microstructure and the dimensions of the sample. Therefore, if the irradiated microstructure of the material of interest is understood, this model can be used to predict and understand the size effects seen in cantilever bend testing.

2.4.5 Fracture in Cantilevers and Clamped Beams

The final in situ testing method to be covered in this review includes two types of beam fracture testing, the cantilever and clamped beam geometries. Both geometries are shown in Figure 2.43 at the SEM scale [134,135]. The cantilever style of fracture testing is used more often because the geometry is easier to analyze through simple beam theory. However, there are advantages to the clamped beam design that make it worth reviewing: 1) the ability to control the crack growth and 2) for in situ TEM testing, avoids losing the fractured sample in the microscope. In most of the literature, the samples are notched to induce a stress intensity. The notching geometry [136] and milling ion [137] can influence the fracture measurements and must be kept in mind when preparing samples. Additionally, ductile small-scale material testing adds complexity.

Most studies utilize finite element modeling (FEM) to generate geometry factors and understand the stress intensities induced. All must consider possible size effects whether using LEFM in the case of brittle materials or using elastic-plastic fracture mechanics models like the J-integral for ductile materials [23,138]. A few studies look at the anisotropy of the fracture behavior [139–141] and others theorize atomistic fracture models only [142–144].

Fracture testing of brittle materials like Si [145–147], alumina [148], fused quartz [148], spinel [139], and various coatings [135,149,150] have been conducted as well as on more ductile materials like W [23,124,134], Fe [138,140,151], and NiAl [125,152]. Single studies on carbon fibers [153], Bi embrittled Cu grains [123], and a Ni-Cr austenitic stainless steel [13] also exist. Many of these studies utilize FEM to generate geometry factors and understand the stress intensities induced. All must consider possible size effects whether using linear elastic fracture mechanics (LEFM) in the case of brittle materials or using elastic-plastic fracture mechanics models like the J-integral for ductile materials [23,138]. A few studies look at the anisotropy of the fracture behavior [139–141] and others theorize atomistic fracture models only [142–144].

Ductile small-scale material testing adds complexity. To get the broad picture, a study by Ritchie will be reviewed first. Here, the samples tested are not SEM or TEM scale, but the relationship between the microstructure and the macroscale continuum fracture mechanics is essential to understanding the types of toughness measurements [154]. The second study uses these continuum fracture mechanics principles and applies them to small-scale tungsten cantilevers. Here, Wurster shows the possibility for small-scale, in situ fracture testing of ductile materials [23].

Ritchie's work compares two measures of toughness in AISI 4340 alloy steel at two different austenizing temperatures, 870˚C and 1200˚C [154]. These two material conditions will be referred to as the 870˚C and the 1200˚C materials, where each temperature results in different grain sizes, which, in turn impacts toughness. Both fail in a stress-controlled manner (quasi-cleavage and intergranular cracking), however Ritchie suggests that these results would also hold for a strain-controlled ductile failure [154,155]. The two measures of toughness used by Ritchie are traditional fracture toughness, K_{IC}, and the Charpy test where J_{IC} is obtained.

The 1200°C condition results in K_{IC} twice as large as the 870°C material. However, the J_{IC} is lower in the 1200°C than the 870°C. This discrepancy could not be explained through a difference in shear lip energy or strain rate, so Ritchie looked to the microstructure. The 1200°C material has grains on the order of 250-350 μm, while the 870°C material grains are an order of magnitude smaller at 25-30 μm in diameter [154]. Due to grain boundary irradiation embrittlement, the grain boundaries are the fracture sites and act as the critical microstructural feature, the characteristic length, *l*.

Figure 2.44 highlights the difference in the two materials' microstructures in relation to the two different toughness tests. The critical stress for fracture, σ_f, is less in the 1200°C material than in the 870°C material in both testing cases. The Charpy testing captures this fact because it evaluates a large volume of material, much larger than the grain size. In comparison, the K_{IC} test acts in a local manner, on the order of a single grain in the 870°C material. When, σ_f acts at the grain boundary, the material fails. This results in the smaller grain material (870°C) giving a smaller K_{IC} result than the larger grain material (1200°C). The 1200°C material doesn't increase toughness, it simply increases the characteristic length over which σ_f must act to induce failure. This gives a false impression of the toughness in the 1200°C material. Both the K_{IC} and J_{IC} values must be understood in relation to the microstructure for a complete picture.

In this work, we can see that microstructure can drastically impact the toughness measurements obtained. When sample dimensions are reduced, to a few grains or even a single grain, it is even more critical to understand the relationship between the microstructure and the sample dimensions. Any model attempting to capture this fracture behavior will need to incorporate the learnings from studies such as this. In the next section, we'll look at an

experiment by Wurster, where continuum scale fracture mechanics, the J-integral approach, is applied to small-scale ductile fracture samples.

Wurster FIB mills single crystal W cantilevers 10 μm long and in situ SEM fracture tests them, utilizing a J-integral model to analyze the results [23]. The cantilevers are notched and the stress intensity, K_Q, at the notch tip can be found using LEFM for the cantilever geometry. Wurster then applies the J-integral model, using the following equation to quantify the absorbed energy [23].

$$J_i = \frac{K_i^2(1-v)^2}{E} + \frac{\eta A_{Pl(i)}}{w(h-a_0)}$$
Equation 2.59

The first term is the elastic energy and the second is the plastic energy, where v is Poisson's ratio, E the elastic modulus, η a constant, A_{pl} the area under the plastic portion of the load-displacement curve, *B* the thickness, *W* the width of the beam, and a_o the initial crack length.

Wurster loads and unloads the cantilevers multiple times to capture the crack growth behavior and after each unloading measures the crack growth, Δa. Plotting the J-integral versus the change in crack length, the critical, J_{IC}, value can be obtained. J_{IC} is the point at which the crack transitions from the blunting regime to the crack growth regime. Wurster's data and this transition point are identified in Figure 2.45.

Using the J_{IC} value, Wurster can calculate an apparent fracture toughness value, $K_{Q,J}$, using the following equation [23].

$$K_{Q,J} = \sqrt{\frac{J_{IC}E}{1-v^2}}$$
Equation 2.60

This allows for a comparison with a traditional K_{IC} measurement as calculated from LEFM. Wurster finds that this $K_{Q,J}$ is significantly larger than the LEFM result, 20 MPa m$^{1/2}$ vs 3 MPa m$^{1/2}$ [23]. The authors suggest that the K_{IC} value from LEFM can be used as a lower bound with

the $K_{Q,J}$ being an upper bound of values. Compared to the literature bulk values (4-8 MPa m$^{1/2}$), the $K_{Q,J}$ values are inflated. The authors attribute this to the small sample size, however they make no assertions about the specific microstructural mechanism driving this size-effect [23]. This leaves a gap in the literature where small scale fracture testing has yet to delve into the microstructure-sample dimension relationship for semi-brittle and ductile material fracture.

Table 2.1 - Chemical composition of model Fe-9%Cr ODS alloy

Chemical Composition (wt.%, balance Fe)														
C	Si	Mn	P	S	Ni	Cr	W	Ti	Y	O	N	Ar	Y_2O_3	Ex. O
0.14	0.048	0.05	<0.005	0.004	0.06	8.67	1.96	0.23	0.27	0.14	0.017	0.004	0.34	0.07
$[Y_2O_3]$ = 1.27 x [Y]														
[Ex.O] = [Total O] – [O in Y_2O_3 powder] = [O] – 0.27 x [Y]														

Table 2.2 - Microstructural characterization of Fe-9%Cr ODS alloy for as-received and irradiated conditions- [6,50]

Feature	Measurement	As-received	Fe2+ irradiated (3 dpa, 500°C)	Fe2+ irradiated (100 dpa, 500°C)	Proton-irradiated (3 dpa, 500°C)
Grains/Laths	# of grains measured	104	104	105	104
	Effective diameter ($\times 10^{-6}$ m)	0.23 ± 0.12	0.28 ± 0.08	0.37 ± 0.19	0.31 ± 0.11
Dislocation lines	# of measurements	17	21	35	46
	Density ($\times 10^{14}$ m^{-2})	19.1 ± 3.8	22.6 ± 4.8	18.4 ± 6.9	17.6 ± 5.3
Carbide Precipitates	# of carbides measured	36	48	34	51
	Effective diameter ($\times 10^{-6}$ m)	0.11 ± 0.07	0.08 ± 0.04	0.08 ± 0.03	0.07 ± 0.03
	Density ($\times 10^{20}$ m^{-3})	0.20	0.76	0.29	0.46
Voids	# of voids measured	0	0	0	8
	Diameter ($\times 10^{-9}$ m)	-	-	-	4.00 ± 1.51
	Density ($\times 10^{21}$ m^{-3})	-	-	-	0.34 ± 0.44
Dislocation loops	# of loops measured	0	48	182	688
	Diameter ($\times 10^{-9}$ m)	-	8.5 ± 2.2	10.7 ± 4.2	8.4 ± 1.7
	Density ($\times 10^{21}$ m^{-3})	-	2.1 ± 0.1	4.3 ± 0.8	10.2 ± 8.0
Oxide nanoclusters	# of clusters measured	413	188	1474	975
	Average diameter (nm)	5.71 ± 0.09	5.74 ± 0.11	5.58 ± 0.06	5.15 ± 0.04
	Density ($\times 10^{21}$ m^{-3})	443	120	433	414
Average Obstacle Spacing on Glide Plane (nm)		19.9	37.6	20.2	21.2
$\Delta\sigma_{ys}$ calculated from microstructure (MPa)		-	-108	-10	25
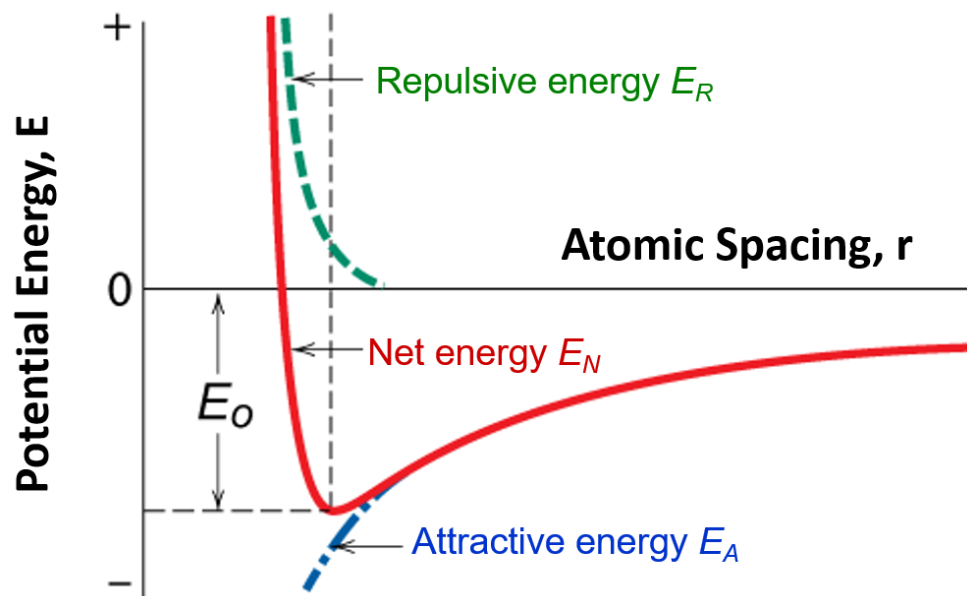
Figure 2.1 – Potential energy vs atomic spacing – adapted from [8]
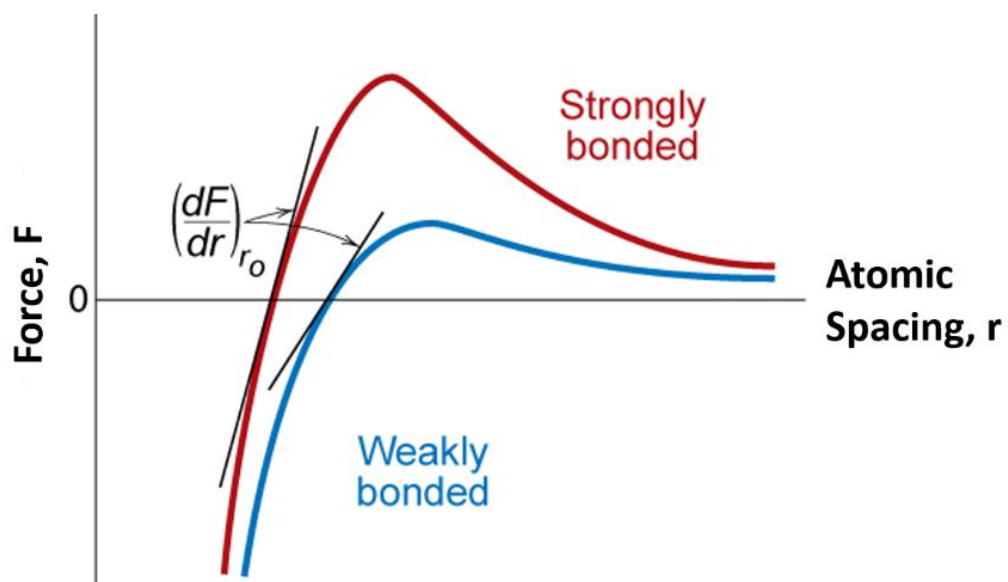
Figure 2.2 – Force vs atomic spacing – adapted from [8]
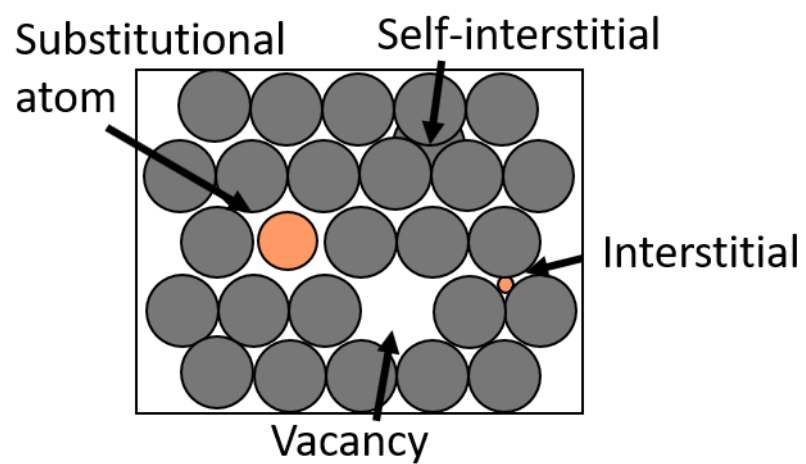
Figure 2.3 – Point defects in a crystal lattice – adapted from [8]
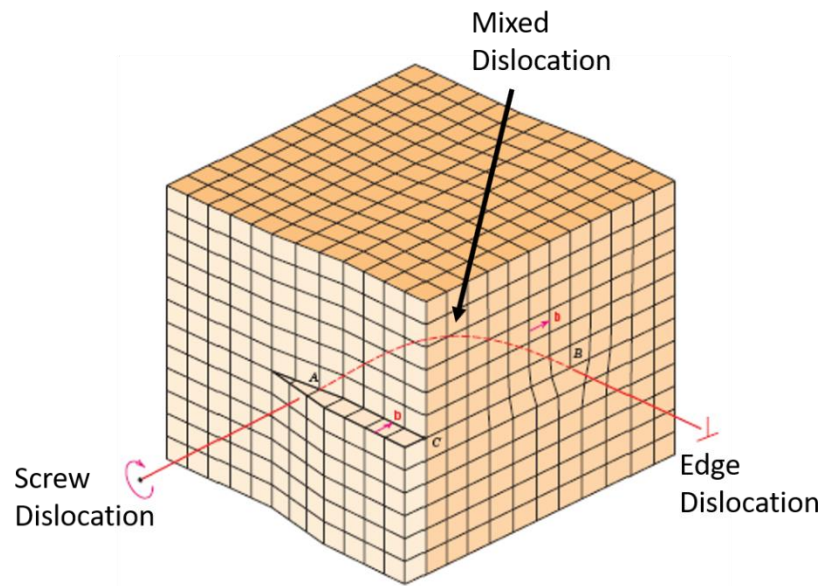
Figure 2.4 – Dislocations in a crystal lattice – adapted from [8]
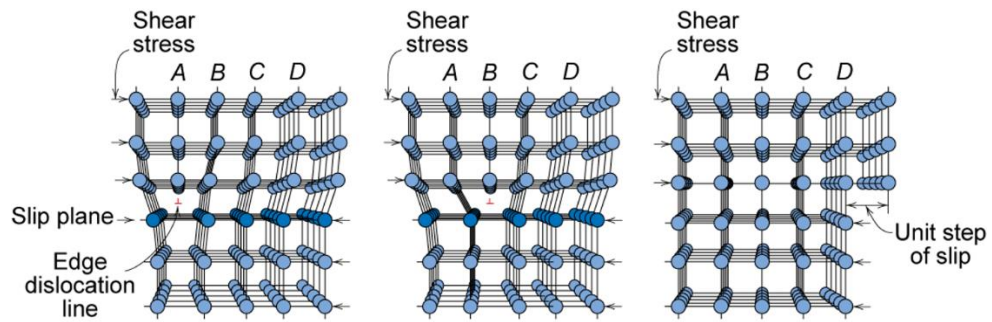
Figure 2.5 – Dislocation motion in a crystal lattice – adapted from [8]
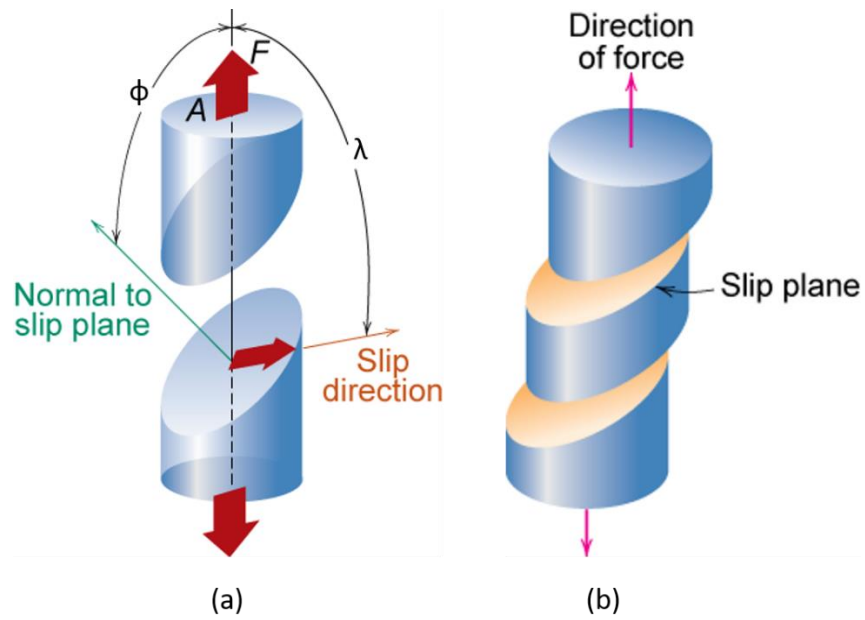
Figure 2.6 – (a) Normal to slip plane, φ, and slip direction, λ, angles from uniaxial tensile load (b) idealized macroscopic slip events in a single crystal – adapted from [8]
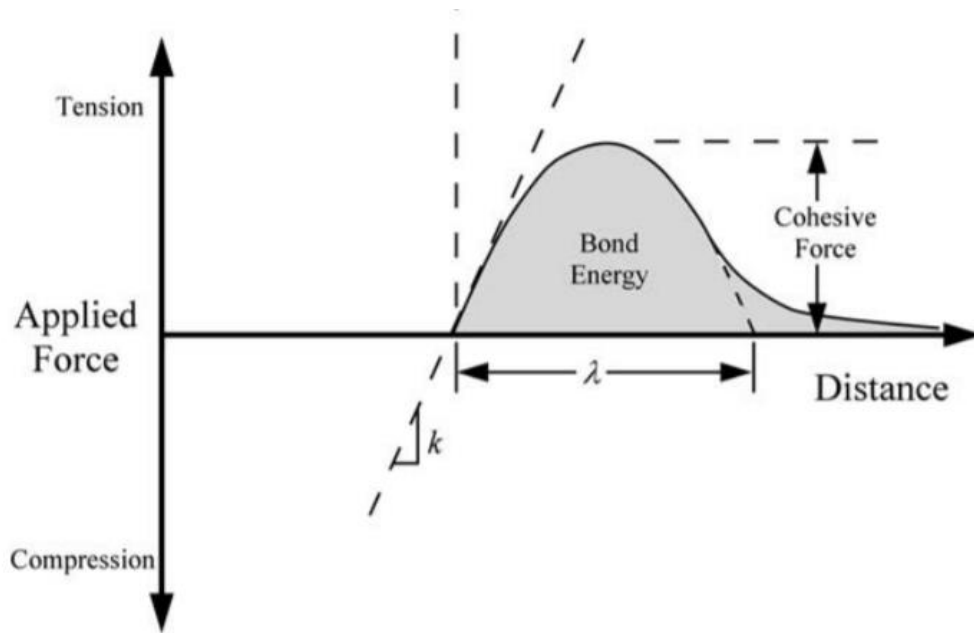
Figure 2.7 – Description of bond energy with applied tension and equilibrium spacing between atoms depicted to overcome cohesive force between atoms – adapted from [12]
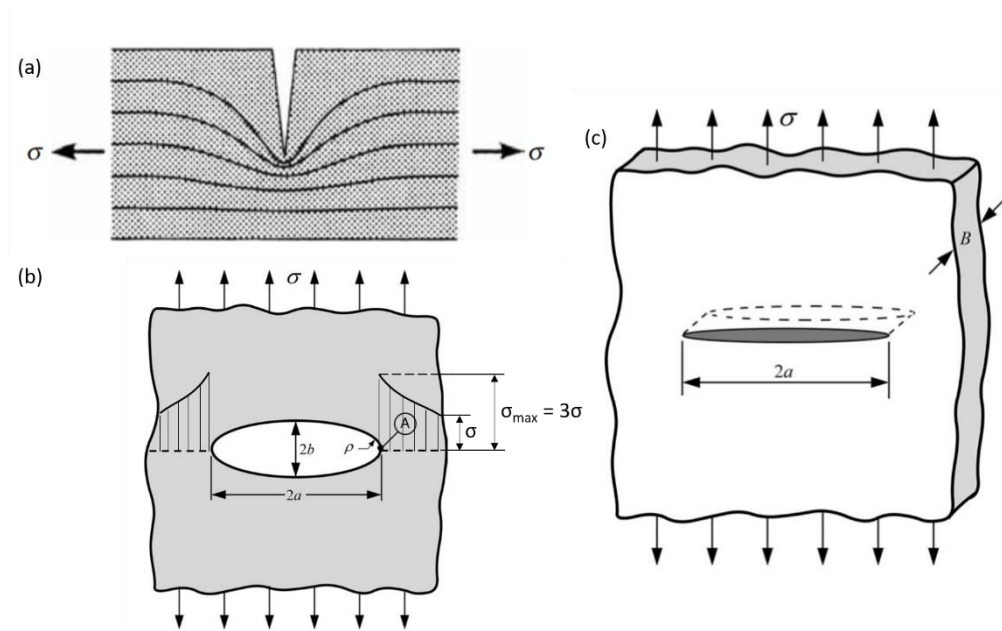
Figure 2.8 – (a) Stress line concentrations in an edge-notched specimen (b) elliptical flaw with major axis, 2a, minor axis 2b, and applied stress, σ. Stress distribution depicted with highest stress at edges of major axis perpendicular to the applied stress direction reaching approximately 3 times the applied stress. (c) Infinitely wide plate subjected to remote tensile stress used in Griffith energy criterion derivation – adapted from [16,20]
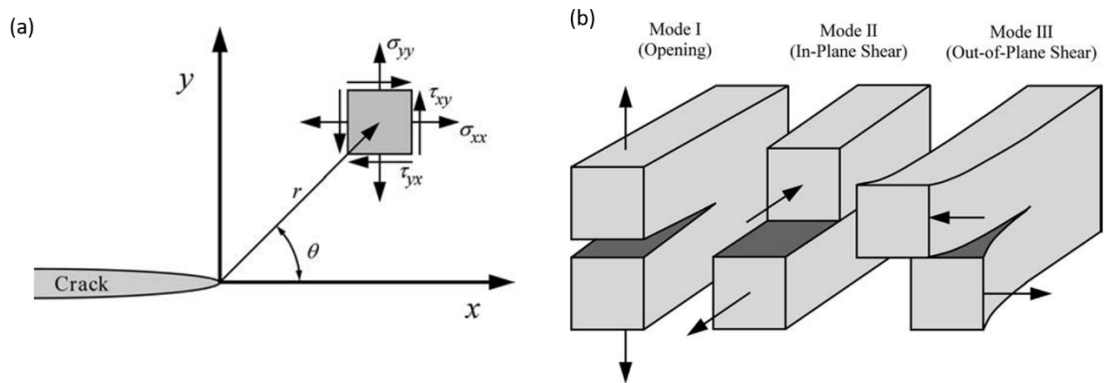
Figure 2.9 – (a) Polar coordinate system defined with origin at crack tip (b) modes of loading around a crack – adapted from [12]
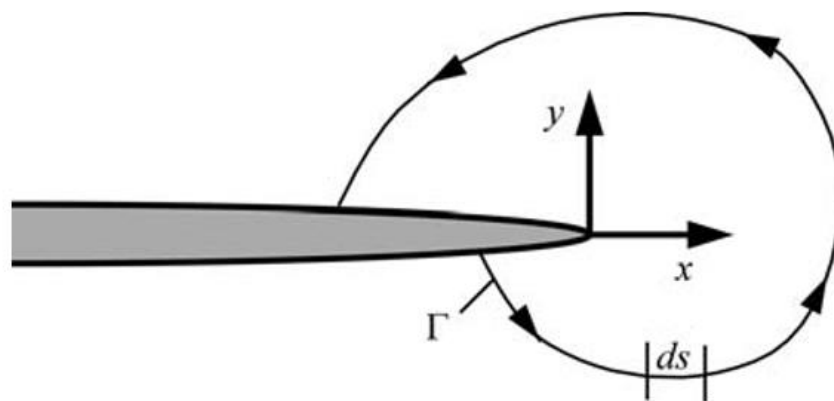
Figure 2.10 – Arbitrary path drawn around the crack tip. Illustrates the path-independent nature of the J-integral – adapted from [12]
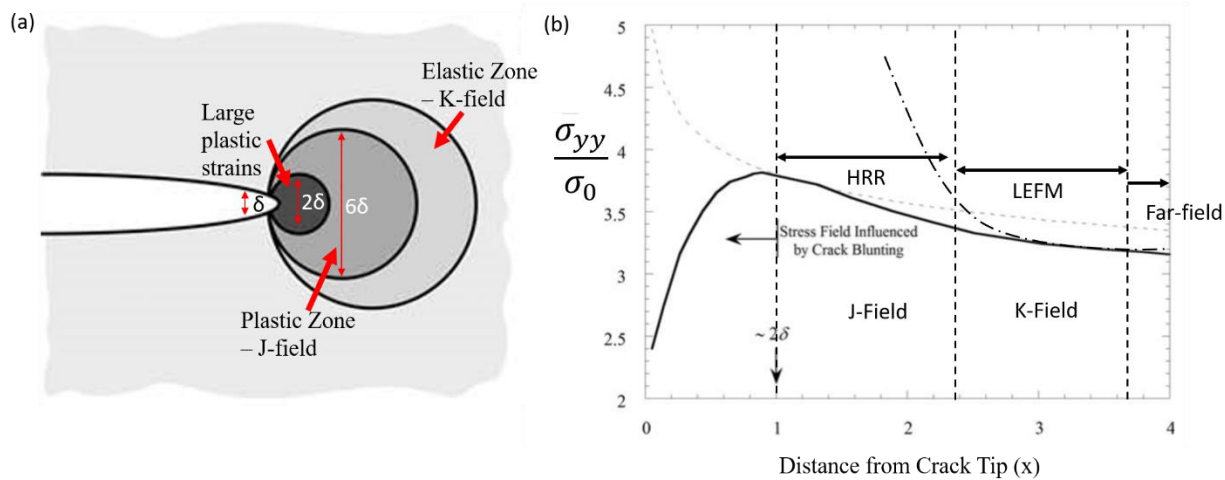
Figure 2.11– (a) Depiction of large plastic strain, plastic J-field, and elastic K-field regions around the crack tip as a function of the crack tip opening displacement, δ. (b) Stress as a function of distance from crack tip with HRR and LEFM models region of influence defined – adapted from [20]
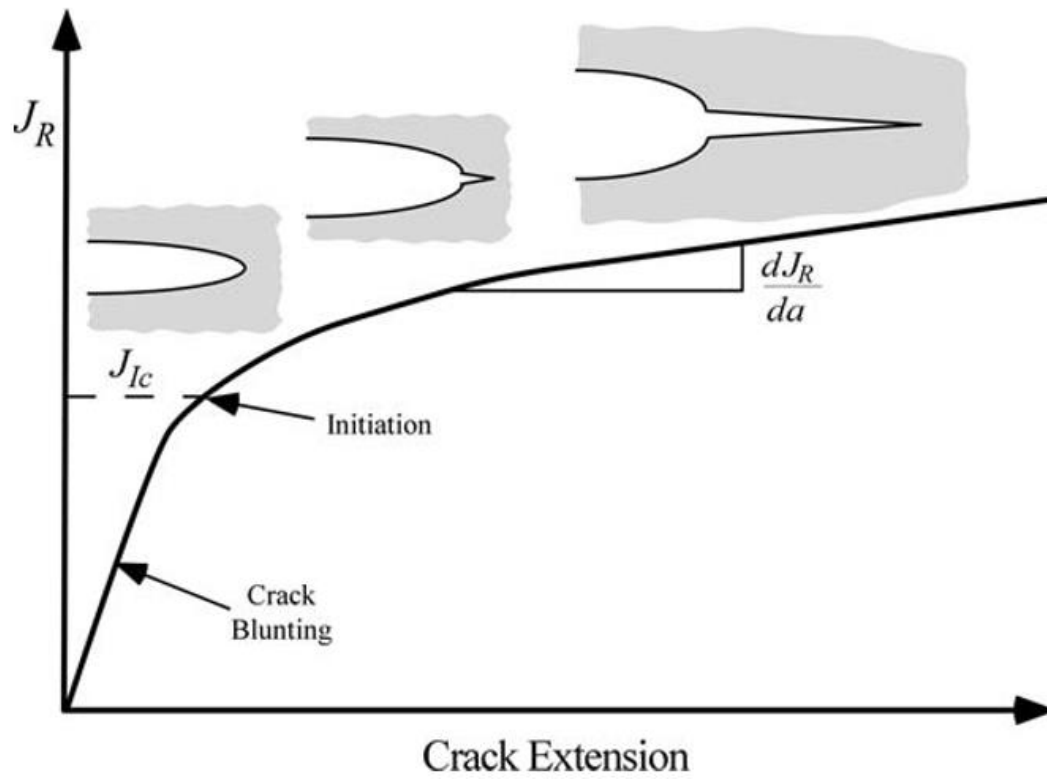
Figure 2.12 – J resistance curve as a function of crack growth. Initially crack blunts, but at critical J value, JIC, the crack begins to grow – adapted from [12]
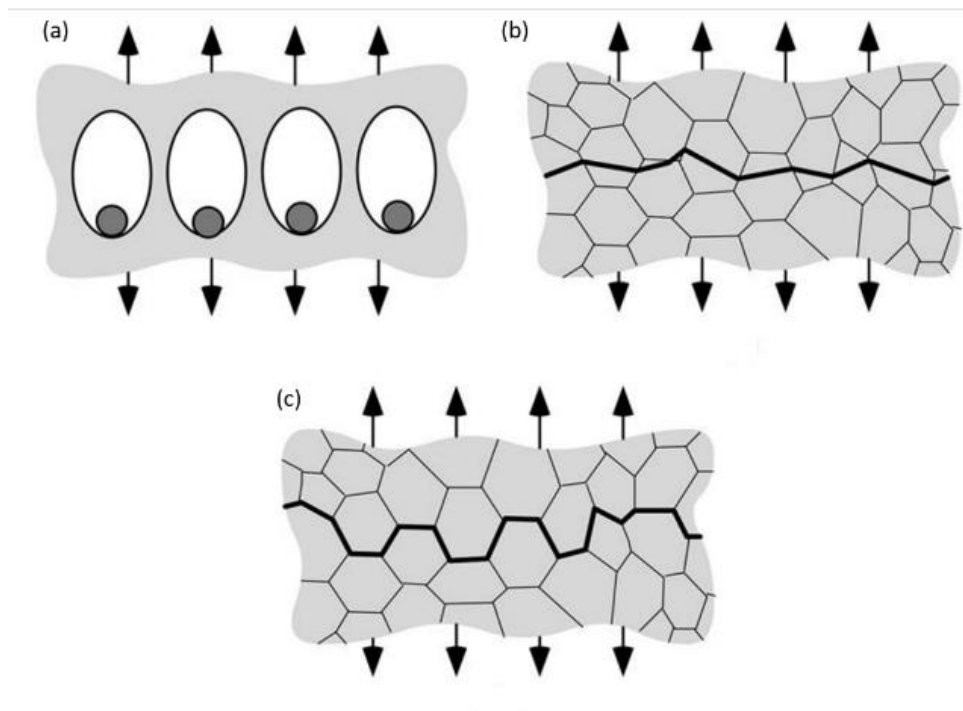
Figure 2.13 – Mechanisms of fracture in metals: (a) ductile fracture from void nucleation and growth, (b) cleavage, and (c) intergranular fracture– adapted from [12]
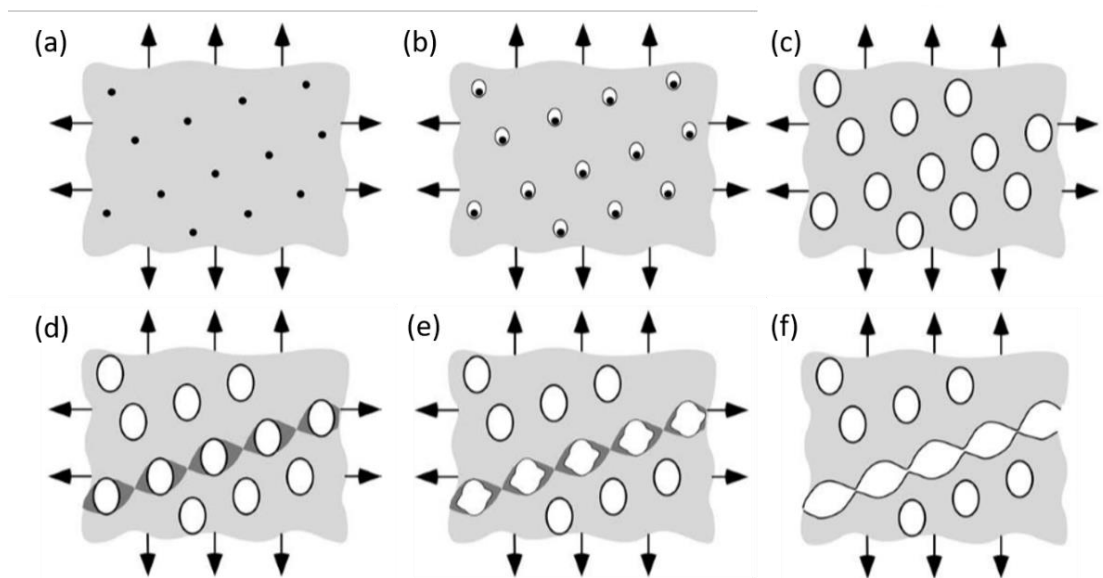
Figure 2.14 – Schematic images showing (a) particles in a matrix, (b) void nucleation, (c) void growth, (d) strain localization between voids, (e) necking between voids and, finally, (f) coalescence and fracture – adapted from [12]
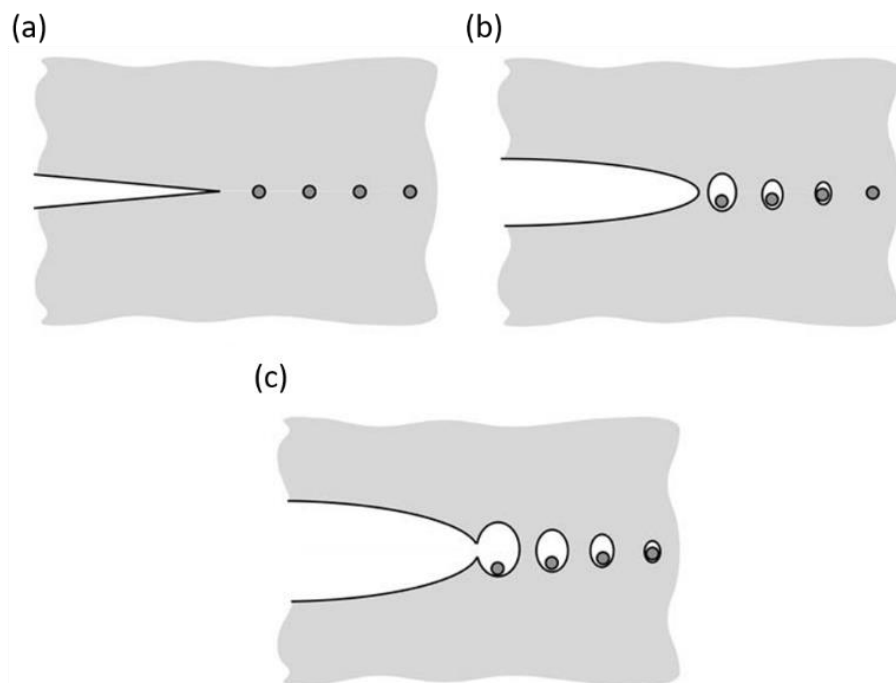
Figure 2.15 – Schematic images showing ductile crack growth (a) particles in a matrix at the crack tip (b) void nucleation and growth, (c) void coalescence results in crack growth – adapted from [12]
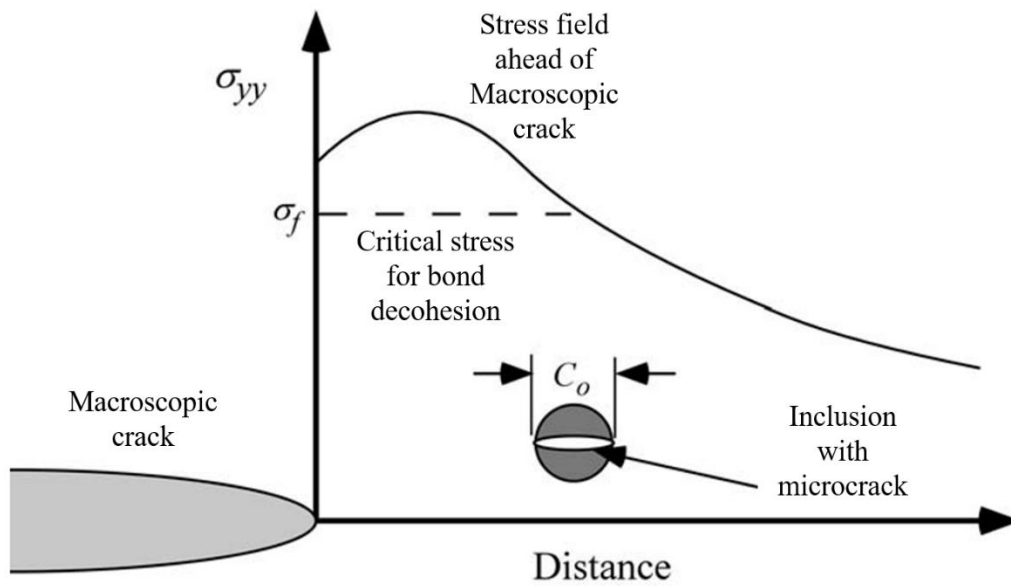
Figure 2.16 – Stress field ahead of macroscopic crack, where an inclusion with a microcrack feels the strain in the matrix due to the macroscopic crack, and propagates into the matrix causing cleavage fracture – adapted from [12]
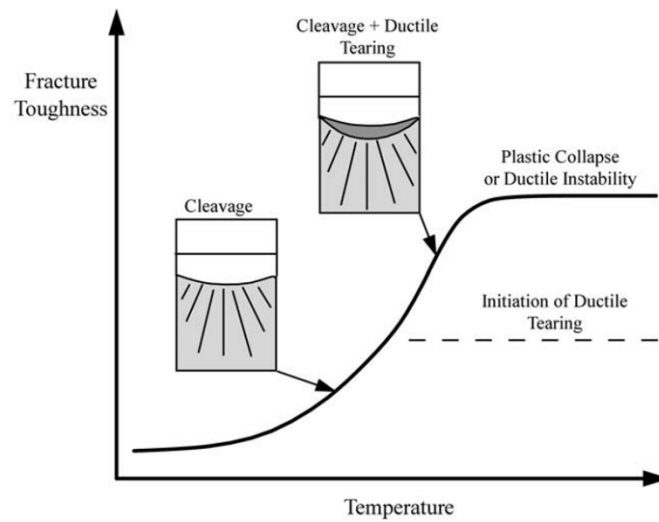
Figure 2.17 – The ductile-to-brittle transition temperature occurs over a narrow band of temperatures in bcc metals; at low temperatures the material cleaves, at higher temperatures the material exhibits ductile microvoid coalescence– adapted from [12]
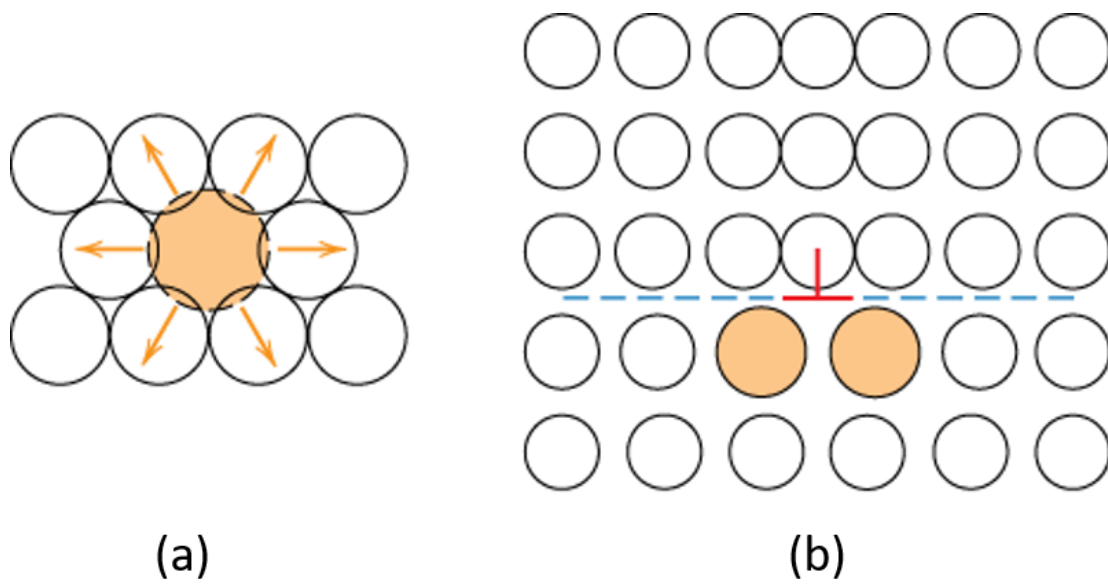
Figure 2.18 – (a) Large impurity atom introducing compressive field in lattice (b) two impurity atoms congregated around an edge dislocation to reduce lattice strain – adapted from [8]
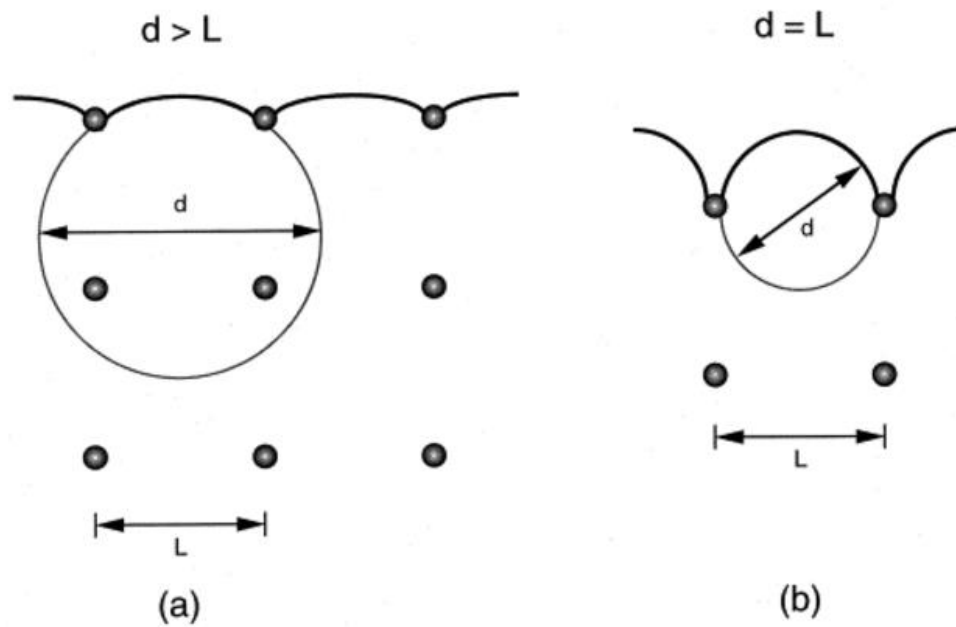
Figure 2.19 – Orowan mechanism relating characteristic length, d, with the obstacle spacing, L
(a) d > L blocks dislocation motion, (b) d = L dislocation motion is uninhibited – adapted from
[8]
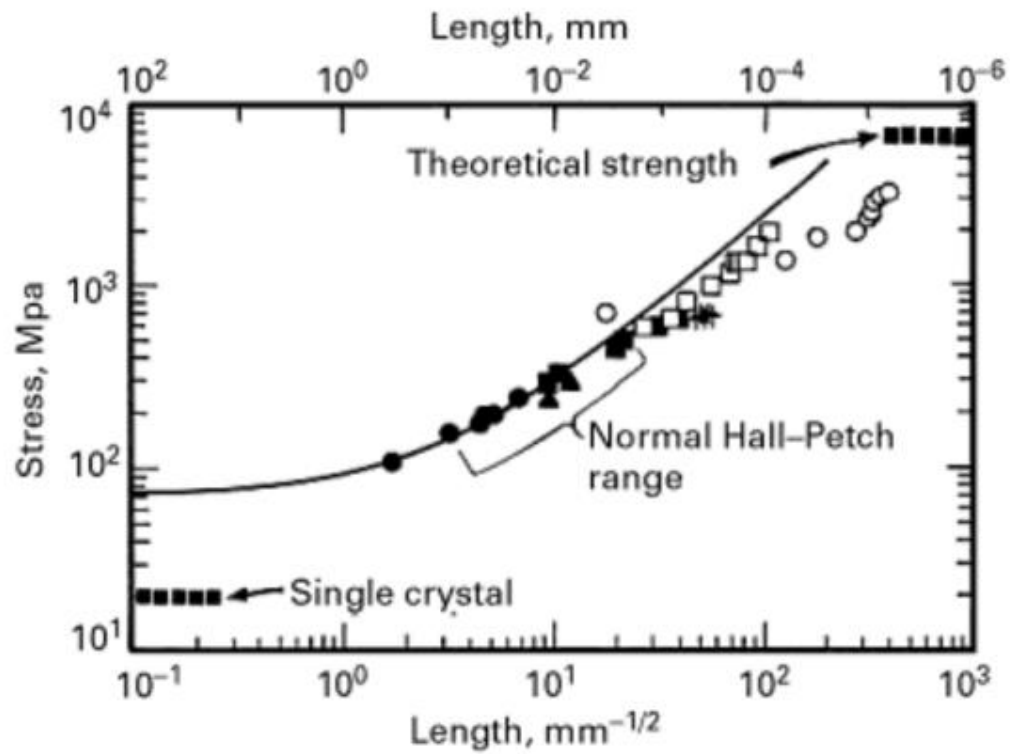
Figure 2.20 – Hall-Petch plot for iron and low-carbon steel across grain sizes ranging from 100 µm to 1 nm – adapted from [9]
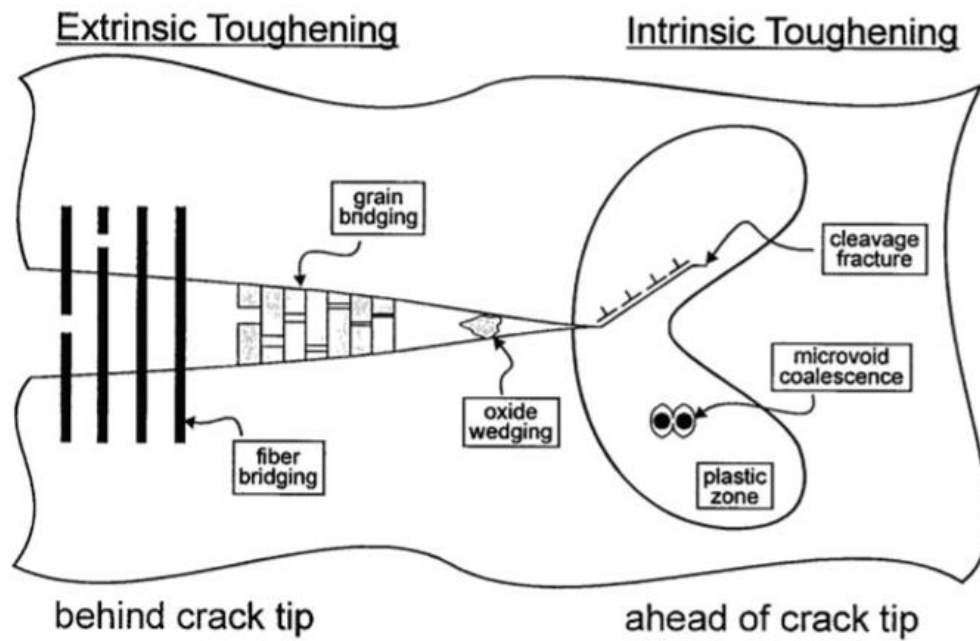
Figure 2.21 – Extrinsic (behind crack tip) and intrinsic (ahead of crack tip) toughening mechanisms - adapted from [13]
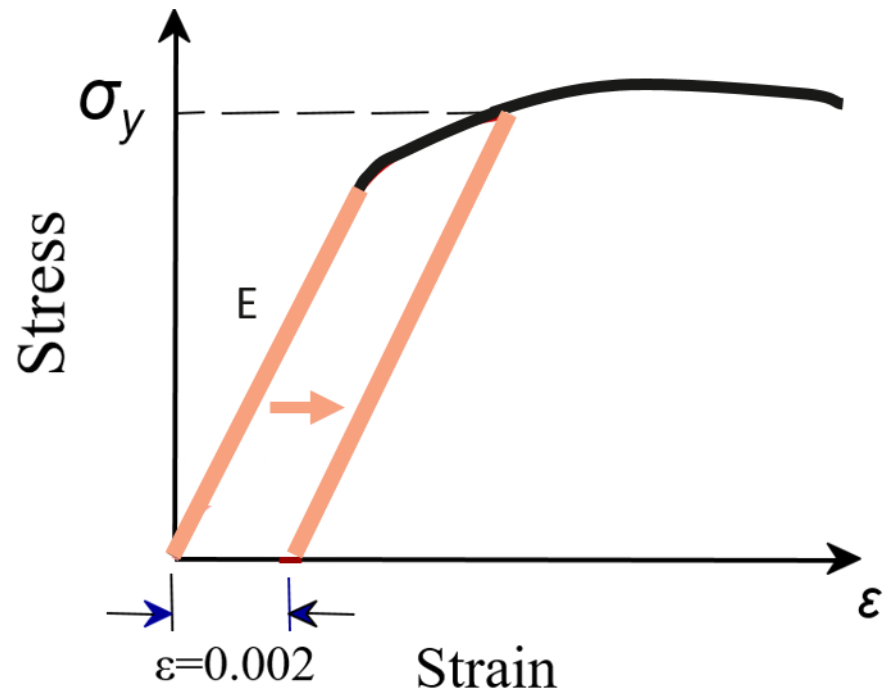
Figure 2.22 – Stress-strain curve showing yield strength at 0.002 strain offset - adapted from [8]
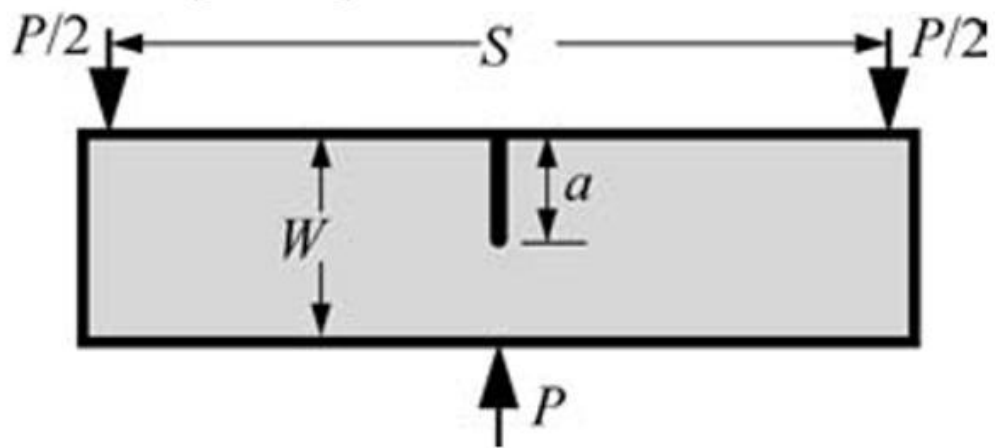
Figure 2.23 – Single edge notched bend (SE(B)) diagram with load, P, width, W, loading separation, S, and crack length, *a* - adapted from [12]
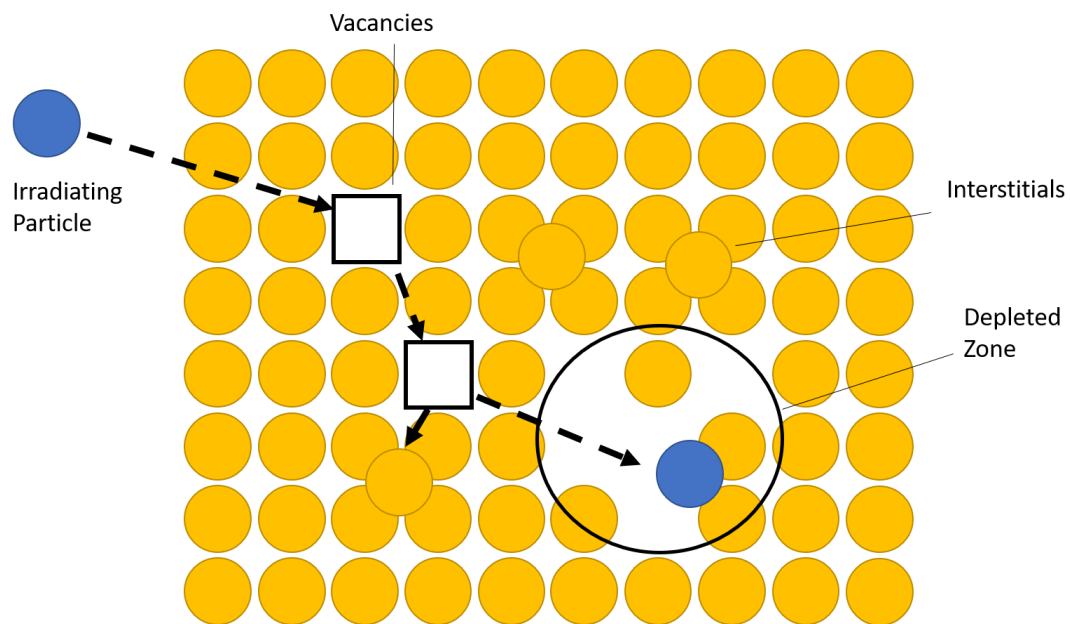
Figure 2.24 – Diagram of damage cascade with irradiating particle, vacancies and interstitials formed, and depleted zone - adapted from [7]

1 MeV electrons
$\bar{T}$ = 60 eV
ε = 50-100%

1 MeV protons
$\bar{T}$ = 200 eV
ε = 25%

1 MeV heavy ions
$\bar{T}$ = 5 keV
ε = 4%

1 MeV neutrons
$\bar{T}$ = 35 keV
ε = 2%

E_i 10^6

10^5
$\overline{T_n}$

10^4
$\overline{T_i}$

10^3
$\overline{T_p}$

10^2
$\overline{T_e}$

E_d 10^1
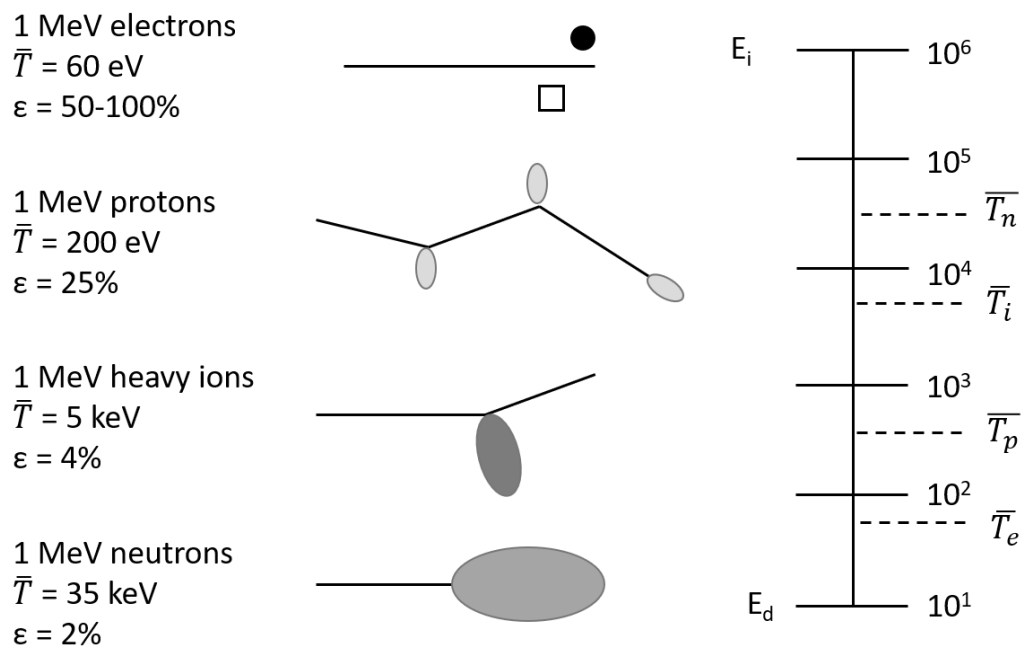
Figure 2.25 – Diagram of damage cascades for different irradiating particles, with average recoil energy, $\bar{T}$, and displacement efficiency, ε, adapted from [7]
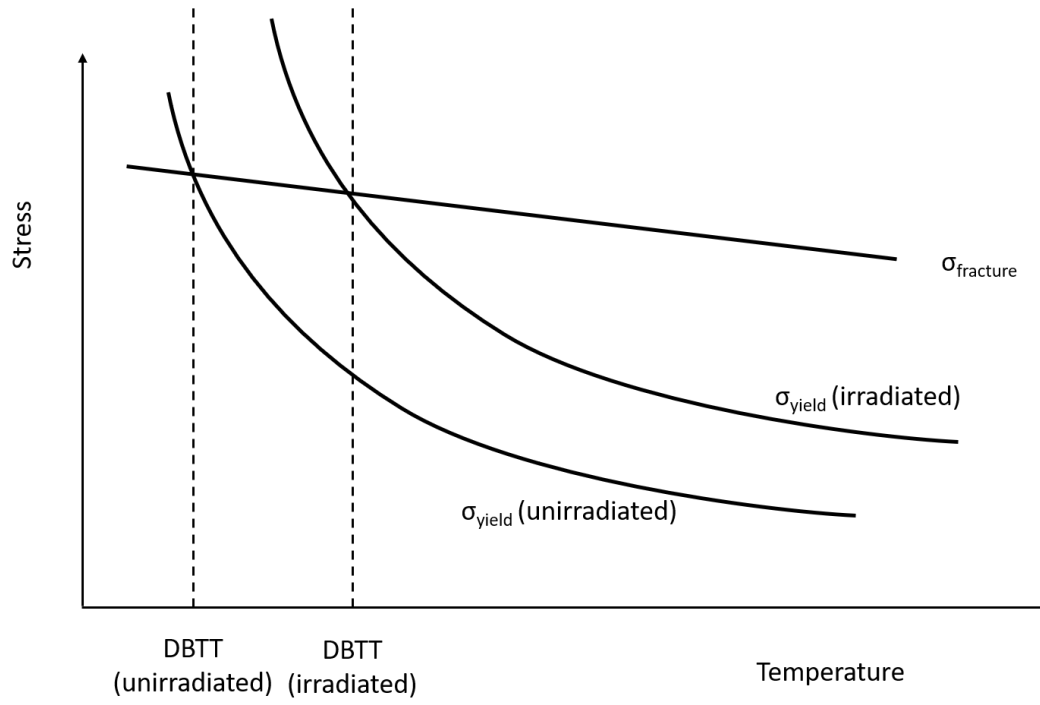
Figure 2.26 – Shift in DBTT with irradiation due to hardening in material from irradiation defects - adapted from [7]
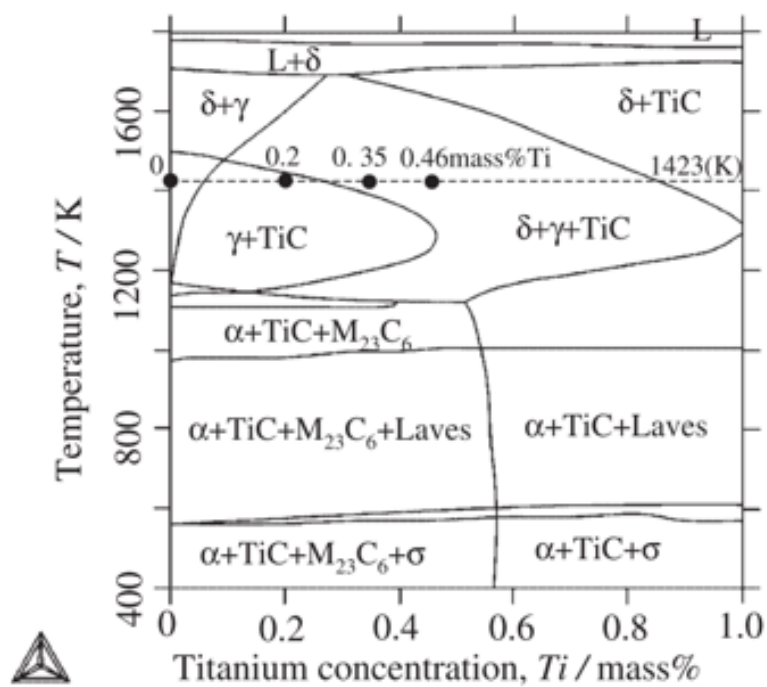
Figure 2.27 – Fe-9%Cr phase diagram predicting a fully martensitic alloy – reproduced from [16]

as-received

Grain boundaries

Dense dislocation region

Oxide nanoparticles

100 nm
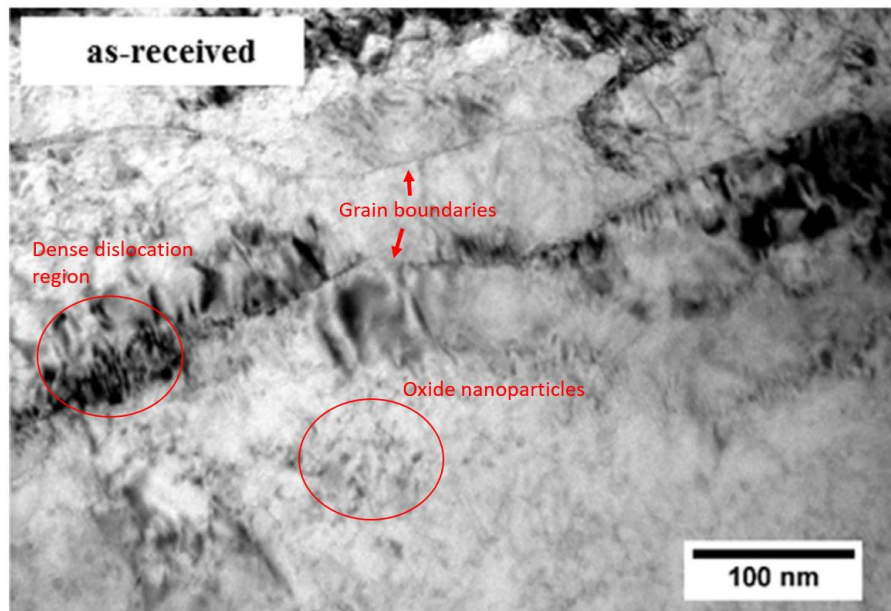
Figure 2.28 – TEM micrograph of as received Fe-9%Cr ODS – reproduced from [6]
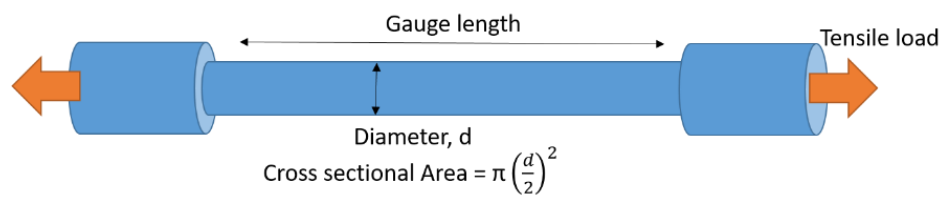
Figure 2.29 – Tensile sample with gauge length, diameter, and cross-sectional area defined.
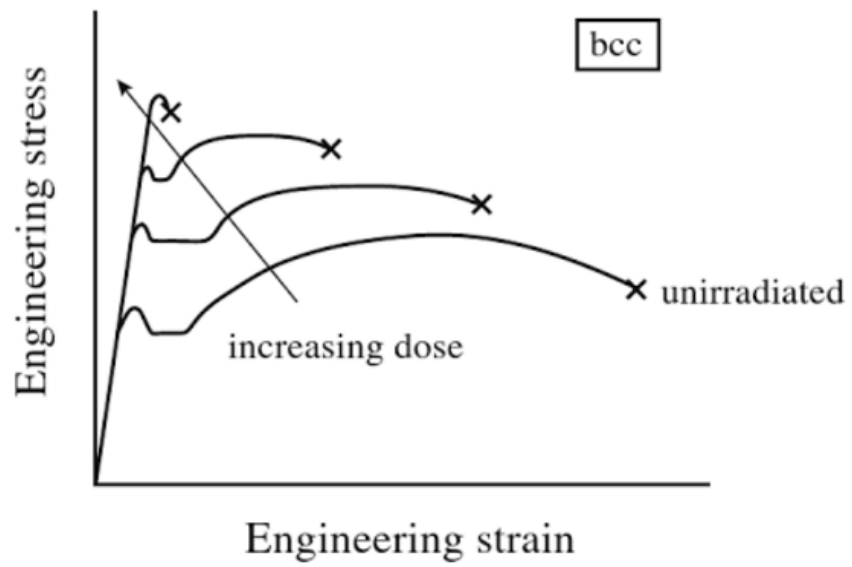
Figure 2.30 – General behavior of irradiated ferritic (bcc) steel undergoing uniaxial tensile loading - adapted from [7] .
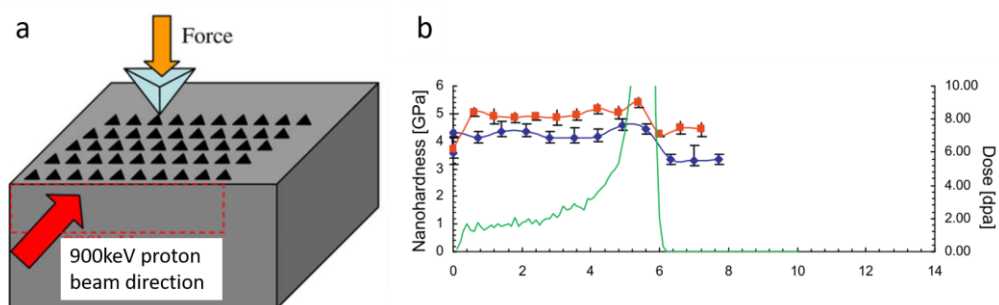
Figure 2.31 - (a) Nanoindentation schematic on HT-9 alloy (b) nanoindentation results as a function of depth on proton irradiated HT-9 at room temperature with damage profile overlayed – adapted from [39]
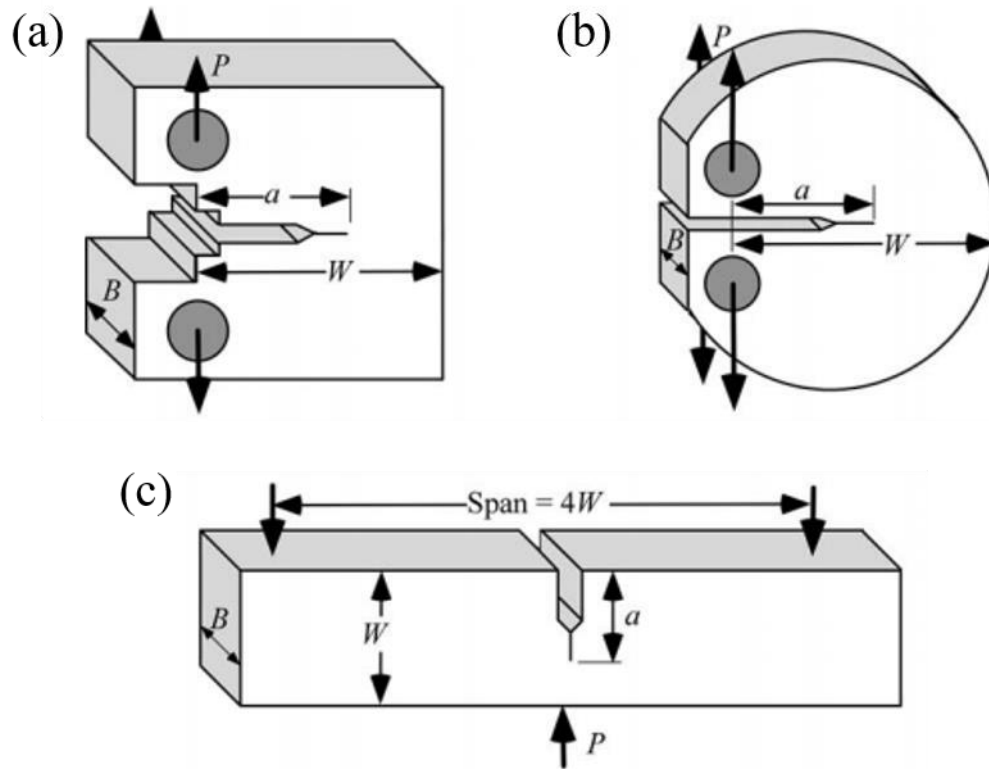
Figure 2.32 – Examples of specimens for (a) compact tension (b) spherical compact tension and (c) charpy impact testing – adapted from [12]
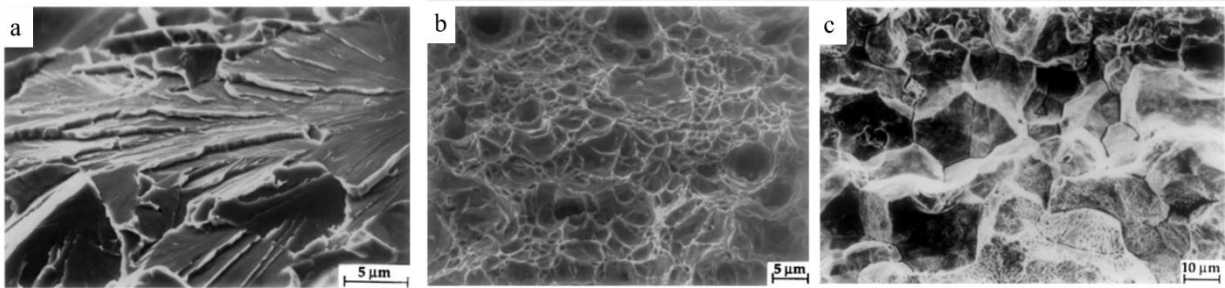
Figure 2.33 – Fractographs of (a) brittle, cleavage fracture, (b) ductile fracture, (c) intergranular fracture – adapted from [12]
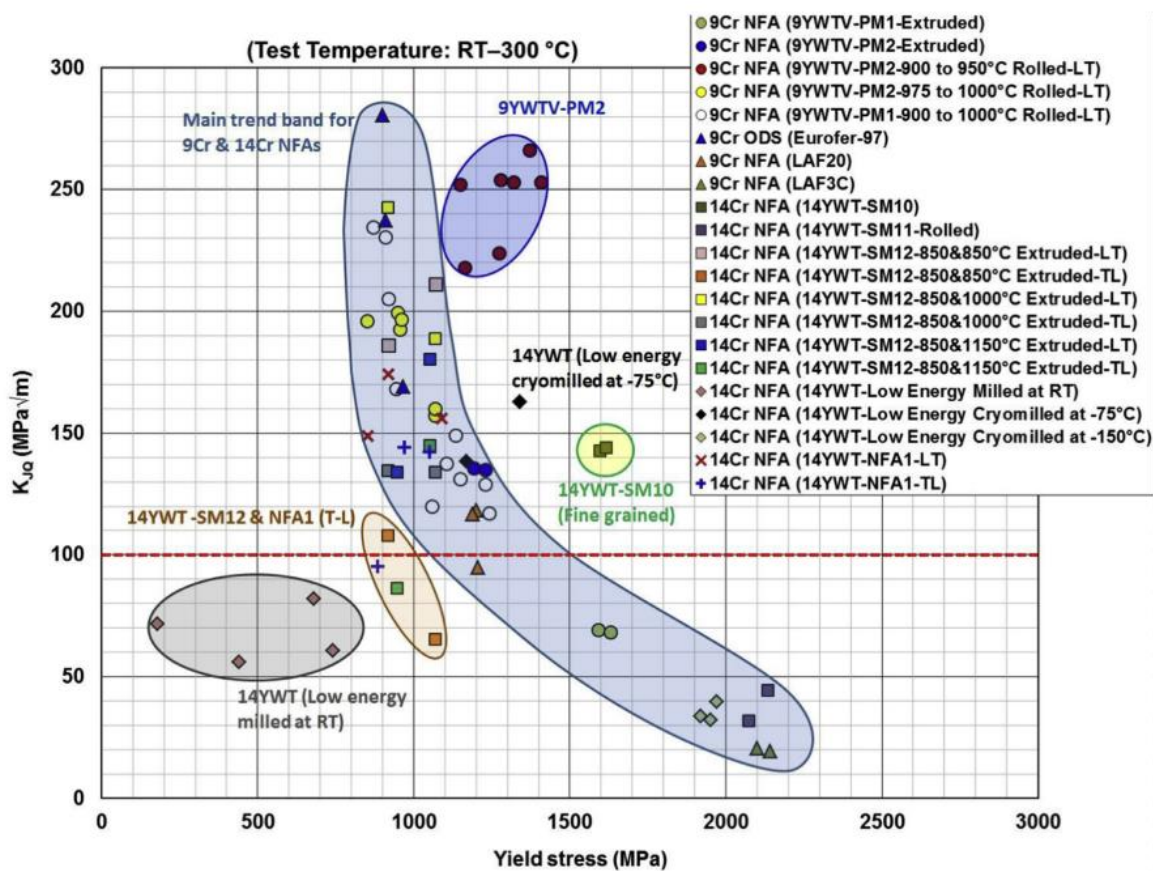
Figure 2.34 – Fracture toughness, KQ,J (MPa m1/2) is plotted as a function of yield strength (MPa) for a variety of Fe-9%Cr and Fe-14%Cr nanostructured alloys – reproduced from [48]
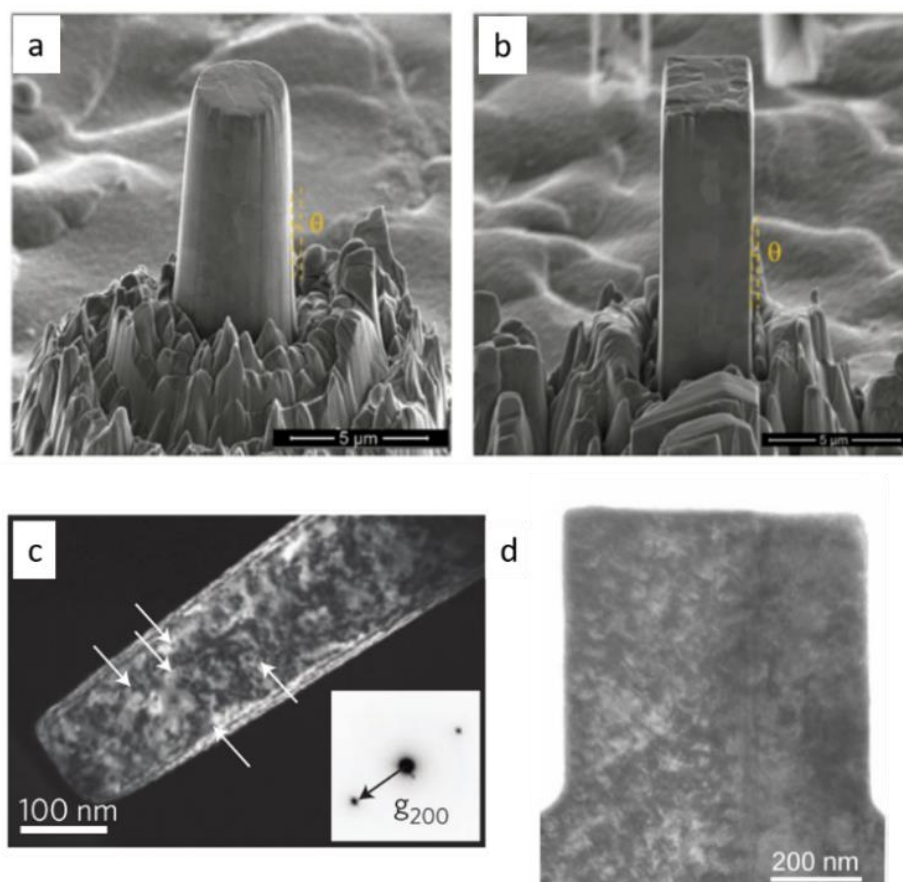
Figure 2.35 – Images from literature showing in situ SEM (a) cylindrical and (b) rectangular micropillars as well as in situ TEM (c) cylindrical and (d) rectangular micropillars for compression – adapted from [42,46,47]
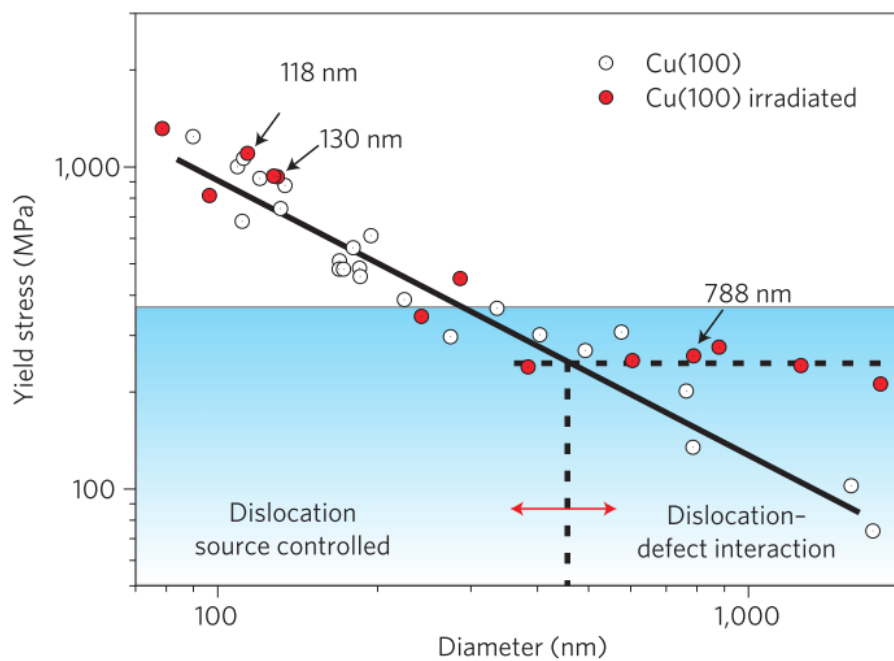
Figure 2.36 – Results of irradiated Cu micropillar compression test conducted by Kiener, et al. – reproduced from [47]
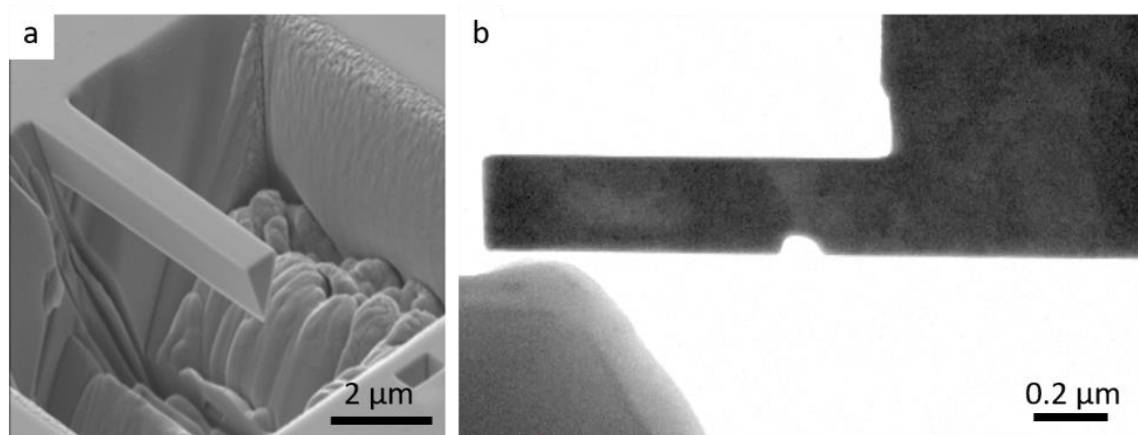
Figure 2.37 – Examples of cantilevers FIB milled at (a) SEM scale and (b) TEM scale – adapted from [90,91].
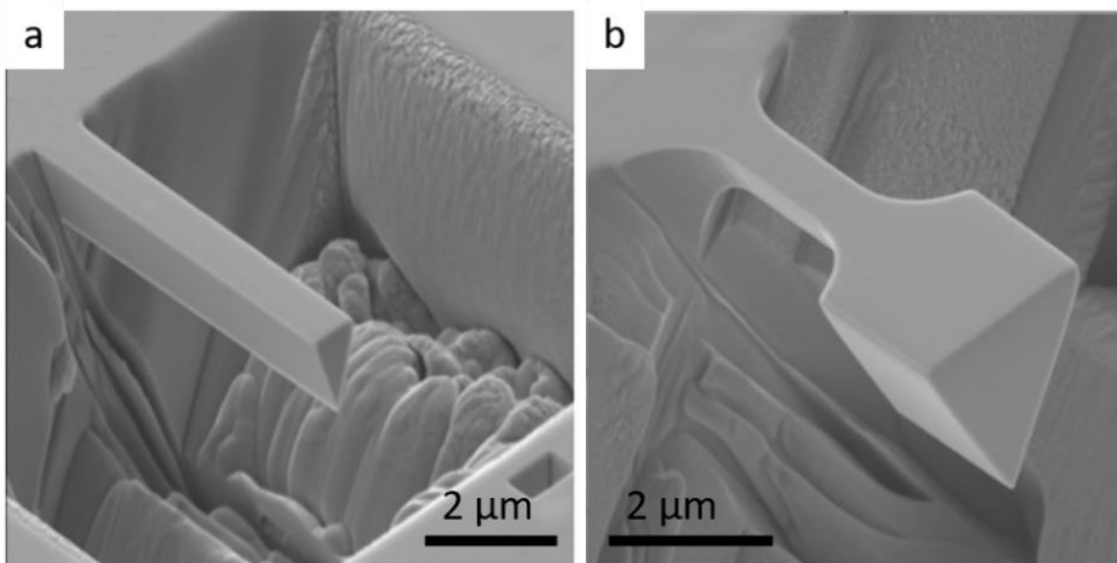
Figure 2.38 – Work by Armstrong et al. displaying the (a) uniform and (b) waisted cross-section cantilever beams – adapted from [90]
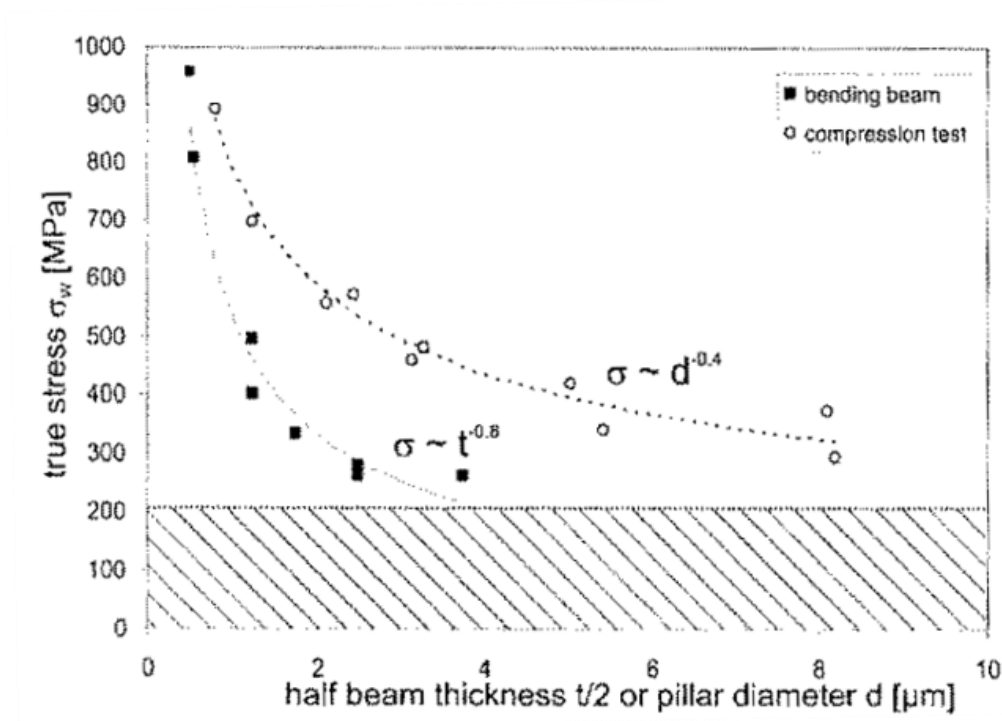
Figure 2.39 – Results from Kiener comparing the true stress (flow stress at 20% strain) measured in micropillar compression and cantilever bending as a function of micropillar diameter or beam thickness. A difference in size-effect is seen for each geometry – reproduced from [127]
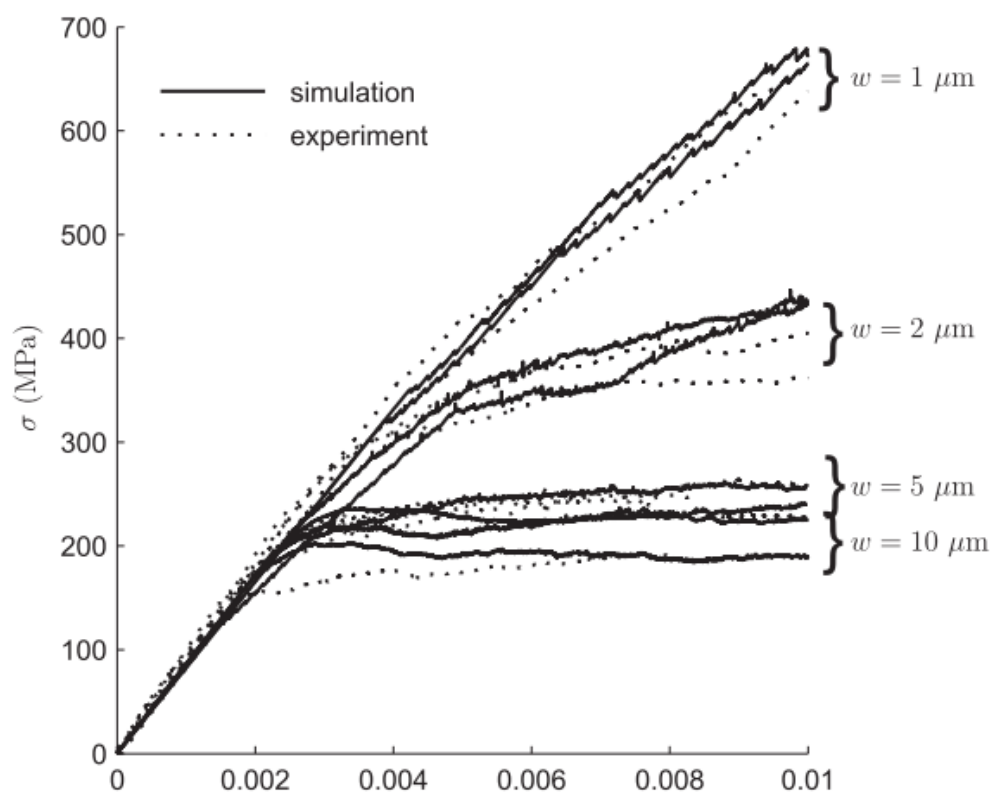
Figure 2.40 – Tarleton model and experimental stress-strain results compared for Ti beams with increasing widths – reproduced from [95]
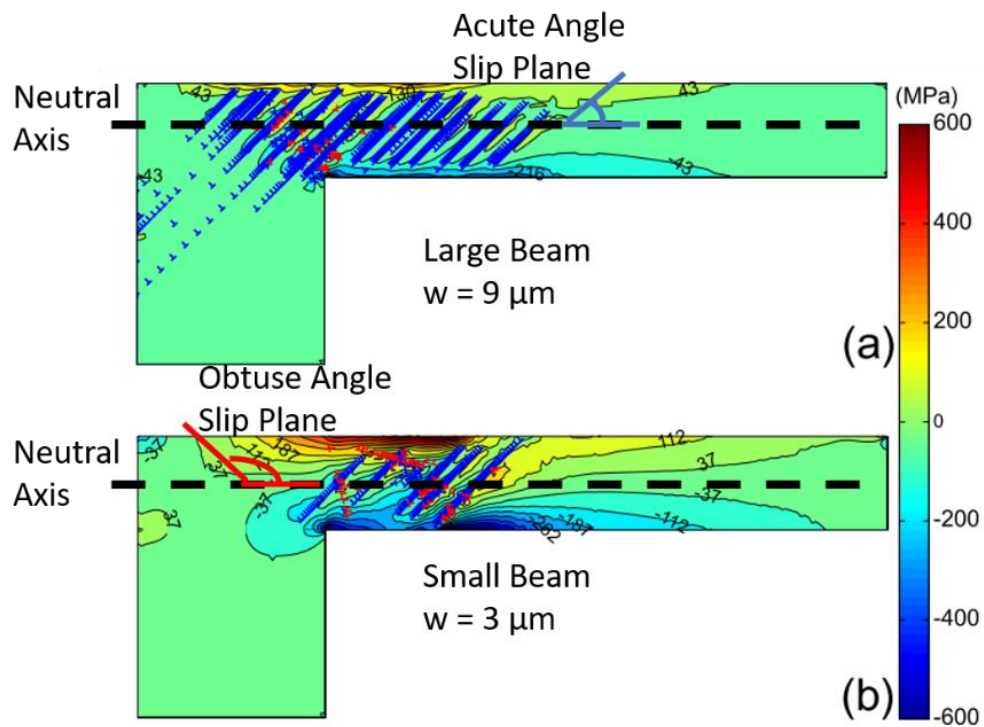
Figure 2.41 – Dislocation structure overlaid on stress finite element model of (a) w = 9 µm and (b) w = 3 µm at a strain of 0.01 – adapted from [95]
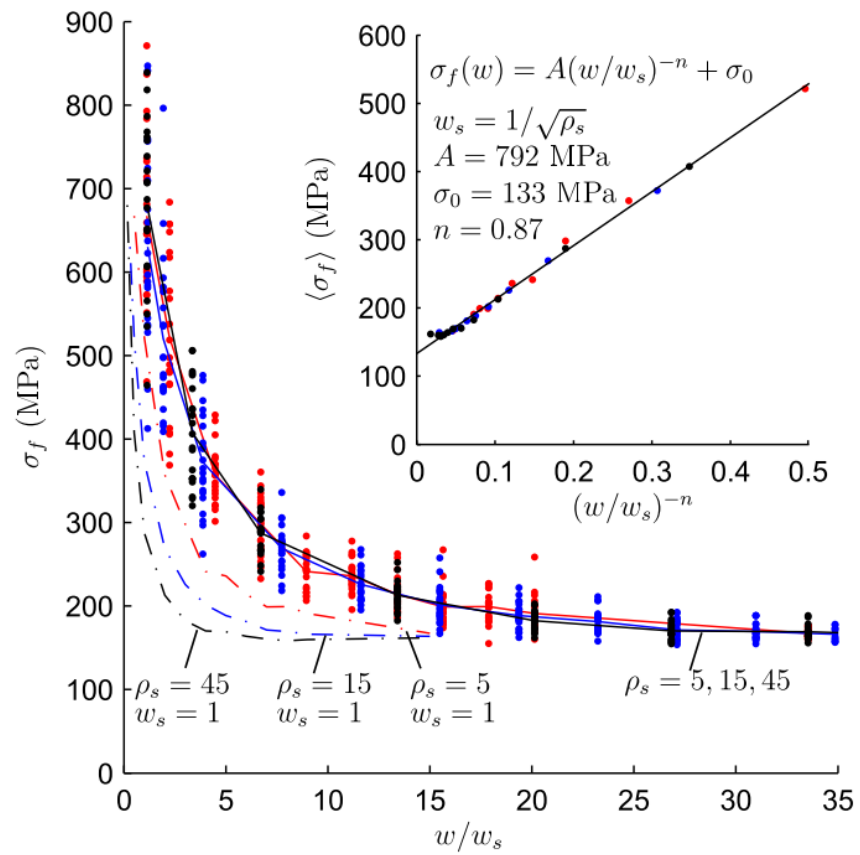
Figure 2.42 – Tarleton model relating the flow stress with the normalized beam size showing a power law relationship, with a bulk flow stress, σ_o, of approximately 133 MPa.
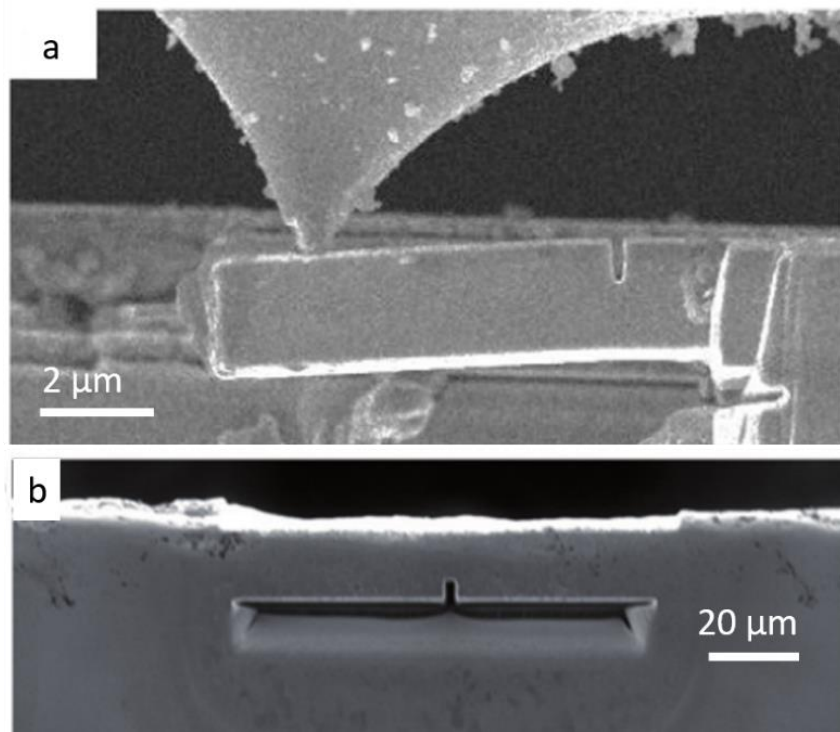
Figure 2.43 – In situ SEM (a) cantilever and (b) clamped beam fracture designs – reproduced from [101,102]
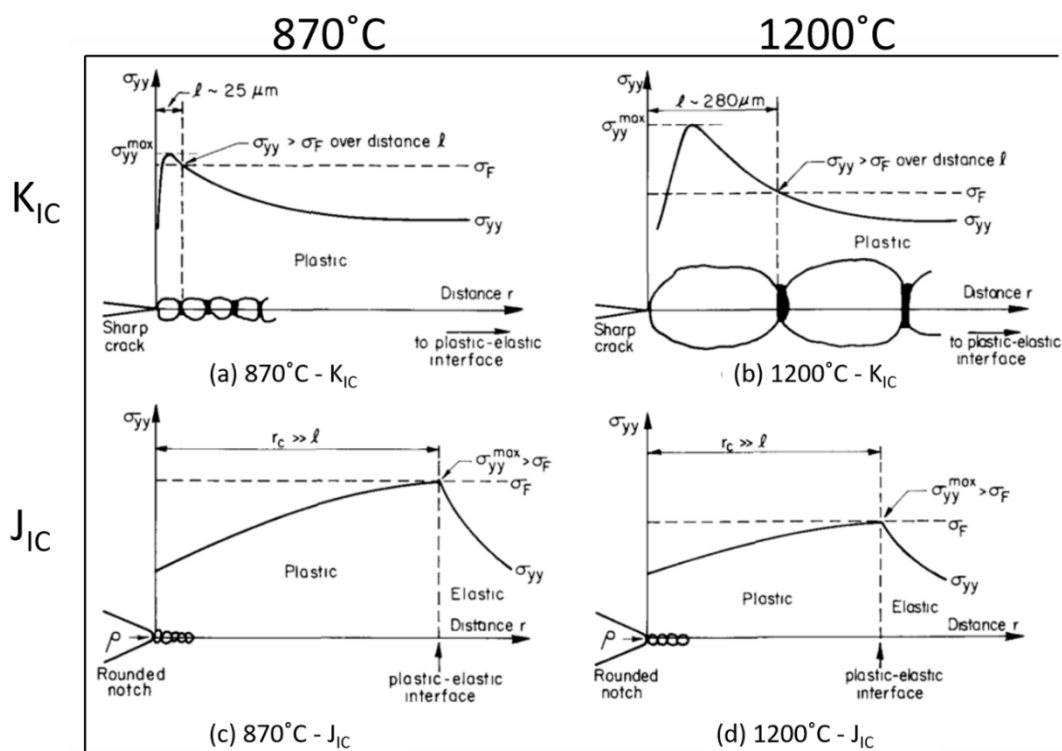
Figure 2.44 – Role microstructure plays in toughness measurements, K_{IC} and J_{IC} – adapted from [125]
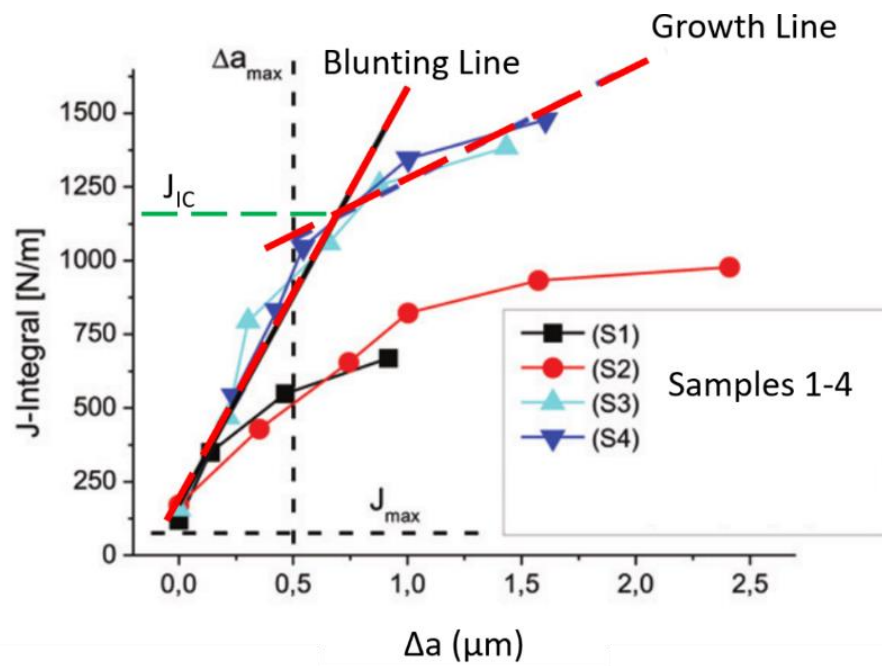
Figure 2.45 – Wurster J- Δa data for W cantilevers, showing blunting and growth line, with the critical JIC at the intersection of these lines – adapted from [15]

3. OBJECTIVE

The objective of this thesis is to demonstrate the use of in situ TEM mechanical testing to find mechanical properties of as received, self-ion, and proton irradiated Fe-9%Cr ODS. The objective will be accomplished with an experimental approach supplemented with finite element modeling to calculate material properties from measured load-displacement. The measure of success in using the in situ TEM mechanical testing techniques has two parts: 1) to build an understanding of how the microstructure and specimen dimensions interact to influence mechanical properties and 2) the application of this understanding to collect small-scale mechanical property data that is consistent with bulk-scale values.

The reviewed literature shows that in small-scale mechanical testing there is a threshold between the intrinsic and extrinsic dimensions where size effects begin to be observed. Therefore, it is hypothesized that by combining an understanding of the microstructure and the in situ TEM mechanical testing techniques, one can find the bulk-like mechanical properties of as received and irradiated Fe-9%Cr ODS alloy.

To accomplish the overall objective, experiments on four different mechanical testing geometries will be conducted; micropillar compression, cantilever bending, lamellae indentation, and clamped beam fracture. The corresponding mechanical properties to be measured are yield stress and elastic modulus, flow stress, strength of obstacles, and fracture toughness, respectively. As such, each geometry has its own sub-objectives.

Micropillar compression:

1) Find yield stress

2) Combine finite element modeling with results to find elastic modulus

3) Define the threshold where the interaction between the extrinsic (minimum sample dimension) with the intrinsic (obstacle spacing) begins to initiate size effects in Fe-9%Cr ODS

Cantilever bending:

1) Find flow stress

2) Confirm threshold between intrinsic and extrinsic dimensions holds true for cantilever geometry

Clamped beam fracture:

1) Demonstrate in situ TEM fracture on Fe-9%Cr ODS

2) Combine with extended finite element modeling and J-integral approach to calculate fracture toughness values

Lamellae indentation:

1) Demonstrate use of lamellae indentation for qualitative analysis

2) Use MicroViBe to better visualize and understand obstacles in Fe-9%Cr ODS

4. EXPERIMENTAL

A version of this chapter has been published in the following journals:

2. K.H. Yano, Y. Wu, J.P. Wharry. *Size Effects in TEM in situ Cantilever Flow Stress Measurements in Irradiated Fe-9%Cr ODS*. Submitted. Materials Science and Engineering: A. (2019).

3. K.H. Yano, S. Thomas, M.J. Swenson, Y. Lu, and J.P. Wharry. *TEM* in situ *cube-corner indentation analysis using ViBe motion detection algorithm*. Journal of Nuclear Materials 502 (2018) 201-212. doi:10.1016/j.jnucmat.2018.02.003

4. K.H. Yano, M.J. Swenson, Y. Wu, and J.P. Wharry. *TEM* in situ *micropillar compression tests of ion irradiated oxide dispersion strengthened alloy.* Journal of Nuclear Materials 483 (2017) 107. doi:10.1016/j.jnucmat.2016.10.049 and doi:10.1016/j.jnucmat.2017.04.054

In this section the material, irradiation, sample preparation techniques, characterization, and indentation settings will be described in detail. The software and settings for finite element analysis are discussed, as well as a description of the MicroViBe algorithm and its use in lamellae indentation.

4.1 Material and Irradiation

A rod of Fe-9%Cr ODS martensitic steel material from the Japan Atomic Energy Agency (composition in Table 2.1) was processed by mechanically alloying ferritic steel with Y_2O_3 powders. It was then hot extruded at 1150°C. The heat treatment consisted of 1 hour at 1050°C, air cooling, tempering at 800°C, with a final air cooling step. Further details regarding the processing and fabrication of the rod are available in ref. [28]

Specimens were prepared for bulk ion irradiation by electrical discharge machining into 1.5 mm × 1.5 mm × 16 mm bars. The bars were then mechanically polished through 4000 grit

SiC paper, followed by electropolishing for 20 seconds in a 10% perchloric acid + 90% methanol solution maintained between -30°C and -40°C, with a 35 V applied potential between the specimen (anode) and platinum mesh cathode.

The specimens are then irradiated. Three irradiating conditions were used. All three irradiations were conducted using a 1.7 MV General Ionex Tandetron accelerator at Michigan Ion Beam Laboratory. The first two irradiating conditions used 5.0 MeV Fe^{2+} ions to doses of 3 dpa or 100 dpa at 500° The beam was rastered at 255 Hz. The irradiation dose rate is ~10^{-4} dpa/s. The third irradiating condition used 2.0 MeV protons to a dose of 3 dpa at 500°C with rastering at 2061 Hz in the vertical and horizontal direction. The irradiation dose rate is ~10^{-5} dpa/s. In all irradiations a combination of resistance heating and air cooling were used to maintain the irradiation temperature at 500±10°C at high vacuum pressures below 1.3×10^{-5} Pa (10^{-7} torr). Beam current is measured throughout the duration of the experiment to ensure accurate dose accumulation.

The displacement damage profile for the 5.0 MeV Fe^{2+} ion and 2.0 MeV protons normally incident on Fe-9%Cr is calculated using the Stopping and Range of Ions in Matter (SRIM) 2013 program in "Quick Calculation" (Kinchin-Pease) mode and displacements are obtained from the vacancy.txt file. The damage profile of the Fe^{2+} irradiation (Figure 4.1a) exhibits a steep gradient between the surface and the damage peak, located approximately 1.2 μm from the surface. The target irradiation doses of 3 and 100 dpa are achieved at a depth of 550 nm from the surface, avoiding both the surface sink and the Fe implantation peak. The surface and peak doses for the 3 dpa condition are approximately 2 dpa and 8.5 dpa, respectively. For the 100 dpa condition the surface dose is 66 dpa and the peak is 2800 dpa. Samples were taken between 200 nm and 800 nm in depth. The proton damage profile (Figure 4.1b) first exhibits a

flat profile from the surface until approximately 15 μm, where a steep gradient results in a peak at 19 μm from the surface. Samples were taken from depths of 200 nm – 2 μm. In this region, the dose ranges from 0.1-0.8 dpa at dose rates of 0.4-4×10^{-6} dpa/sec. In this irradiation, the target dose of 3 dpa is reached at 16 µm in depth.

4.2   Microstructure Characterization

Microstructural characterization was conducted using TEM and APT. TEM lamellae were prepared using the FIB lift-out technique [156] on an FEI Quanta 3D FEG FIB at the Center for Advanced Energy Studies (CAES). Lamellae were oriented perpendicular to the irradiated surfaces, resulting in a cross-section of the irradiation damage profile within the lamella. Lamellae dimensions were approximately 15 μm × 7 μm × 100 nm. TEM analysis consisted of characterizing the size and number density of grains, dislocations, carbide precipitates, voids, and dislocation loops. The analyzed regions consisted of 300-700 nm from the surface for the Fe^{2+}. Material characterization of the proton irradiated material (published first in [4]) was conducted at depths of 1-7 µm, where the dose ranges 0.6-1.1 dpa at a dose rate of 3-5×10^{-6} dpa/sec. The data is averaged over this entire depth. The TEM used was a FEI Tecnai TF30-FEG scanning transmission electron microscope (STEM), also at CAES.

Using bright field mode, grains and carbides were imaged. Voids were also imaged in bright field mode using the through-focus technique. Dislocation line density was determined from measuring the linear density of dislocations in perpendicular directions and calculating an effective area density. Dislocation loops were imaged using a bright field STEM technique [157]. Further details are provided in refs. [4,6,50].

To resolve the < 2 nm in diameter oxide nanoclusters APT was used. APT enables atomic resolution. The needles for APT were also FIB milled and analyzed at CAES using a Cameca

LEAP 4000X HR. The data sets were then reconstructed using the Integrated Visualization and Analysis Software (IVAS) Version 3.6.2. Further details are provided in refs. [4,6,50].

4.3   Focused Ion Beam Sample Preparation

Samples for in situ TEM mechanical testing were all prepared from bulk as received and ion irradiated bars. Using FIB milling, different specimen geometries can be manufactured. A sample preparation technique published by Imrich [11] and Legros [10] was modified to fabricate a TEM lamella containing multiple compression micropillar specimens. This general technique can be modified and used to create micropillars, thin lamellas, cantilevers, and clamped beams. First, we will detail the steps for micropillar creation, then discuss the modifications necessary for the other three geometries. All FIB specimen work has been conducted on two FEI Quanta 3D FEG FIB: one at CAES and one at the Purdue Life Sciences Microscopy Lab.

First, we adhere a three-pillar copper TEM half grid to the copper sample mount using conductive silver epoxy (Figure 4.2). The nano-sized dimensions of the ODS and small loads limits the amount of stress in the copper grid and epoxy to < 0.015% of the stress seen in the ODS. Hence, we assume no deformation is occurring in the copper grid and silver epoxy.

A lamella having approximate dimensions 40 μm × 20 μm × 3 μm is lifted normal to the irradiated surface using FIB. Throughout this procedure, the FIB operating voltage is maintained at 30 kV, while the current is varied at each step to control the precision of each cut. The irradiated surface is first protected depositing a 40 μm × 3 μm × 0.8 μm platinum strip over the area of interest using a 0.3 nA beam current. The lamella is then lifted following the conventional FIB lift-out technique for TEM specimens [156], using trenching around the

platinum strip, freeing the lamella from the bulk, and finally, lifting the lamella using an Omniprobe needle.

The lamella is then affixed to the TEM half-grid on the center post, which simplifies alignment of the indenter tip to the compression micropillar or indentation window. Before attaching the lamella to the grid, the center grid post is milled to create a straight edge >40 μm wide. The lamella is then aligned such that its lower third overlaps the post before it is brought into slight contact with the post. Subsequently, a platinum weld is made across the bottom length of the lamella (Figure 4.3a), after which the lamella is detached from the Omniprobe. Next, the stage is rotated ±45° and fillet welds are placed along each side of the lamella (Figure 4.3b). A top-down view of all three welds is shown in Figure 4.3c. After the lamella is securely welded to the grid, the entire sample mount is installed onto a pre-tilted 45° stage to allow for perpendicular milling of the lamella surface to shape the compression micropillars.

Micropillars are fabricated with rectangular (as opposed to circular) cross-sections to reduce the extent of taper along the micropillar height, simplifying the evaluation of mechanical properties [127,158]. Indentation windows, if made, should be electron transparent to enable observation of dislocation movement during indentation. Ideal geometries of both thinned lamellae and micropillars are shown in Figure 4.4a.

Each micropillar is shaped to position its top surface ~300 nm below the original irradiated surface such that the entire testing volume is located within the ion irradiated region. This configuration also avoids any surface oxidation and sputtering effects of irradiation. The sample preparation technique presented here accommodates 6-8 micropillars on a single TEM lamella, spaced 2-2.5 μm apart. Sites of interest are now ready for thinning. Thinning proceeds after tilting such that the ion beam is parallel to the lamella (incident on the irradiated surface).

Cleaning cuts are made with progressively decreasing ion beam currents, beginning with 0.3 nA and decrementing to 10 pA for final thinning. Samples can be thinned to the desired thickness. For lamella indentation samples, <100 nm thickness is required to ensure electron transparency. Targeted micropillar thicknesses vary from 150 nm to 600 nm at the nominal dimensions with the quantity tested shown in Table 4.1.

After thinning, lamellae are ready for indentation. Micropillars, however, require further shaping by using cleaning cross-section cuts at 10 pA. The sample is rotated incident on face A (as identified in Figure 4.4a) of the micropillar. These shaping cuts remove what remains of the protecting platinum layer. For cuts milled in the direction of irradiated surface (Figure 4.4b), the sample is over-tilted by +1.5° to account for taper. When shaping from the B faces of the micropillar, the sample is also rotated ±1.5° to keep the micropillars as square as possible (Figure 4.4c). Completed micropillars and windows are shown in Figure 4.5. Heights and lengths were confirmed using TEM images to measure the dimensions with ImageJ and thickness was measured using electron energy loss spectroscopy (EELS).

Adjustments for cantilevers consist of the following steps. Approximately 6 cantilevers can be made on the same 40 μm × 20 μm × 3 μm sized lamella. Each beam is designated a 5-6 μm region from which to be shaped. Each of these regions is thinned to 200-350 nm in thickness (Figure 4.6a). Also included in Figure 4.6a is the proton damage profile overlaid on the cantilever sites. Because the alloy contains nanostructure grains and cantilevers would be polycrystalline, the cantilever positions were selected based on ease of milling.

The cantilever shape was milled (Figure 4.6b) using the same steps as shaping for the micropillars. Cantilever shapes varied in length, thickness and height. Existing stress-strain calculations exist for simple beams, where aspect ratio (i.e. ratio of cantilever beam length to

height) is a critical parameter in determining whether a beam is simple [122]. Suggested aspect ratios range from 2-10 [122]. Twenty cantilevers were made using this recommendation based on 200 or 500 nm nominal cantilever heights. Lengths of 1, 1.5, and 2 µm were used. Figure 4.6c labels the dimensions corresponding to length and height, while thickness of the sample is the dimension into the page (or the direction of the electron column in the TEM). Notches were milled using the 'line' pattern in the FIB using a voltage of 10-30 keV at 10 pA current. Notch lengths were nominally 100 nm long in the 500 nm tall samples and 50 nm tall in the 200 nm tall samples. Table 4.2 shows the number and nominal dimensions of cantilevers tested.

The last geometry to be discussed is that of the clamped beam. Again, the same 40 µm × 20 µm × 3 µm sized lamella as in the micropillars and the cantilevers was taken from the bulk sample and attached to the copper grid. Here though, only 3 – 4 clamped beams can be made from each lamella, as clamped beams required 8 µm sections with 2 µm between. Beams with dimensions labeled are shown in Figure 4.7a before and (b) during indentation. Targeted beam height was 500 nm, length was 4 µm, and thickness was 200 nm. Table 4.3 shows the number of beams tested per material condition and number fractured.

4.4 Transmission Electron Microscopy

4.4.1 EDS, ASTAR, EELS

Before in-TEM testing, samples were characterized using a variety of (S)TEM techniques. Each sample's thickness, no matter the geometry, was measured using EELS. This measurement was conducted using the log-ratio absolute calculation with a beam energy of 300 keV, a convergence angle of 3.58 mrad, and a collection angle of 11.47 mrad. As all samples were Fe-9%Cr, an effective atomic number of 26 was used.

Automatic TEM phase orientation mapping (NanoMEGAS ASTAR) was conducted on lamella's after indentation and clamped beams before indentation to determine grain orientations. The ASTAR system uses in-TEM precession electron diffraction (PED) to identify the crystal orientation of a grain contained within an electron-transparent lamella by collection the electron diffraction patterns during a scan of the selected region. The diffraction patterns are then matched with known patterns, revealing the grain orientations within the subject lamellae. This is advantageous for fine-grained to nanocrystalline materials (e.g. the subject Fe-9%Cr ODs, which has 200-300 nm diameter grains), as it provides superior spatial resolution as compared to traditional SEM electron backscatter diffraction (EBSD) [159]. In this study a spot size of 6, a camera length of 135 mm, and a precession angle of 0.48° is used. Scans were taken across the width and height of the lamellae. For the clamped beams, scans were taken around the notch.

Finally, energy dispersive x-ray spectroscopy (EDS) line scans were taken across grain boundaries in the clamped beam geometries to understand if their mechanical properties depended on grain boundary chemistry. Lines scans were taken before bending in the clamped beams. The EDS scans were taken in the FEI Tecnai TF30-FEG STEM at CAES. Tecnai Imaging Analysis (TIA) software was used to analyze the data profiles.

A 600-800 nm line scan, with 10 nm spacing between measurements and a 10 second dwell time was used. This resulted in 50,000-60,000 total counts per point, representing <1% counting statistics error. TIA software was used to extract counts from the K_α Fe and Cr peaks in the collected spectra. The Cliff-Lorimer equations were used to calculate composition from counts.

4.4.2   TEM Mechanical Testing and Video Capture Settings

To conduct the indentation testing, a Hysitron/Bruker PI95 Picoindenter TEM holder was used. The main mechanical testing settings to define include the indentation as either displacement or load controlled, the indentation limit (either depth or load), and the rate of indentation. All indentations conducted in this work were displacement controlled. Depending on the geometry, indentation depths and rates were adjusted. Two indentation tips were used: cube-corner for the lamellae indentation and a 1 μm diameter flat punch tip for the other geometries.

Using the flat punch, micropillar compression indentation depths were set to half the height of the micropillar. For example, if the micropillar was 400 nm tall, the indentation depth was 200 nm. For each test, the load time was 20 seconds, with a 5 second hold time and 10 second unload time. For lamellae indentation a depth of 100 nm was used with a load time of 25 seconds and unload time of 10 seconds. Cantilever bending consisted of using the flat punch to make contact with the free end of the cantilever (Figure 4.6b). Each indent was displacement controlled to the near-maximum bending, i.e. to the point where the cantilever would be bent into their base with further displacement. Load time ranged from 20-30 seconds with unload time of 10 seconds. Finally, for clamped beams, 2-3 indents were made on each beam to induce fracture. Due to the depth limitations of the PI95, each indent was held to 500-600 nm in depth. Indentation rate was kept at 10 nm/s with a 5 second hold time and 10 nm/s unload rate.

The PI95 control software records the displacement and load of the indentation tip, along with the TEM charge-couple device (CCD) output as a video file. In all tests, the output was recorded at 30 frames per second (fps) and stored using MJPEG compression. Subsequent analysis of the quantitative data was conducted through a Microsoft Excel import of the data text files. Qualitative image analysis was conducted using ImageJ software.

4.5   Finite Element Modeling

FEM was used to aid in the quantitative analysis of the micropillars and clamped beams. In the micropillars, plastic deformation below the micropillar, in the base, needed to be accounted for. Due to the unique clamped beam geometry, the model was necessary to find a stress intensity at the notch. Two different FEM software packages were used for each geometry.

A two-dimensional FEM was constructed in ANSYS® Workbench, Academic Research release 15.0 [160], with the micropillar and base supported solely along the bottom surface, restricted in the 'Z-direction', and using a quadrilateral mesh. Representative FEM simulations are shown in Figure 4.8 (Figure 4.8a for a micropillar on a 1 μm base, and Figure 4.8b for a micropillar on a 5 μm base). In these simulations, displacement has been normalized, with maximum displacement occurring at the top of the micropillar. The deformation in the base of each needed to be quantified to adjust the measured elastic modulus values. This is further discussed in the results, §5.1.2.

A three-dimensional FEM was constructed in ABAQUS® version 6.13. This model followed the design of Jaya in [145]. A stationary crack was modeled using the extended finite element modeling (XFEM) feature, from which a corresponding stress intensity was calculated. This stress intensity was then used to calculate a J-integral for each beam. This calculation is further discussed in §5.3. The ABAQUS reference manual [161] outlines the stress intensity factor determination. Each beam was individually modeled, but a representative model is shown in Figure 4.9 after indentation. The maximum principal strain (MAXPE) of 0.035 was used as the failure criterion for the Fe-9%Cr material. This was chosen as it was the average strain seen before fracture across clamped beams. The elements were 8-node linear bricks in 3D (C3D8R). Input files for both the micropillar ANSYS model and the clamped beam ABAQUS model are included in Appendix A.

4.6   MicroViBe

Given the microstructural and geometric complexities of these experiments, there is a critical need for a consistent, non-subjective approach to more definitively discern plasticity in the microstructure. As such, we utilized a motion detection and background subtraction-based post-processing approach to carry out an unbiased qualitative interpretation of TEM lamellae indentation videos. Given that the background subtraction algorithms used in the macroscale are reasonably mature [162,163], evaluating them as tools for analyzing TEM scale videos is well motivated.

The image processing algorithm developed in this work, hereafter referred to as "MicroViBe", uses as its first step the widely accepted ViBe [164] algorithm for foreground detection, due to its reliability and computational performance [165]. The MicroViBe algorithm will generate a "heatmap" of the indentation region, which will identify areas having the highest degree of foreground motion. This heatmap, in combination with post-mortem TEM images, was subsequently used to qualitatively assess the relative strengths of microstructural features in the lamellae.

The underlying principle of motion detection is to identify the foreground pixels (associated with moving objects) and differentiate them from the background pixels (associated with stationary objects). The approach used here is known as the "background subtraction" technique [166], wherein each pixel is compared with either a background frame or a background model. The background frame consists of a single "control" frame to which all subsequent frames are compared, whereas the background model considers the evolution of the background frames over time. Because the background subtraction method considers time evolution, it is not fully reliant on knowledge about the video subjects [166]. Consequently, the background subtraction method parameters are generally more transferrable between

applications for motion detection, thus why we choose to utilize the pixel-based background subtraction technique with a background model in this work.

ViBe [164], is used for its motion detection features as one sub-step in the heatmap generation algorithm. Owing to the μm sized lamellae, this algorithm is called "MicroViBe." MicroViBe relies on several key input parameters, which have been determined to be ideal at the macroscale [164] based on Percentage of Correct Classification (PCCs); i.e. the algorithm identifies changes that a human observer would recognize at the macroscale. These parameters are R=20, ϕ=16, N=20, and $\#_{min}$ =2 where R is a threshold value for determining the match between pixel from the current frame and the background model, ϕ is a time subsampling factor, N is the number of samples stored for each pixel in the background model, and $\#_{min}$ is the number of close pixels needed to classify a new pixel as background. Since there are no existing optimized parameter sets at the μm scale, we utilize the macroscale parameters in MicroViBe.

The application of MicroViBe to an indentation video is a five-step process illustrated in Figure 4.10. The first step in the workflow is to load the first frame from the indentation video and assign it as the background model. This frame is referred to as the "background reference" in Figure 4.10. Next, a binary segmented image is obtained from the next frame using the existing ViBe [164] algorithm. In this segmented image, white pixels represent the foreground and black pixels represent the background; pixels are detected as foreground when they differ from their appearance in the background model, indicating movement from frame to frame.

The third step in MicroViBe builds a heatmap histogram by incrementing each white pixel from the segmented image, by a tally of one in the heatmap. "Heatmap" is a term used in motion detection science to connote areas of movement; here, "heat" refers to accumulation of motion, not to be confused with thermal "heat". A corresponding heatmap image having the

same dimensions as the background reference image is also created, where each pixel stores 16 bits of data. The pixel values are initialized with the value 0. The data stored in the heatmap image are the count of frames in which the corresponding pixel is detected as foreground. Hence, MicroViBe in its current form is limited to a maximum movie length of 65536 frames (for example, 36 minutes of video footage at 30 frames per second (fps)); i.e. if the same pixel changes in every frame, the algorithm reaches its size limit after 65536 frames. The histogram inset in the heatmap image in Figure 4.10 shows that some pixels detect motion as many as 331 times out of the 1080 frames in the given video.

The fourth step in MicroViBe involves data normalization. Since the heatmaps are 16-bit images, the data must be normalized to the maximum value of 65536 to provide sufficient contrast for visualization on computer displays (which usually have an 8-bit color depth). This normalized image is labelled as the saturated image in Figure 4.10. Finally, in the fifth step of MicroViBe, the grey levels of the saturated image are converted to a false color heatmap for more intuitive visualization. The tones within the heatmap are scaled so that the pixels tallying the largest number of changes throughout the video are colored red, while pixels with zero change throughout the video are colored dark blue. The saturated image and false color heatmap are only necessary for visualization purposes; any further image analyses need only use the original heatmap image.

This five-step cycle is repeated for each subsequent frame of the video, comparing one frame to the previous, until all frames have been processed. At this juncture, the false color heatmaps can be compiled into a video for direct comparison with the original TEM indentation video and/or taken as still frames for image analysis; these compiled false color heatmaps will be the format of MicroViBe output discussed and presented in the lamellae indentation results §5.4.

Table 4.1 - Quantity tested of targeted nominal micropillar dimensions

Width and Height (nm)		Thickness (nm)								
		100	150	200	250	300	350	400	500	600
As Received	150	–	1	–	–	–	–	–	–	–
	200	1	–	1	–	–	–	–	–	–
	250	–	–	–	1	–	–	–	–	–
	300	1	–	–	–	1	–	–	–	–
	350	–	–	–	–	–	1	–	–	–
	400	2	–	1	–	1	–	2	–	–
	500	1	–	–	–	–	–	–	1	–
	600	–	–	1	–	–	–	–	–	1
Width and Height (nm)		Thickness (nm)								
		100	150	200	250	300	350	400	500	600
Fe^{2+} Irradiated ODS 3 dpa 500°C	150	–	1	–	–	–	–	–	–	–
	200	1	–	–	–	–	–	–	–	–
	250	–	–	–	1	–	–	–	–	–
	300	–	–	–	–	2	–	–	–	–
	350	–	–	–	–	–	–	–	–	–
	400	2	–	1	–	–	–	1	–	–
	500	1	–	–	–	–	–	–	1	–
	600	–	–	–	–	–	–	–	–	2
Width and Height (nm)		Thickness (nm)								
		100	150	200	250	300	350	400	500	600
Fe^{2+} Irradiated ODS 100 dpa 500°C	150	–	1	–	–	–	–	–	–	–
	200	–	–	1	–	–	–	–	–	–
	250	–	–	–	1	–	–	–	–	–
	300	–	–	–	–	1	–	–	–	–
	350	–	–	–	–	–	–	–	–	–
	400	5	–	–	–	1	–	1	–	–
	500	–	–	–	–	–	–	–	–	–
	600	–	–	–	–	–	–	–	–	1

Table 4.2 – Quantity tested of targeted nominal cantilever dimensions

Beam Length (nm)	Beam Height (nm)	Notch Length (nm)	As Received	Proton Irradiated (3 dpa 500°C)
1000	200	50	2	2
1000	500	100	2	2
1500	200	50	2	1
1500	500	100	1	2
2000	200	50	2	2
2000	500	100	1	1

Table 4.3 – Clamped beam quantity tested and fractured by material condition

	As Received	Fe^{2+} 3 dpa 500°C	Fe^{2+} 100 dpa 500°C	Proton 3 dpa 500°C
Tested	6	9	9	9
Fractured	4	5	1	5
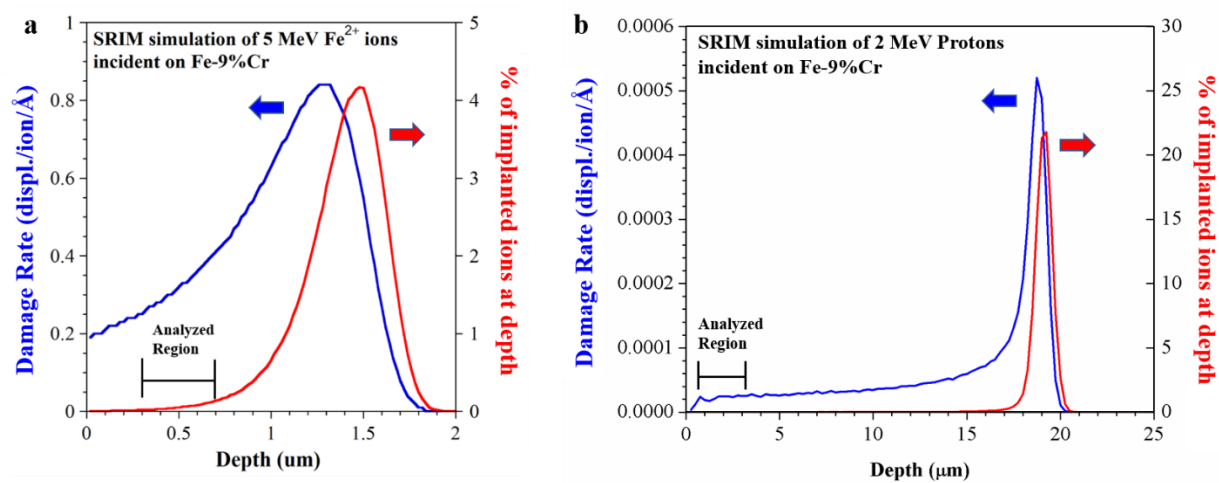
Figure 4.1 – Damage and implantation profiles of (a) Fe2+ ions and (b) protons on Fe-9%Cr
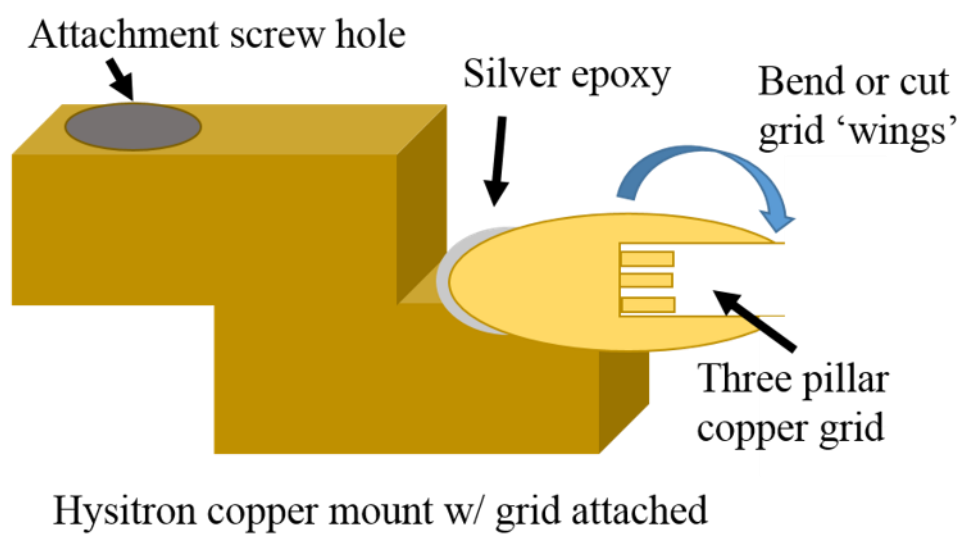
Figure 4.2 – Diagram of PI95 copper sample mount with silver epoxy and three pillar copper grid attached

142
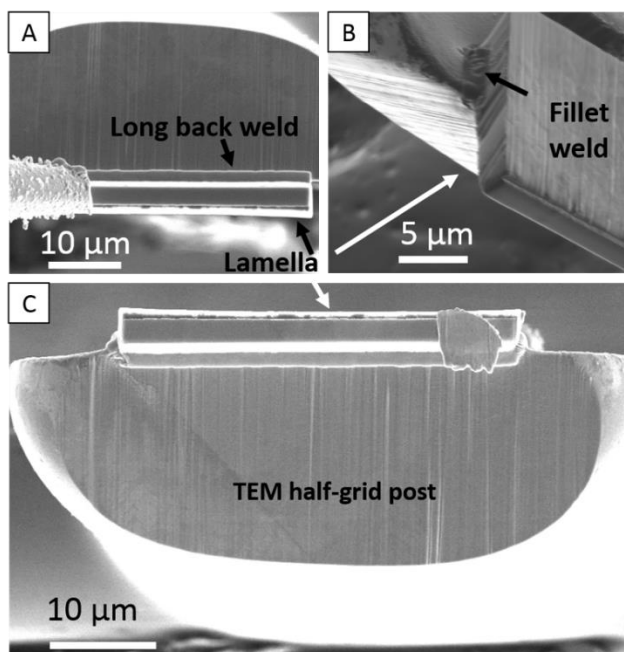
Figure 4.3 – SEM images showing (a) overlap of the lamella on the TEM half-grid post with weld across the bottomedge of the lamella, (b) fillet weld along sides of lamella at 45°, and (c) the three welds used to attach the lamella to the TEM half-grid post
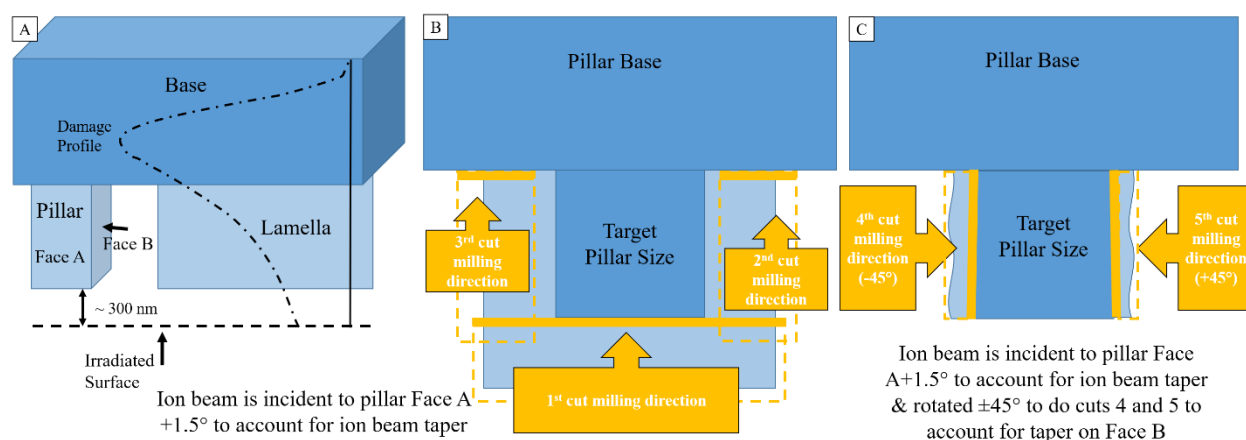
Figure 4.4 – (a) Ideal micropillar and window geometries with SRIM damage profile for 5 MeV Fe2+ overlaid; (b) first three cuts to shape micropillar, with milling direction indicated; (c) the fourth and fifth cuts clean up B faces of the micropillar to final desired dimensions
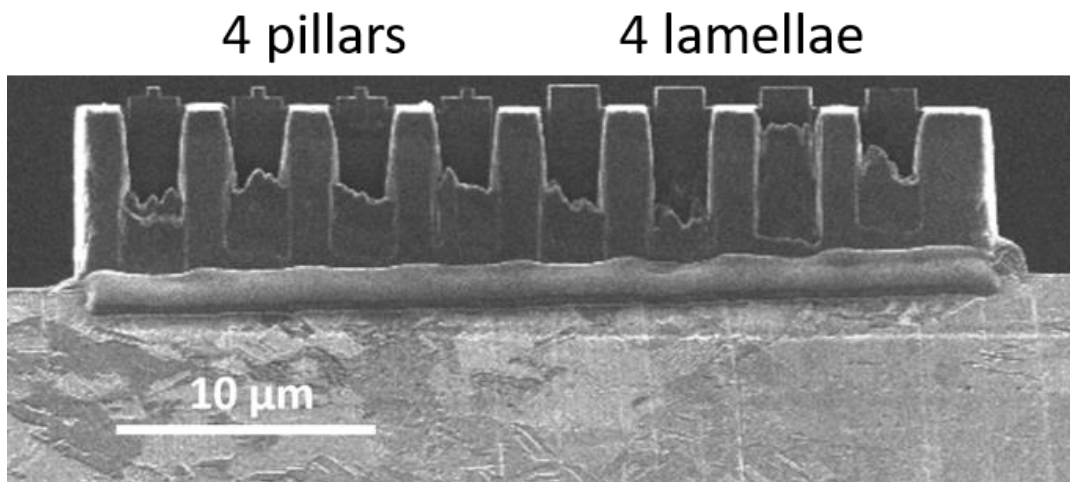
Figure 4.5 – Four (of each) completed micropillars (left) and lamellae (right)
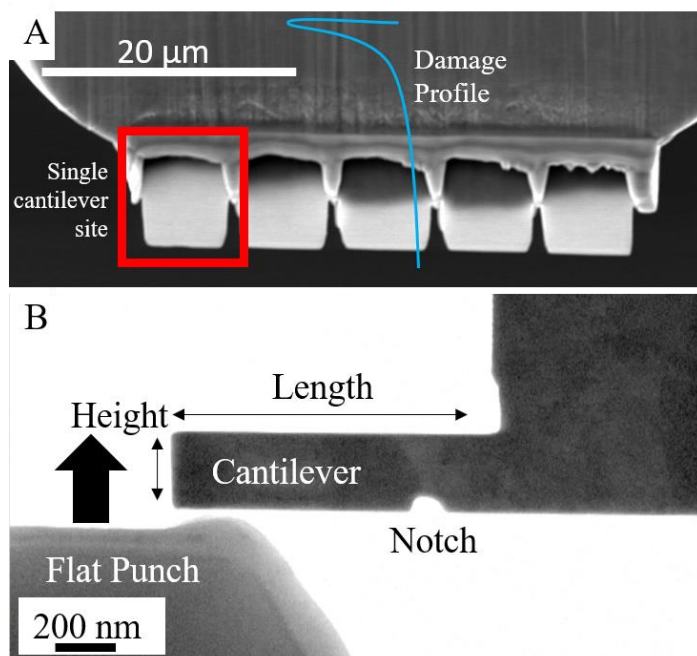
Figure 4.6 – Cantilever manufacturing process: (a) thinned cantilever sites with damage profile overlayed, (b) milled cantilever in bright field TEM with flat punch and notch labeled
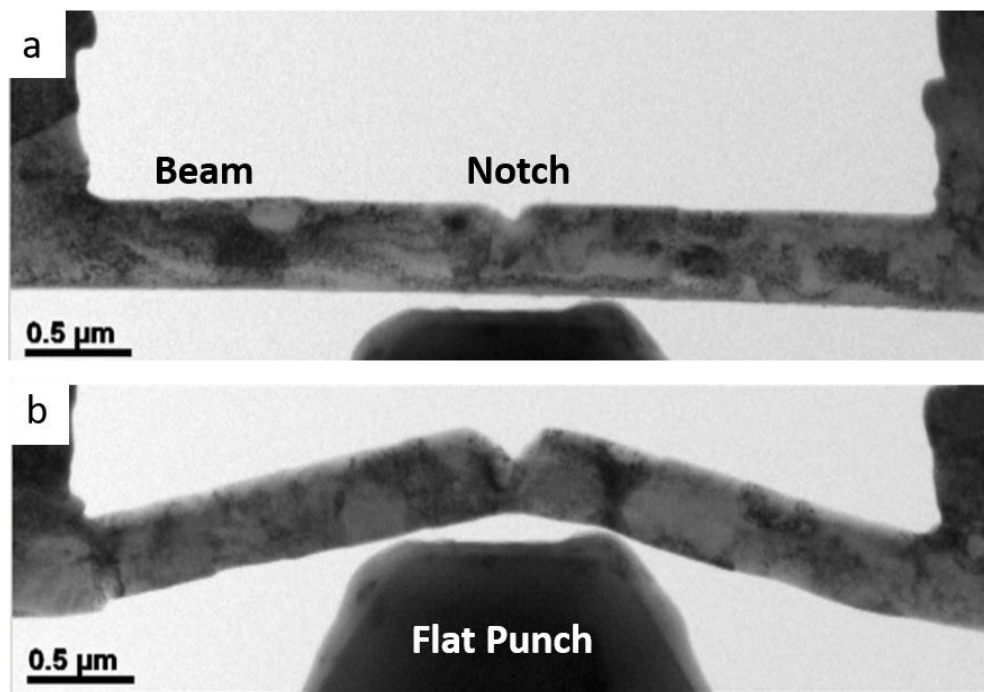
Figure 4.7 – Clamped beam (a) before indentation and (b) during indentation, prior to fracture
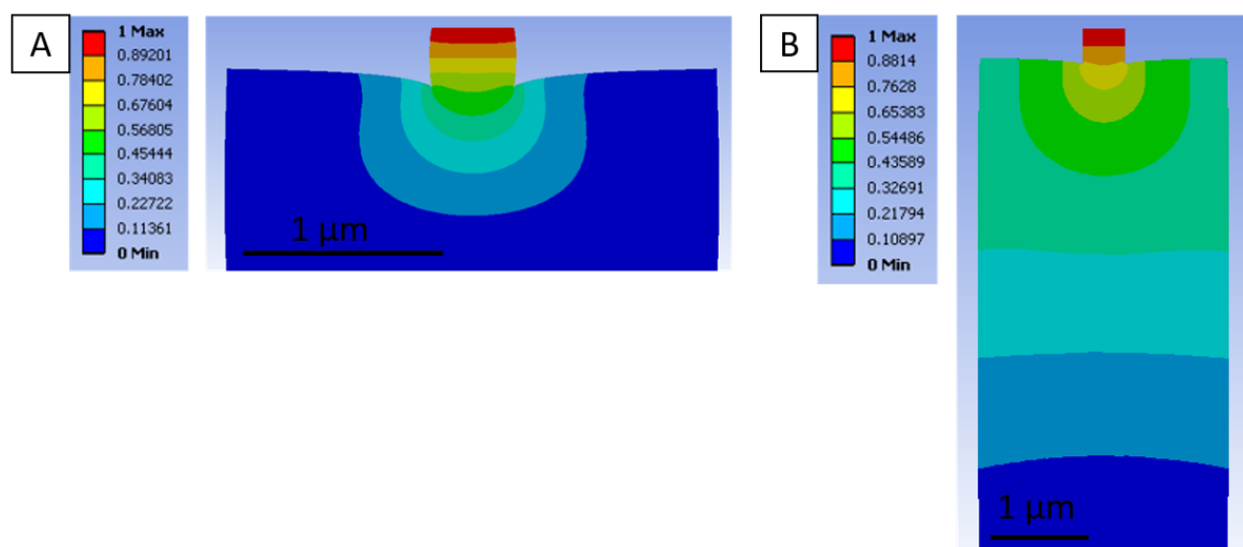
Figure 4.8 – FEM showing normalized displacement of (a) pillar with 1 μm base and (b) pillar with 5 μm base
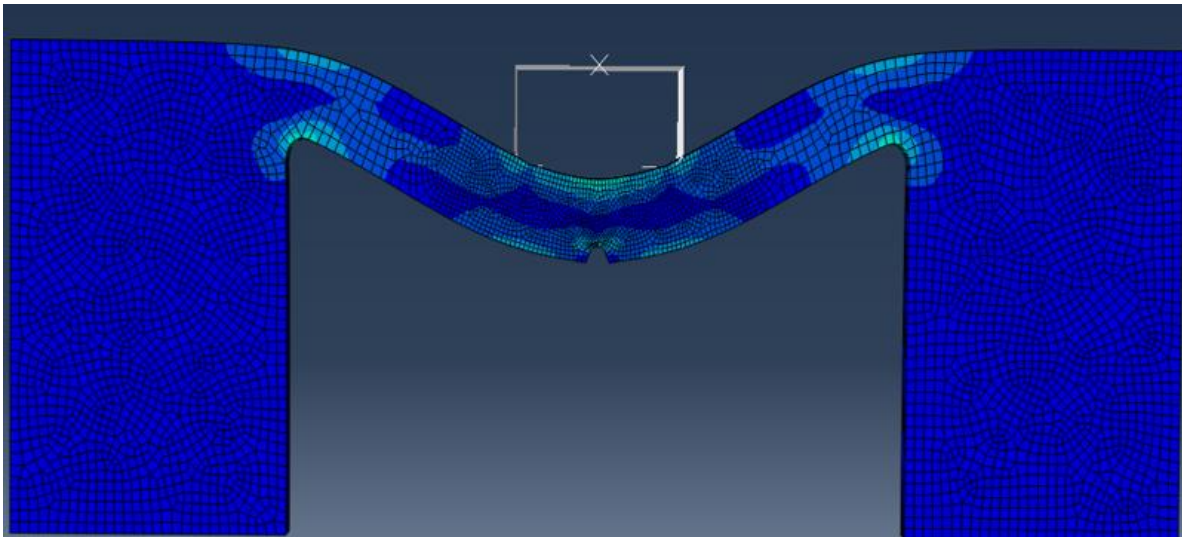
Figure 4.9 – FEM of clamped beam. Stress seen in notch area and at left and right portions where the beam is 'clamped'
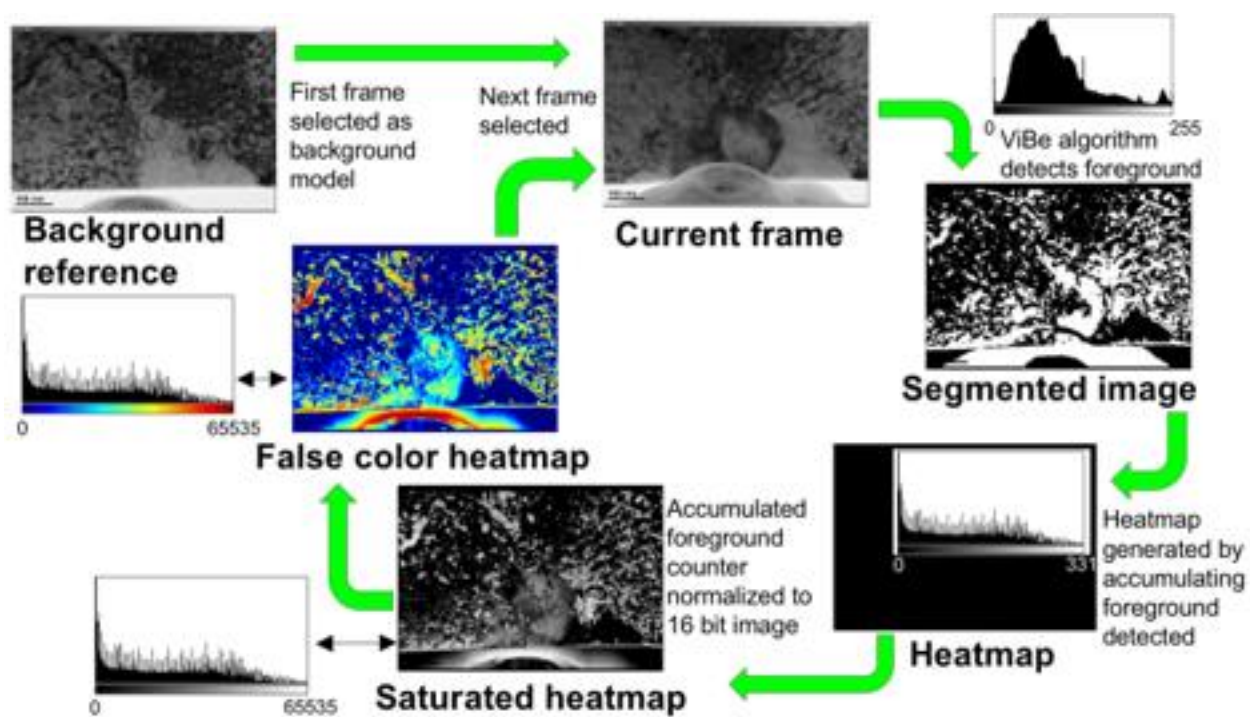
Figure 4.10 – Schematic representation of the MicroViBe software flowchart. Thick green arrows represent direction of workflow. Thin arrows indicate the histogram "legend" to the heatmap

5. RESULTS

A version of this chapter has been published in the following journals:

1. K.H. Yano, Y. Wu, J.P. Wharry. *Size Effects in TEM in situ Cantilever Flow Stress Measurements in Irradiated Fe-9%Cr ODS*. Submitted. Materials Science and Engineering: A. (2019).

2. K.H. Yano, S. Thomas, M.J. Swenson, Y. Lu, and J.P. Wharry. *TEM* in situ *cube-corner indentation analysis using ViBe motion detection algorithm*. Journal of Nuclear Materials 502 (2018) 201-212. doi:10.1016/j.jnucmat.2018.02.003

3. K.H. Yano, M.J. Swenson, Y. Wu, and J.P. Wharry. *TEM* in situ *micropillar compression tests of ion irradiated oxide dispersion strengthened alloy*. Journal of Nuclear Materials 483 (2017) 107. doi:10.1016/j.jnucmat.2016.10.049 and doi:10.1016/j.jnucmat.2017.04.054

The results section is organized such that each geometry and its associated mechanical property is presented individually. First, the micropillar compression results with yield stress and elastic modulus values are presented. Next the cantilever bending flow stress results are provided along with EDS measurements at the notch. Third are the clamped beam fracture results with calculated apparent fracture toughness values. Finally, the lamellae indentation will be presented. Videos of all results are included in the supplementary material in Appendix B. Though size effects play a major role in all of these results, their role will not be discussed until §6. As the author did not conduct the microstructural characterization, that information has been provided in the background, §2.3.

5.1   Micropillar Compression

Three material conditions are studied (as received, Fe^{2+} at 3 dpa 500°C, Fe^{2+} at 100 dpa 500°C) and in each condition, micropillars are fabricated such that dimensions are varied to evaluate dependencies on thickness, width/height, and total volume. Micropillars range from 50

nm – 600 nm in thickness, 100 nm – 600 nm in width and height, and total volumes ranging 2.5

μm^3 – 246 μm^3 (Table 4.1).

Micropillar dimensions are measured from EELS and using Digital Micrograph software.

A stress-strain curve is generated from the load-displacement data collected during each

micropillar test. As there is deflection in the base material of the micropillar, the maximum

deflection (acquired from the real-time video of the compress tests) is subtracted from the

transducer displacement data before calculating the strain. Yield strength and elastic modulus are

extracted from these stress-strain curves. Representative curves are shown in Figure 5.1 for each

material condition. The nominal dimensions of these samples are as follows: as received – 500

nm × 500 nm × 500 nm, Fe^{2+} 3 dpa 500°C – 600 nm × 600 nm × 600 nm, Fe^{2+} 100 dpa 500°C –

400 nm × 400 nm × 400 nm. Each micropillar tested is tabulated in Table 5.1 with dimensions,

yield stress, and elastic modulus values listed.

Frames from a single compression test of a 400 nm × 400 nm × 100 nm micropillar in the

as received condition have been extracted from the video recording and are shown in Figure 5.2.

Corresponding points on the stress-strain curve are identified for each image. Before

compression (Figure 5.2a), the micropillar contains no grain boundaries but does contain

characteristic ODS oxides and dislocations interspersed. After yielding, plasticity occurs in large

dislocation burst events (5.2c and 5.2d). The test concludes with a highly deformed micropillar

containing a dense network of dislocations (5.2e).

5.1.1   Yield Strength

As evaluations on dimensional dependency is key to our work, yield stress values are

plotted in Figure 5.3 as a function of either sample volume or sample minimum dimension

(either thickness or height/width). Average values are also provided in Table 5.2. Moving

forward, sample minimum dimension is determined as the key extrinsic parameter and will be solely used. This is discussed in §6.

The expected yield strength for as received Fe-9%Cr ODS is 1000-1200 MPa [57]. Within the 95% confidence interval, 9 of 15 micropillars tested exhibit yield strengths in this expected range. We measure an average reduction in yield stress of ~129 ± 321 MPa in the 3 dpa condition and ~217 ± 264 MPa in the 100 dpa condition (Figure 5.3). These differences were calculated using the average yield strength of micropillars with a minimum dimension greater than 100 nm and propagating the uncertainty in quadrature. The standard deviations being on the same order as the yield stresses suggests statistical invariance between conditions. Dolph, et al. [63] observed minimal strengthening (~110-130 MPa) in the same alloy irradiated to 100 dpa at 400°C, which is reasonable given the higher irradiation temperature of the specimens studied herein. A possible size effect is also observed for micropillar thicknesses below ~100 nm (Figure 5.3), which are identified by open symbols, while micropillars having minimum dimension >100 nm are depicted with closed symbols.

5.1.2   Elastic Modulus

As with the yield stress, elastic modulus values are plotted as a function of sample volume (Figure 5.4a) or sample minimum dimension (Figure 5.4b). The expected elastic modulus for as received ODS ranges 190-220 GPa [27,57,63]. Yet the values measured by in situ TEM compression micropillars (Figure 5.4, Table 5.3) are an order of magnitude lower. This discrepancy is attributed to two factors. First, deformation is not isolated in the micropillar; the base also deforms [11]. The acquired load-displacement curve does not adjust for the deformation in the base, resulting in lower elastic modulus measurements. It also follows that as the micropillar volume increases (here highlighted by the thick vs thin samples), more of the

deformation can be accommodated in the micropillar than in the base, resulting in more consistent modulus measurements (Figure 5.4b). Secondly, in such small volumes, the elastic modulus can be significantly affected by microstructural inhomogeneities such as varying grain orientations and distribution of oxide nanoclusters.

To account for the first factor, deformation in the base, two steps were taken. First, as mentioned in the stress-strain calculations, we subtract the maximum deflection of the base, which is visible in the real-time video of the compression tests, from the maximum displacement measured by the flat punch during the compression test. This is a basic and necessary step to analyzing any of the data. To show the difference, we have quantified the change in the results. Depending on the material condition, measured elastic modulus increases by a factor of 1.2-2.7, resulting in a range of elastic moduli from 42-112 GPa (Figure 5.5 or Table 5.3, "Deflection adjusted"). However, the modulus generally remains below expected values, especially for the irradiated conditions. The second step, then, is to account for plastic deformation occurring in the base using the FEM as described in §4.5. According to FEM calculations, the micropillar base height has a strong influence on the percent of the displacement occurring in the base relative to in the micropillar (Table 5.4).

For the irradiated conditions, a base height of 5 μm is representative of our micropillar fabrication technique, and at this height, 76% of the deformation occurs in the base (and thus only 24% of the deformation occurs in the micropillar). Normalizing the measured displacement by this fraction, the irradiated elastic modulus values now fall into closer agreement with bulk values and range from 130 GPa to 309 GPa (Figure 5.5, "Deformation adjusted"). For the as received ODS micropillars, some of the deflection adjusted modulus values fall within the expected range (190-220 GPa), even before deformation adjustments are applied. It then follows

that the deformation adjusted modulus values exceed the expected range (Figure 5.5). The average difference between deflection adjusted and measured moduli is ~3 times greater for the as received material than for the irradiated conditions, suggesting that the base of the as received material deforms more than the base of the irradiated material.

Even after adjusting irradiated elastic moduli to account for deformation in the base, modulus values span a wide range (130-309 GPa). Microstructural inhomogeneities could explain these variations, especially for the <100 nm micropillars. Since the average grain diameter of this material is ~300 nm, only ~14% of a single grain could be contained within a micropillar of dimensions of 400 nm × 400 nm × 100 nm. Considering the directionality of elastic modulus, the crystal orientation relative to the compressive direction then becomes a significant factor influencing the measured elastic modulus. For bcc iron, elastic modulus calculations can range from 131 GPa in the [100] orientation, to 284 GPa in the [111] direction and have been confirmed experimentally [16,167]. This directionality provides a large enough variation in moduli to explain the range measured in the irradiated moduli (Figure 5.5).

5.2   Cantilever Bending

Two material conditions were tested in the cantilever geometry, as received and proton irradiated to 3 dpa at 500°C. This section presents the flow stress and microstructure sequentially. Videos of the as received and irradiated cantilever beams are provided in Appendix B.

For each cantilever, load and displacement data are collected and video recorded of the TEM CCD screen during the bending test. With this combination of data frame-by-frame analysis is conducted and linked to points along the load-displacement curve. Frames of a proton irradiated

cantilever with dimensions of 1500nm long × 500 nm tall × 320 nm thick are provided in Figure 5.6. The accompanying load-displacement curve is marked where the still frames were taken in Figure 5.6J. Because this cantilever sample is ⪞200 nm thick, fine resolution of the microstructure is limited. Hence, there are no obvious microstructural features in 5.6A-I that link directly to features of 5.6J. But there is a visible grain in the center of the beam (light contrast Figure 3C). A dislocation line can be observed in 3D and 3E. Contour banding occurs readily and is evidenced in the quick contrast change of the center grain between Figures 3D and 3E and then Figure 3G and 3H. Figures 3H, 3F, and 3I show a precipitate of some sort near the tip of the beam. Extensive plasticity occurs in the beam. With a displacement of 900 nm, the beam bends and the notch broadens, but the notch does not grow into a crack, nor does the beam fracture. This is consistent with the super plasticity seen in other materials at comparable length scales [98,134,168].

Stress-strain (σ-ε) curves are generated for each of the cantilevers tested using the load and displacement data collected by the Hysitron PI95, based on beam dimensions. Equations 2.49 and 2.50 are used to calculate the stress and strain, respectively, from the measured load, *P*, and displacement, *d*. Representative stress-strain curves are shown for as received and proton irradiated cantilevers in Figure 5.7a and Figure 5.7b, respectively. From the stress-strain curves, the flow stress is taken as the average stress after the onset of plastic yielding. The data averaged to determine flow stress is marked by a double-headed arrow in both the as received (Figure 5.7a) and proton irradiated (Figure 5.7b) conditions.

Flow stress measurements are summarized in Table 5.5 for all as received and proton irradiated beams. Beam dimensions range 1000-2000 nm in length, 200-500 nm in height, and 250-390 nm in thickness. Flow stress values vary 2004 – 5658 MPa for the as received material,

and 2059-4592 MPa for the proton irradiated material. The corresponding total strain at the notch ranges 0.06-0.36 for the as received cantilevers, and 0.10-0.53 for the irradiated cantilevers. Flow stress values vary 2000 – 3130 MPa within samples unaffected by size effects. In contrast, size effected flow stress values vary 2700-5600 MPa (highlighted rows in Table 5.5). Generally, size effected samples are those with strain < 0.15 nm/nm and flow stress > 3100 MPa. But extrinsic dimension is not determinative and as discussed in §3.2, the dimensions are normalized in our analysis of size effects. The representative stress-strain curves in Figure 5.7A and B also differentiate cantilevers experiencing size effect and those without size effects.

Considering only the non-size effected samples, the average flow stress for the proton irradiated beams is 2864 ± 360 MPa. This is nominally a 200 MPa increase over the average flow stress for as received beams, 2680 ± 410 MPa (Table 5.5). Yet accounting for the error, this 200 MPa difference is negligible. The absence of hardening at irradiation temperatures of 500°C is demonstrated in the literature by Hosemann et al. on tempered martensitic HT-9 irradiated to 2 dpa with protons at 500°C [66], Ando et al. on F82H with Fe^{3+} at 500°C to 5 dpa [169], and Heintze et al. on an Fe-9%Cr alloy self-ion irradiated to 1 dpa at 500°C [67].

It is unsurprising that the cantilevers would experience extreme plasticity (as opposed to fracture) because ODS and their related bcc Fe-Cr F/M alloys are ductile and do not tend to exhibit intergranular fracture [25,170]. Further, the archival literature suggests a tendency for super plasticity to occur as mechanical testing samples are miniaturized [98,134,168]. This finding is consistent with the work of Armstrong et al. [119] on self-ion irradiated tungsten cantilever beams tested in situ in a SEM with beam lengths >10 µm. In that study, W beams were unable to achieve fracture without simultaneous helium implantation, which sufficiently embrittles the material to induce intragranular fracture [119].

5.3   Clamped Beam Fracture

Four material conditions were tested for in situ clamped beam fracture testing: as received, Fe^{2+} at 3 dpa 500°C, Fe^{2+} at 100 dpa 500°C, and proton at 3 dpa 500°C. The number of each condition tested and fractured are included in Table 4.3. As discussed in §4, beams were bent using displacement controlled 'hits' of 500 nm. Beams took 2-3 hits to reach fracture between 600-1400 nm total displacement. Beams that did not fracture through the center often fractured at the high stress regions at the clamped corners (Figure 4.9). Still images of an as received clamped beam during testing are shown sequentially in Figure 5.8A-I with a corresponding load-displacement curve (Figure 5.8J) where the still frame locations are identified. Figure 5.8A-F are from the initial 500 nm displacement hit. Figure 5.8G-I are from the second hit, with fracture at 716 nm displacement. This beam has a thickness of 140 nm with a single grain located in the center. Contour bands are prevalent in the clamped beam bend tests (C-F - particularly to the left of the notch). Yet the crack propagation at the notch can be readily seen in still frames C-H. Final fracture surfaces (I) appear ductile in nature.

To calculate the apparent fracture toughness of each fractured beam, a J-integral approach demonstrated on tungsten beams by Wurster et al [23] and described in §2.1.5 was employed. First, to understand the stress intensity at the notch, XFEM simulations were run for each beam geometry tested. A representative stress intensity (K_I) vs displacement depth (in nm) plot is provided in Figure 5.9. As it is a linear set of points, a linear extrapolation is used to calculate the stress intensity factor. This stress intensity was used to calculate the elastic energy contribution of the J-integral for each beam, every 50 nm, using Equation 2.56.

Load-displacement curves were collected and the area under each load curve was measured. This value was used to calculate the plastic contribution using Equation. 2.57.

Combining the elastic and plastic portions, a J-integral value was calculated for each beam at increments of 50 nm displacement. Crack length was measured from still images of the bend videos, and the crack growth, Δa was calculated at each 50 nm segment. Figure 5.10 is the representative J-Δa curves for each material condition. Appendix C shows all J-Δa curves.

J-Δa curves show crack growths ranging from 100 nm (Fe^{2+} 3 dpa) up to 200 nm (Fe^{2+} 100 dpa). J-integral values reach maximum in the as received condition at approximately 1000 N/m. To determine where the crack behavior changed from a blunting to a growth regime, the first of three points where the combined crack growth was visually larger than the combined J-integral growth was used as the cross-over point. This crossover point is the critical J-integral (J_{IC}) value. The J_{IC} is then used to calculate the apparent fracture toughness, $K_{Q,J}$ through Equation 2.58. Each beam with dimensions and $K_{Q,J}$ value (if it fractured) are tabulated – Table 5.6.

Rather than trending with material condition, fracture toughness results hewed to three broad categories based on broad microstructure trends around notches: single grain, multiple grains, or precipitate along notch axis. EDS and ASTAR results for each beam are included in Appendix C while Figure 5.11 is provided to demonstrate representative results of these three prevailing trends. Line scans were centered below and perpendicular to the notch. Line scans taken across single grains (as received) show consistent Fe and Cr content at expected levels, 90% and 8-9%, respectively. Crack growth and fracture along the notch axis was most prevalent in single crystal beams. Eleven of fifteen successful fractures occurred in single crystal beams. In contrast, beams that spanned multiple grains (proton 3 dpa example in Figure 5.11) had only 2 of the 15 fractures. Finally, in the Fe^{2+} 3 dpa example, the line scan passes through a carbide along the notch axis. Here fracture toughness was lower than the average. Two beams had precipitates along the notch axis and both successfully fractured. This is tabulated in Table 5.7.

Figure 5.12a shows the calculated apparent fracture toughness values for each beam, while Figure 5.12b demonstrates the averages for each material condition. As received and proton averages are nearly identical at 16.9 and 16.7 MPa $m^{1/2}$, respectively. There is a wide range of values for the Fe^{2+} at 3 dpa, though the average (13.68 MPa $m^{1/2}$) is less than the as received.

It is important to note that while it appears the Fe^{2+} at 100 dpa shows a significant decrease in fracture toughness, only one of the 9 samples at this condition tested, fractured at the notch. Of the remaining 8 samples, 6 fractured at the clamped corners and 2 were punched through. While some of the beams from the other material conditions also fractured at the corners, the punching through was unique to the 100 dpa material.

The bulk literature values for unirradiated Fe-Cr nanostructured ferritic alloys (NFA) and ODS alloys range widely. Work by Byun et al. (Figure 5.13), surveyed a variety of Fe-9%Cr and Fe-14%Cr NFA alloys finding $K_{Q,J}$ values from 18 MPa $m^{1/2}$ to 280 MPa $m^{1/2}$ [71]. Work by Fournier on Fe-14%Cr ODS steels found a range of K_{IC} values between 12-30 MPa $m^{1/2}$ [56]. The $K_{Q,J}$ values calculated for the Fe-9%Cr ODS clamped beams tested in this study fall on the lower end of these ranges (included in Figure 5.13), suggesting an underestimation, yet still within realistic bounds. This is further discussed in §6.2.

5.4   Lamellae Indentation

The only material condition tested for in situ lamellae indentation was the Fe^{2+} irradiated at 3 dpa 500°C. Two lamellae were indented. The chronological steps involved with the lamellae indentation in this work is as follows: 1) Indentation, 2) subsequent MicroViBe processing of recorded indentations, 3) post-mortem ASTAR analysis and STEM loop imaging, and finally, 4) loop analysis and strength. For the purposes of this dissertation, steps 1 and 2 will be presented

here in §5.4, while steps 3 and 4 will be part of §6.3. However, it is important to note, that all 4 steps are required to connect the observed microstructural changes in the original lamella indentation with irradiation induced obstacles.

Still frames from the indentation video and MicroViBe false color heatmap, coupled with a grain orientation map, provide an overview of the changes occurring during the indentation. Still frames taken at ~6 second intervals during the indentation videos are provided in Figures 5.14a-f and 5.15a-f for Lamella 1 and Lamella 2, respectively. The ASTAR grain orientation map corresponding to each lamella is shown in Figures 5.14g and 5.15g. Finally, still frames from the MicroViBe false color heatmaps, also taken at ~6 second intervals, are shown in Figures 5.14h-l and 5.15h-l. Since the false color heatmap shows the accumulation of foreground changes in each pixel in the frame, the first image of the series (time 0) is entirely blue, since no change in the contrast has yet occurred; hence, we do not show this heatmap. Videos of each indentation and the corresponding MicroViBe videos are provided as supplementary material.

In the indentations shown in Figures 5.14 and 5.15, the indenter tip moves upward from the original irradiated surface (at the bottom of the images), into the Fe-9%Cr ODS lamella. As the indenter tip moves into the lamella, plastic deformation occurs and changes in the microstructure can be observed. We organize the following paragraphs chronologically, discussing the time evolution of Lamella 1 and Lamella 2 together, as both lamellae exhibit similar behaviors.

Time 0 – Lamella 1 (Figure 5.14) contains a single, nearly vertical, grain boundary that extends from the original irradiated surface to ~200 nm into the lamella, separating grains 1 and 2. Correlating the stills with the ASTAR grain map suggests grain 1 is near the [001] orientation, grain 2 is near the [111] orientation, and grain 3 is a mix of [111] and [013]. Lamella 2 has a carbide to the left of the indenter (indicated as 'C' in Figure 5.15a) as well as two main grain

boundaries. The first runs along the bottom of grains 1 and 3, separating them from grain 4. The second boundary separates grain 2 from grains 1 and 3. The region directly below the indenter tip (marked grain 4) is relatively unresolvable in ASTAR after indentation. Thus, we focus on the three grains (grains 1, 2, and 3) comprising most of the lamella; these three grains meet near the center of the lamella. From the ASTAR image, grains 1 and 3 are both oriented near [113], while grain 2 is oriented near [001].

Time 0-6 seconds – When the indenter first contacts the lamella, the darkest contrasted area changes to a lighter contrast. These changes are circled in Figures 5.14h-i and 5.15h-i. As a result of this initial contact, MicroViBe immediately marks these initially dark-contrasting spots as hotspots. The reader can notice that the grains in Lamella 2 which are initially darkly contrasted (grains 1 and 3) contain more hotspots than the initially light contrasted grain 2.

Time 6-12 seconds – During loading of Lamella 1, a dark contrasting band moves from the center of the lamella, through the [001] grain in the direction of the lower right side of the lamella (marked with an arrow in Figure 5.14c). This band corresponds to pixel changes in the heatmap (Figure 5.15i). It is unknown whether this band is comprised of a group of dislocations or is simply a bend contour. In both lamellae, toward the bottom of the image, "hotspots" from the motion of the indenter tip overwhelm any microstructural changes; so this region is rendered unfeasible for heatmap analysis. The boundaries between dark and light contrasting grains show a large accumulation of pixel changes in the heatmap; one grain and one carbide-to-grain boundary is shown by arrows in Figure 5.15i.

Time 18-24 seconds – In Lamella 2, a dark contrasting band moves from grains 1 and 3, into grain 2, as indicated by an arrow in Figure 5.15. There is a corresponding accumulation of

pixel changes in the heatmap, Figure 5.15k. Again, it is unknown whether this is a band of dislocations or a bend contour.

Time 30 seconds – Hotspots that form in the first 5-6 seconds of indentation, remain "hot" throughout the indentation test, because the algorithm accumulates change. In both lamellae, the dark contrast band (initially indicated in Figures 5.14c and 5.15e) remains in the grain after unloading (Figure 5.14f, 5.14l, 5.15f, and 5.15l). Also, in both lamellae, the ~50-100 nm region in closest proximity to the indenter tip (i.e. grain 1 in Lamella 1, grain 4 in Lamella 2) initially begins as a single grain (Figures 5.14a and 5.15a) but is comprised of several smaller grains after indentation (Figures 5.14g and 5.15g). Indentation-induced grain size reduction has been observed in the same alloy in the region immediately below nanoindentations [27]. In Lamella 2, the junction between grains 1, 2, and 3 remains unchanged throughout the indentation (circled in Figure 5.15f). The carbide remains unchanged throughout the indentation, only changing contrast with the flexing of the lamella due to the indentation and plastic deformation nearby.

Table 5.1 - Each micropillar tested with dimensions and mechanical properties

	Sample #	Thickness (nm)	Width (nm)	Height (nm)	Yield Stress (MPa)	Elastic Modulus (GPa)	Deflection Adjusted Modulus (GPa)	FEM Adjusted Modulus (GPa)
As Received	1	247	266	258	1351	48.2	74.9	170.3
	2	386	309	361	1383	52.1	209.1	475.3
	3	180	431	469	1485	44.5	100.5	228.3
	4	323	429	479	1750	59.7	302.8	688.3
	5	562	405	524	1740	53.8	193.7	440.3
	6	565	527	623	1348	50.7	98.5	223.8
	7	274	638	686	1323	53.4	114.7	260.6
	8	185	189	143	1156	30.8	292.1	663.8
	9	321	398	378	1035	58.6	70.1	159.3
	10	374	451	443	1412	48.6	81.5	185.3
	11	579	688	620	995	41.5	60.1	136.6
	12	71	203	242	1124	16.4	24.2	55.0
	13	87	355	336	1062	11.5	11.1	25.3
	14	87	457	455	954	16.3	21.3	48.4
	15	102	572	532	915	19.4	17.5	39.8
Fe^{2+} 3 dpa 500°C	1	83	152	185	1512	21.5	32.9	137.1
	2	165	292	294	1022	35.9	59.9	249.7
	3	204	307	283	1418	34.7	47.6	198.5
	4	206	303	292	1332	35.7	19.9	82.9

	5	311	480	392	1399	34.9	35.8	149.3
	6	396	585	535	898	34.7	61.1	254.4
	7	471	665	615	1580	32.6	48.0	200.0
	8	566	710	617	1039	28.0	35.6	148.3
	9	59	203	223	899	7.8	9.2	38.3
	10	67	529	513	1011	18.4	32.7	136.2
	11	76	517	435	1902	72.5	82.0	341.7
	12	77	505	412	1004	36.0	39.2	163.5
	13	171	443	478	1174	55.0	37.7	157.3
Fe^{2+} 100 dpa 500°C	1	170	207	231	1015	27.8	54.4	226.7
	2	188	291	238	1375	29.5	40.9	170.2
	3	254	266	294	1151	26.9	74.2	309.1
	4	203	351	332	1082	42.9	61.8	257.5
	5	453	426	391	978	25.7	37.0	154.2
	6	617	692	579	1212	24.8	49.5	206.5
	7	63	433	413	1203	17.7	44.6	185.9
	8	75	443	428	949	18.6	50.4	209.9
	9	65	430	394	1784	25.8	37.8	157.4
	10	69	436	439	1029	18.5	74.0	308.3
	11	65	404	422	1285	18.1	48.9	203.9
	12	311	438	400	1202	29.0	39.6	165.2

Table 5.2 – Yield strength measurements from compression micropillars

		As Received	Fe^{2+} Irradiated 3 dpa, 500°C	Fe^{2+} Irradiated 100 dpa, 500°C
All	Average yield strength (MPa)	1269 ± 256	1245 ± 294	1188 ± 217
	# of micropillars	15	13	12
Minimum dimension <100 nm	Average yield strength (MPa)	1014 ± 83	1266 ± 383	1250 ± 293
	# of micropillars	4	5	5
Minimum dimension >100 nm	Average yield strength (MPa)	1362 ± 233	1233 ± 221	1145 ± 125
	# of micropillars	11	8	7

Table 5.3 – Elastic modulus measurements and adjustments from compression micropillars

	As Received	Fe^{2+} Irradiated 3 dpa, 500°C	Fe^{2+} Irradiated 100 dpa 500°C
Number of micropillars	15	13	12
Measured elastic modulus (GPa)	40.8 ± 15.3	34.4 ± 15.3	25.4 ± 6.8
Deflection adjusted elastic modulus (GPa)	112 ± 92.0	41.7 ± 18.0	51.1 ± 12.4
Deformation adjusted elastic modulus (GPa)	253 ± 209	174 ± 74.8	213 ± 51.6

Table 5.4 – Finite element results of percent deformation occurring in micropillar and base for varying base heights

Base height (μm)	% deformation in micropillar	% deformation in base
1	43	57
3	30	70
5	24	76
6	21	79

Table 5.5 – Nominal dimensions and flow stress of tested as received and proton irradiated cantilever beams. Highlighted rows indicate beams experiencing size effect

As Received	Length (nm)	Height (nm)	Thickness (nm)	Notch Length (nm)	Flow Stress (MPa)
Test 1	1000	200	300	50	2004
Test 2	1000	200	260	50	3060
Test 3	1000	500	380	100	3064
Test 4	1000	500	290	100	2571
Test 5	1500	200	320	50	3685
Test 6	1500	200	250	50	2705
Test 7	1500	500	390	100	2339
Test 8	2000	200	380	50	4718
Test 9	2000	200	240	50	5658
Test 10	2000	500	380	100	3052
Average - No Size Effects					2682 ± 410

Proton Irradiated	Length (nm)	Height (nm)	Thickness (nm)	Notch Length (nm)	Flow Stress (MPa)
Test 1	1000	200	350	50	2805
Test 2	1000	200	270	50	3208
Test 3	1000	500	380	100	2820
Test 4	1000	500	290	100	3063
Test 5	1500	200	340	50	2759
Test 6	1500	500	320	100	3136
Test 7	1500	500	410	100	2059
Test 8	2000	200	360	50	4592
Test 9	2000	200	340	50	3135
Test 10	2000	500	320	100	3105
Average - No Size Effects					2885 ± 360

Table 5.6 – Each tested clamped beam with dimensions and fracture toughness if fractured. Also includes notes on grain and precipitate information around notch.

Material Condition	Beam #	Length (nm)	Height (nm)	Thickness (nm)	Notch Length (nm)	$K_{Q,J}$ (MPa m$^{1/2}$)	Grain (Single/ Multiple)	Precipitate	Note
As Received	1	4200	550	140	110	15.33	S		
	2	4300	410	100	130	17.70	S		
	3	4080	480	130	120	15.60	S		
	4	4370	490	250	110	15.75	S		
	5	4200	650	250	110	-	M		
	6	4270	590	220	140	-	M		
Fe^{2+} 3 dpa 500°C	1	4060	450	130	90	8.63	S		
	2	4140	380	60	70	-	S		
	3	4090	430	100	80	10.18	S	C	
	4	4170	550	70	120	-	M		
	5	3920	600	110	120	-	M		
	6	3800	490	100	140	-	M	Fractured - large notch
	7	4750	520	360	90	-	M		
	8	3950	520	300	110	13.98	M		
	9	4110	530	310	100	15.56	S		
	10	3980	450	250	70	20.06	S		
	1	4100	470	220	110	-	S		

Fe^{2+} **100 dpa** **500°C**	2	3970	470	210	110	-	M		
	3	4070	470	220	110	-	S		
	4	4100	430	260	90	-	S		
	5	4000	370	230	60	-	M		
	6	3950	400	240	60	-	M		left punch
	7	4010	570	210	110	7.03	S		
	8	4180	530	190	130	-	M		right punch
	9	4030	550	210	120	-	M		left punch
Proton **3 dpa** **500°C**	1	4150	660	210	120	19.55	S		
	2	4300	710	190	110	-	M		
	3	4310	650	170	120	19.46	S		
	4	4210	610	220	150	19.98	M		
	5	4180	650	210	100	-	M		
	6	4240	470	190	100	11.12	M	Cr	
	7	4210	420	240	90	-	M		
	8	4200	380	210	110	-	M		
	9	4370	420	220	120	13.32	S		

Table 5.7 – Clamped beam quantity tested and fractured by material condition

	As Received		Fe^{2+} 3 dpa 500°C		Fe^{2+} 100 dpa 500°C		Proton 3 dpa 500°C	
	Fractured	Tested	Fractured	Tested	Fractured	Tested	Fractured	Tested
Total	4	6	5	10	1	9	5	9
Single Crystal	4	4	3	4	1	4	3	3
Polycrystal	0	2	1	5	0	5	1	5
Precipitate	0	0	1	1	0	0	1	1
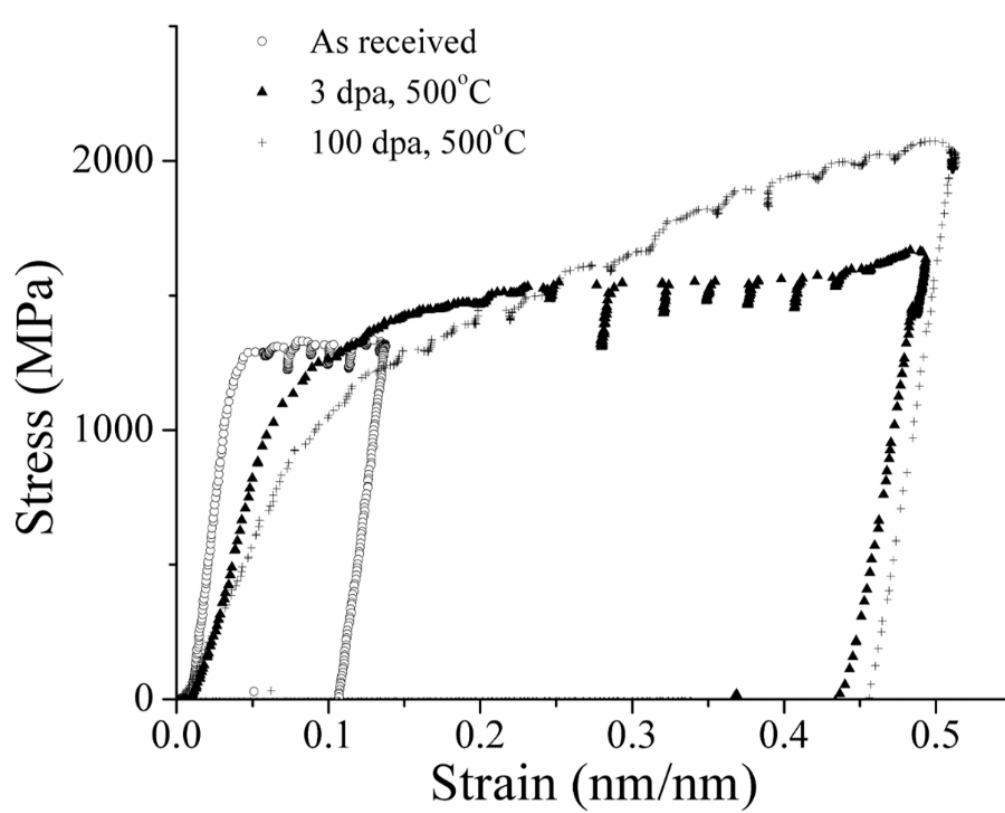
Figure 5.1 – Representative stress-strain curves of three micropillars with nominal dimensions: as received – 500 nm × 500 nm × 500 nm, Fe2+ 3 dpa 500°C – 600 nm × 600 nm × 600 nm, Fe2+ 100 dpa 500°C – 400 nm × 400 nm × 400 nm
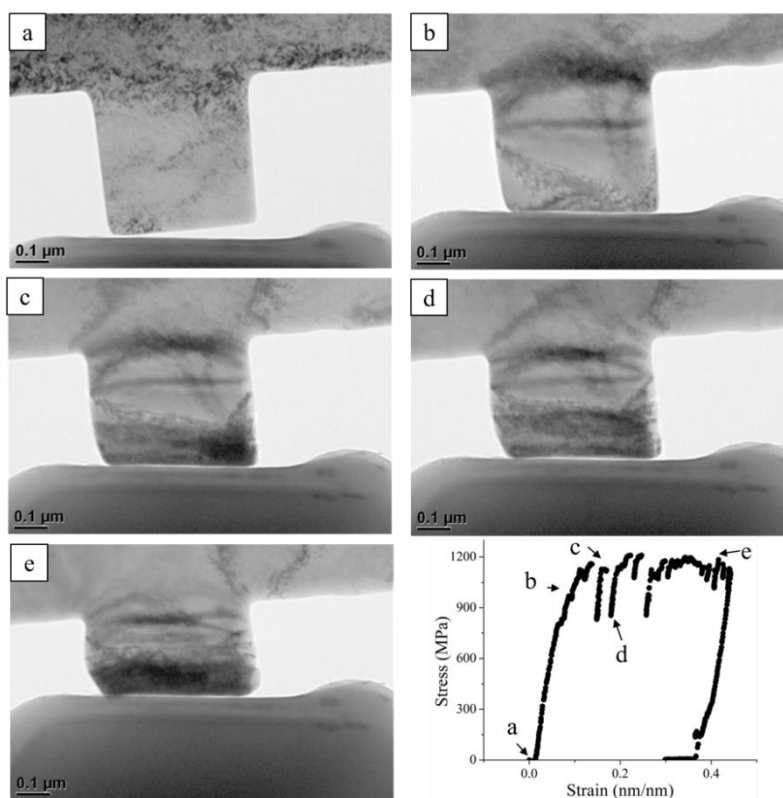
Figure 5.2 – In situ compression test of as received ODS 400 nm × 400 nm × 100 nm micropillar. (a-e) show micropillar condition at each labeled point in stress-strain curve. Dislocation bursts are observed at (c) and (d), representing load drops observed on stress-strain curve
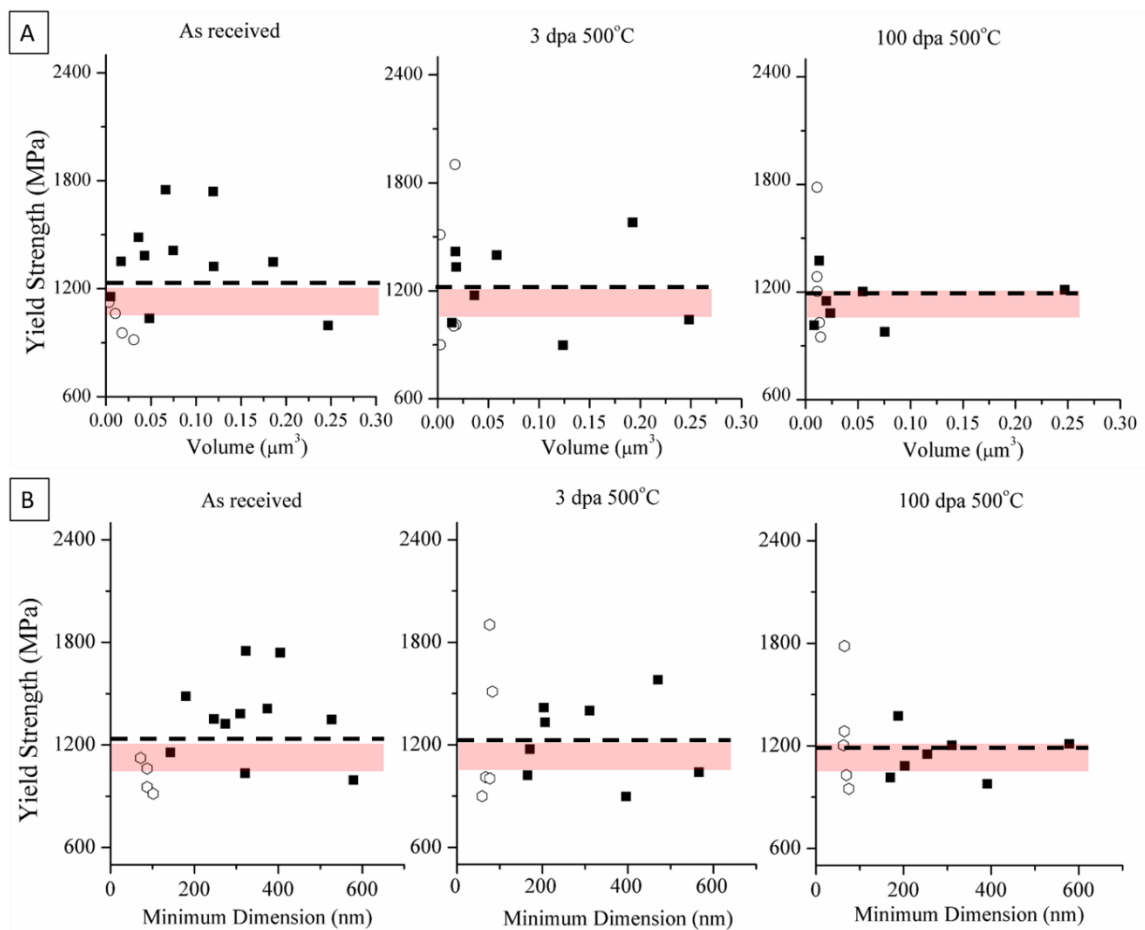
Figure 5.3 – In situ compression test of as received ODS 400 nm × 400 nm × 100 nm micropillar. (a-e) show micropillar condition at each labeled point in stress-strain curve. Dislocation bursts are observed at (c) and (d), representing load drops observed on stress-strain curve
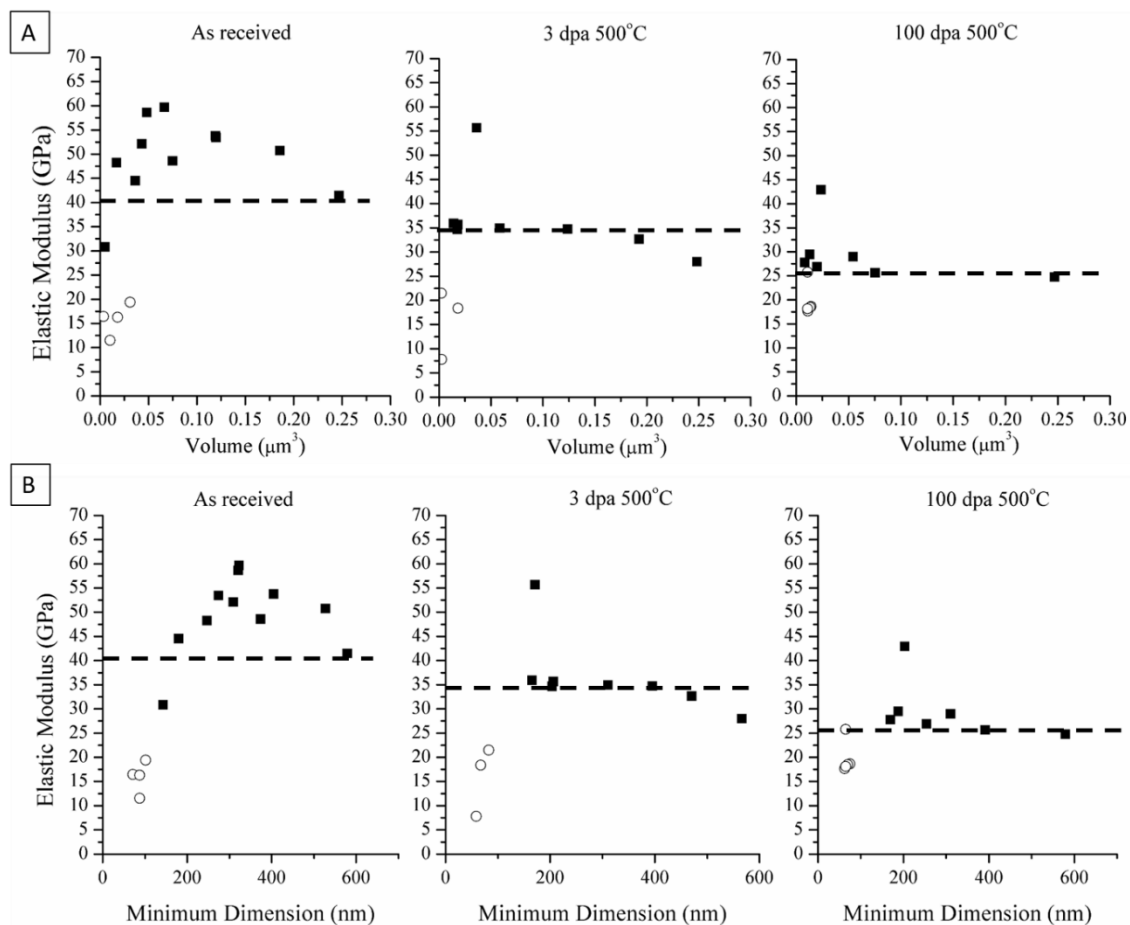
Figure 5.4 – Measured elastic modulus as a function of (a) micropillar volume or (b) minimum micropillar dimension. Open symbols represent micropillars having minimum dimension <100 nm; closed symbols represent micropillars having minimum dimension >100 nm. Dashed line represents the average of measurements
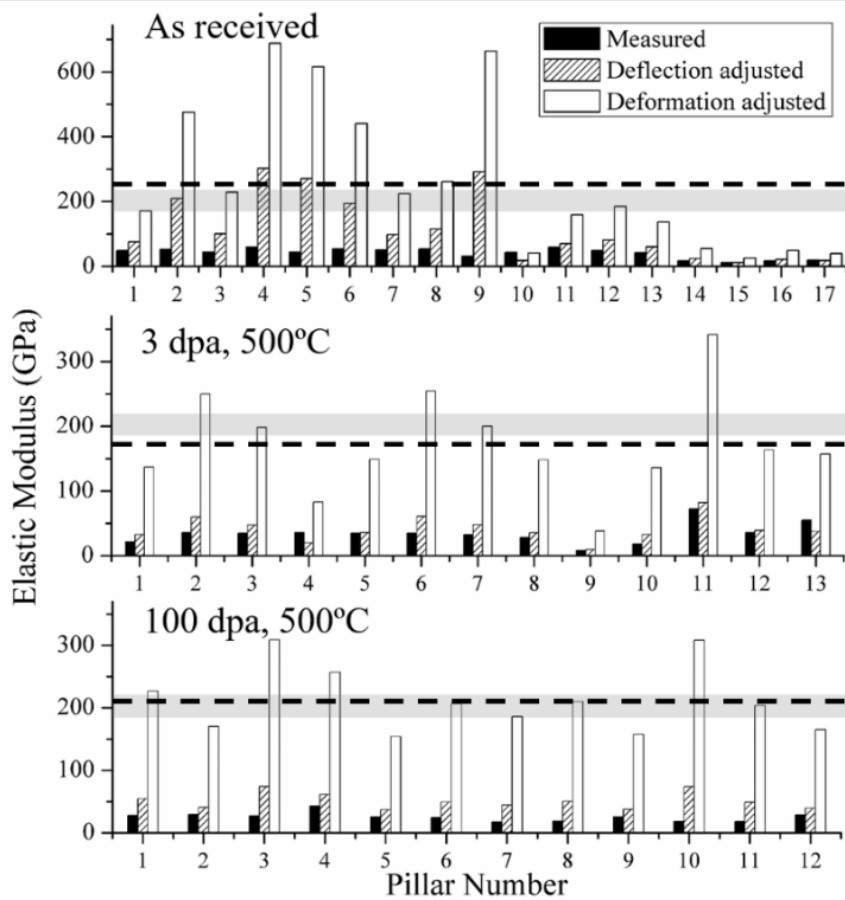
Figure 5.5 – Measured and adjusted elastic modulus values for all micropillars. Gray shaded band shows expected range (190-220 GPa). Dotted line shows average of the deformation adjusted values in a given condition.
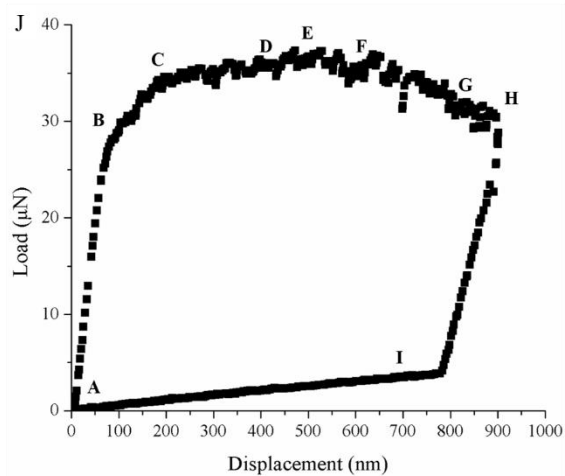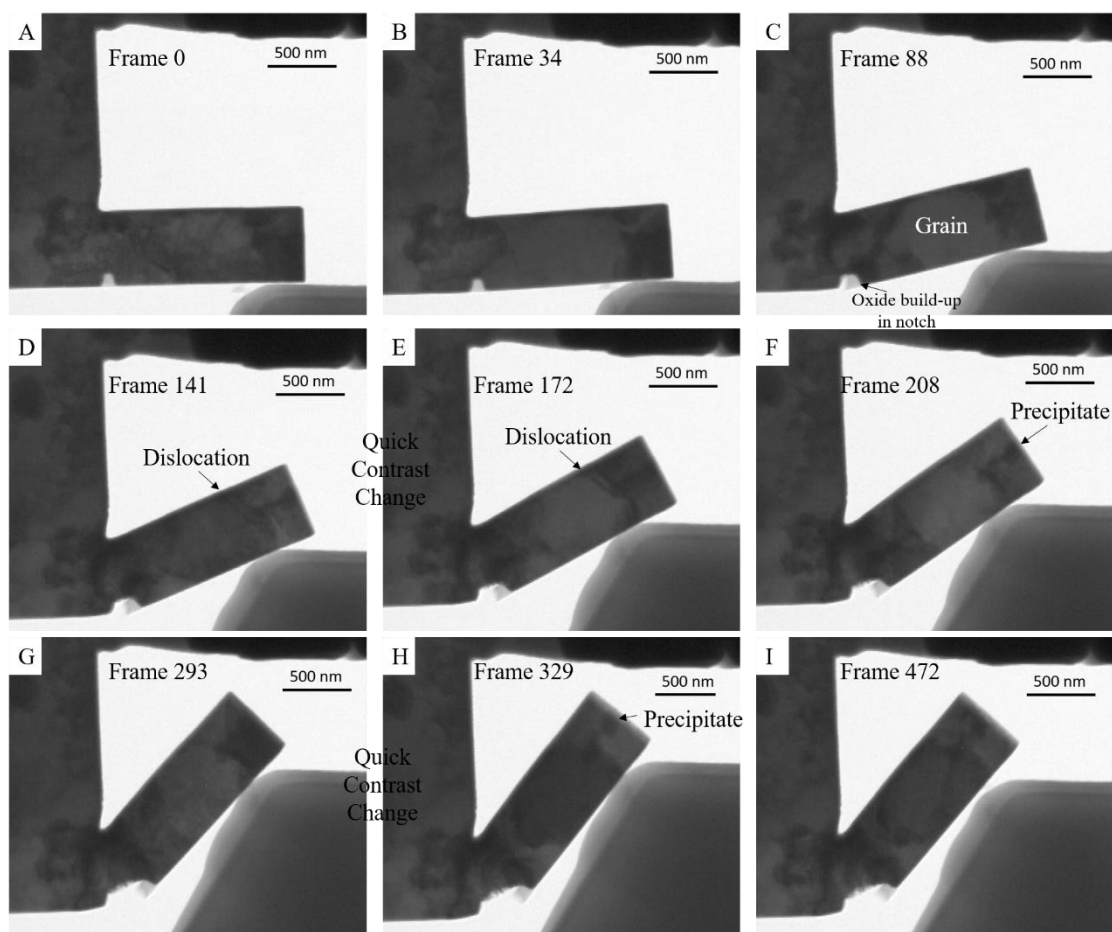
Figure 5.6 – (A-I) Still frames taken from bend test of proton irradiated cantilever with dimensions 1500nm long × 500 nm tall × 300 nm tick. (J) Load-displacement curve for tested cantilever with locations of still frames identified
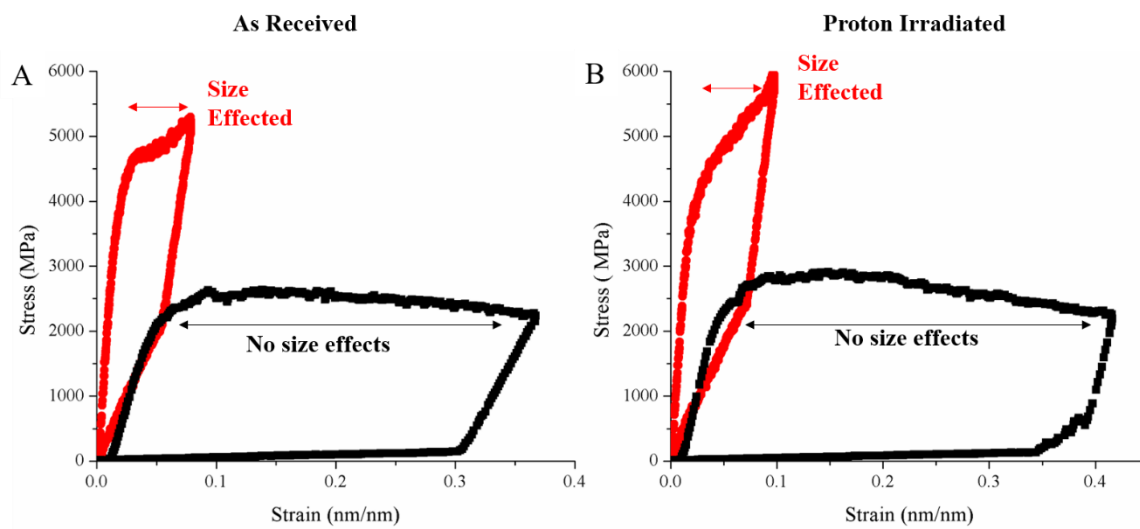
Figure 5.7 – Representative stress-strain curves for (a) as received and (b) proton irradiated cantilevers
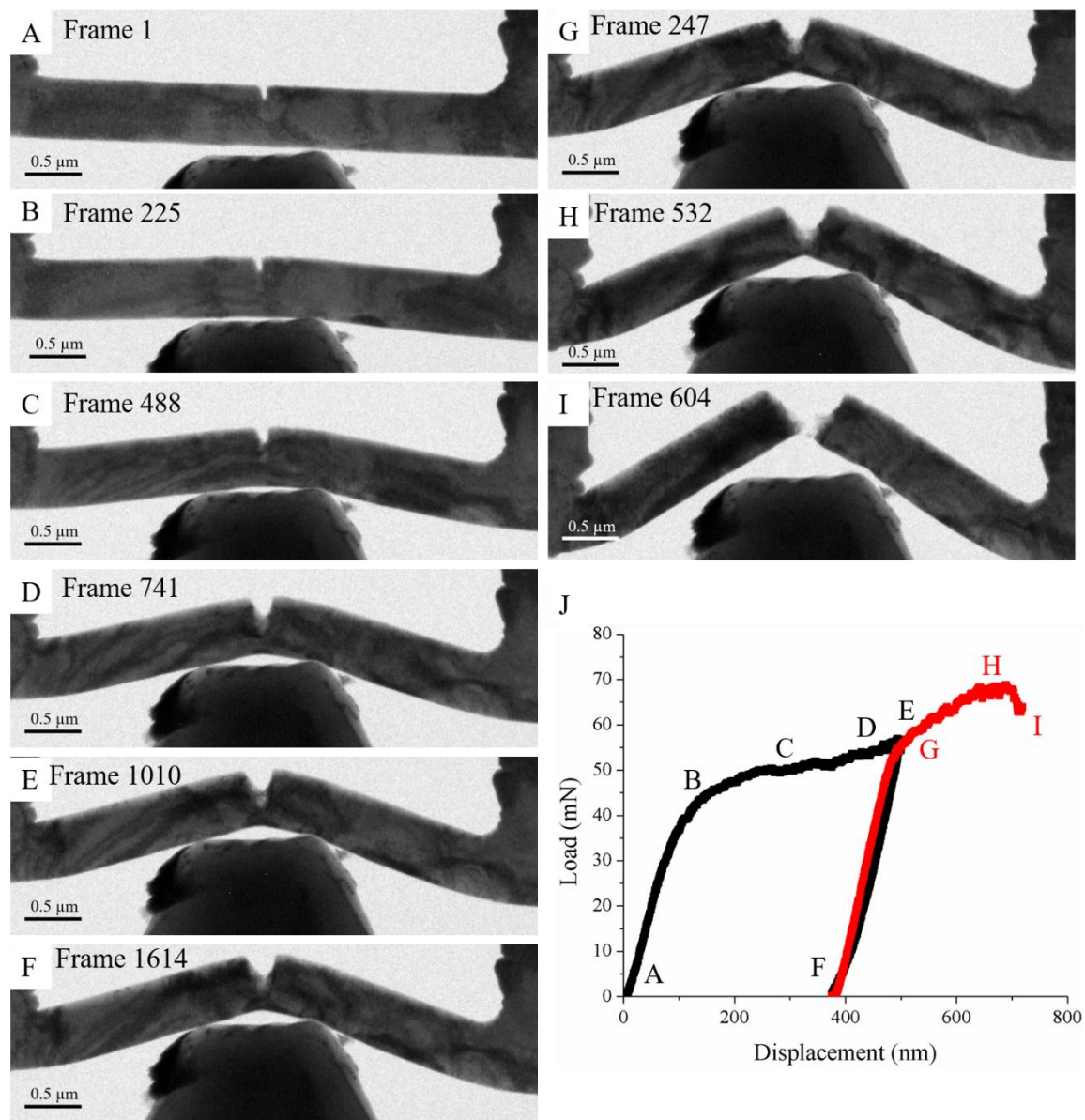
Figure 5.8 – (A-I) still frames taken from initial 'hit' (A-F) and second hit (G-I) until fracture (I). (J) is the corresponding load-displacement curve for both hits with still frame locations identified
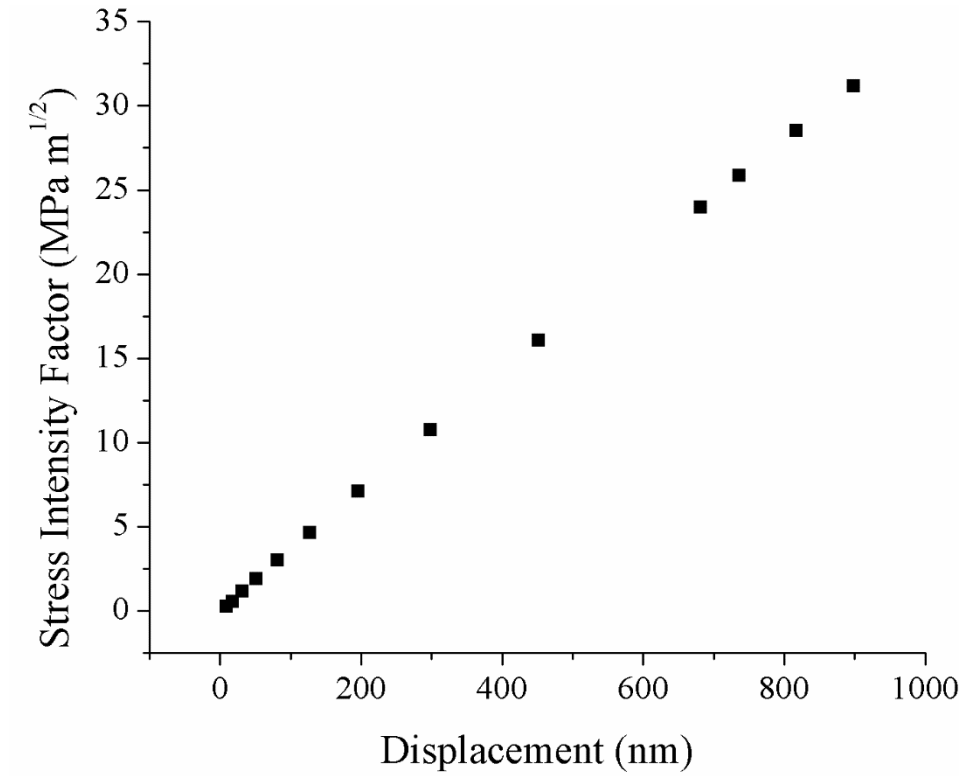
Figure 5.9 – Representative stress intensity factor vs displacment for XFEM simulation of clamped beam
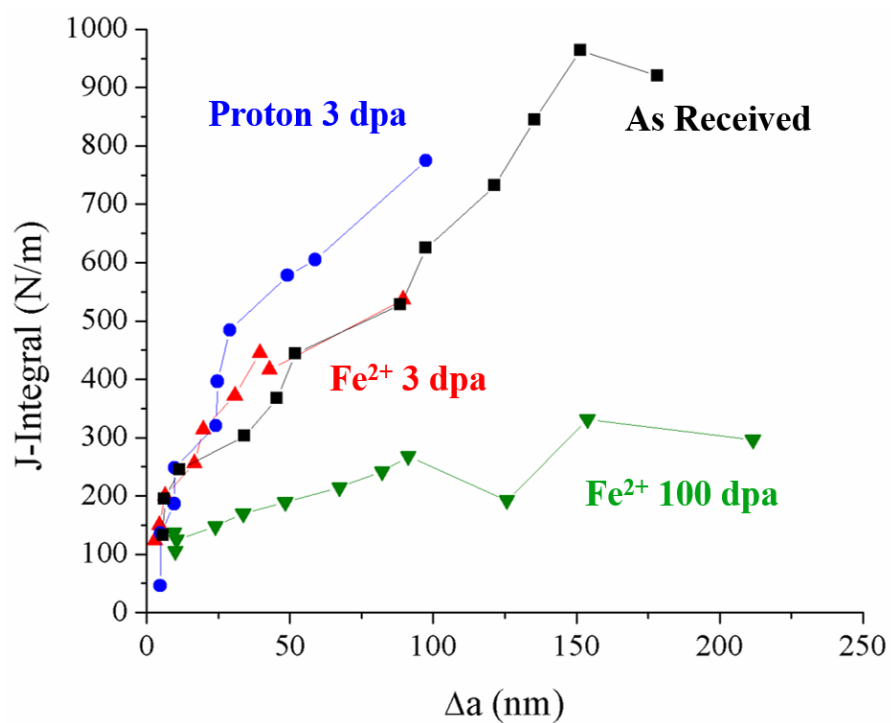
Figure 5.10 – Representative J-Δa curves for each material condition tested
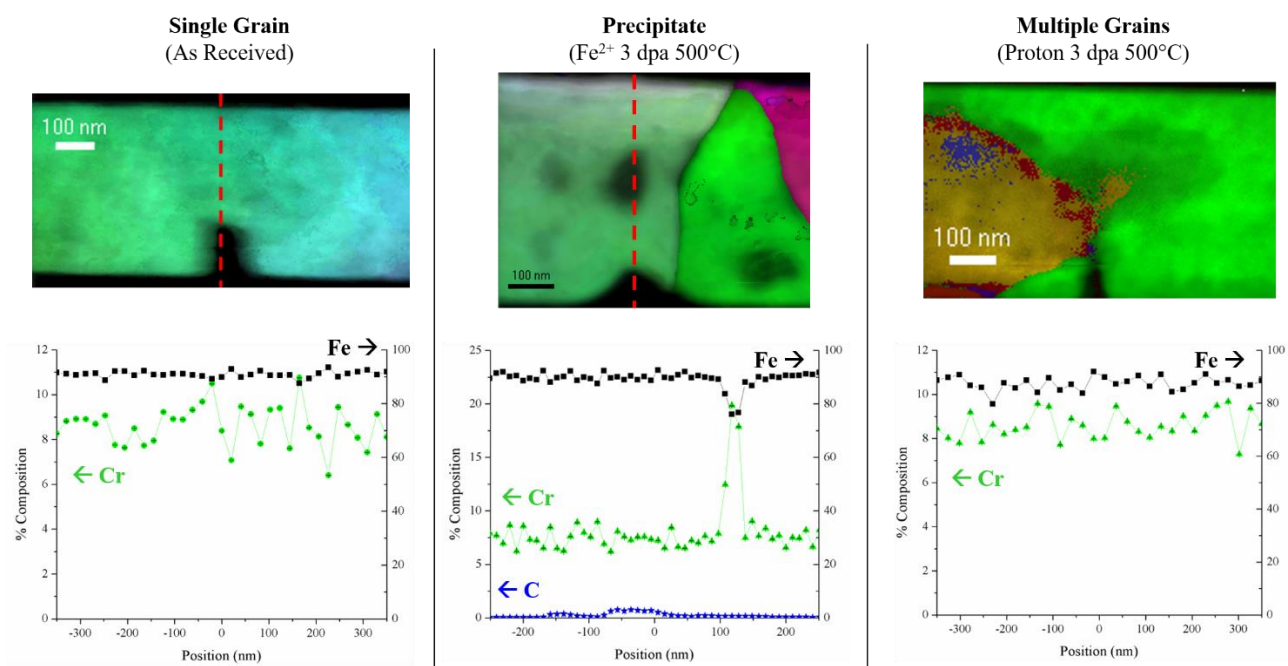
Figure 5.11 - Representative ASTAR and EDS plots for each material condition
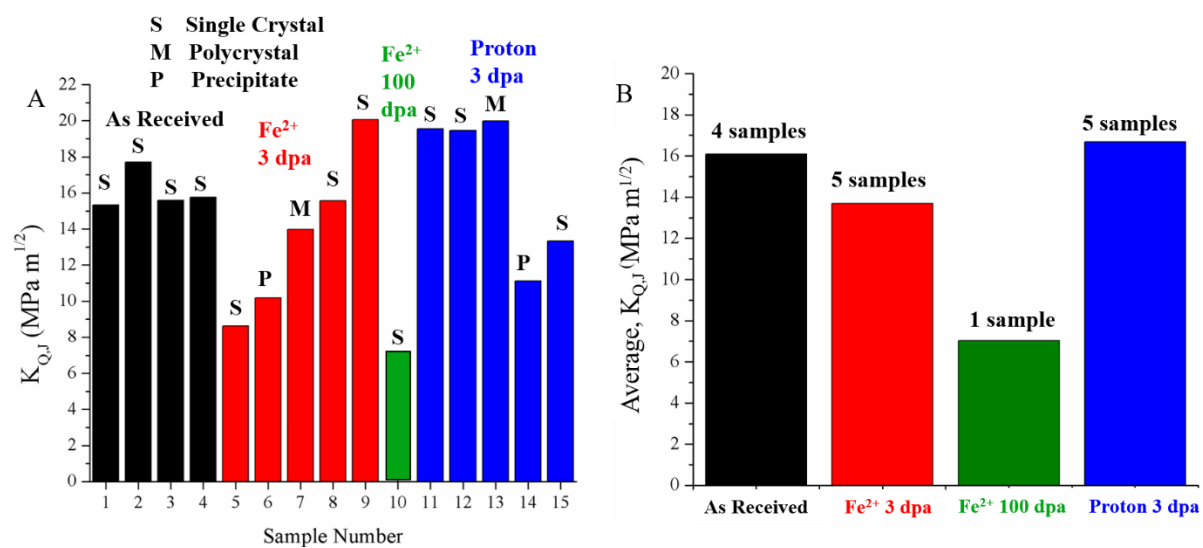
Figure 5.12 - (a) KQ,J values for each tested beam (b) average KQ,J values by material condition with number of samples
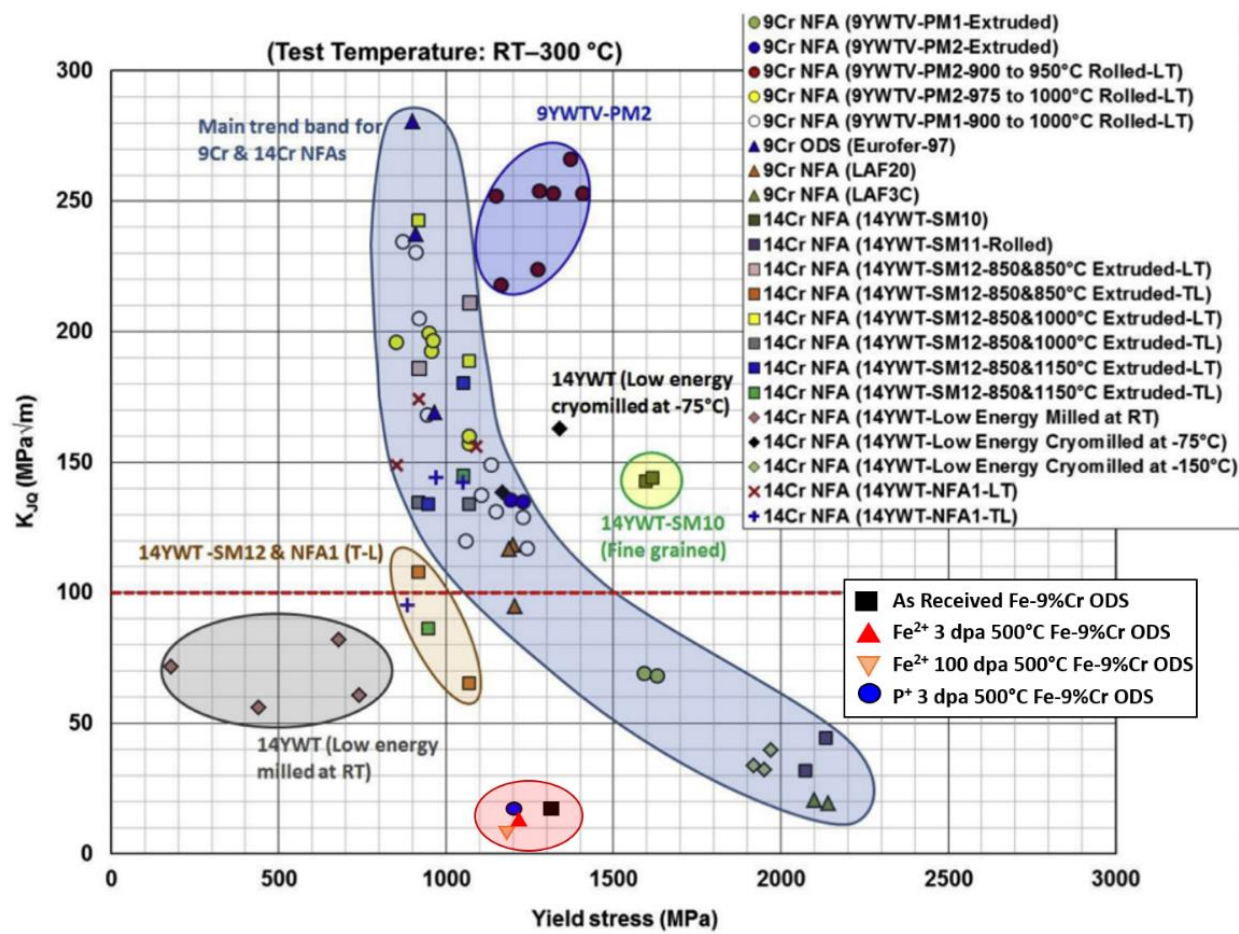
Figure 5.13 – Fracture toughness vs yield strength for Fe-9%Cr and Fe-14%Cr NFA and ODS bulk alloys. Original work by Byun et al [49]. Added in results from clamped beam in situ TEM fracture testing. Results are on the low range of bulk values.
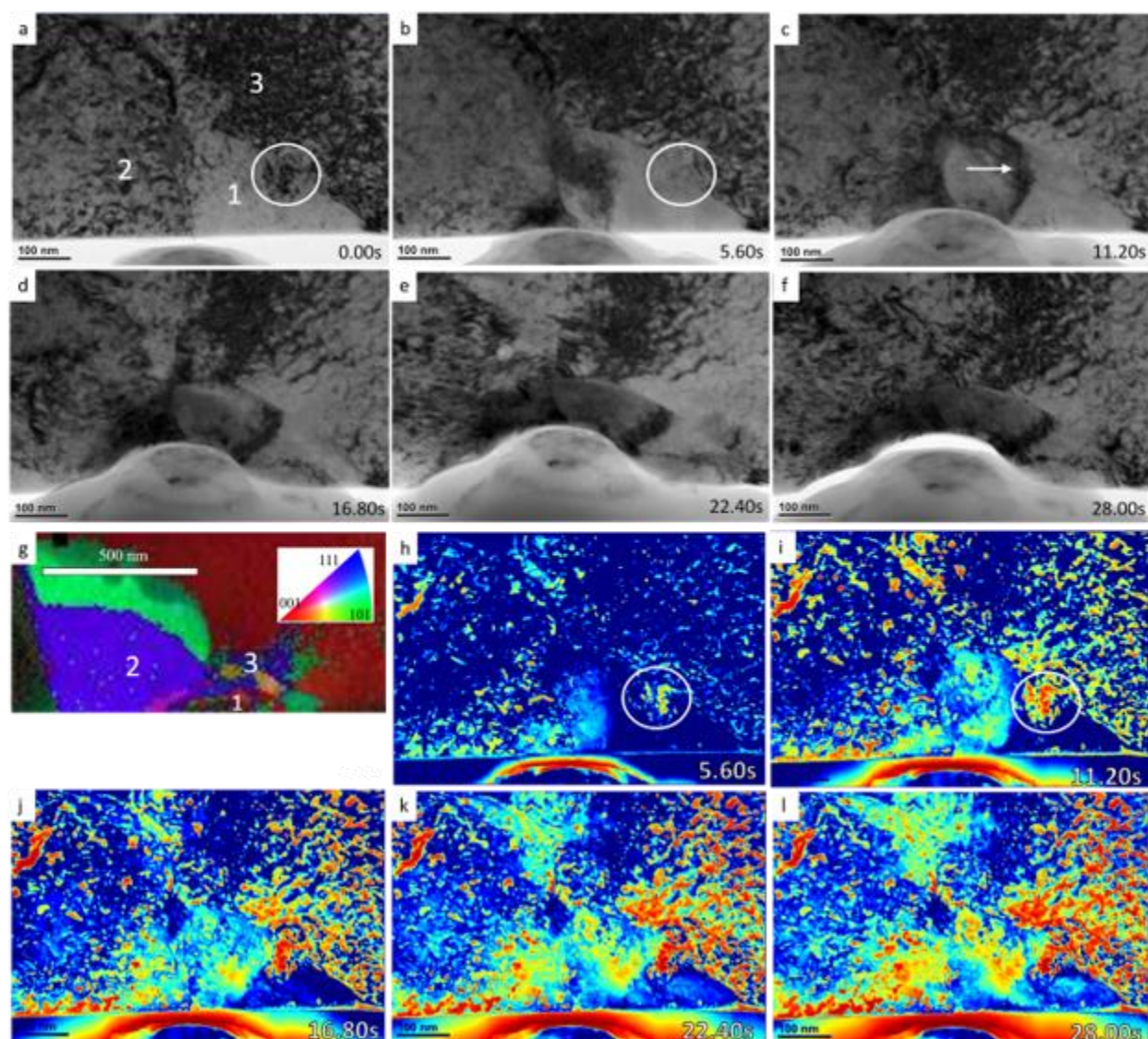
Figure 5.14 - Lamella 1 (a-f) still images collected at ~6 second intervals from the original TEM video, grains are numbered 1-3 with a dark contrast region of interest circled and a dark contrast band identified with an arrow, (g) ASTAR grain orientation map of indented lamella with grains numbered, and (h-l) still images from the MicroViBe algorithm at same time intervals as in figures 3(b-f), and the same region of dark contrast spots circled. Indent is displacement controlled to a depth of 100 nm. Time stamps are included on the images in the lower right-hand corner
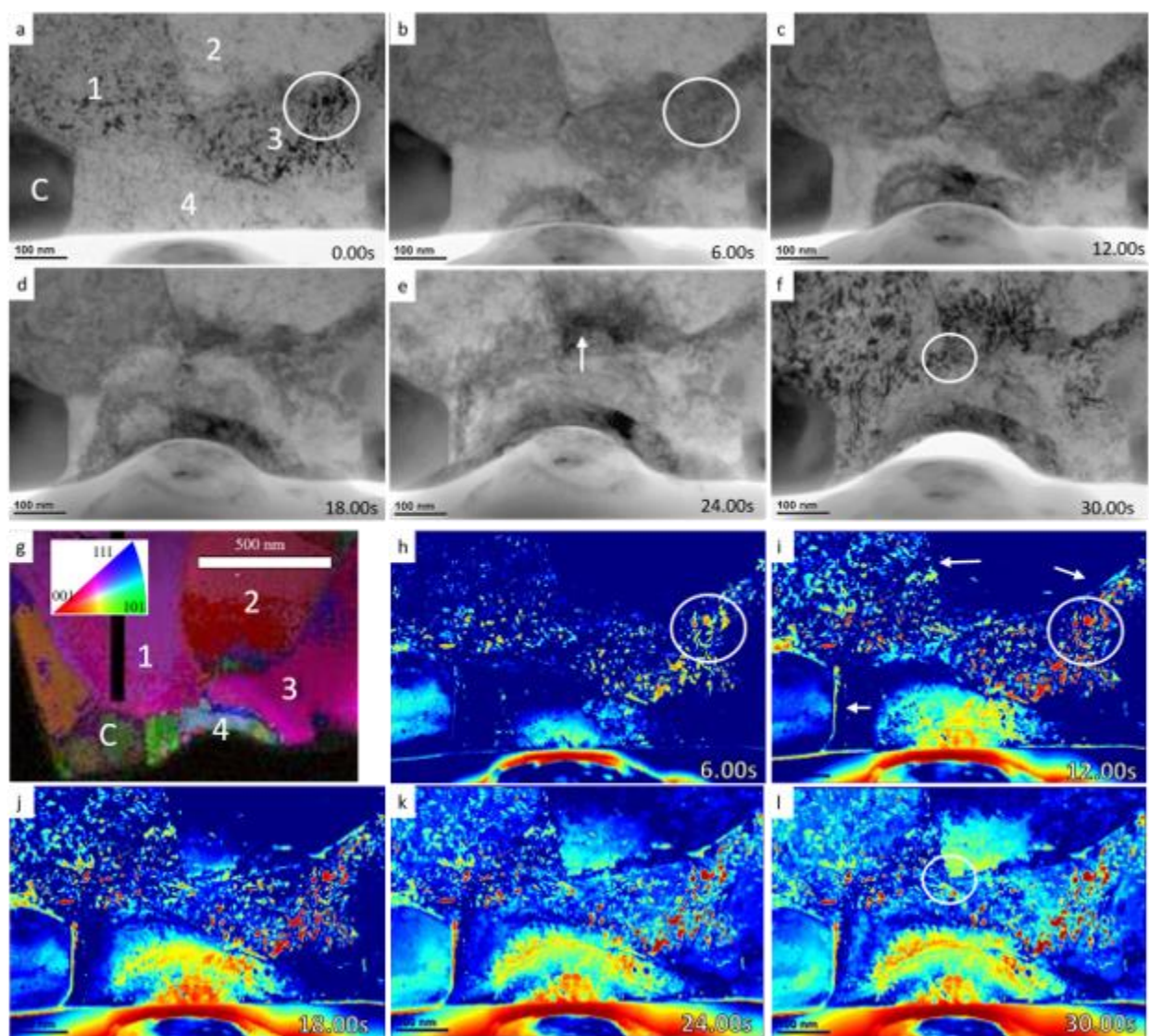
Figure 5.15 – Lamella 2 (a-f) still images collected at ~6 second intervals from the original TEM video, with grains numbered 1-4 and a carbide identified with 'C', circled spots of dark contrast are of interest and an arrow is used to mark dark contrast bands moving, (g) ASTAR grain orientation map of indented lamella, with corresponding labels of grains and the carbide, and (h-l) still images from the MicroViBe algorithm at same time intervals as in figures 4(a-f), with corresponding circled regions, here, however the arrows identify grain boundaries accumulating pixel changes in the MicroViBe algorithm. Indent is displacement controlled to a depth of 100 nm. Time stamps are included on the images in the lower right-hand corner

6. DISCUSSION

A version of this chapter has been published in the following journals:

1. K.H. Yano, Y. Wu, J.P. Wharry. *Size Effects in TEM in situ Cantilever Flow Stress Measurements in Irradiated Fe-9%Cr ODS*. Submitted. Materials Science and Engineering: A. (2019).

2. K.H. Yano, S. Thomas, M.J. Swenson, Y. Lu, and J.P. Wharry. *TEM* in situ *cube-corner indentation analysis using ViBe motion detection algorithm*. Journal of Nuclear Materials 502 (2018) 201-212. doi:10.1016/j.jnucmat.2018.02.003

3. K.H. Yano, M.J. Swenson, Y. Wu, and J.P. Wharry. *TEM* in situ *micropillar compression tests of ion irradiated oxide dispersion strengthened alloy.* Journal of Nuclear Materials 483 (2017) 107. doi:10.1016/j.jnucmat.2016.10.049 and doi:10.1016/j.jnucmat.2017.04.054

The discussion will be split into three subsections. The first is the size effect in both the micropillar and cantilever geometries. As will be discussed, these two geometries begin to exhibit inflated yield/flow stress as the extrinsic dimensions approach intrinsic dimensions. The second section will study fracture at in situ TEM scales on elastic-plastic materials. Finally, a discussion of obstacle strength determination from the use of MicroViBe and in situ lamellae indentation will be undertaken.

6.1 Size Effects in Micropillar Compression & Cantilever Bending

As discussed in §2.1.4, as sample dimensions (extrinsic) approach the material obstacle spacing (intrinsic), size effects begin to manifest as inflated mechanical properties. By varying the dimensions in the micropillars experiment, an extrinsic threshold at which size effects begin can be found for Fe-9%Cr ODS. This threshold is discussed in §6.1.1.

Yet, micropillar compression is not the only mechanical testing geometry through which the relationship between intrinsic and extrinsic parameters impact size effects can be understood.

The second subsection will discuss the size effect relationship found in the cantilever geometry. This can be modeled using a logarithmic relationship between the flow stress and the ratio between the extrinsic and intrinsic parameters of the material tested. This logarithmic approach is discussed in §6.1.2.

Finally, a brief summary of size effects in small-scale testing is discussed in §6.1.3. Here, the results of the micropillar and cantilever testing on the Fe-9%Cr ODS are put into context with other literature results and summarized.

6.1.1   Size Effect in Micropillars

It has been suggested [78] that there is a threshold micropillar diameter above which yield strength measured by TEM in situ methods is independent of size. This threshold is lower for irradiated materials than for unirradiated materials due to the high density of irradiation-induced obstacles [78]. Since the study herein uses a square or rectangular micropillar cross-section, the minimum micropillar dimension will be used in place of diameter. By plotting the yield strength as a function of the minimum micropillar dimension (Figure 5.3b), the size effect is apparent. In both irradiated conditions, thinner micropillars (i.e. those having minimum dimension ≤100 nm) exhibit a wide spread in yield strength (Figure 5.3b, Table 5.1). Although some of these micropillars fall within the expected range (highlighted bands, Figure 5.3b), some of these micropillars also result in excessively high yield strength measurements. Larger micropillars (i.e. those having minimum dimension >100 nm) produce a narrower distribution of yield strengths closer to expected values. These results suggest a potential size effect for irradiated materials similar to that observed by Kiener [78]: measured yield strength plateaus to bulk values with an increasing micropillar minimum dimension above >100 nm.

Calculated obstacle spacing (Table 2.2 and Equation 2.36) ranges between 19.9 and 33.7 nm and is influenced primarily by the high density of oxide nanoclusters. These values are well below the minimum dimension of each micropillar sample studied herein, so it follows that the obstacles – not the micropillar dimensions – will be the limiting factor in determining the dislocation source size, which is consistent with references [78,85]. However, as the minimum dimension of micropillars approach 100 nm and below (closer to the average obstacle spacing), the influence of the micropillar size on the dislocation source size becomes more relevant, leading to a likely size effect for smaller micropillars (i.e. < 100 nm). A plausible explanation for why the as-received material exhibits no size effect is that its L_{ob} is smaller than the irradiated steels.

6.1.2 Size Effect in Cantilever Bending

For yield stress, size effects have been understood by directly relating the minimum specimen dimension to the measured yield stress. But for flow stress, one must consider that an increasing dislocation density implies more extensive dislocation interactions during plasticity, which requires higher flow stress to sustain. This consideration manifests as a logarithmic relationship between dislocation density and flow stress, and has been observed in simulations of single crystal Ni micropillars [171], and experimental studies on Au nanopillars [172] and Fe pillars [81]. A model developed by Tarleton [129] formalizes this relationship for Ti and Zr cantilevers; the model relates flow stress (σ_{flow}) with the minimum sample dimension (w) and the average dislocation source spacing (w_s), Equation 6.1. The bulk flow stress, σ_0, is the flow stress for large w.

$$\sigma_{flow} = A \left(\frac{w}{w_s}\right)^{-n} + \sigma_0 \qquad\qquad \text{Equation 6.1}$$

where the dislocation source density, ρ_s, is used to calculate the dislocation source spacing, w_s, according to:

$$w_s = \frac{1}{\sqrt{\rho_s}}$$ Equation 6.2

Because this model is based on the normalized minimum dimension (i.e. ratio of w to w_s), increasing the dislocation source density has the same effect on flow stress as decreasing the cantilever size. Hence, Tarleton's model is based on source limitation in the existing volume.

This model has been used effectively for Ti and Zr [129] and also fits the flow stresses measured from pure Fe micropillars having an even lower source density of 1 μm^{-2} with corresponding source spacing of 1000 nm [81]. Here, we apply the model to the Fe-9%Cr ODS cantilevers. Figure 6.1 shows flow stress as a function of normalized specimen dimension for both the pure Fe from ref. [81] and the as received and irradiated Fe-9%Cr ODS from the present study. For the pure Fe, the normalized specimen dimension is determined by taking the ratio of minimum dimension to the dislocation source spacing, which is 1000 nm. But for the Fe-9%Cr ODS, the total obstacle spacing is utilized instead of the dislocation source spacing.

The obstacle spacing is determined from microstructure characterization of the as received and irradiated materials, and is primarily adopted from Swenson and Wharry [4,7]. Unirradiated Fe-9%Cr ODS consists of dense dislocation regions, a fine dispersion of oxide nanoclusters, and 200-300 nm diameter grains. After irradiation, voids and dislocation loops nucleate at number densities 0.34×10^{21} m^{-3} and 10.2×10^{21} m^{-3}, with diameters of 4 nm and 8.4 nm, respectively. Grain diameter and dislocation line density remain statistically unchanged with irradiation, at 230-310 nm and 17.6-19.1×10^{14} m^{-2}, respectively. Nanocluster diameter reduces

(5.96 nm to 4.77 nm), while their overall number density remains constant (560×10^{21} as compared to 568×10^{21} m^{-3}). The microstructure quantification from ref. [7] for both the as received and proton irradiated conditions are summarized in Table 2.2. Considering all of these microstructural features, the obstacle spacing is calculated for both the as received and irradiated ODS through a diameter-weighted number density approach as outlined in ref. [50]. There is little difference in obstacle spacing between the as received and proton irradiated conditions: 19.9 nm as compared to 21.2 nm (§5.2.1). This calculated obstacle spacing is also included in Table 2.2 for easy comparison.

The as received and irradiated ODS both exhibit the expected decaying exponential relationship between the flow stress and the normalized minimum dimension, Figure 6.1. These trends reveal that elevated flow stress values occur at normalized dimensions <9 nm/nm for the Fe-9%Cr ODS; whereas the flow stress reaches a constant value of ~3000 MPa at normalized dimensions > 9 nm/nm. The Fe-9%Cr ODS flow stress results are consistent with the specimen size effect as reported for yield strength [72,118,173], and the normalization of the minimum dimension to the microstructure highlights the role of source or obstacle spacing within an existing specimen volume.

The power law can be fit to the flow stresses of the as received and proton irradiated ODS, but an additional factor, B, is necessary for the fit:

$$\sigma_{flow} = A \left(\frac{w}{w_s} - B \right)^{-n} + \sigma_0 \qquad \text{Equation 6.3}$$

where A and n are the stress proportionality constant and stress exponent, respectively. In the following paragraphs, each of the three key variables (A, n, B) is determined for the experiments performed herein, and their meaning and implications on plasticity are subsequently discussed. The values of each variable used to fit the ODS and pure Fe data are summarized in Table 6.1.

Stress proportionality constant – The stress proportionality constant, A, for the as received and proton irradiated ODS are 3324 and 3546, respectively. In comparison, the pure Fe has a stress proportionality constant of 720. This constant is tied to the bulk flow stress. The difference between the ODS and pure Fe can be primarily understood through the addition of solid solution strengthening to the ODS [15,16]. Hence a larger flow stress is required to continually plastically deform the ODS than the pure Fe.

Stress exponent – The stress exponent n, has values 0.12 and 0.06 for as received and proton irradiated ODS, respectively. Direct empirical measurements in the literature show n varying 0.2-0.5 for bcc metals depending on orientation and loading conditions [84], which is notably higher than the values determined here. However, Dunstan and Bushby [174] argue that the stress exponent is an arbitrary value, controlled by the sample dimension and the flow strain, rather than any fundamental mechanism. Rather than compare stress exponents across experiments in the archival literature, they suggest relating the sample dimensions (w) and flow strain (c) from the experimental conditions to calculate an expected stress exponent range:

$$n = \frac{1.5/w}{(c + 1.5)/w} \qquad \text{Equation 6.4}$$

In this study, the flow strain measured at the notch varies from 0.06 to 0.53 for both as received and proton irradiated cantilevers. Using the minimum and maximum values for beam heights of 140 and 515 nm for w, Equation 6.4 predicts a stress exponent range of 0.01-0.15, which is consistent with n values fit to our empirical data in Figure 6.1.

Offset factor – The pure Fe and ODS exhibit the most notable difference in behavior when considering the offset factor B. Specifically, B can be taken to be 0 in pure Fe (i.e. per Equation 6.3), 8.5 nm/nm for the as received ODS, and 9 nm/nm for the proton irradiated ODS. This difference in B values is likely attributed to differences in deformation mechanisms

between pure Fe and ODS, which are associated with the influence of the varying obstacle and source spacings on dislocation motion. For instance, pure Fe has a low dislocation source density (i.e. high dislocation source spacing), and dislocation-dislocation interaction is minimal. The grain size is such that Rogne's pillars [81] are often fully contained within a single grain. The material plasticity is limited by dislocation glide on available slip planes without grain boundary interactions or constraints from neighboring grains [16]. In contrast, the Fe-9%Cr ODS has a considerably lower obstacle spacing than pure Fe; as such, dislocation-dislocation interactions as well as dislocation interactions with oxide nanoclusters and irradiation-induced dislocation loops and voids are plentiful. In the Fe-9%Cr ODS microstructure, dislocations must bow around obstacles and/or cross-slip in order for plasticity (i.e. flow) to continue, and the plastic zone is increasingly confined. Further, since the ODS grain size is on the order of 200-300 nm, the studied cantilever beams can contain multiple grains. This suggests that the resolved shear stress and dislocation mobility at the notch could be affected by adjacent grains having high Schmid or Taylor factors. This argument can be visualized by considering a fixed nano/microscale specimen volume but containing low (B~0-1) or high (B>8) source/obstacle spacing; the reader is referred to the cartoons overlaid on Figure 6.1 for a pictorial representation. The offset factor B must be considered in flow stress testing of more complex materials, to account for the increased complexity of dislocation slip, constraints, and the associated consequences of these complexities on the deformation mechanisms.

6.1.3   Size Effect Summary

A summary of size effects in small-scale testing is provided in Figure 6.2. Here minimum dimension is plotted against obstacle spacing for a variety of materials and testing geometries. These include irradiated Cu [78], Cu-10Ta [175], MA6000 [85], Ni [176,177], Fe [81], and LiF

[178] micropillars. Other geometries include work on pure Cu cantilevers [118] and Ni films [179]. This plot demonstrates that as obstacle spacing reduces, the allowable minimum dimension to avoid size effects also reduces. As obstacle spacing increases (towards perfect crystallinity) the minimum allowable dimension becomes increasingly large. Included is the micropillar and cantilever work conducted on the Fe9%Cr ODS. This phenomena holds with existing literature, where materials with increased obstacle density enable smaller sized samples to be tested [174,180]. The data in Figure 6.2 demonstrates that electron transparent extrinsic dimensions require intrinsic dimensions on the order of nanocrystalline and/or irradiated material. Therefore, using in situ TEM mechanical testing on as received and irradiated Fe-9%Cr ODS results in meaningful measurements of mechanical properties.

This relationship is further elucidated when we look specifically at the context of the B factor in the cantilever power law relationship (Equation 6.3). Because of their differences in *B* values, the size effect threshold occurs at a larger normalized minimum dimension for the ODS than for pure Fe. This normalized minimum dimension is essentially the slope of a line on a plot of the minimum allowable specimen dimension (i.e. extrinsic size) versus obstacle spacing (i.e. internal microstructural size), as shown in Figure 6.2, after ref. [180]. Specifically, two lines having slopes 1 and 10 are shown on Figure 6.2 as an attempt to bound the observed *B* values for pure Fe (*B*~0) and Fe-9%Cr ODS (*B* = 8.5-9). These lines show that as obstacle spacing is reduced, the allowable minimum dimension to avoid size effects also reduces; likewise, as obstacle spacing increases (towards perfect crystallinity) the minimum allowable dimension becomes increasingly large. This is consistent with observations in the archival literature that suggest that progressively smaller specimen geometries can be used to obtain meaningful mechanical properties in materials having increased obstacle density [78,81,180,85,118,174–

179]. Notably, size effect threshold data points from pure materials fall closer to the line having slope of 1, whereas materials of increasing complexity fall closer to the line having slope 10. This observation corroborates the idea that the shift in **B** from 0 to ~9 with increasing material complexity is due to fundamental differences in deformation mechanisms inherent to more complex materials. These complexities are not fully captured with the parameters of Equation 6.1 (original power law), thus requiring the offset factor **B** to fit the size effect power law for more complex materials, i.e. Equation 6.3. Consequently, the non-normalized minimum dimension for meaningful flow stress measurements in Fe-9%Cr ODS is 180-190 nm, whereas that for pure Fe is a factor of five larger at 900 nm. This can be visualized in Figure 6.2, where minimum dimension (non-normalized) is plotted against obstacle spacing. Normalized allowable minimum dimension is the slope of a line drawn on Figure 7 – we show slopes of 1and 10 to approximately bound the behaviors of pure Fe and ODS, respectively.

6.2 Clamped Beam Fracture

While fracture toughness values for the clamped beams generally fall within bulk literature values (§5.3), two questions arise. First, what is the nature of the size effect and its impact? Secondly, does this technique afford fine enough resolution to describe differences in the fracture behavior of the irradiated conditions? To answer the first question, this section will consider the impact of large-scale plasticity at the notch and notch radius on fracture toughness. Then to understand the resolution of this technique, fracture toughness results will be compared to the microstructurally predicted changes in material toughness.

Generally small-scale testing finds elevated measurements of properties like yield strength and flow stress due to the interaction of intrinsic and extrinsic material dimensions [17]. In the

case of fracture toughness, however, the results herein, fall on the low side of literature results, suggesting an underestimation in the material property. We attribute this to the impact of large scale plasticity in the sample. ASTM standards for fracture toughness require dimensions such that the width to thickness ratio (*W/B*) falls between 1 and 4 for single edge-notched beams [181]. This is to ensure that the plastic zone size around the crack is very small, relative to an infinite-sized plate (Figure 2.11). This allows for linear elastic fracture mechanics to be used. For in situ TEM fracture testing, samples do not meet this criterion. The *W/B* ratio for the beams in this study is 5. As such, we use the J-integral approach to account for some plasticity. Even still, there may be large scale factors that are unaccounted for in the J-integral approach. As such the large plastic zone size results in a more brittle material, with a lower calculated fracture toughness than that from bulk-scale testing.

An additional concern is the notch tip radius. As the notch tip radius governs the stress intensity, it can impact the fracture toughness, especially in small-scale testing [125]. Due to variability in the FIB notching, the notches on the clamped beams were not of a purely uniform size. Figure 6.3 plots the $K_{Q,J}$ values for each fractured beam as a function of notch tip radius. Generally, large notch tip radii had correspondingly large fracture toughness values. Yet the trend did not hold across all material conditions, specifically the Fe^{2+} 3 dpa; these beams had a fairly consistent notch tip radii centered on 40 nm ± 10 nm, but resulted in a wide range of $K_{Q,J}$ values ranging between 8-21 MPa $m^{1/2}$.

Another concern regarding the notches, as discussed in work by Best et al [137] relates to the FIB ion damage. In the work, Best compares Ga^+ FIB notches with Xe^+ and He^+ FIB notches, finding higher K_{IC} values for the Ga^+ FIB notches. They speculate that this increase could be due to residual stresses due to the ion implantation [137]. This dissertation solely used Ga^+ to create

the notches. Yet the resulting $K_{Q,J}$ values are on the low end of the expected bulk fracture toughness values. This, along with the non-determinative results of notch tip radius (Figure 6.3), lead the authors to suggest that any impact from FIB damage on the notch, and the size of the notch, is superseded by the small specimen dimensions; where the plastic zone is large, as compared to ASTM standards [181].

As discussed in §4.2, a study of the microstructure was conducted. This data will be used to understand the impact of dislocation loop size and density or oxide nanocluster density on the fracture properties of the four material conditions. Figure 6.4A contains a summary of the oxide nanocluster distribution in the materials, while 6.4B contains the dislocation loop data. The data is split into number, diameter, and density categories first, and then by material condition. Diameters for both oxide nanoclusters and dislocation loops remain consistent across material conditions. As such, the detailed look at each will focus on the number and density within each material.

Oxides contribute to the temperature stability of the material, but literature values for their dispersed barrier obstacle strength, α, are an order smaller than those of dislocation loops (0.03-0.06 vs 0.17-0.33) [50,182]. As such, they are not the major contributor to retarding dislocation motion and play a minor role in making the material more brittle. Yet, with mechanical alloying, there is some thought that the oxide nanoparticles can contribute to porosity and degrade the impact properties of a material by acting as sites for crack nucleation [183,184]. The two material conditions with a considerable increase in oxide number over as received conditions are Fe^{2+} 100 dpa and proton irradiated; and they behave in two different ways. The proton irradiated condition results in $K_{Q,J}$ values similar to the as received condition. In contrast, the single Fe^{2+} 100 dpa fracture has the lowest $K_{Q,J}$ value, an order of magnitude less than the as received

material. This contradictory data could be a result of the uneven dispersion of the oxides within each beam at such small specimen volume. Work by Hoelzer et al. finds a reduction in mechanical properties with a less fine distribution of the oxides within various Fe-Cr alloys [32]. Ultimately, it is hard to determine if the oxide nanoclusters play a role, if any, in the fracture properties due to limited sample size.

The dislocation loop diameter remains consistent across material conditions. Dislocation loop number and density increase from the Fe^{2+} at 3 dpa to the 100 dpa by ~125 and 2×10^{21} m^{-3}, respectively. The proton irradiated condition has a large increase in number (~200 to 700) and in density (~3×10^{21} m^{-3} to 10×10^{21} m^{-3}). Dislocation loops play a significant role in retarding dislocation motion and can contribute significantly to the DBH prediction. Yet at the 500°C irradiating temperature, the DBH model predicts a small increase in yield strength of 21 MPa for the proton irradiated condition and softening of 131 MPa and 33 MPa for the Fe^{2+} 3dpa and 100 dpa conditions, respectively. All these values are of negligible change, considering a bulk yield strength of 1200 MPa, yet generally, the fracture toughness has an inverse relationship to yield strength [20]. As such, if we saw a change in the fracture toughness corresponding inversely to the change in irradiation hardening, we would expect the proton irradiated beams to exhibit lower fracture toughness values, with the Fe^{2+} irradiated conditions having higher fracture toughness than the as received. This is not what is observed.

Finally, as the ASTAR and EDS results show in Figure 5.12 and Appendix C, the gross microstructure – number of grains or the presence of a precipitate at the notch dominate the fracture behavior of each beam. Beams with grain junctions near the notch can accommodate more plastic strain than single crystals and crack growth is slowed or halted in these beams [151,185–187]. At this point the stress intensities at the clamped edges drive crack growth or

shearing due to the applied load. Additionally, precipitates along the notch axis of beams contribute to a more brittle fracture than single crystals. This is observed in the 2 beams (one Fe^{2+} to 3 dpa and one proton 3 dpa) which have two of the lowest $K_{Q,J}$ values.

Though these gross microstructural features drive fracture behavior, it must be stated that the sample size of this clamped beam work is too small to quantitatively understand the changes in fracture properties due to irradiation. This is supported by literature results suggesting hundreds of samples must be tested to fully characterize the mechanical properties at small-scale [188]. Yet 16 clamped beams were successfully fractured in situ TEM for the ductile Fe-9%Cr ODS, with results approaching the bulk literature values (12 – 30 MPa $m^{1/2}$) for Fe-Cr ODS [56]. As such, this component of the dissertation is a foundation and proof of concept for future in situ TEM fracture work on engineering materials.

6.3   Lamellae Indentation

6.3.1   Irradiated Microstructure and Expected Visibility

The Fe^{2+} 3 dpa at 500°C irradiated microstructure for the Fe-9%Cr ODS is reported in §2.3.3and summarized in Table 2.2. Whether dislocation motion can be observed in both the original TEM videos and/or the heatmap videos is dependent on the material strain and the frame rate of the camera. At high strain rate (>10^5 s^{-1}), dislocation motion is known to be supersonic [16,189]. Given that the indentation performed in this study is at a strain rate of 0.04 s^{-1}, a medium strain rate (10^{-4} s^{-1} < $\dot{\varepsilon}$ < 10^{-2} s^{-1}) as defined by Chawla and Meyers [16], we can assume that the dislocations move slower than the longitudinal wave velocity (C_L). The longitudinal and transverse (C_T) wave velocities in steel are ~5700 m/s and ~3200 m/s, respectively [190,191]. The videos used in this study are captured at a frame rate of 30 frames per second, resulting in a

time delay of 0.033 seconds between frames. The maximum distance that dislocations traveling at the wave velocity can travel between two frames is 188 m, which is much larger than the size of a lamella. However, by visual inspection of the videos, foreground objects move <50 nm in one second, suggesting that the moving objects in the video are more likely the result of moving dislocation aggregates or changes in grain orientation due to bending, rather than individual dislocation emissions.

The expected behavior of other microstructural features under loading can be ascertained from the literature, based on how they are known to interact with dislocations (regardless of whether those dislocations can individually be discerned). Oxide particles, carbides, and dislocation loops will act as barriers to dislocation motion and can either be sheared or overcome through dislocation climb depending on their strength [15]. For oxide particles, the dispersed barrier obstacle strength, α, is expected to be low (0.03-0.06) [50,182], hence it is expected that dislocations will shear through them [117,182,192,193]. Oxide particles have limited Z-contrast against the alloy matrix [157]; this generally precludes the visibility of oxide particles by conventional bright field TEM in materials such as this Fe-9%Cr ODS which has an abundance of irradiation damage defects and dislocation loops, dislocation lines, and nanoscale grains that create a highly-contrasting, complex microstructure. Hence, the oxide shearing process is not likely to be identified by MicroViBe.

Dislocation loops, on the other hand, are stronger barriers to dislocation motion, with α ranging 0.17-0.33 [50,182]. In bcc Fe-Cr, dislocation loops generally have one of two burgers vectors, **b**= ½ <111> or **b**=<100>, and they reside on the {111} or {200} habit planes, respectively [47]. The slip direction in bcc Fe is along the <111> direction. Studies simulating the interaction between dislocations and dislocation loops demonstrate differences in the strength

of the interaction depending on the loop burgers vector [195–197]. Loops of **b**= ½ <111>

provide a stronger barrier to dislocations than loops of **b**=<100> [195]. Of the total loop

population in the subject ODS alloy, 55-70% are of the **b**= ½ <111> type [50].

The MicroViBe algorithm identifies changes in the Laue contrast of features visible in the

bright field TEM video. For loops, visibility is a function of the grain orientation relative to the

electron beam. These loops are visible on the [111] and [001] zone axes in two beam conditions,

and while using the STEM technique discussed in §4.2 [43]. Their visibility is variably limited in

the conventional bright field imaging conditions with sub-optimal tilt, as utilized during the

indentation testing. While loop visibility is secondarily a function of their size, the average loop

size in the subject ODS is within TEM resolution limits. Hence, the MicroViBe foreground is

likely to include some combination of aggregate dislocation interactions with dislocation loops,

whereas the background will likely include the unaltered lattice and oxide particles.

6.3.2   Post-Mortem TEM Analysis

In the original TEM indentation video, lamellae are not tilted prior to imaging or

indentation, so grains are not necessarily oriented at their optimal imaging conditions. For

example, **g·b** criteria are favorable for dislocation loop visibility in the [111] grain in Lamella 1

and the [001] grain in Lamella 2, especially in a two-beam condition. On the other hand, all other

grains in these lamellae are oriented such that dislocation loops cannot be seen (or can be seen

only weakly) due to the **g·b** invisibility criterion. By loading the indented sample into a double

tilt holder, the lamella can be oriented such that the zone axes, either [111] or [001] can be

imaged using the STEM technique outlined in §4.2, providing the most unobstructed image of

the dislocation loops within the grains of interest.

Using the grain orientations from ASTAR as a map, on-zone axis STEM imaging can provide improved understanding of the MicroViBe hotspots and the dislocation loops strengths. STEM images of dislocation loops are taken in grains already near the favorable axes (i.e. [111] and [001] zone axes); these grains are grain 3 in Lamella 1 and grains 2 and 3 in Lamella 2. While grain 2 in Lamella 1 is near the [111] zone axis, it is too darkly contrasting to effectively image loops, even in STEM mode; the same is true for the left region of grain 1 in Lamella 2. Figures 6.5 and 6.6 show for Lamellae 1 and 2, respectively: the (a) final heatmap from each lamella; (b) an original TEM video frame from the conclusion of the indentation, with boxes denoting the locations of subsequent STEM images shown in (c) and (d); and (e) the ASTAR grain orientation map of the lamellae after indentation. In each of the STEM images (Figures 6.5c-d and 6.6c-d), dislocation loops are identified with circles and numerical labels. Positions on the MicroViBe heatmap that are coincident with STEM-observed loops are indicated in Figures 6.5a and 6.6a with the corresponding numerical labels.

In Lamella 1, two STEM images are taken of grain 3 on the [111] zone axis. The five loops identified (Figures 6.5c-d and 6.6c-d) are circular in shape. Loop orientation maps for Fe-Cr alloys [43] can be used to determine the loop habit planes: in Figure 6.5d, the [111] zone axis loop orientation map is overlaid and indicates that the circular loop is of the (111) habit plane [43]. All five loops in the STEM images for Lamella 1 have **b**=½ <111>, which is coincident with the <111> slip direction in bcc crystals. Dislocations will interact with loops along this slip direction, driving changes in Laue contrast that can then be detected by the MicroVibe algorithm [195]. All five loops therefore correspond to a hotspot position on the heatmap (Figure 6.5a).

In Lamella 2, STEM images are taken of grains 2 and 3 on the [001] zone axis. Again, the loop orientation map is overlaid in Figure 6.6d. Here, loops 1 and 2 (Figure 6c) appear circular,

suggesting their habit plane is (200) with **b**=<100>. These loops have a weak interaction with dislocations on the slip plane, and therefore may not create any detectable Laue contrast changes [195]. Indeed, the positions of these loops do not correspond to any hotspots in Figure 6.6a. The remaining loops (Figures 6.6c-d) can be characterized as residing on the (111) habit plane for loops 3-6, or on the (11$\bar{1}$) habit plane for loops 7-9. Both of these habit planes have **b**= ½ <111>, so these loops all interact with dislocations and are detected by MicroViBe. It follows that loops 3-9 all correspond to a hotspot position on the heatmap (Figure 6.6a).

In summary, the MicroViBe heatmap is capable of detecting dislocation loops residing on the (111) habit plane with **b**= ½ <111> in the subject ODS alloy. The interaction between these loops and dislocations slipping in the <111> direction, produce Laue contrast that is detected by the MicroViBe algorithm. By comparison, the loops on the (100) habit plane do not correspond with the bcc <111> slip direction, so there is no detectable Laue contrast change during indentation [195]. The **b**= ½ <111> loops correspond to MicroViBe hotspots as long as they have some degree of visibility (i.e. not entirely invisible based on **g·b** criteria) in the original TEM video due to their interaction with dislocations. While these dislocation loops may not always be readily discernible in the TEM original video, due to the grain orientations and surrounding Laue contrast from the surrounding microstructure, the MicroViBe algorithm clearly identifies these loops.

6.3.3   Loop Analysis and Strength

Because dislocation loop counting is known to be a subjective task and results can vary between experimenters [198], we now attempt to utilize the MicroViBe algorithm to provide a more objective and consistent method to identify dislocation loops. We compare the number density of dislocation loops as previously characterized by STEM (on an unindented lamella) [6]

with the number density of hotspots on the indented lamellae. For the purpose of this exercise, we assume all hotspots correspond to mobile dislocation loops or obstacles with similar strengths to these loops (e.g. stronger oxide particles [117,192]).

Using the heatmap histogram of pixel changes, a threshold of the top 2% of those heatmap pixels exhibiting the greatest amount of change throughout the video gives a hotspot number density of 7.8×10^{21} m^{-3} in Lamella 1, and 4.72×10^{21} m^{-3} in Lamella 2. These values are of the same order of magnitude, though 2-4 times larger, than the STEM dislocation loop number densities (Figures 6.5c-d and 6.6c-d) of 1.04×10^{21} m^{-3} and 1.98×10^{21} m^{-3} for Lamella 1 and Lamella 2, respectively. These STEM loop number densities are consistent with the value of 2.1×10^{21} m^{-3} previously measured in the same alloy/condition on an un-indented lamella [6].

Differences in heatmap number density and loop number density arise because not all hotspots in the heatmap necessarily correspond to a dislocation loop – some of the hotspots may be associated with dislocation lines, subgrain boundaries, or bend contours that are not clearly resolvable in the post-mortem STEM images. It is also plausible that some of the hotspots not associated with loops may be attributed to oxide particles. However, the dispersed barrier obstacle strength, α, of dislocation loops (0.17-0.33) is much larger than that of the oxides (0.03-0.06), particularly in the subject ODS alloy [50,182]. Hence, the oxides will likely be sheared by dislocations [117,182,192,193] and not identified by the MicroViBe algorithm. Thus, the hotspot number density can provide a reasonable estimate of the magnitude of the dislocation loop density, although it may also include other obstacles or features with similar strengths as loops.

Table 6.1 – Values for the stress proportionality constant, *A*, minimum dimension/obstacle spacing offset, *B*, and the stress exponential, *n*, from power law fits of the pure Fe And ODS data

	Stress Proportionality Constant (*A*)	Minimum Dimension/ Obstacle Spacing Offset (*B*)	Stress Exponential (*n*)
Pure Fe	720	0	0.6
As Received ODS	3546	8.5	0.12
Proton Irr. ODS	3324	9	0.09
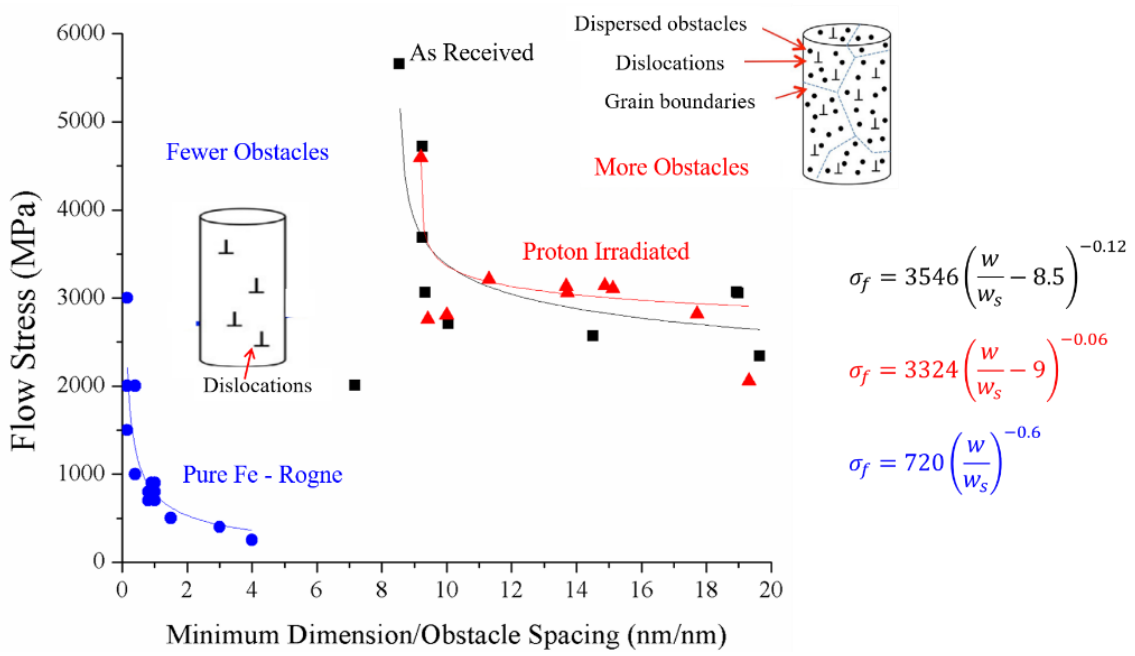
Figure 6.1 – Flow stress as a function of normalized minimum dimension for (a) pure Fe micropillars [81] and (b) as received and (c) proton irradiated Fe-9%Cr ODS cantilevers. The as received and proton irradiated charts include the logarithmic relationship for both
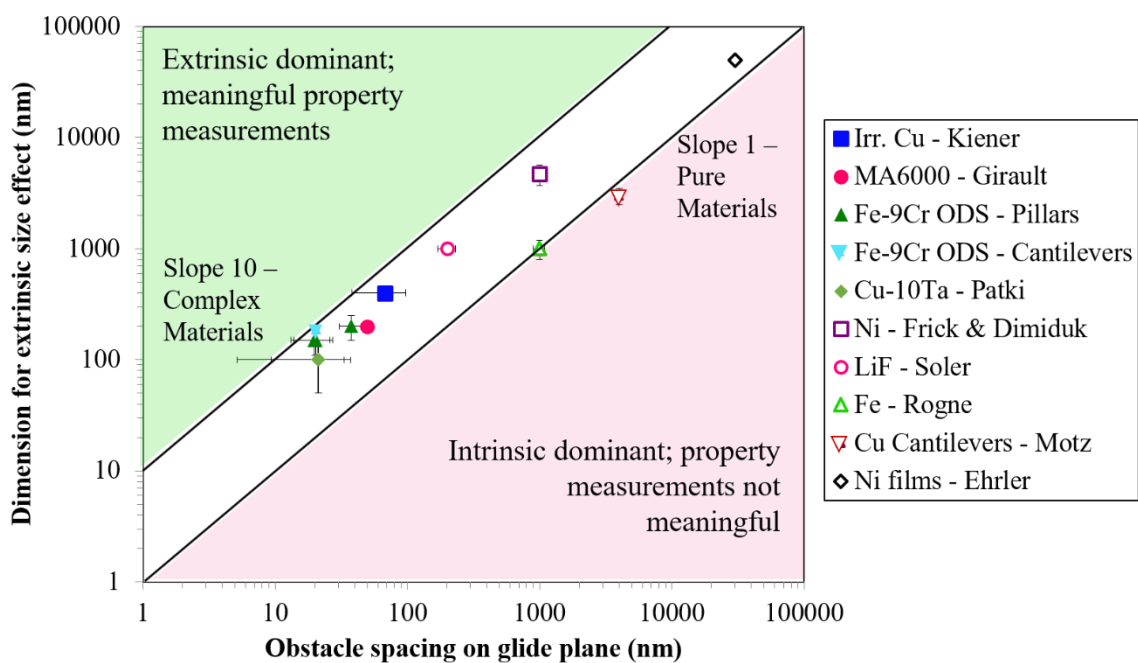
Figure 6.2 – Minimum dimensions vs obstacle spacing for a variety of literature materials [78,81,85,118,175–179] and this study's Fe-9%Cr ODS micropillars and cantilevers. Pure materials designated with an open symbol, complex materials with a filled symbol
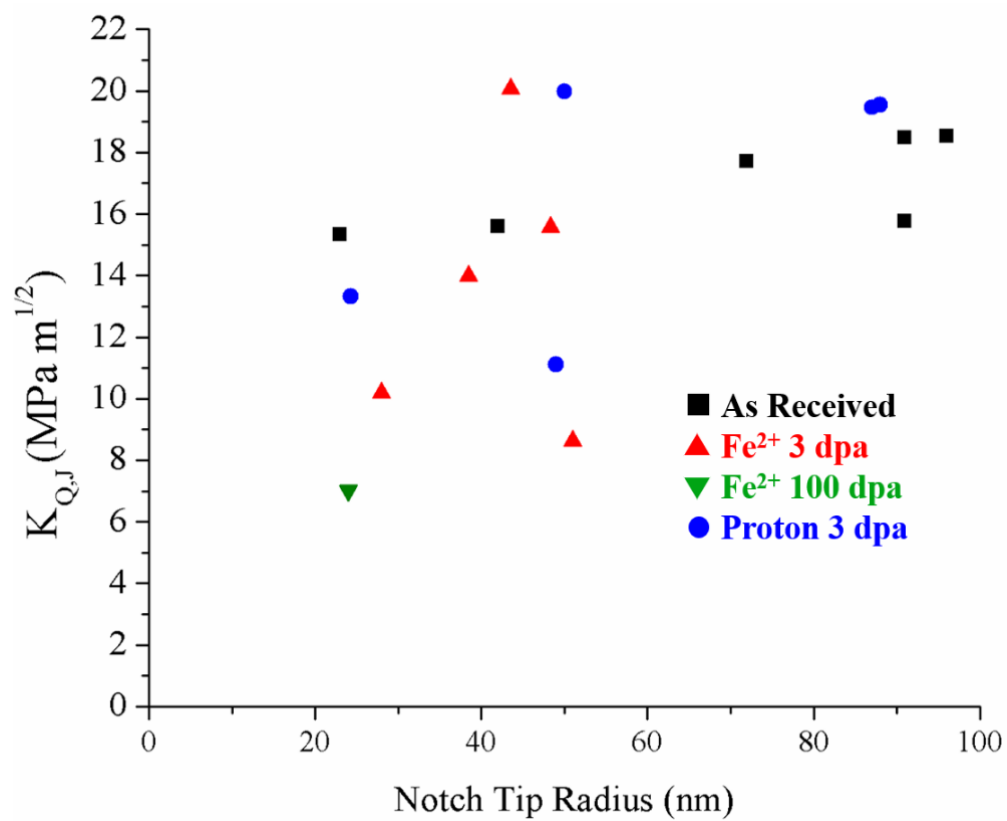
Figure 6.3– Fracture toughness of clamped beams as a function of the notch tip radius. Though larger notch tips had higher KQ,J values, this impact was not observed across material conditions
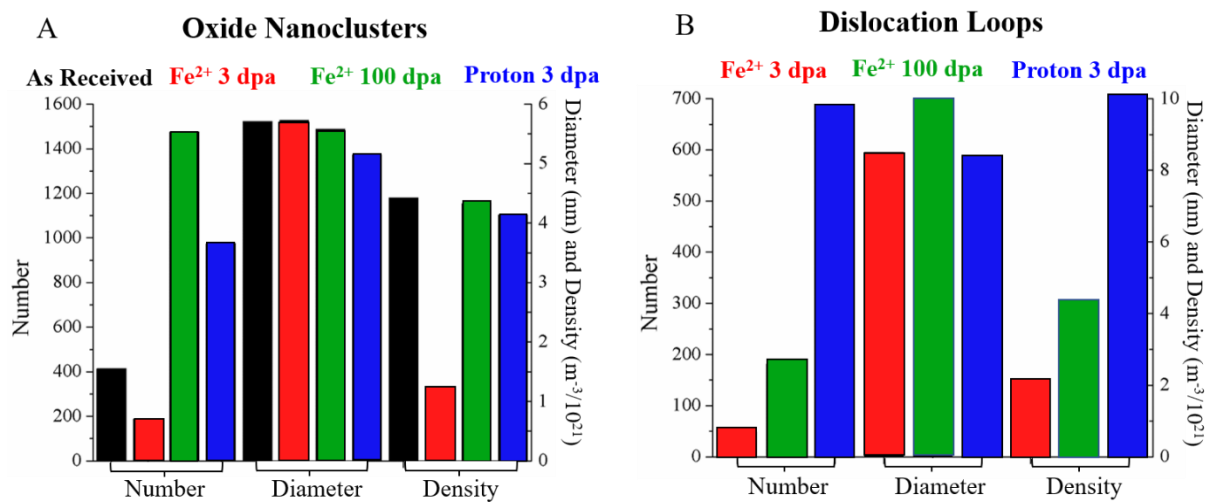
Figure 6.4 – Microstructural data for each material condition for the (a) oxides and (b) dislocation loops
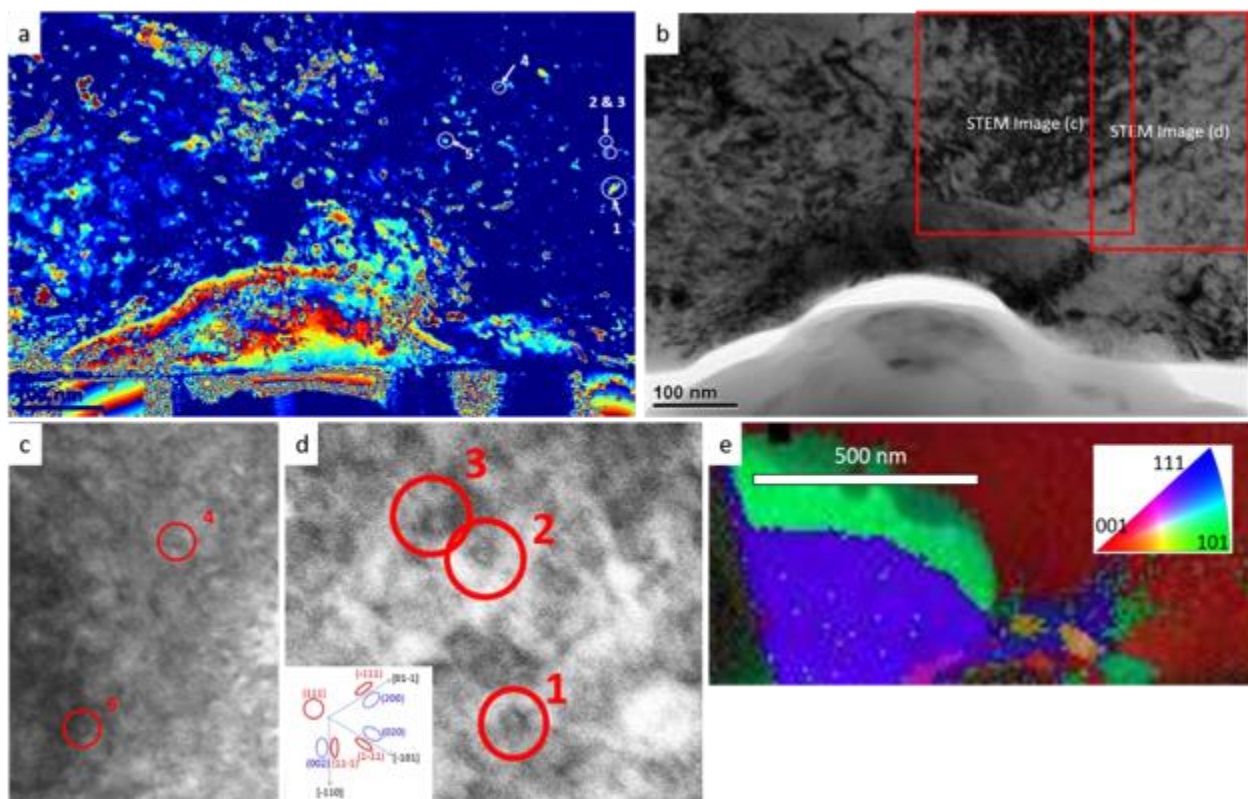
Figure 6.5 – Lamella 1 indentation shown in (a) final heatmap, (b) final image after indentation, (c-d) STEM images of respective areas identified in 5b showing dislocation loops, and (e) ASTAR image of entire lamella area above indentation
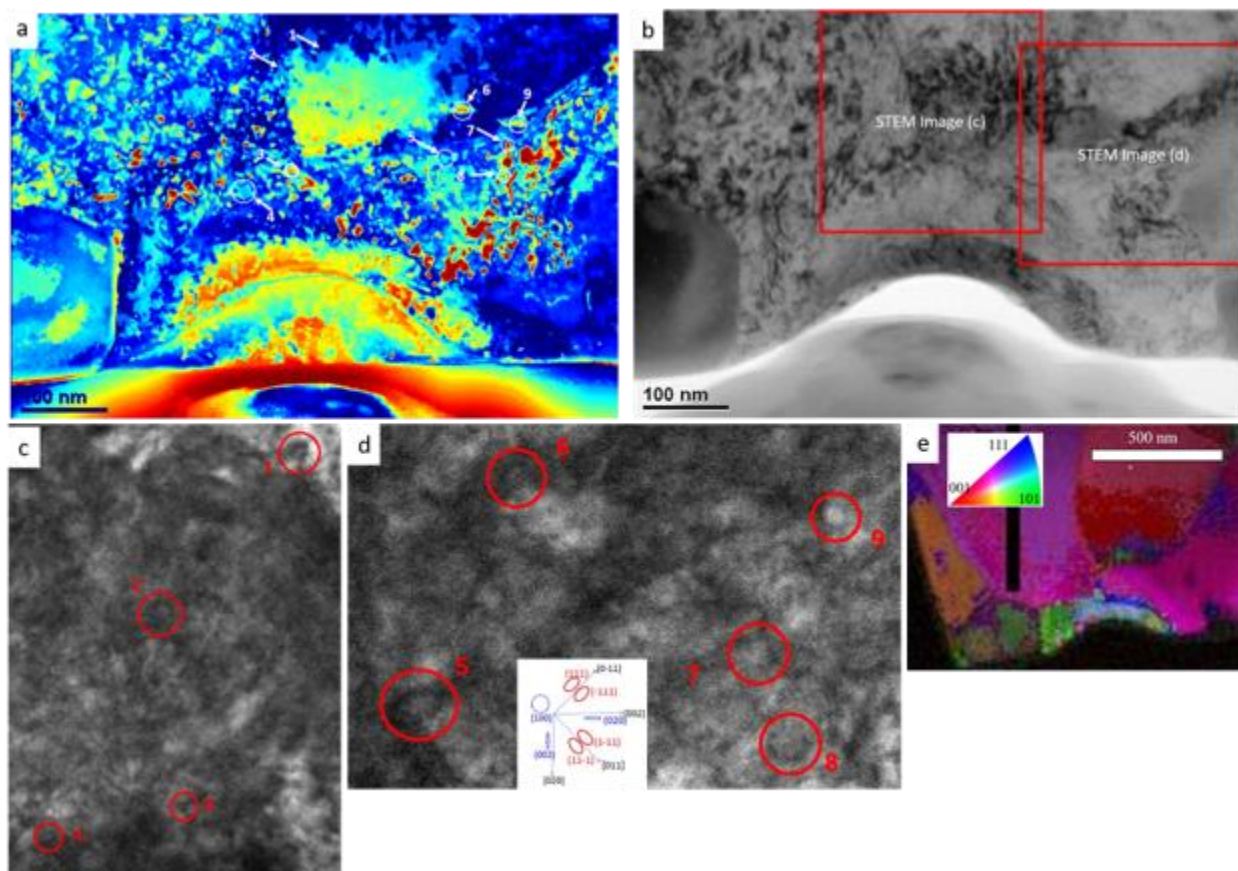
Figure 6.6 – Lamella 2 indentation shown in (a) final heatmap, (b) final image after indentation, (c-d) STEM images of respective areas identified in 5b showing dislocation loops, and (e) ASTAR image of entire lamella area above indentation

7. CONCLUSIONS AND RECOMMENDATIONS

This thesis has reached the following conclusion:

For as received and irradiated Fe-9%Cr ODS, the relationship between extrinsic and intrinsic dimensions can be defined such that size effect can be precluded during in situ TEM mechanical testing.

This conclusion is supported by the following sub-conclusions:

1) The yield strength and elastic modulus of Fe-9%Cr ODS micropillars can be determined using in situ TEM compression with supplementary finite element modeling. Micropillars of dimensions varying between 100-600 nm in width, height, and thickness of as received and Fe^{2+} irradiated to 3 dpa and 100 dpa at 500°C Fe-9%Cr ODS were compressed in situ TEM. Load-displacement curves were collected and converted to stress-strain using in situ dimensional measurements. From the stress-strain curves, yield strength was acquired. Finite element modeling accounted for the deformation in the base of the micropillars, resulting in elastic modulus values. Both yield strength and elastic modulus values were within expected bulk literature values.

The obstacle spacing in the 3 material conditions of Fe-9%Cr ODS was determined through prior TEM and APT characterization work. The obstacle spacing ranged from 19.9-37.6 nm. By testing at varying dimensions, a threshold, where yield strength and elastic modulus values began to inflate due to the interaction between extrinsic and intrinsic dimensions was determined. This began to occur in specimens with minimum dimension <100 nm. Hence, this work supports our main conclusion.

2) Flow stress can be determined of cantilevers in bending. Cantilevers with varying dimensions ranging between 1-2 μm in length, with height of 200-500 nm, and thickness values

of 200-300 nm, were manufactured and bent in situ TEM. Load-displacement data was collected and converted to stress-strain values using measurements of the cantilever dimensions. Flow stress values were taken from these stress-strain curves.

A logarithmic relationship was seen in the literature between flow stress and minimum dimension. This approach was applied to the cantilever flow stress where a power-law description was fitted to the data. Again, a threshold where minimum dimension and material obstacle spacing began to interact was found through varying the beam dimensions and calculating values of inflated flow stress. This threshold confirmed the micropillar results, with the minimum (extrinsic) dimension being approximately 150 nm and the obstacle spacing for as received and proton irradiated Fe-9%Cr ODS being ~20 nm.

3) Fracture properties of Fe-9%Cr ODS can be determined using a clamped beam geometry and extended finite element modeling. Four material conditions were tested: as received Fe^{2+} irradiated to 3 and 100 dpa at 500°C, and proton irradiated to 3 dpa at 500°C. Beams were fractured in situ TEM. Using a model by Wurster and extended finite element analysis to determine the stress intensity at the notch, fracture toughness values were calculated. These ranged from 8-20 MPa m$^{1/2}$ falling at the low end of bulk literature values. This underestimation can be attributed to the large plastic zone size in the small-scale samples.

Variability in fracture toughness from material condition to material condition and from beam to beam, could not be accounted for through fine differences in microstructure. Yet the presence of grain junctions or precipitates did predict fracture behavior. Notch radius did not contribute significantly to the resulting fracture properties. Future work will need to be conducted to increase sample size to better understand the variables contributing to the fracture toughness measurements.

4) Using in situ lamella indentation and MicroViBe image analysis, one can determine the strength and location of obstacles in Fe-9%Cr ODS. Two lamellae were indented and the TEM video was treated to the MicroViBe analysis. Subsequent STEM BF imaging was conducted on two grains of interest. Dislocation loops on the {111} habit plane with Burger's vector $\mathbf{b}$=1/2 <111> corresponded to hot spots on the MicroViBe analysis. Suggesting these dislocations were strong obstacles to dislocation motion on the bcc {111} slip plane. In comparison dislocation loops on the {100} habit plane with $\mathbf{b}$=<100> did not correspond to hot spots and therefore were not strong obstacles to dislocation motion. Correspondingly, oxide nanoclusters with small obstacle strength did not appear on the MicroViBe analysis.

This work is a beginning for doing in situ TEM analysis on complex materials, where the microstructure is not easily observed with the human eye during mechanical deformation. Further refinement on the MicroViBe analysis and its use on other materials is needed to fully understand its limitations and opportunities to better understand deformation mechanisms in engineering and irradiated materials.

APPENDIX A. INPUT FILES FOR ANSYS AND ABAQUS MODELS

Micropillar Compression - ANSYS

Mechanical Properties

E = 220000 MPa

Yield strength = 1200 MPa

Poisson's ratio = 0.3

Geometry input file (.txt):

"fini

/clear

/prep7

blc4,-0.0103,-0.002304,0.00241,0.003,0

blc4,-0.00929,0.000696,0.0004,0.000404,0

cdwrite,solid,,,,geom,iges"
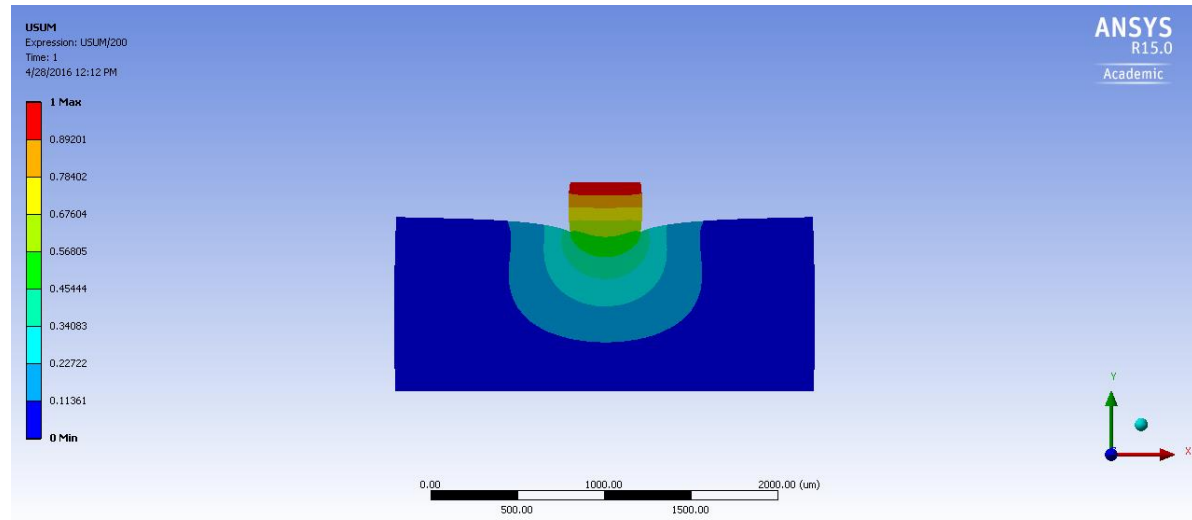
Clamped Beam - ABAQUS

Mechanical Properties

E = 220000 MPa

Max Principal Strain = 0.033

Poisson's ratio = 0.3

Part and assembly text files: https://doi.org/10.4231/SWHB-WD33
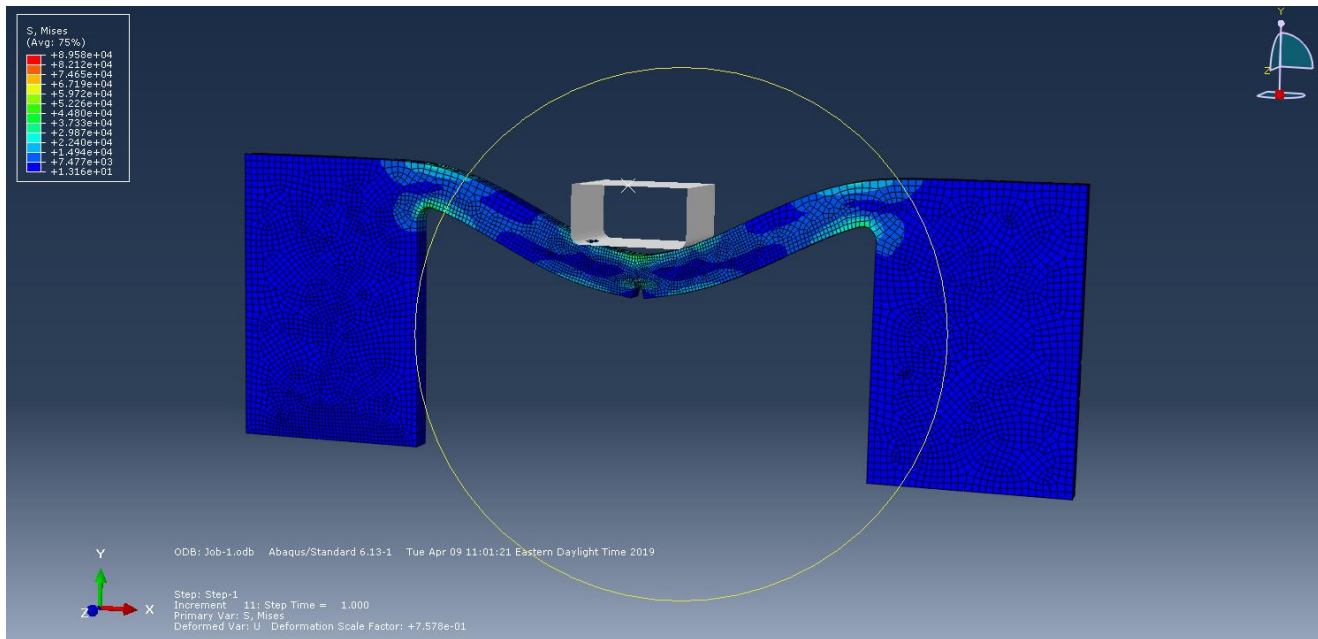
APPENDIX B. IN SITU TEM VIDEOS

In situ TEM videos are stored in online repositories. DOI numbers are provided for each set of specimens. The series is published in: https://doi.org/10.4231/100X-1R88

Micropillar Videos

As Received: https://doi.org/10.18122/B2VM5G

Fe^{2+} 3 dpa 500°C: https://doi.org/10.18122/B2QX4Z

Fe^{2+} 100 dpa 500°C: https://doi.org/10.18122/B2M41Z

Cantilever Bending

https://doi.org/10.4231/6899-GK44

Clamped Beam Fracture

https://doi.org/10.4231/M543-8C24

Lamellae Indentation

https://doi.org/10.4231/NGCG-PG03

APPENDIX C. J-Δa CURVES, ASTAR, & EDS DATA OF CLAMPED BEAMS

All J- Δa Curves
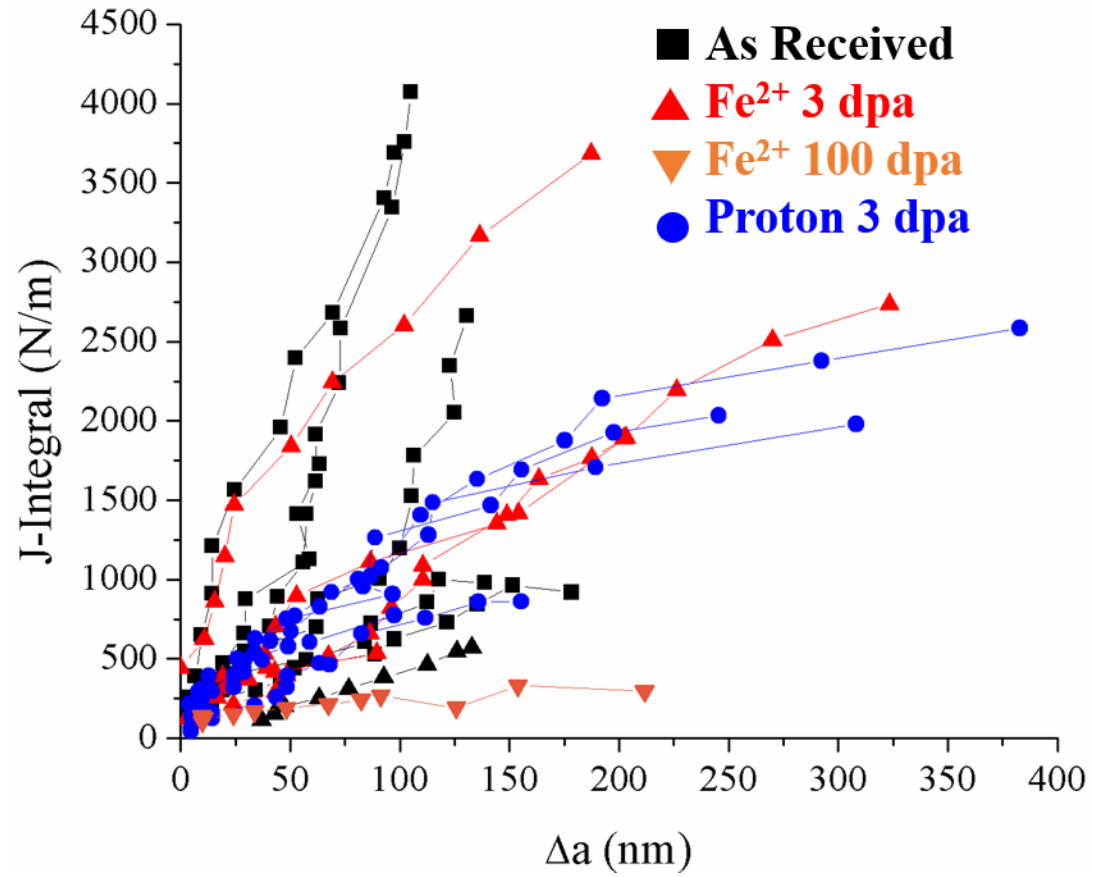
As Received – Grid 1
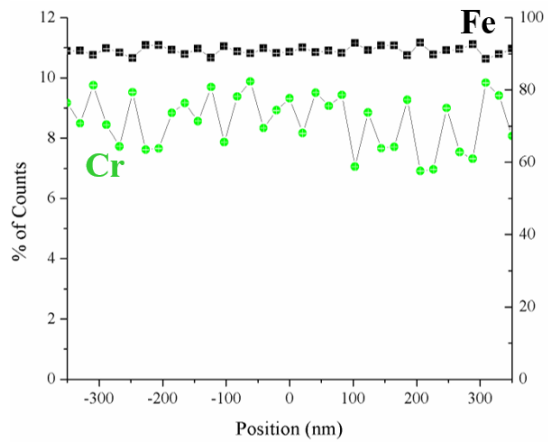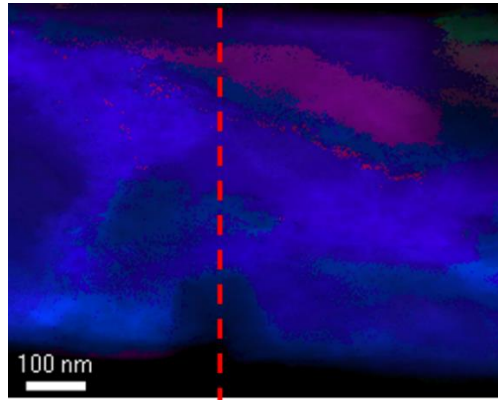
$K_{Q,J}$ = 15.3 MPa m$^{1/2}$
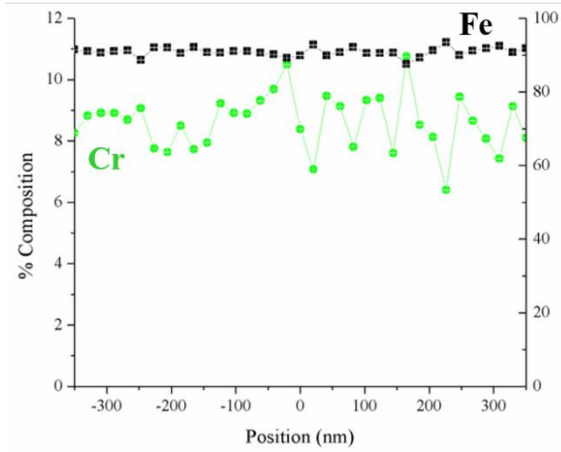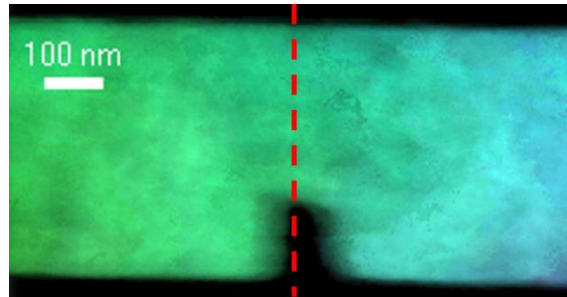
$K_{Q,J}$ = 17.7 MPa m$^{1/2}$
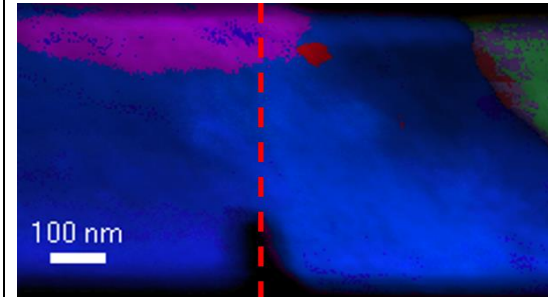
Did Not Capture EDS

$K_{Q,J}$ = 15.6 MPa m$^{1/2}$

As Received – Grid 2
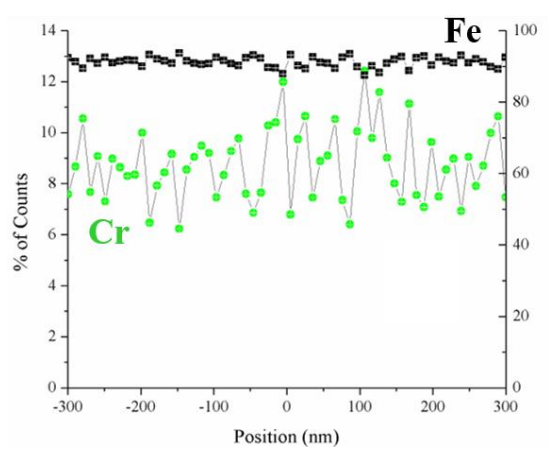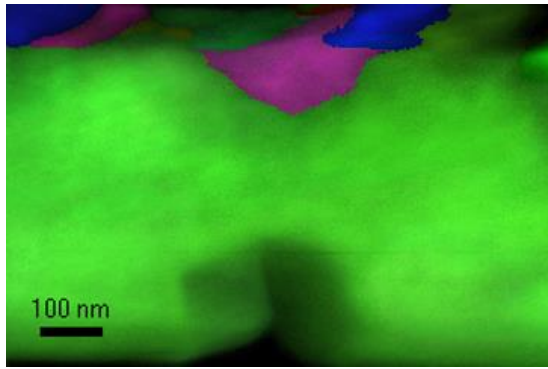
$K_{Q,J}$ = 15.8 MPa m$^{1/2}$
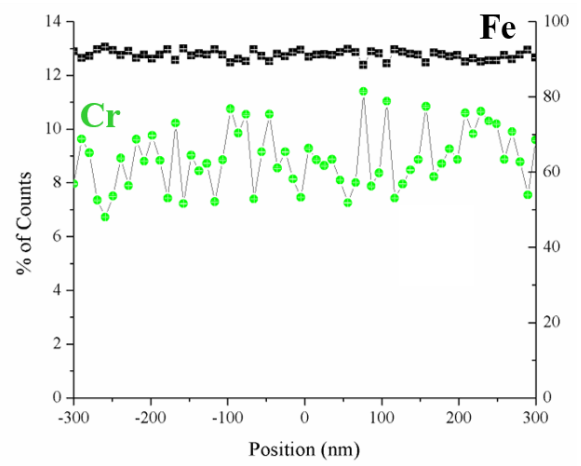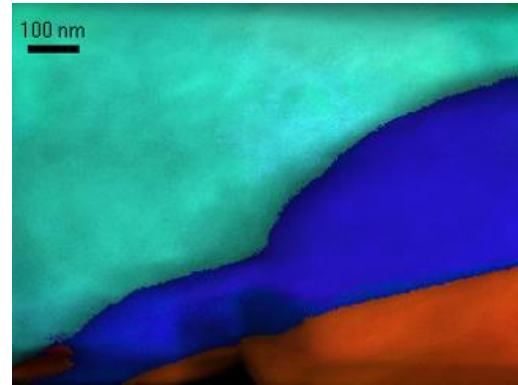
Did Not Fracture
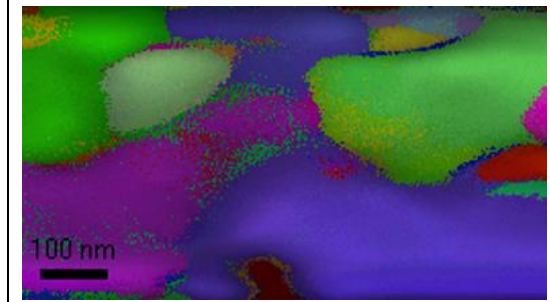
Did Not Capture EDS

Did Not Fracture

Fe²⁺ 3 dpa 500°C – Grid 1
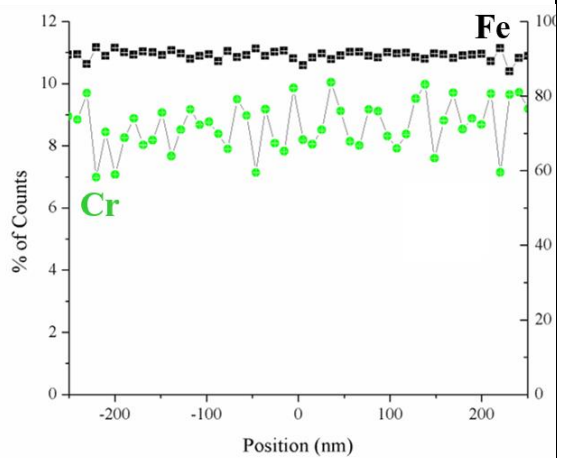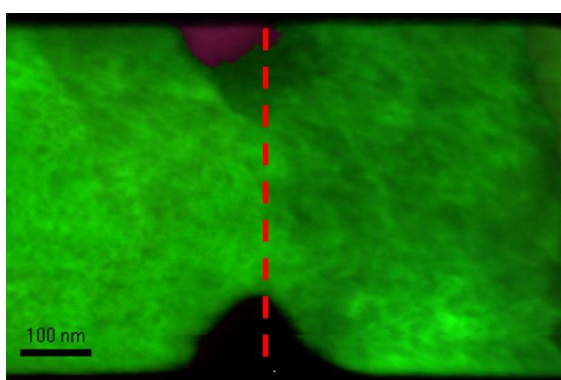
$K_{Q,J} = 8.6$ MPa m$^{1/2}$
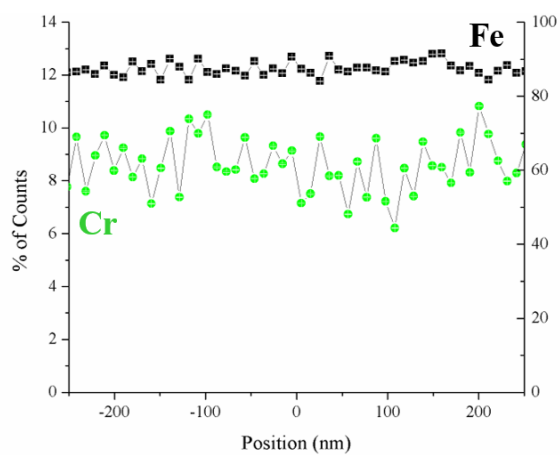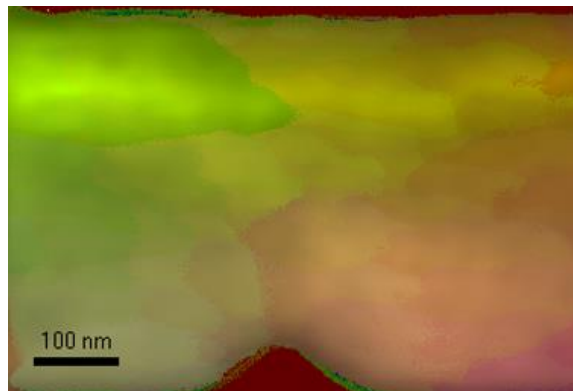
Did Not Fracture
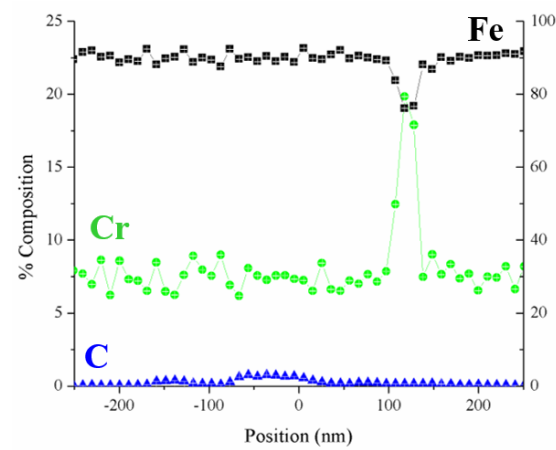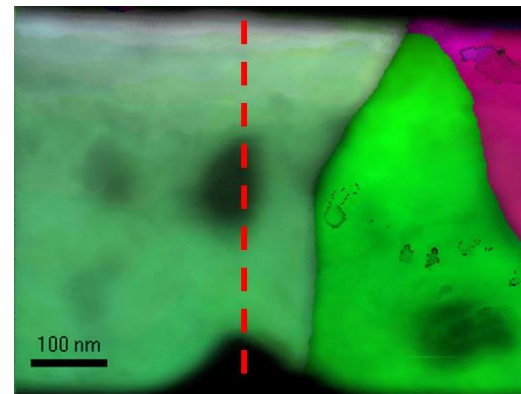
$K_{Q,J} = 10.2$ MPa m$^{1/2}$

Fe²⁺ 3 dpa 500°C – Grid 2
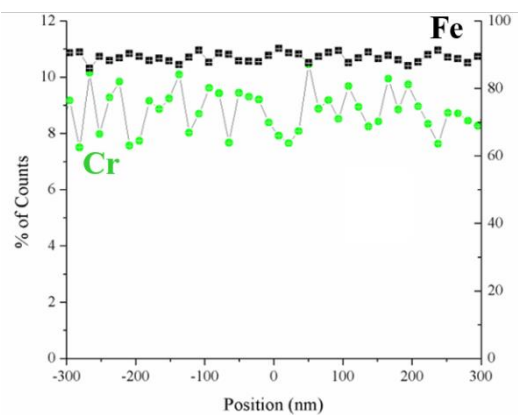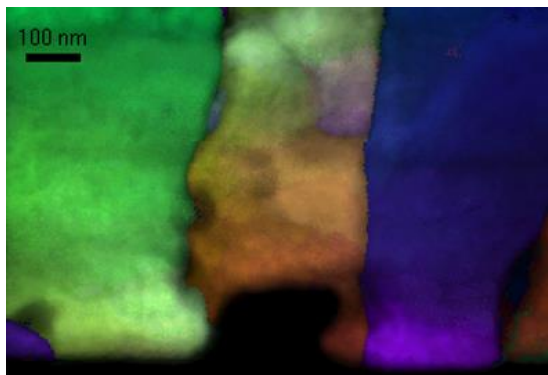
Did Not Fracture
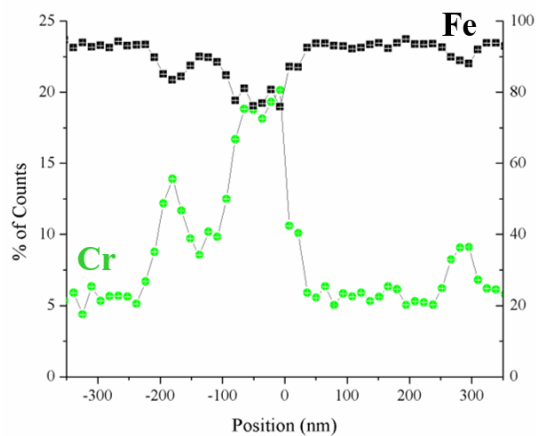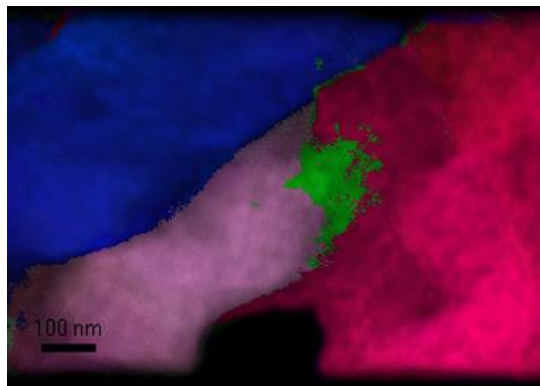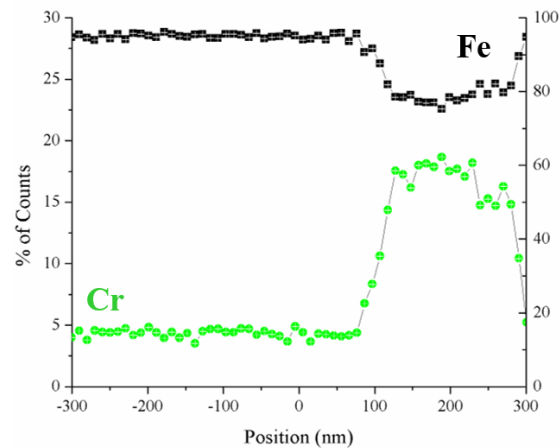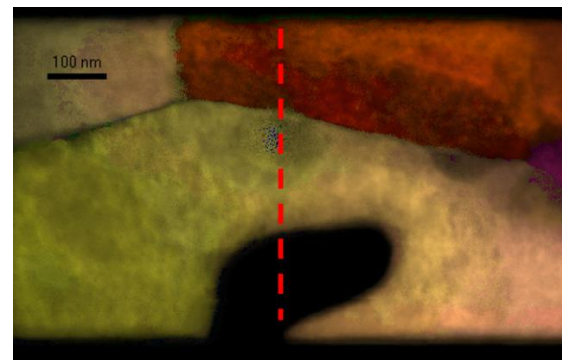
Did Not Fracture

Fractured – Did not use due to large notch

Fe²⁺ 3 dpa 500°C – Grid 3
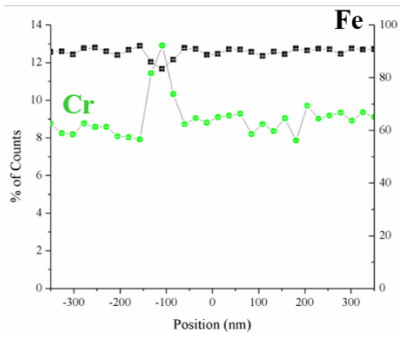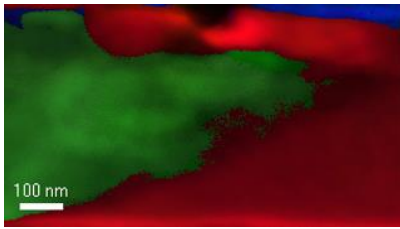

Did Not Fracture
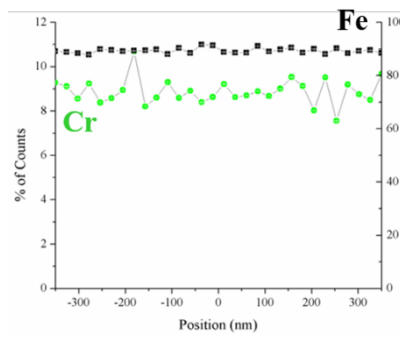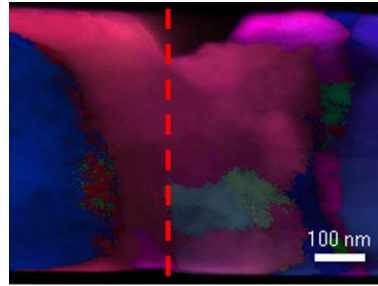
$K_{Q,J} = 14.0$ MPa m$^{1/2}$
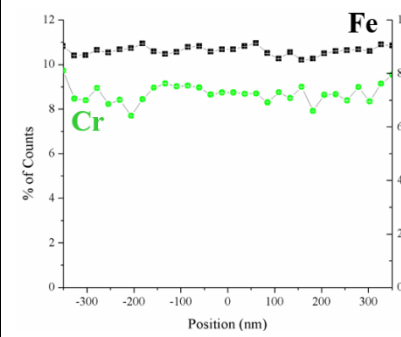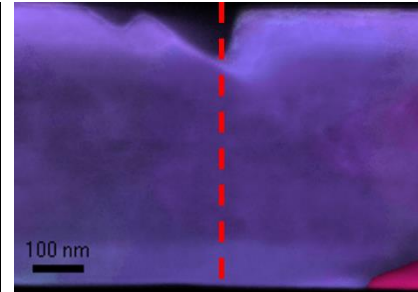
$K_{Q,J} = 15.6$ MPa m$^{1/2}$
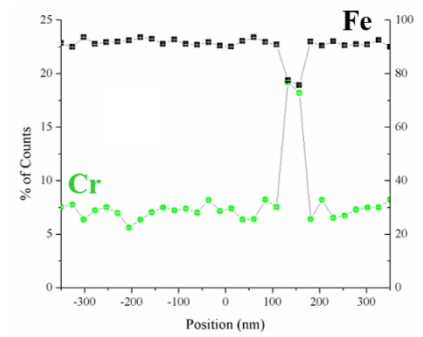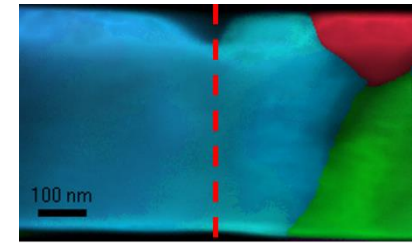
$K_{Q,J} = 20.1$ MPa m$^{1/2}$

Fe^{2+} 100 dpa 500°C – Grid 1
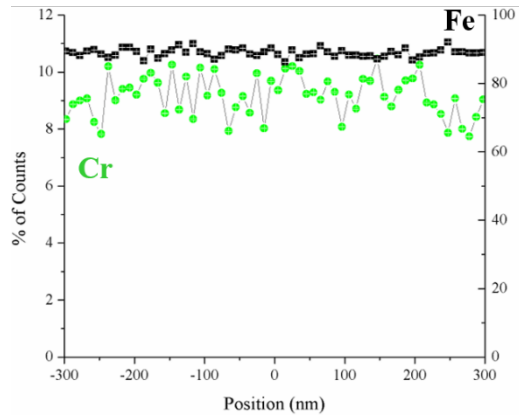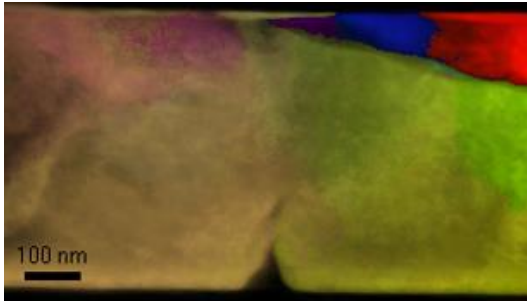
Fractured Left Edge
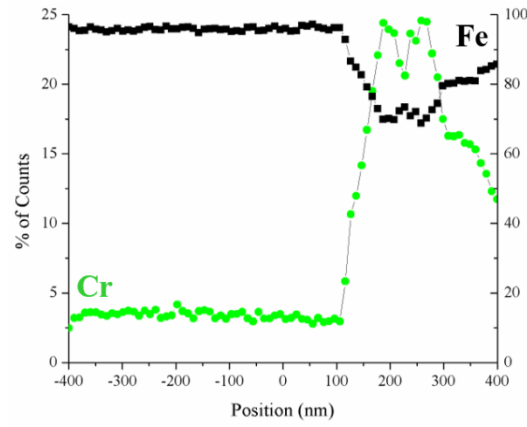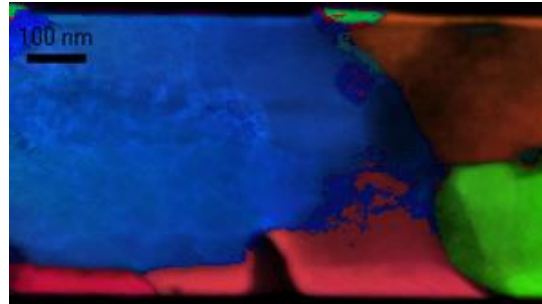
Fractured Left Edge
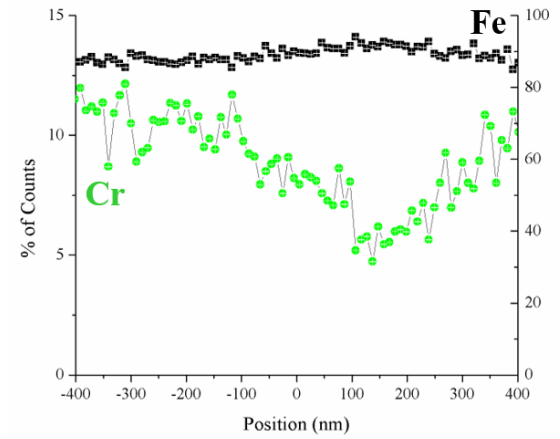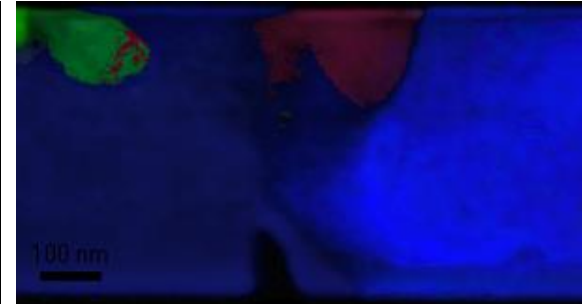
Fractured Right Edge

Fe^{2+} 100 dpa 500°C – Grid 2
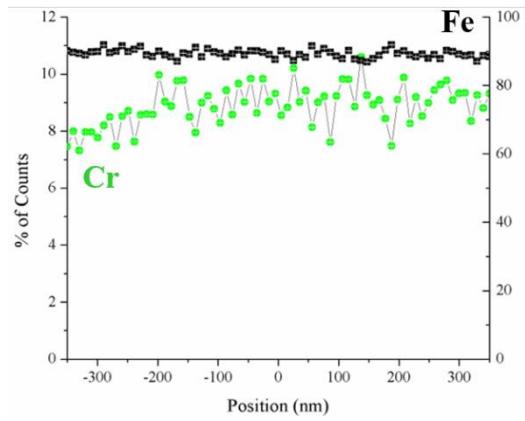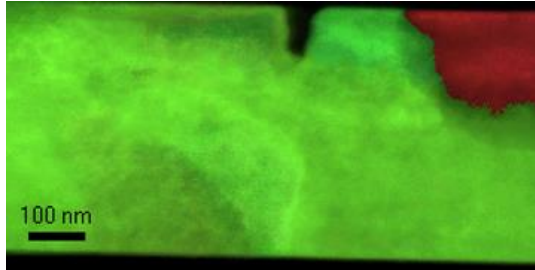
Fractured Left Edge
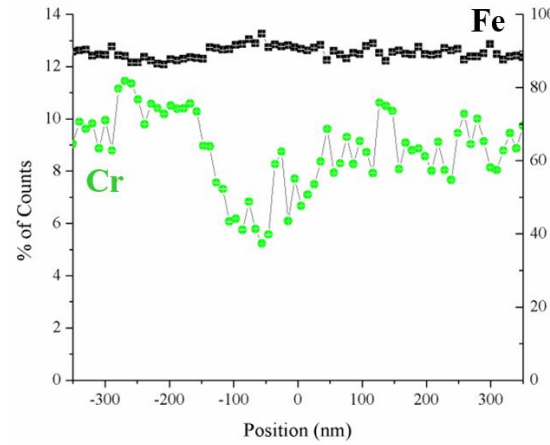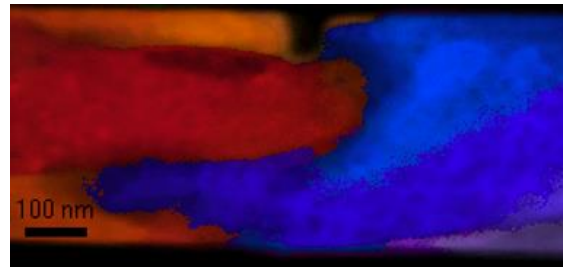
Fractured Right Edge
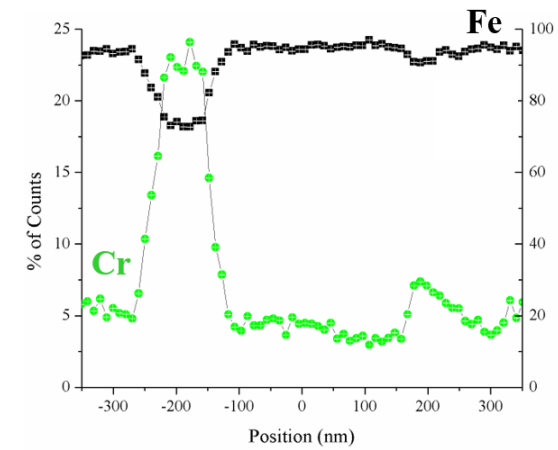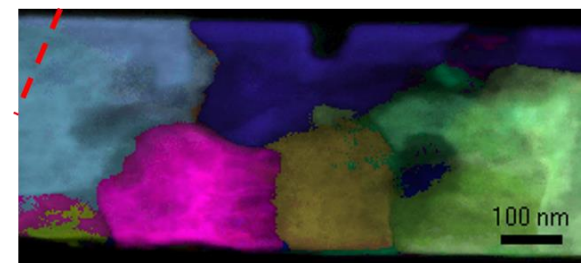
Sheared on Left

Fe^{2+} 100 dpa 500°C – Grid 3
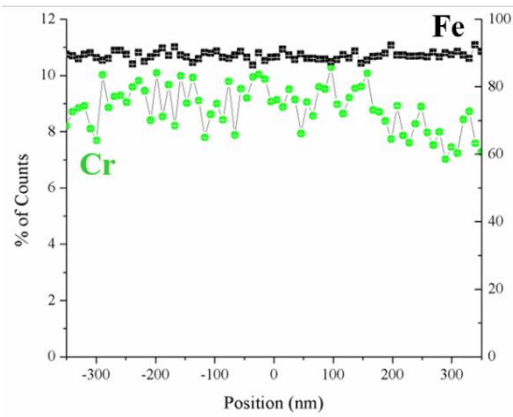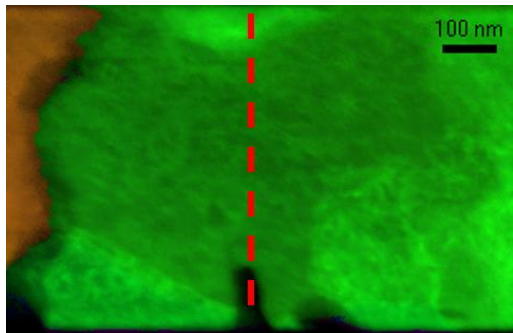
$K_{Q,J} = 7.0$ MPa m$^{1/2}$
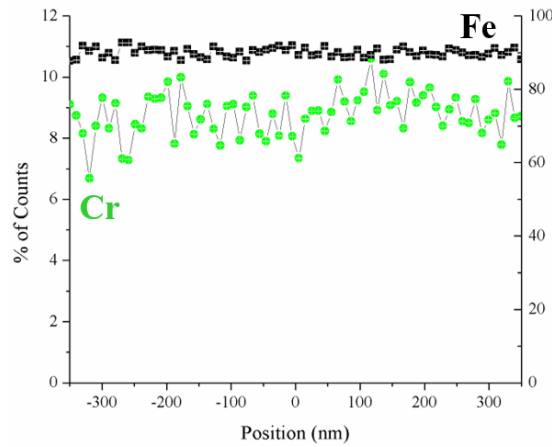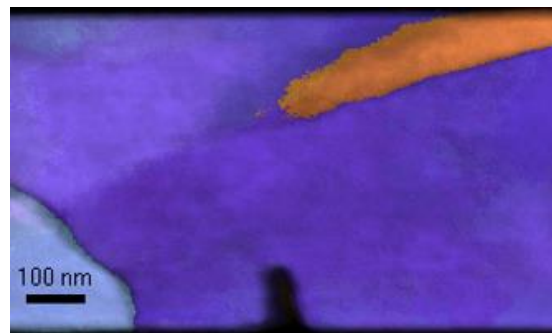
Did Not Fracture
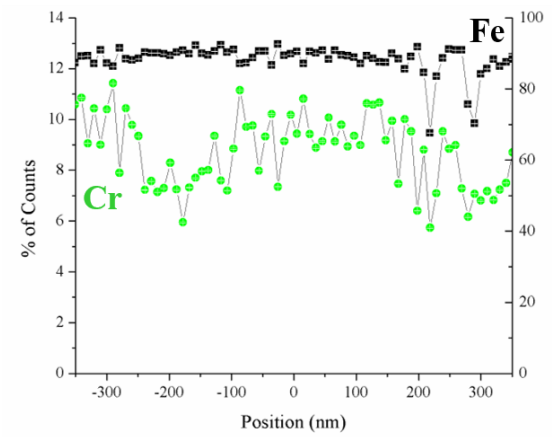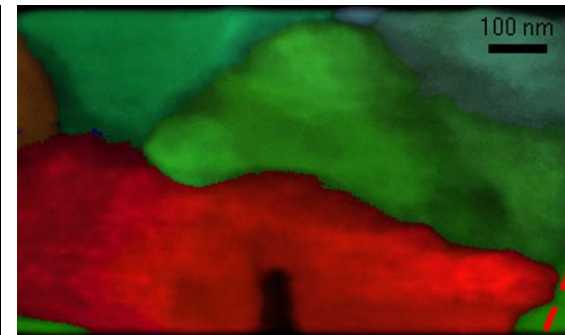
Sheared on Left

Proton 3 dpa 500°C – Grid 1
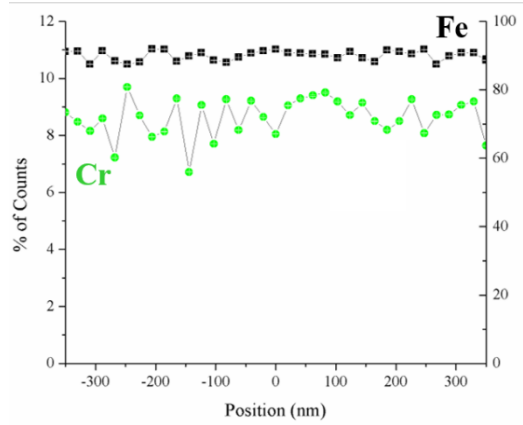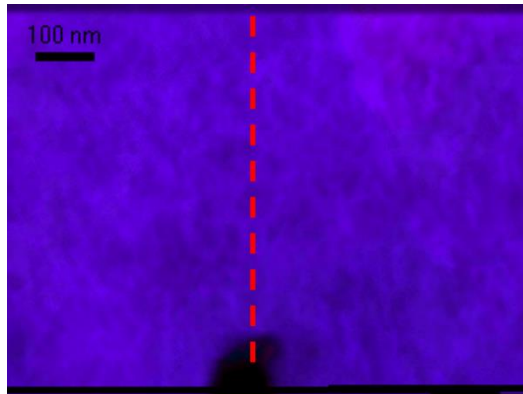
$K_{Q,J}$ = 19.5 MPa m$^{1/2}$
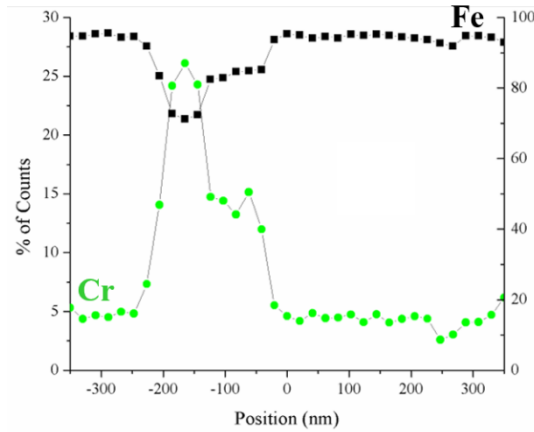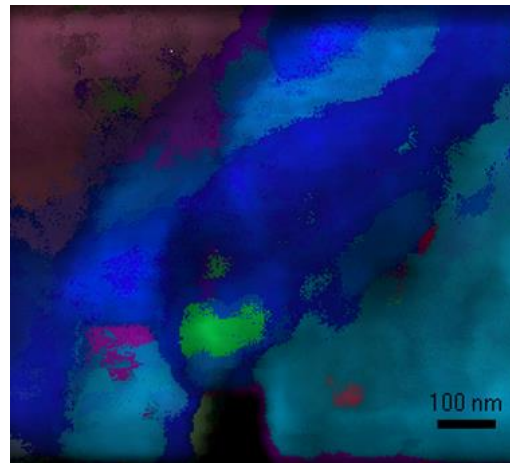
Did Not Fracture
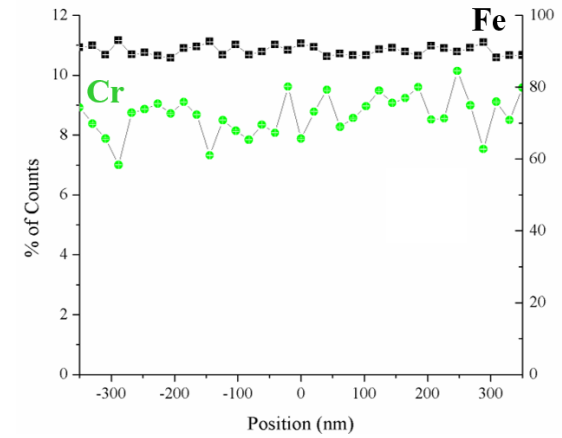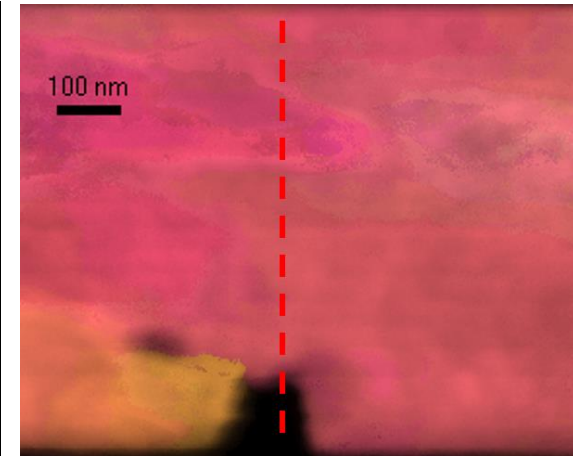
$K_{Q,J}$ = 19.4 MPa m$^{1/2}$

Proton 3 dpa 500°C – Grid 2
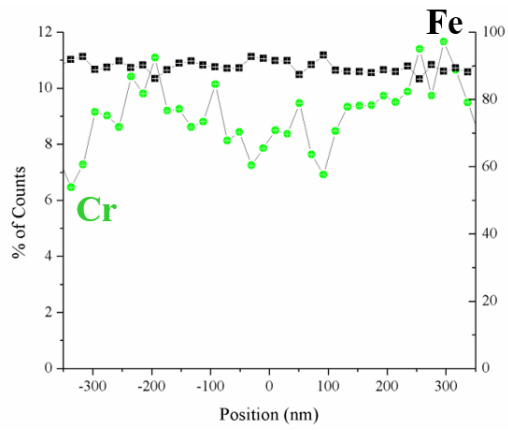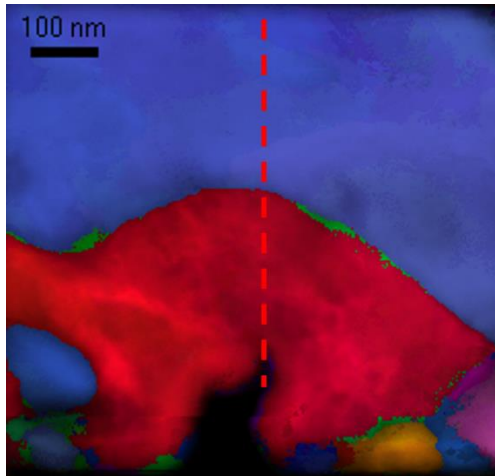
$K_{Q,J}$ = 20.0 MPa m$^{1/2}$
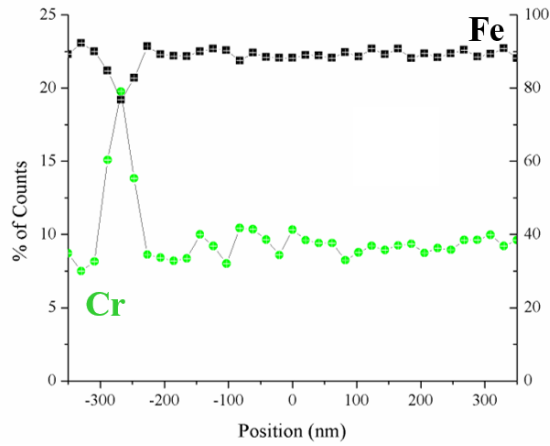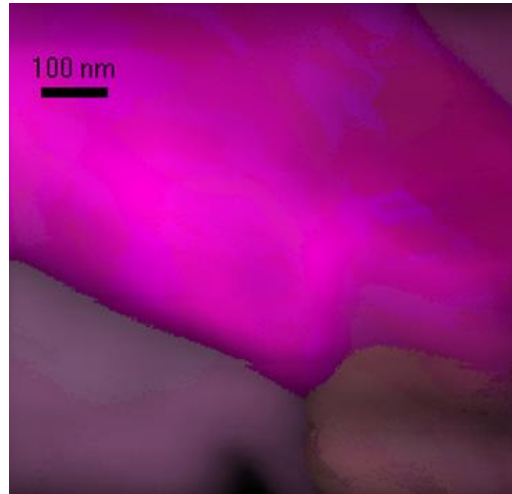
Did Not Fracture
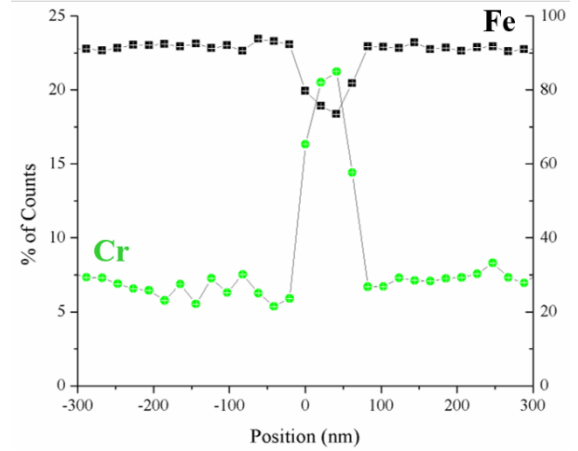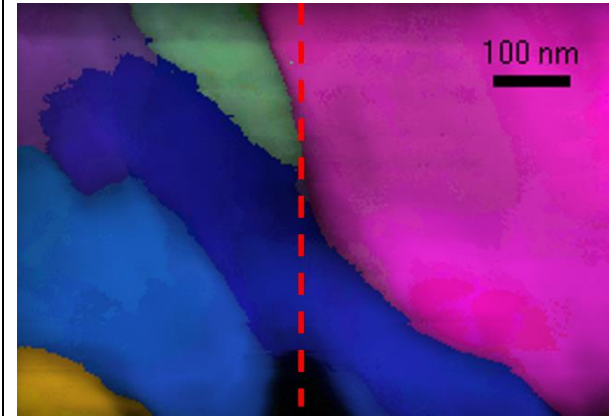
$K_{Q,J}$ = 11.1 MPa m$^{1/2}$

Proton 3 dpa 500°C – Grid 3
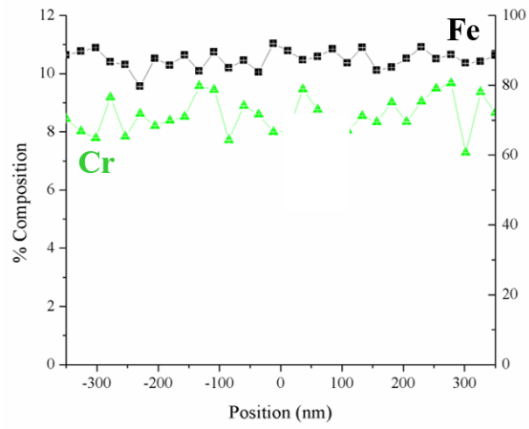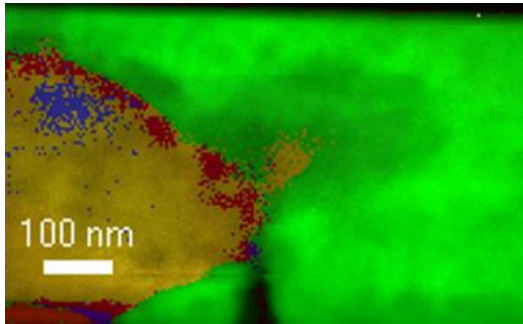
Did Not Fracture
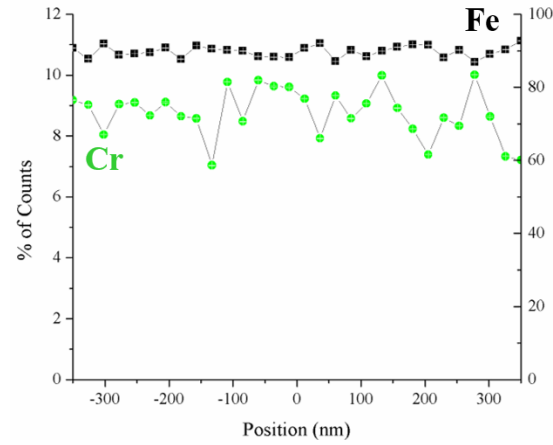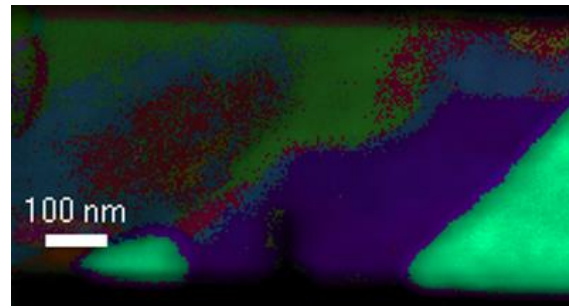
Did Not Fracture
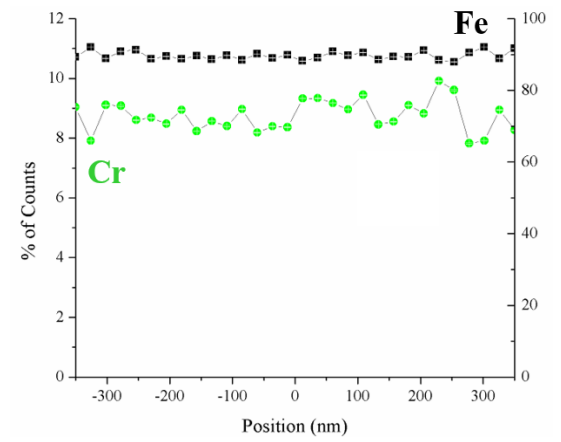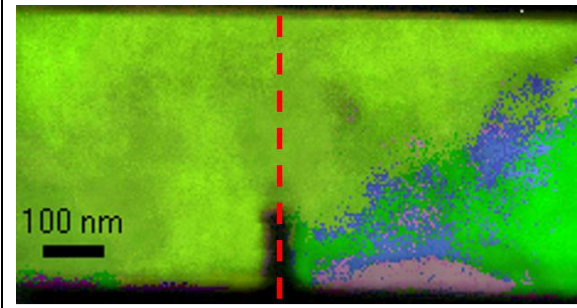
$K_{Q,J} = 13.3$ MPa m$^{1/2}$

REFERENCES

[1]   S.J. Zinkle, L.L. Snead, Opportunities and limitations for ion beams in radiation effects studies: Bridging critical gaps between charged particle and neutron irradiations, Scr. Mater. (2017). doi:10.1016/j.scriptamat.2017.06.041.

[2]   J.F. Ziegler, SRIM, (2013).

[3]   S.J. Zinkle, J.T. Busby, Structural materials for fission & fusion energy, Mater. Today. 12 (2009) 12–19. doi:10.1016/S1369-7021(09)70294-9.

[4]   M.J. Swenson, J.P. Wharry, Nanocluster irradiation evolution in Fe-9%Cr ODS and ferritic-martensitic alloys, J. Nucl. Mater. 496 (2017) 24–40. doi:10.1016/j.jnucmat.2017.08.045.

[5]   J.P. Wharry, M.J. Swenson, K.H. Yano, A review of the irradiation evolution of dispersed oxide nanoparticles in the b.c.c. Fe-Cr system: Current understanding and future directions, J. Nucl. Mater. 486 (2017) 11–20. doi:10.1016/j.jnucmat.2017.01.009.

[6]   K.H. Yano, M.J. Swenson, Y. Wu, J.P. Wharry, TEM in situ micropillar compression tests of ion irradiated oxide dispersion strengthened alloy, J. Nucl. Mater. 483 (2017) 107–120. doi:10.1016/j.jnucmat.2016.10.049.

[7]   M.J. Swenson, J.P. Wharry, The comparison of microstructure and nanocluster evolution in proton and neutron irradiated Fe-9%Cr ODS steel to 3 dpa at 500c, J. Nucl. Mater. 467 (2015) 97–112. doi:10.1016/j.jnucmat.2015.09.022.

[8]   G.S. Was, Fundamentals of Radiation Materials Science, Springer, New York, 2007.

[9]   Q. Yu, M. Legros, A.M. Minor, In situ TEM nanomechanics, MRS Bull. 40 (2015) 62–70. doi:10.1557/mrs.2014.306.

[10]   M. Legros, In situ mechanical TEM: Seeing and measuring under stress with electrons, Comptes Rendus Phys. 15 (2014) 224–240. doi:10.1016/j.crhy.2014.02.002.

[11]   P.J. Imrich, C. Kirchlechner, D. Kiener, G. Dehm, In Situ TEM Microcompression of Single and Bicrystalline Samples: Insights and Limitations, JOM. 67 (2015). doi:10.1007/s11837-015-1440-6.

[12]   S.H. Oh, M. Legros, D. Kiener, G. Dehm, In situ observation of dislocation nucleation and escape in a submicrometre aluminium single crystal., Nat. Mater. 8 (2009) 95–100. doi:10.1038/nmat2370.

[13]   E. Hintsala, D. Kiener, J. Jackson, W.W. Gerberich, In-Situ Measurements of Free-Standing, Ultra-Thin Film Cracking in Bending, Exp. Mech. 55 (2015) 1681–1690. doi:10.1007/s11340-015-0069-2.

[14]   D. Kiener, P. Kaufmann, A.M. Minor, Strength, hardening, and failure observed by in situ TEM tensile testing, Adv. Eng. Mater. 14 (2012) 960–967. doi:10.1002/adem.201200031.

[15]   W.D.J. Callister, D.G. Rethswich, Materials Science and Engineering, 9th ed., John Wiley & Sons, Inc., Hoboken, New Jersey, 2014.

[16]   M. Meyers, K. Chawla, Mechanical Behavior of Materials, Cambridge University Press, New York, 2009.

[17]   E. Arzt, Size Effects in Materials Due to Microstructural and Dimensional Constraints: A Comparative Review, Acta Mater. 46 (1998) 5611–5626. doi:10.1177/0261927X99018004006.

[18]   P. Hosemann, C. Shin, D. Kiener, Small scale mechanical testing of irradiated materials, J. Mater. Res. (2015) 1–15. doi:10.1557/jmr.2015.26.

[19]   D.J. Dunstan, A.J. Bushby, Grain size dependence of the strength of metals: The Hall–Petch effect does not scale as the inverse square root of grain size, Int. J. Plast. 53 (2014) 56–65. doi:10.1016/j.ijplas.2013.07.004.

[20]   T.L. Anderson, Fracture Mechanics, 4th ed., Taylor & Francis, Bocca Raton, FL, 2017.

[21]   M.E. Launey, R.O. Ritchie, On the fracture toughness of advanced materials, Adv. Mater. 21 (2009) 2103–2110. doi:10.1002/adma.200803322.

[22]   Tada, Stress Analysis Results for Common Test Specimen Configurations, in: Stress Anal. Cracks Handb., 2000: pp. 39–80.

[23]   S. Wurster, C. Motz, R. Pippan, Characterization of the fracture toughness of micro-sized tungsten single crystal notched specimens, Philos. Mag. 92 (2012) 1803–1825. doi:10.1080/14786435.2012.658449.

[24]   S. Ukai, M. Fujiwara, Perspective of ODS alloys application in nuclear environments, J. Nucl. Mater. 307–311 (2002) 749–757. doi:10.1016/S0022-3115(02)01043-7.

[25]   R.L. Klueh, D.R. Harries, High-Chromium Ferritic and Martensitic Steels for Nuclear Applications, 2001. doi:10.1520/MONO3-EB.

[26] S.J. Zinkle, J.L. Boutard, D.T. Hoelzer, A. Kimura, R. Lindau, G.R. Odette, M. Rieth, L. Tan, H. Tanigawa, Development of next generation tempered and ODS reduced activation ferritic/martensitic steels for fusion energy applications, Nucl. Fusion. 57 (2017) 092005. doi:10.1088/1741-4326/57/9/092005.

[27] C.K. Dolph, M.J. Swenson, J.P. Wharry, Plastic zone size for nanoindenation of irradiated Fe-9%Cr ODS, (2016).

[28] S. Ohtsuka, S. Ukai, M. Fujiwara, T. Kaito, T. Narita, Improvement of Creep Strength of 9CrODS Martensitic Steel by Controlling Excess Oxygen and Titanium Concentrations, Mater. Trans. 46 (2005) 487–492.

[29] T. Tanno, S. Ohtsuka, Y. Yano, T. Kaito, Y. Oba, M. Ohnuma, S. Koyama, K. Tanaka, Evaluation of mechanical properties and nano-meso structures of 9–11%Cr ODS steels, J. Nucl. Mater. 440 (2013) 568–574. doi:10.1016/j.jnucmat.2013.04.006.

[30] M.J. Alinger, G.R. Odette, D.T. Hoelzer, The development and stability of Y-Ti-O nanoclusters in mechanically alloyed Fe-Cr based ferritic alloys, J. Nucl. Mater. 329–333 (2004) 382–386. doi:10.1016/j.jnucmat.2004.04.042.

[31] L. Barnard, G.R. Odette, I. Szlufarska, D. Morgan, An ab initio study of Ti-Y-O nanocluster energetics in nanostructured ferritic alloys, Acta Mater. 60 (2012) 935–947. doi:10.1016/j.actamat.2011.11.011.

[32] D.T. Hoelzer, J. Bentley, M. a. Sokolov, M.K. Miller, G.R. Odette, M.J. Alinger, Influence of particle dispersions on the high-temperature strength of ferritic alloys, J. Nucl. Mater. 367–370 A (2007) 166–172. doi:10.1016/j.jnucmat.2007.03.151.

[33] S. Ukai, M. Harada, H. Okada, M. Inoue, S. Nomura, S. Shikakura, K. Asabe, T. Nishida, M. Fujiwara, Alloying design of ods ferritic steel for long life FBRs core materials, J. Nucl. Mater. 204 (1993) 65–73.

[34] M.J. Alinger, G.R. Odette, D.T. Hoelzer, On the role of alloy composition and processing parameters in nanocluster formation and dispersion strengthening in nanostuctured ferritic alloys, Acta Mater. 57 (2009) 392–406. doi:10.1016/j.actamat.2008.09.025.

[35] M. Yamamoto, S. Ukai, S. Hayashi, T. Kaito, S. Ohtsuka, Reverse phase transformation from α to γ in 9Cr-ODS ferritic steels, J. Nucl. Mater. 417 (2011) 237–240. doi:10.1016/j.jnucmat.2010.12.250.

[36] R. Miyata, S. Ukai, X. Wu, N. Oono, S. Hayashi, S. Ohtsuka, T. Kaito, Strength correlation with residual ferrite fraction in 9CrODS ferritic steel, J. Nucl. Mater. 442 (2013) 138–141. doi:10.1016/j.jnucmat.2013.04.086.

[37] A. Chauhan, D. Litvinov, Y. de Carlan, J. Aktaa, Study of the deformation and damage mechanisms of a 9Cr-ODS steel: Microstructure evolution and fracture characteristics, Mater. Sci. Eng. A. 658 (2016) 123–134. doi:10.1016/j.msea.2016.01.109.

[38] J.H. Kim, T.S. Byun, D.T. Hoelzer, S.W. Kim, B.H. Lee, Temperature dependence of strengthening mechanisms in the nanostructured ferritic alloy 14YWT: Part I-Mechanical and microstructural observations, Mater. Sci. Eng. A. 559 (2013) 101–110. doi:10.1016/j.msea.2012.08.042.

[39] N. Akasaka, S. Yamashita, T. Yoshitake, S. Ukai, a Kimura, Microstructural changes of neutron irradiated ODS ferritic and martensitic steels, J. Nucl. Mater. 329–333 (2004) 1053–1056. doi:10.1016/j.jnucmat.2004.04.133.

[40] I. Monnet, P. Dubuisson, Y. Serruys, M.O. Ruault, O. Kaïtasov, B. Jouffrey, Microstructural investigation of the stability under irradiation of oxide dispersion strengthened ferritic steels, J. Nucl. Mater. 335 (2004) 311–321. doi:10.1016/j.jnucmat.2004.05.018.

[41] F. Li, H. Abe, T. Ishizaki, Y. Li, T. Nagasaka, T. Muroga, T. Nagase, H. Yasuda, Stability of oxide particles under electron irradiation in a 9Cr ODS steel at 400°C, J. Nucl. Mater. 455 (2014) 724–727. doi:10.1016/j.jnucmat.2014.09.011.

[42] A. Certain, S. Kuchibhatla, V. Shutthanandan, D.T. Hoelzer, T.R. Allen, Radiation stability of nanoclusters in nano-structured oxide dispersion strengthened (ODS) steels, J. Nucl. Mater. 434 (2013) 311–321. doi:10.1016/j.jnucmat.2012.11.021.

[43] B. Yao, D.J. Edwards, R.J. Kurtz, TEM characterization of dislocation loops in irradiated bcc Fe-based steels, J. Nucl. Mater. 434 (2013) 402–410. doi:10.1016/j.jnucmat.2012.12.002.

[44] J. Chen, P. Jung, J. Henry, Y. De Carlan, T. Sauvage, F. Duval, M.F. Barthe, W. Hoffelner, Irradiation creep and microstructural changes of ODS steels of different Cr-contents during helium implantation under stress, J. Nucl. Mater. 437 (2013) 432–437. doi:10.1016/j.jnucmat.2013.02.071.

[45] G.S. Was, J.P. Wharry, B. Frisbie, B.D. Wirth, D. Morgan, J.D. Tucker, T.R. Allen, Assessment of radiation-induced segregation mechanisms in austenitic and ferritic-martensitic alloys, J. Nucl. Mater. 411 (2011) 41–50. doi:10.1016/j.jnucmat.2011.01.031.

[46] J.P. Wharry, Z. Jiao, G.S. Was, Application of the inverse Kirkendall model of radiation-induced segregation to ferritic-martensitic alloys, J. Nucl. Mater. 425 (2012) 117–124. doi:10.1016/j.jnucmat.2011.10.035.

[47] S. Yamashita, Y. Yano, S. Ohtsuka, T. Yoshitake, T. Kaito, S. Koyama, K. Tanaka, Irradiation behavior evaluation of oxide dispersion strengthened ferritic steel cladding tubes irradiated in JOYO, J. Nucl. Mater. 442 (2013) 417–424. doi:10.1016/j.jnucmat.2013.04.051.

[48] E. Lucon, A. Leenaers, W. Vandermeulen, Mechanical response of oxide dispersion strengthened (ODS) EUROFER97 after neutron irradiation at 300C, Fusion Eng. Des. 82 (2007) 2438–2443. doi:10.1016/j.fusengdes.2007.05.018.

[49] R.L. Klueh, A.T. Nelson, Ferritic/martensitic steels for next-generation reactors, J. Nucl. Mater. 371 (2007) 37–52. doi:10.1016/j.jnucmat.2007.05.005.

[50] M.J. Swenson, C.K. Dolph, J.P. Wharry, The effects of oxide evolution on mechanical properties in irradiated Fe-9%Cr ODS, J. Nucl. Mater. 479 (2016) 426–435. doi:10.1016/j.jnucmat.2016.07.022.

[51] M. Dadé, J. Malaplate, J. Garnier, F. De Geuser, F. Barcelo, P. Wident, A. Deschamps, Influence of microstructural parameters on the mechanical properties of oxide dispersion strengthened Fe-14Cr steels, Acta Mater. 127 (2017) 165–177. doi:10.1016/j.actamat.2017.01.026.

[52] M.A. Auger, T. Leguey, A. Muñoz, M.A. Monge, V. De Castro, P. Fernández, G. Garcés, R. Pareja, Microstructure and mechanical properties of ultrafine-grained Fe-14Cr and ODS Fe-14Cr model alloys, J. Nucl. Mater. 417 (2011) 213–216. doi:10.1016/j.jnucmat.2010.12.060.

[53] M. Nagini, R. Vijay, M. Ramakrishna, a. V. Reddy, G. Sundararajan, Influence of the duration of high energy ball milling on the microstructure and mechanical properties of a 9Cr oxide dispersion strengthened ferritic–martensitic steel, Mater. Sci. Eng. A. 620 (2015) 490–499. doi:10.1016/j.msea.2014.10.050.

[54]   Y. de Carlan, J.L. Bechade, P. Dubuisson, J.L. Seran, P. Billot, A. Bougault, T. Cozzika, S. Doriot, D. Hamon, J. Henry, M. Ratti, N. Lochet, D. Nunes, P. Olier, T. Leblond, M.H. Mathon, CEA developments of new ferritic ODS alloys for nuclear applications, J. Nucl. Mater. 386–388 (2009) 430–432. doi:10.1016/j.jnucmat.2008.12.156.

[55]   Z. Shi, F. Han, The microstructure and mechanical properties of micro-scale Y2O3 strengthened 9Cr steel fabricated by vacuum casting, Mater. Des. 66 (2015) 304–308. doi:10.1016/j.matdes.2014.10.075.

[56]   B. Fournier, A. Steckmeyer, A.L. Rouffie, J. Malaplate, J. Garnier, M. Ratti, P. Wident, L. Ziolek, I. Tournie, V. Rabeau, J.M. Gentzbittel, T. Kruml, I. Kubena, Mechanical behaviour of ferritic ODS steels-Temperature dependancy and anisotropy, J. Nucl. Mater. 430 (2012) 142–149. doi:10.1016/j.jnucmat.2012.05.048.

[57]   L. Toualbi, C. Cayron, P. Olier, R. Logé, Y. de Carlan, Relationships between mechanical behavior and microstructural evolutions in Fe 9Cr–ODS during the fabrication route of SFR cladding tubes, J. Nucl. Mater. 442 (2013) 410–416. doi:10.1016/j.jnucmat.2013.04.052.

[58]   B. Hary, T. Guilbert, P. Wident, T. Baudin, R. Logé, Y. de Carlan, Investigation of the relationships between mechanical properties and microstructure in a Fe-9%Cr ODS steel, EPJ Nucl. Sci. Technol. 2 (2016) 7. doi:10.1051/epjn/e2016-50008-7.

[59]   S. Zinkle, Thermophysical and Mechanical Properties of Fe-(8-9)% Cr reduced activation steels, US. Dept. Energy. Off. Adm. Serv. (1998). http://cds.cern.ch/record/474544.

[60]   J. Henry, X. Averty, A. Alamo, Tensile and impact properties of 9Cr tempered martensitic steels and ODS-FeCr alloys irradiated in a fast reactor at 325C up to 78 dpa, J. Nucl. Mater. 417 (2011) 99–103. doi:10.1016/j.jnucmat.2010.12.203.

[61]   C.D. Hardie, S.G. Roberts, A.J. Bushby, Understanding the effects of ion irradiation using nanoindentation techniques, J. Nucl. Mater. 462 (2014) 391–401. doi:10.1016/j.jnucmat.2014.11.066.

[62]   T. Miura, K. Fujii, K. Fukuya, K. Takashima, Influence of crystal orientation on hardness and nanoindentation deformation in ion-irradiated stainless steels, J. Nucl. Mater. 417 (2011) 984–987. doi:10.1016/j.jnucmat.2010.12.197.

[63]   C.K. Dolph, Plastic deformation and effective strain hardening coefficient of irradiated Fe-9wt%Cr ODS alloy by nano-indentation and TEM, Boise State University, 2015.

[64]   H. Vo, A. Reichardt, C. Howard, M.D. Abad, D. Kaoumi, P. Chou, P. Hosemann, Small-Scale Mechanical Testing on Proton Beam-Irradiated 304 SS from Room Temperature to Reactor Operation Temperature, JOM. 67 (2015) 2959–2964. doi:10.1007/s11837-015-1596-0.

[65]   J.S. Weaver, S. Pathak, A. Reichardt, H. Vo, S.A. Maloy, P. Hosemann, N.A. Mara, Spherical nanoindentation of proton irradiation 304 stainless steel: a comparison of small scale mechanical test techniques for measuring irradiation hardening, Rev. (2017).

[66]   P. Hosemann, C. Vieh, R.R. Greco, S. Kabra, J.A. Valdez, M.J. Cappiello, S.A. Maloy, Nanoindentation on ion irradiated steels, J. Nucl. Mater. 389 (2009) 239–247. doi:10.1016/j.jnucmat.2009.02.026.

[67]   C. Heintze, F. Bergner, M. Hernández-Mayoral, Ion-irradiation-induced damage in Fe-Cr alloys characterized by nanoindentation, J. Nucl. Mater. 417 (2011) 980–983. doi:10.1016/j.jnucmat.2010.12.196.

[68]   C. Heintze, F. Bergner, M. Hernandez-Mayoral, R. Kogler, G. Muller, A. Ulbricht, Irradiation hardening of Fe-9Cr-based alloys and ODS Eurofer: Effect of helium implantation and iron-ion irradiation at 300C including sequence effects, J. Nucl. Mater. 470 (2016) 258–267.

[69]   N.S. Cannon, D.S. Gelles, Charpy impact test results from low activation alloys irradiated to 10 dpa at 365°C, J. Nucl. Mater. 186 (1991) 68–76. doi:10.1016/0022-3115(91)90354-A.

[70]   F. Abe, T. Noda, H. Araki, M. Okada, M. Narui, H. Kayano, Effect of specimen size on the ductile-brittle transition behavior and the fracture sequence of 9Cr-W steels, J. Nucl. Mater. 150 (1987) 292–301. doi:10.1016/0022-3115(87)90007-9.

[71]   T.S. Byun, D.T. Hoelzer, J.H. Kim, S.A. Maloy, A comparative assessment of the fracture toughness behavior of ferritic-martensitic steels and nanostructured ferritic alloys, J. Nucl. Mater. 484 (2017) 157–167. doi:10.1016/j.jnucmat.2016.12.004.

[72]   M.D. Uchic, D.M. Dimiduk, J.N. Florando, W.D. Nix, Sample dimensions influence strength and crystal plasticity., Science. 305 (2004) 986–989. doi:10.1126/science.1098993.

[73] M.D. Uchic, D.M. Dimiduk, A methodology to investigate size scale effects in crystalline plasticity using uniaxial compression testing, Mater. Sci. Eng. A. 400–401 (2005) 268–278. doi:10.1016/j.msea.2005.03.082.

[74] C. Shin, S. Lim, H. Jin, P. Hosemann, J. Kwon, Development and testing of microcompression for post irradiation characterization of ODS steels, J. Nucl. Mater. 444 (2014) 43–48. doi:10.1016/j.jnucmat.2013.09.025.

[75] J. Ye, R.K. Mishra, A.K. Sachdev, A.M. Minor, In situ TEM compression testing of Mg and Mg-0.2 wt.% Ce single crystals, Scr. Mater. 64 (2011) 292–295. doi:10.1016/j.scriptamat.2010.09.047.

[76] E.A. Withey, A.M. Minor, D.C. Chrzan, J.W. Morris, S. Kuramoto, The deformation of Gum Metal through in situ compression of nanopillars, Acta Mater. 58 (2010) 2652–2665. doi:10.1016/j.actamat.2009.12.052.

[77] D. Kiener, A.M. Minor, O. Anderoglu, Y. Wang, S.A. Maloy, P. Hosemann, Application of small-scale testing for investigation of ion-beam-irradiated materials, J. Mater. Res. 27 (2012) 2724–2736. doi:10.1557/jmr.2012.303.

[78] D. Kiener, P. Hosemann, S.A. Maloy, A.M. Minor, In situ nanocompression testing of irradiated copper., Nat. Mater. 10 (2011) 608–613. doi:10.1038/nmat3055.

[79] Q. Yu, J. Sun, J.W. Morris, A.M. Minor, Source mechanism of non-basal <c+a> slip in Ti alloy, Scr. Mater. 69 (2013) 57–60. doi:10.1016/j.scriptamat.2013.03.009.

[80] P.J. Imrich, C. Kirchlechner, D. Kiener, G. Dehm, Internal and external stresses: In situ TEM compression of Cu bicrystals containing a twin boundary, Scr. Mater. 100 (2015) 94–97. doi:10.1016/j.scriptamat.2014.12.023.

[81] B.R.S. Rogne, C. Thaulow, Strengthening mechanisms of iron micropillars, Philos. Mag. 95 (2015) 1814–1828. doi:10.1080/14786435.2014.984004.

[82] R. Fritz, V. Maier-Kiener, D. Lutz, D. Kiener, Interplay between sample size and grain size: Single crystalline vs. ultrafine-grained chromium micropillars, Mater. Sci. Eng. A. 674 (2016) 626–633. doi:10.1016/j.msea.2016.08.015.

[83] J.Y. Kim, J.R. Greer, Size-dependent mechanical properties of molybdenum nanopillars, Appl. Phys. Lett. 93 (2008) 91–94. doi:10.1063/1.2979684.

[84] A.S. Schneider, B.G. Clark, C.P. Frick, P.A. Gruber, E. Arzt, Effect of orientation and loading rate on compression behavior of small-scale Mo pillars, Mater. Sci. Eng. A. 508 (2009) 241–246. doi:10.1016/j.msea.2009.01.011.

[85] B. Girault, A.S. Schneider, C.P. Prick, E. Arzt, Strength effects in micropillars of a dispersion strengthened superalloy, Adv. Eng. Mater. 12 (2010) 385–388. doi:10.1002/adem.201000089.

[86] M.A. Pouchon, J. Chen, R. Ghisleni, J. Michler, W. Hoffelner, Characterization of irradiation damage of ferritic ODS alloys with advanced micro-sample methods, Exp. Mech. 50 (2010) 79–84. doi:10.1007/s11340-008-9214-5.

[87] P. Hosemann, J.G. Swadener, D. Kiener, G.S. Was, S.A. Maloy, N. Li, An exploratory study to determine applicability of nano-hardness and micro-compression measurements for yield stress estimation, J. Nucl. Mater. 375 (2008) 135–143. doi:10.1016/j.jnucmat.2007.11.004.

[88] C.P. Frick, S. Orso, E. Arzt, Loss of pseudoelasticity in nickel-titanium sub-micron compression pillars, Acta Mater. 55 (2007) 3845–3855. doi:10.1016/j.actamat.2007.02.034.

[89] P. Landau, Q. Guo, P. Hosemann, Y. Wang, J.R. Greer, Deformation of as-fabricated and helium implanted 100 nm-diameter iron nano-pillars, Mater. Sci. Eng. A. 612 (2014) 316–325. doi:10.1016/j.msea.2014.06.052.

[90] W.A. Soer, J.T. De Hosson, A.M. Minor, E.A. Stach, J. Morris, Direct observations of grain boundary phenomena during indentation of Al and Al-Mg thin films, Mater. Res. Soc. Symp. - Proc. 795 (2003) 369–374. http://www.scopus.com/scopus/inward/record.url?eid=2-s2.0-2442573731&partnerID=40.

[91] W.A. Soer, J.T.M. De Hosson, A.M. Minor, J.W. Morris, E.A. Stach, Effects of solute Mg on grain boundary and dislocation dynamics during nanoindentation of Al-Mg thin films, Acta Mater. 52 (2004) 5783–5790. doi:10.1016/j.actamat.2004.08.032.

[92] D.S. Gianola, S. Van Petegem, M. Legros, S. Brandstetter, H. Van Swygenhoven, K.J. Hemker, Stress-assisted discontinuous grain growth and its effect on the deformation behavior of nanocrystalline aluminum thin films, Acta Mater. 54 (2006) 2253–2263. doi:10.1016/j.actamat.2006.01.023.

[93] L. De Knoop, M. Legros, Absorption of crystal/amorphous interfacial dislocations during in situ TEM nanoindentation of an Al thin film on Si, Scr. Mater. 74 (2014) 44–47. doi:10.1016/j.scriptamat.2013.10.003.

[94] M. Legros, M. Cabie, D.S. Gianola, In situ deformation of thin films on substrates, Microsc. Res. Tech. 72 (2009) 270–283. doi:10.1002/jemt.20680.

[95] A.M. Minor, E.T. Lilleodden, E.A. Stach, J.W. Morris Jr., In-Situ Transmission Electron Microscopy Study of the Nanoindentation Behavior of Al, J. Electron. Mater. 31 (2002) 958–964.

[96] H. Idrissi, A. Kobler, B. Amin-Ahmadi, M. Coulombier, M. Galceran, J.P. Raskin, S. Godet, C. Kübel, T. Pardoen, D. Schryvers, Plasticity mechanisms in ultrafine grained freestanding aluminum thin films revealed by in-situ transmission electron microscopy nanomechanical testing, Appl. Phys. Lett. 104 (2014). doi:10.1063/1.4868124.

[97] M. Legros, O. Ferry, F. Houdellier, A. Jacques, A. George, Fatigue of single crystalline silicon: Mechanical behaviour and TEM observations, Mater. Sci. Eng. A. 483–484 (2008) 353–364. doi:10.1016/j.msea.2006.10.200.

[98] D. Kiener, A.M. Minor, Source-controlled yield and hardening of Cu(1 0 0) studied by in situ transmission electron microscopy, Acta Mater. 59 (2011) 1328–1337. doi:10.1016/j.actamat.2010.10.065.

[99] G. Wang, J. Lian, Q. Jiang, S. Sun, T. Zhang, High resolution transmission electron microscopic in-situ observations of plastic deformation of compressed nanocrystalline gold, 103518 (2014) 1–6.

[100] Z.W. Shan, R.K. Mishra, S.A. Syed Asif, O.L. Warren, A.M. Minor, Mechanical annealing and source-limited deformation in submicrometre-diameter Ni crystals., Nat. Mater. 7 (2008) 115–119. doi:10.1038/nmat2085.

[101] A.M. Minor, E.T. Lilleodden, E.A. Stach, J.W. Morris, Direct observations of incipient plasticity during nanoindentation of Al, J. Mater. Res. 19 (2004) 176–182. doi:10.1557/jmr.2004.19.1.176.

[102] Z. Shan, In situ TEM investigation of the mechanical behavior of micronanoscaled metal pillars, Jom. 64 (2012) 1229–1234. doi:10.1007/s11837-012-0436-8.

[103] J.W. Morris, M. Jin, A.M. Minor, In situ studies of the transmission of strain across grain boundaries, Mater. Sci. Eng. A. 462 (2007) 412–417. doi:10.1016/j.msea.2006.02.461.

[104] M. Jin, A.M. Minor, E.A. Stach, J.W. Morris, Direct observation of deformation-induced grain growth during the nanoindentation of ultrafine-grained Al at room temperature, Acta Mater. 52 (2004) 5381–5387. doi:10.1016/j.actamat.2004.07.044.

[105] M.A. Meyers, A. Mishra, D.J. Benson, Mechanical properties of nanocrystalline materials, Prog. Mater. Sci. 51 (2006) 427–556. doi:10.1016/j.pmatsci.2005.08.003.

[106] T.J. Rupert, D.S. Gianola, Y. Gan, K.J. Hemker, Experimental observations of stress-driven grain boundary migration., Science. 326 (2009) 1686–1690. doi:10.1126/science.1178226.

[107] M. Legros, D.S. Gianola, K.J. Hemker, In situ TEM observations of fast grain-boundary motion in stressed nanocrystalline aluminum films, Acta Mater. 56 (2008) 3380–3393. doi:10.1016/j.actamat.2008.03.032.

[108] G. Casillas, A. Ponce, J.J. Velázquez-Salazar, M. José-Yacamán, Direct observation of liquid-like behavior of a single Au grain boundary, Nanoscale. 5 (2013) 6333. doi:10.1039/c3nr01501g.

[109] F. Mompiou, D. Caillard, M. Legros, H. Mughrabi, In situ TEM observations of reverse dislocation motion upon unloading in tensile-deformed UFG aluminium, Acta Mater. 60 (2012) 3402–3414. doi:10.1016/j.actamat.2012.02.049.

[110] Q. Yu, L. Qi, K. Chen, R.K. Mishra, J. Li, A.M. Minor, The nanostructured origin of deformation twinning, Nano Lett. 12 (2012) 887–892. doi:10.1021/nl203937t.

[111] Q. Yu, R.K. Mishra, A.M. Minor, The effect of size on the deformation twinning behavior in hexagonal close-packed Ti and Mg, Jom. 64 (2012) 1235–1240. doi:10.1007/s11837-012-0437-7.

[112] V. Sriram, J.-M. Yang, J. Ye, A.M. Minor, In-situ metrology and testing of nanotwinned copper pillars for potential air gap applications, Microelectron. Eng. 87 (2010) 2046–2049. doi:10.1016/j.mee.2010.04.019.

[113] B.-Y. Liu, J. Wang, B. Li, L. Lu, X.-Y. Zhang, Z.-W. Shan, J. Li, C.-L. Jia, J. Sun, E. Ma, Twinning-like lattice reorientation without a crystallographic twinning plane., Nat. Commun. 5 (2014) 3297. doi:10.1038/ncomms4297.

[114] F. Mompiou, M. Legros, C. Ensslen, O. Kraft, In situ TEM study of twin boundary migration in sub-micron Be fibers, Acta Mater. 96 (2015) 57–65. doi:10.1016/j.actamat.2015.06.016.

[115] D. Häussler, B. Reppich, M. Bartsch, U. Messerschmidt, Interaction processes between dislocations and particles in the ODS nickel-base superalloy INCONEL MA 754 studied by means of in situ straining in an HVEM, Mater. Sci. Eng. A. 309–310 (2001) 500–504. doi:10.1016/S0921-5093(00)01642-7.

[116] D. Häussler, M. Bartsch, U. Messerschmidt, B. Reppich, HVTEM in situ observations of dislocation motion in the oxide dispersion strengthened superalloy MA 754, Acta Mater. 49 (2001) 3647–3657. doi:10.1016/S1359-6454(01)00285-3.

[117] Y. Ijiri, N. Oono, S. Ukai, S. Ohtsuka, T. Kaito, Y. Matsukawa, Oxide particle-dislocation interaction in 9Cr-ODS steel, Nucl. Mater. Energy. 9 (2016) 378–382. doi:10.1016/j.nme.2016.06.014.

[118] C. Motz, T. Schöberl, R. Pippan, Mechanical properties of micro-sized copper bending beams machined by the focused ion beam technique, Acta Mater. 53 (2005) 4269–4279. doi:10.1016/j.actamat.2005.05.036.

[119] D.E.J. Armstrong, C.D. Hardie, J.S.K.L. Gibson, A.J. Bushby, P.D. Edmondson, S.G. Roberts, Small-scale characterisation of irradiated nuclear materials: Part II nanoindentation and micro-cantilever testing of ion irradiated nuclear materials, J. Nucl. Mater. 462 (2015) 374–381. doi:10.1016/j.jnucmat.2015.01.053.

[120] J. Herring, Small Scale Mechanics Applied to Nuclear Materials, St Anne ' s College , University of Oxford, 2015.

[121] J. Gong, A.J. Wilkinson, Anisotropy in the plastic flow properties of single-crystal α titanium determined from micro-cantilever beams, Acta Mater. 57 (2009) 5693–5705. doi:10.1016/j.actamat.2009.07.064.

[122] D.E.J. Armstrong, A.J. Wilkinson, S.G. Roberts, Measuring anisotropy in Young's modulus of copper using microcantilever testing, J. Mater. Res. 24 (2009) 3268–3276. doi:10.1557/jmr.2009.0396.

[123] D.E.J. Armstrong, A.J. Wilkinson, S.G. Roberts, Micro-mechanical measurements of fracture toughness of bismuth embrittled copper grain boundaries, Philos. Mag. Lett. 91 (2011) 394–400. doi:10.1080/09500839.2011.573813.

[124] C. Bohnert, N.J. Schmitt, S.M. Weygand, O. Kraft, R. Schwaiger, Fracture toughness characterization of single-crystalline tungsten using notched micro-cantilever specimens, Int. J. Plast. 81 (2016) 1–17. doi:10.1016/j.ijplas.2016.01.014.

[125] F. Iqbal, J. Ast, M. Göken, K. Durst, In situ micro-cantilever tests to study fracture properties of NiAl single crystals, Acta Mater. 60 (2012) 1193–1200. doi:10.1016/j.actamat.2011.10.060.

[126] K.H. Yano, J.P. Wharry, TEM in situ Cantilever Bending Flow Stress Measurements in Fe-9%Cr ODS, 2018.

[127] D. Kiener, C. Motz, T. Schöberl, M. Jenko, G. Dehm, Determination of Mechanical Properties of Copper at the Micron Scale, Adv. Eng. Mater. 8 (2006) 1119–1125. doi:10.1002/adem.200600129.

[128] M.W. Kapp, C. Kirchlechner, R. Pippan, G. Dehm, Importance of dislocation pile-ups on the mechanical properties and the Bauschinger effect in microcantilevers, J. Mater. Res. 30 (2015) 791–797. doi:10.1557/jmr.2015.49.

[129] E. Tarleton, D.S. Balint, J. Gong, a. J. Wilkinson, A discrete dislocation plasticity study of the micro-cantilever size effect, Acta Mater. 88 (2015) 271–282. doi:10.1016/j.actamat.2015.01.030.

[130] D.E.J. Armstrong, E. Tarleton, Bend Testing of Silicon Microcantilevers from 21C to 770C, JOM. 67 (2015) 2914–2920. doi:10.1007/s11837-015-1618-y.

[131] F.M. Halliday, D.E.J. Armstrong, J.D. Murphy, S.G. Roberts, Nanoindentation and Micromechanical Testing of Iron-Chromium Alloys Implanted with Iron Ions, Adv. Mater. Res. 59 (2009) 304–307. doi:10.4028/www.scientific.net/AMR.59.304.

[132] T.P. Weihs, ,S Hong, J.C. Bravman, W.D. Nix, Mechanical deflection of cantilever microbeams: A new technique for testing the mechanical properties of thin films, J. Mater. Res. 3 (1988) 931–942. doi:10.1557/JMR.1988.0931.

[133] H.H.M. Cleveringa, E. Van Der Giessen, a. Needleman, Discrete dislocation analysis of bending, Int. J. Plast. 15 (1999) 837–868. doi:10.1016/S0749-6419(99)00013-3.

[134] J. Ast, M. Göken, K. Durst, Size-dependent fracture toughness of tungsten, Acta Mater. 138 (2017) 198–211. doi:10.1016/j.actamat.2017.07.030.

[135] N. Jaya B, V. Jayaram, S.K. Biswas, A new method for fracture toughness determination of graded (Pt,Ni)Al bond coats by microbeam bend tests, Philos. Mag. 92 (2012) 3326–3345. doi:10.1080/14786435.2012.669068.

[136] S. Brinckmann, K. Matoy, C. Kirchlechner, G. Dehm, On the influence of microcantilever pre-crack geometries on the apparent fracture toughness of brittle materials, Acta Mater. 136 (2017) 281–287. doi:10.1016/j.actamat.2017.07.014.

[137] J.P. Best, J. Zechner, I. Shorubalko, J.V. Oboňa, J. Wehrs, M. Morstein, J. Michler, A comparison of three different notching ions for small-scale fracture toughness measurement, Scr. Mater. 112 (2016) 71–74. doi:10.1016/j.scriptamat.2015.09.014.

[138] B.D. Snartland, A.B. Hagen, C. Thaulow, Fracture mechanical testing of single crystal notched α-iron micro-cantilevers, Eng. Fract. Mech. 175 (2017) 312–323. doi:10.1016/j.engfracmech.2017.01.024.

[139] W. Cao, Micro-scale Fracture Toughness Testing and Finite Element Analysis in Brittle Materials Micro-scale Fracture Toughness Testing and, Thesis. (2013).

[140] J. Skogsrud, C. Thaulow, Effect of crystallographic orientation on nanomechanical modelling of an iron single crystal cracked cantilever beam, Mater. Sci. Eng. A. 685 (2017) 274–283. doi:10.1016/j.msea.2016.12.060.

[141] S. Brinckmann, C. Kirchlechner, G. Dehm, Stress intensity factor dependence on anisotropy and geometry during micro-fracture experiments, Scr. Mater. 127 (2017) 76–78. doi:10.1016/j.scriptamat.2016.08.027.

[142] N.M. Pugno, R.S. Ruoff, Quantized fracture mechanics, Philos. Mag. 84 (2004) 2829–2845. doi:10.1080/14786430412331280382.

[143] E. Bitzek, J.R. Kermode, P. Gumbsch, Atomistic aspects of fracture, Int. J. Fract. 191 (2015) 13–30. doi:10.1007/s10704-015-9988-2.

[144] M. Sakai, On the fracture toughness of brittle materials, J. Mater. Res. 8 (1993) 668–674. http://adsabs.harvard.edu/abs/1979PhiJR..34....1V.

[145] B.N. Jaya, S. Bhowmick, S.A.S. Asif, O.L. Warren, V. Jayaram, Optimization of clamped beam geometry for fracture toughness testing of micron-scale samples, Philos. Mag. 95 (2015) 1945–1966. doi:10.1080/14786435.2015.1010623.

[146] K. Matoy, H. Schönherr, T. Detzel, T. Schöberl, R. Pippan, C. Motz, G. Dehm, A comparative micro-cantilever study of the mechanical behavior of silicon based passivation films, Thin Solid Films. 518 (2009) 247–256. doi:10.1016/j.tsf.2009.07.143.

[147] B.N. Jaya, J.M. Wheeler, J. Wehrs, J.P. Best, R. Soler, J. Michler, C. Kirchlechner, G. Dehm, Microscale Fracture Behavior of Single Crystal Silicon Beams at Elevated Temperatures, Nano Lett. 16 (2016) 7597–7603. doi:10.1021/acs.nanolett.6b03461.

[148] M.G. Mueller, V. Pejchal, G. Žagar, A. Singh, M. Cantoni, A. Mortensen, Fracture toughness testing of nanocrystalline alumina and fused quartz using chevron-notched microbeams, Acta Mater. 86 (2015) 385–395. doi:10.1016/j.actamat.2014.12.016.

[149] D. Di Maio, S.G. Roberts, Measuring fracture toughness of coatings using focused-ion-beam-machined microbeams, J. Mater. Res. 20 (2005) 299–302. doi:10.1557/JMR.2005.0048.

[150] A. Riedl, R. Daniel, M. Stefenelli, T. Schöberl, O. Kolednik, C. Mitterer, J. Keckes, A novel approach for determining fracture toughness of hard coatings on the micrometer scale, Scr. Mater. 67 (2012) 708–711. doi:10.1016/j.scriptamat.2012.06.034.

[151] I.A. Ovid'Ko, A.G. Sheinerman, Ductile vs. brittle behavior of pre-cracked nanocrystalline and ultrafine-grained materials, Acta Mater. 58 (2010) 5286–5294. doi:10.1016/j.actamat.2010.05.058.

[152] J. Ast, T. Przybilla, V. Maier, K. Durst, M. Göken, Microcantilever bending experiments in NiAl – Evaluation, size effects, and crack tip plasticity, J. Mater. Res. 29 (2014) 2129–2140. doi:10.1557/jmr.2014.240.

[153] S. Ogihara, Y. Imafuku, R. Yamamoto, Y. Kogo, Application of FIB technique to introduction of a notch into a carbon fiber for direct measurement of fracture toughness, J. Phys. Conf. Ser. 191 (2009). doi:10.1088/1742-6596/191/1/012009.

[154] R.O. Ritchie, B. Francis, W.L. Server, Evaluation of Toughness in Aisi 4340 Alloy Steel Austenized At Low and High Temperatures, Metall. Trans. A. 7A (1976) 831–838.

[155] R.O. Ritchie, A.W. Thompson, On macroscopic and microscopic analyses for crack initiation and crack growth toughness in ductile alloys, Metall. Trans. A. 16 (1985) 233–248. doi:10.1007/BF02815305.

[156] L.A. Giannuzzi, J.L. Drown, S.R. Brown, R.B. Irwin, F.A. Stevie, Applications of the FIB lift-out technique for TEM specimen preparation, Microsc. Res. Tech. 41 (1998) 285–290. doi:10.1002/(SICI)1097-0029(19980515)41:4<285::AID-JEMT1>3.0.CO;2-Q.

[157] C.M. Parish, K.G. Field, A.G. Certain, J.P. Wharry, Application of STEM characterization for investigating radiation effects in BCC Fe-based alloys, J. Mater. Res. 30 (2015) 1275–1289. doi:10.1557/jmr.2015.32.

[158] D. Kiener, C. Motz, G. Dehm, Micro-compression testing: A critical discussion of experimental constraints, Mater. Sci. Eng. A. 505 (2009) 79–87. doi:10.1016/j.msea.2009.01.005.

[159] S. Nicolopoulos, D. Bultreys, Precession electron diffraction and TEM applications, (n.d.).

[160] A. Inc., ANSYS Workbench, Academic Research, (n.d.).

[161] Simulia, ABAQUS/Standard User's Manual, n.d.

[162] B. Emile, H. Laurent, C. Rosenberger, B. Cedex, Review and Evaluation of Commonly-Implemented Background, (2008) 2–5.

[163] S. Brutzer, B. Hoferlin, G. Heidemann, Evaluation of background subtraction techniques for video surveillance, Proc. IEEE Comput. Soc. Conf. Comput. Vis. Pattern Recognit. (2011) 1937–1944. doi:10.1109/CVPR.2011.5995508.

[164] O. Barnich, M. Van Droogenbroeck, ViBe: A universal background subtraction algorithm for video sequences, IEEE Trans. Image Process. 20 (2011) 1709–1724. doi:10.1109/TIP.2010.2101613.

[165] O. Barnich, V.D. Marc, VIBE : A POWERFUL RANDOM TECHNIQUE TO ESTIMATE THE BACKGROUND IN VIDEO SEQUENCES Olivier Barnich and Marc Van Droogenbroeck University of Liège Montefiore Institute , INTELSIG Group Liège , Belgium, Int. Conf. Acoust. Speech Signal Process. (2009) 945–948. doi:10.1109/ICASSP.2009.4959741.

[166] M. Van Droogenbroeck, O. Barnich, ViBe: A Disruptive Method for Background Subtraction, Backgr. Model. Foregr. Detect. Video Surveill. (2014) 7-1-7–23. doi:10.1201/b17223-10.

[167] G. Zhang, Z. Zhou, K. Mo, Y. Miao, S. Li, X. Liu, M. Wang, J.-S. Park, J. Almer, J.F. Stubbins, The comparison of microstructures and mechanical properties between 14Cr-Al and 14Cr-Ti ferritic ODS alloys, Mater. Des. 98 (2016) 61–67. doi:10.1016/j.matdes.2016.02.117.

[168] K. Dám, P. Lejček, A. Michalcová, In situ TEM investigation of microstructural behavior of superplastic Al-Mg-Sc alloy, Mater. Charact. 76 (2013) 69–75. doi:10.1016/j.matchar.2012.12.005.

[169] M. Ando, H. Tanigawa, S. Jitsukawa, T. Sawai, Y. Katoh, a. Kohyama, K. Nakamura, H. Takeuchi, Evaluation of hardening behaviour of ion irradiated reduced activation ferritic/martensitic steels by an ultra-micro-indentation technique, J. Nucl. Mater. 307–311 (2002) 260–265. doi:10.1016/S0022-3115(02)01250-3.

[170] A. Chauhan, J. Hoffman, D. Litvinov, J. Aktaa, High-temperature low-cycle fatigue behavior of a 9Cr-ODS steel: Part 1 - pure fatigue, microstructure evolution and damage characteristics, 2Materials Sci. Eng. A. 707 (2017) 207–220.

[171] H. Tang, K.W. Schwarz, H.D. Espinosa, Dislocation escape-related size effects in single-crystal micropillars under uniaxial compression, Acta Mater. 55 (2007) 1607–1616. doi:10.1016/j.actamat.2006.10.021.

[172] S.W. Lee, S.M. Han, W.D. Nix, Uniaxial compression of fcc Au nanopillars on an MgO substrate: The effects of prestraining and annealing, Acta Mater. 57 (2009) 4404–4415. doi:10.1016/j.actamat.2009.06.002.

[173] W.D. Nix, H.J. Gao, Indentation size effects in crystalline materials: A law for strain gradient plasticity, J. Mech. Phys. Solids. 46 (1998) 411–425. doi:10.1016/s0022-5096(97)00086-0.

[174] D.J. Dunstan, A.J. Bushby, The scaling exponent in the size effect of small scale plastic deformation, Int. J. Plast. 40 (2013) 152–162. doi:10.1016/j.ijplas.2012.08.002.

[175] P. V. Patki, Microstructure Evolution and TEM in situ Mechanical Testing of Proton Irradiated Nanocrystalline Copper Tantalum Alloy, Purdue University, 2018.

[176] C.P. Frick, B.G. Clark, S. Orso, A.S. Schneider, E. Arzt, Size effect on strength and strain hardening of small-scale [1 1 1] nickel compression pillars, Mater. Sci. Eng. A. 489 (2008) 319–329. doi:10.1016/j.msea.2007.12.038.

[177] D.M. Dimiduk, M.D. Uchic, T.A. Parthasarathy, Size-affected single-slip behavior of pure nickel microcrystals, Acta Mater. 53 (2005) 4065–4077. doi:10.1016/j.actamat.2005.05.023.

[178] R. Soler, J.M. Wheeler, H.J. Chang, J. Segurado, J. Michler, J. Llorca, J.M. Molina-Aldareguia, Understanding size effects on the strength of single crystals through high-temperature micropillar compression, Acta Mater. 81 (2014) 50–57. doi:10.1016/j.actamat.2014.08.007.

[179] B. Ehrler, X.D. Hou, T.T. Zhu, K.M.Y. P'Ng, C.J. Walker, A.J. Bushby, D.J. Dunstan, Grain size and sample size interact to determine strength in a soft metal, Philos. Mag. 88 (2008) 3043–3050. doi:10.1080/14786430802392548.

[180] J.P. Wharry, K.H. Yano, P. V. Patki, Intrinsic-extrinsic size effect relationship for micromechanical tests, Scr. Mater. 162 (2019) 63–67. doi:S1359646218306742.

[181] ASTM E1820, Standard Test Method for Measurement of Fracture Toughness, Current. 03 (2001) 8–9. doi:10.1520/E1820-11.2.

[182] K.G. Field, X. Hu, K.C. Littrell, Y. Yamamoto, L.L. Snead, Radiation tolerance of neutron-irradiated model Fe-Cr-Al alloys, J. Nucl. Mater. 465 (2015) 746–755. doi:10.1016/j.jnucmat.2015.06.023.

[183] S. Ukai, M. Harada, H. Okada, M. Inoue, S. Nomura, S. Shikakura, T. Nishida, M. Fujiwara, K. Asabe, Tube manufacturing and mechanical properties of oxide dispersion strengthened ferritic steel, J. Nucl. Mater. 204 (1993) 74–80. doi:10.1016/0022-3115(93)90201-9.

[184] J. Chao, R. Rementeria, M. Aranda, C. Capdevila, J.L. Gonzalez-Carrasco, Comparison of ductile-to-brittle transition behavior in two similar ferritic oxide dispersion strengthened alloys, Materials (Basel). 9 (2016). doi:10.3390/ma9080637.

[185] F. Yang, W. Yang, Crack growth versus blunting in nanocrystalline metals with extremely small grain size, J. Mech. Phys. Solids. 57 (2009) 305–324. doi:10.1016/j.jmps.2008.10.011.

[186] E. Hornbogen, K.H. Zum Gahr, Microstructure and fatigue crack growth in a γ-Fe-Ni-Al alloy, Acta Metall. 24 (1976) 581–592. doi:10.1016/0001-6160(76)90104-8.

[187] A. Das, H.W. Viehrig, E. Altstadt, C. Heintze, J. Hoffmann, On the influence of microstructure on the fracture behaviour of hot extruded ferritic ODS steels, J. Nucl. Mater. 497 (2017) 60–75. doi:10.1016/j.jnucmat.2017.10.051.

[188] N. V. Malyar, B. Grabowski, G. Dehm, C. Kirchlechner, Dislocation slip transmission through a coherent Σ3{111} copper twin boundary: Strain rate sensitivity, activation volume and strength distribution function, Acta Mater. 161 (2018) 412–419. doi:10.1016/j.actamat.2018.09.045.

[189] P. Gumbsch, H. Gao, J.D. Eshelby, R.J. Archuletta, J. Schiotz, K.W. Jacobsen, O.H. Nielsen, P. Gumbsch, M.W. Finnis, J.E. Sinclair, G.J. Ackland, R. Thetford, P. Rosakis, H. Tsai, A.I. Yeliseyenko, V.A. Fedorov, Dislocations faster than the speed of sound, Science. 283 (1999) 965–8. doi:10.1126/science.283.5404.965.

[190] I.Y. Kuo, B. Hete, K.K. Shung, A novel method for the measurement of acoustic speed, J. Acoust. Soc. Am. 88 (1990) 1679–1682. doi:10.1121/1.400242.

[191] F. Lanza di Scalea, P. Rizzo, F. Seible, Stress Measurement and Defect Detection in Steel Strands by Guided Stress Waves, J. Mater. Civ. Eng. 15 (2003) 219–227. doi:10.1061/(ASCE)0899-1561(2003)15:3(219).

[192] L. Tan, J.T. Busby, Formulating the strength factor α for improved predictability of radiation hardening, J. Nucl. Mater. 465 (2015) 724–730. doi:10.1016/j.jnucmat.2015.07.009.

[193] E. Arzt, D.S. Wilkinson, Threshold stresses for dislocation climb over hard particles: The effect of an attractive interaction, Acta Metall. 34 (1986) 1893–1898. doi:10.1016/0001-6160(86)90247-6.

[194] J.C. Haley, S.A. Briggs, P.D. Edmondson, K. Sridharan, S.G. Roberts, S. Lozano-Perez, K.G. Field, Dislocation loop evolution during in-situ ion irradiation of model FeCrAl alloys, Acta Mater. 136 (2017) 390–401. doi:10.1016/j.actamat.2017.07.011.

[195] D. Terentyev, Y.N. Osetsky, D.J. Bacon, Competing processes in reactions between an edge dislocation and dislocation loops in a body-centred cubic metal, Scr. Mater. 62 (2010) 697–700. doi:10.1016/j.scriptamat.2010.01.034.

[196] D. Terentyev, F. Bergner, Y. Osetsky, Cr segregation on dislocation loops enhances hardening in ferritic Fe-Cr alloys, Acta Mater. 61 (2013) 1444–1453. doi:10.1016/j.actamat.2012.11.021.

[197] A. Nomoto, N. Soneda, A. Takahashi, S. Ishino, Interaction Analysis between Edge Dislocation and Self Interstitial Type Dislocation Loop in BCC Iron Using Molecular Dynamics, Mater. Trans. 46 (2005) 463–468. doi:10.2320/matertrans.46.463.

[198] S.J. Zinkle, Radiation Effects in Solids, in: NATO Adv. Study Inst. 32nd Course Int. Sch. Solid State Phys., Erice, Sicily, Italy, n.d.

PUBLICATIONS

1. Yano, K. H., Wharry, J. P. (2019). *In Situ TEM Mechanical Testing of Irradiated Oxide Dispersion Strengthened Alloys.* Purdue University Research Repository. doi:10.4231/100X-1R88

2. K.H. Yano, Y. Wu, J.P. Wharry. *TEM in situ Clamped Beam Fracture in Fe-9%Cr ODS.* In progress.

3. K.H. Yano, Y. Wu, J.P. Wharry. *Size Effects in TEM in situ Cantilever Flow Stress Measurements in Irradiated Fe-9%Cr ODS.* Submitted. Materials Science and Engineering: A. (2019).

4. K.H. Yano, K. Mao, J.P. Wharry, and D.M. Porterfield. *Investing in a permanent and sustainable nuclear waste disposal solution.* Progress in Nuclear Energy 108 (2018) 474-479.

5. K.H. Yano, S. Thomas, M.J. Swenson, Y. Lu, and J.P. Wharry. *TEM* in situ *cube-corner indentation analysis using ViBe motion detection algorithm.* Journal of Nuclear Materials 502 (2018) 201-212. doi:10.1016/j.jnucmat.2018.02.003

6. J.P. Wharry, M.J. Swenson, and K.H. Yano. *A review of the irradiation evolution of dispersed oxide nanoparticles in b.c.c. Fe-Cr alloys: current understanding and future directions.* Journal of Nuclear Materials 486 (2017) 11-20. doi:10.1016/j.jnucmat.2017.01.009 **PlumX Top Ten of 2017**.

7. K.H. Yano, M.J. Swenson, Y. Wu, and J.P. Wharry. *TEM* in situ *micropillar compression tests of ion irradiated oxide dispersion strengthened alloy.* Journal of Nuclear Materials 483 (2017) 107. doi:10.1016/j.jnucmat.2016.10.049 and doi:10.1016/j.jnucmat.2017.04.054